THE SIGNIFICANCE OF ATYPICAL HIGH-SILICA IGNEOUS ROCKS

Ryan Edward Frazer

A dissertation submitted to the faculty of the University of North Carolina at Chapel Hill in partial fulfillment of the requirements for the degree of Doctor of Philosophy in the Department of Geological Sciences.

Chapel Hill
2017

Approved by:

Drew S. Coleman

Allen F. Glazner

Ryan D. Mills

John M. Bartley

Kevin G. Stewart

ABSTRACT

RYAN E. FRAZER: The significance of atypical high-silica igneous rocks
(Under the direction of Drew S. Coleman)

The origins of high-silica igneous rocks are debated, as they may be products of high-degree fractional crystallization or low-degree partial melting. They may play a role in the generation of intermediate igneous rocks and are responsible for large, ash-rich volcanic eruptions. High-silica granites and rhyolites in the Sierra Nevada, California, and the Colorado Mineral Belt (CMB) are investigated using isotope geochemistry to better understand how they bear on these issues.

Zircon U-Pb geochronology identifies two intrusive suites comprising large volumes of high-silica granites emplaced in the mid-Cretaceous Sierra Nevada batholith: the 106-98 Ma Shaver Intrusive Suite (SIS) in the central part of the batholith, and the 103-100 Ma Kearsarge intrusive suite (KIS) on the Sierra Crest and Owens Valley. High-silica granites in both suites have relatively high concentrations of middle rare earth and high field strength elements. Data for these and other discrete high-silica plutons in the batholith suggest they were derived from titanite-free sources in the deep crust, unlike similarly felsic parts of zoned intrusive suites. Despite similar trace element signatures, SIS and KIS high-silica granites have divergent isotopic compositions. High-silica granites of the SIS have supracrustal O in zircon, crustal Sr and Nd whole rock isotopic compositions, and negative Ce anomalies suggesting the SIS granites may have been derived from oceanic sedimentary sources. In contrast, KIS granites have mantle-like

isotopic compositions. The location and geochemistry of the KIS suggests it may have resulted from backarc magmatism in the mid-Cretaceous Sierra.

Volcanic and plutonic rocks in the central CMB were emplaced during the Laramide orogeny and subsequent Oligocene-Eocene volcanic flare-up. Strontium and Nd data suggest the 63-39 Ma Twin Lakes pluton and igneous rocks as young as 24 Ma were derived from a persistent mafic lower crust or enriched lithospheric mantle source. In contrast, the ~35 Ma Grizzly Peak Tuff and resurgent plutons are isotopically dissimilar from each other and the CMB as a whole, suggesting derivation by partial melting of ancient felsic lower crust. This distinct source could account for the lack Mo mineralization in the Grizzly Peak caldera relative to other high-silica parts of the CMB.

To Sarah,
who makes me a better person every day

ACKNOWLEDGMENTS

I am forever thankful to have had Drew Coleman as my advisor for seven years and two degrees. His knowledge and humor helped me through thick and thin, making me a better scientist, teacher, and person. I thank him and Ryan Mills, who mentored me as an officemate, committee member, and friend, for introducing me to coffee. I am indebted to Allen Glazner for recruiting me to Carolina and making me a more thoughtful geologist. Committee members Kevin Stewart and John Bartley provided valuable insights that improved this work considerably. I owe a debt of gratitude to Jade Star Lackey for introducing me to Sierra Nevada geology, and for support and patience as I continually expanded and reworked chapter 1 of this dissertation. Jennifer Wenner and Matt Zimmerer kindly provided samples that were essential to this work. My dissertation benefitted from conversations and help from numerous graduate students over the years, in particular Courtney Beck, Tom Chapman, Adam Curry, Maggie Ellis, Connor Lawrence, Roger Putnam, and Josh Rosera. I especially thank Sean Gaynor for his assistance with fieldwork in the Alabama Hills and Grizzly Peak, his lab and science expertise, and his sunny disposition.

This work was generously funded by the Geological Society of America, the National Science Foundation, Sigma Xi, the UNC Department of Geological Sciences Martin Fund, and a UNC Graduate School Dissertation Completion Fellowship.

Finally, I would like to thank my family. My parents, Brett and Tricia, who unwaveringly encouraged me and always seemed to know how to help. And my wife, Sarah, who supported me through all of this, and with whom I am so lucky to build a life and a family.

TABLE OF CONTENTS

LIST OF TABLES

LIST OF FIGURES

Chapter 2

Chapter 3

CHAPTER 1: INTRODUCTION

The relationships between intrusive and extrusive igneous rocks have been discussed and disputed for centuries (e.g., Lyell, 1838; Daly, 1933). However, methodological improvements of the past two decades have breathed new life into the debate. For example, advances in ultraclean lab procedures and pre-treatment of zircons (e.g., Parrish, 1987; Mattinson, 2005) now permit accurate and precise dating of individual zircon grains and fragments to 0.1% (e.g., Samperton et al., 2015). These enhancements have led to the application of high-precision geochronology to multiple samples from single plutons, and dozens of samples dated from entire intrusive suites. Coleman et al. (2004) were among the first to date an intrusive suite at high sample density by U-Pb in zircon, finding that emplacement of the Tuolumne Intrusive Suite in the Sierra Nevada batholith spanned a ~10 Ma period, and a single pluton was intruded over at least 4 Ma. That study raised questions regarding the links between plutonic and volcanic rocks because it implied that large magma chambers may be ephemeral. Glazner et al. (2004) extended this line of thinking, suggesting that intrusion rates may govern the fate of magmas in the upper crust.

Numerous studies in the past decade have used Coleman et al. (2004) and Glazner et al. (2004) as touchstones for investigations of plutonic-volcanic connections. A review of those works is beyond the scope of this introduction. However, much of the work since 2004 has focused on intermediate-composition rocks (e.g., Bachmann et al., 2007; Lipman, 2007; Wotzlaw et al., 2013; Mills and Coleman, 2013; Lee and Bachmann, 2014). This is logical because granodiorite plutons are common in batholiths such as the Sierra Nevada (Bateman, 1992), and

dacites comprise the spectacular crystal-rich ash-flow tuffs known as monotonous intermediates (Hildreth, 1981). I contributed to this body of work with my Masters (Frazer et al., 2014), in which I investigated the postulated links between the 4500 km^3 Mount Givens Granodiorite and compositionally and volumetrically similar monotonous intermediates, such as the 5000 km^3 Fish Canyon Tuff. I concluded that zircon in both plutonic and volcanic intermediate rocks faithfully reflects their respective accumulation histories and therefore, despite their superficial similarities, the exposed Mount Givens Granodiorite accumulated too slowly to have supported a Fish Canyon-like super-eruption.

High-silica igneous rocks (i.e., greater than 70 wt% SiO_2; granites and rhyolites *sensu lato*) have not been overlooked in the volcano-pluton debate (e.g., Glazner et al., 2008; Bachmann and Bergantz, 2008; Coleman et al., 2012; Lundstrom and Glazner, 2016). High-silica igneous rocks are important because they may represent either very high-degree fractional crystallization (e.g., Tuttle and Bowen, 1958; Lee and Morton, 2015) or low-degree partial melting (e.g., Sisson et al., 2005; Stevens et al., 2007) of more mafic progenitors, and because they also bear on the elemental and isotopic compositions of intermediate-composition rocks that may result from magma mixing (Eichelberger, 1975; Wenner and Coleman, 2004; Gray et al., 2008). Debate continues as to whether chemical signatures in high-silica igneous rocks reflect fractional crystallization (Keller et al., 2015; Lee and Morton, 2015) or partial melting (Glazner et al., 2015; Clemens and Stevens, 2016). Another question in this debate is whether high-silica intrusive rocks represent new additions to the crust, or are the products of recycling pre-existing crust. Some models call for high-silica magmas to be the extensively recycled (Bindeman and Simakin, 2014), or to be the results of fractional crystallization after homogenization of primitive mantle and Proterozoic rocks in deep crustal hot zones (Lee and Bachmann, 2014). In contrast, others

suggest that high silica magmas may be generated through partial melting of juvenile mafic materials that were themselves recently derived from the mantle (Coleman et al., 1992; Wenner and Coleman, 2004), thus representing new crustal growth.

This dissertation investigates the occurrence and significance of high-silica granites and rhyolites from mid-Cretaceous parts of the Sierra Nevada batholith, California, and the Cenozoic central Colorado Mineral Belt using compositional and isotopic analyses of whole rocks and the mineral zircon. The first two chapters concern the mid-Cretaceous Sierra Nevada. Chapter one examines the compositionally diverse Shaver Intrusive Suite; whereas its largest pluton is granodiorite, like the Tuolumne and other Late Cretaceous Sierra suites, the suite also comprises nearly a dozen discrete high-silica granite plutons. Many of those plutons preserve chemical and isotopic evidence suggesting they represent significant crustal recycling. Chapter two investigates the origins of the Alabama Hills block east of the Sierra Nevada, which includes a high-silica granite that is now known to be ~102 Ma and therefore is similar in age to high silica granites on the Sierra crest. New age and isotopic data suggest those granites (part of the informal Kearsarge intrusive suite) may be mantle-derived and represent new crustal additions, in contrast to the Shaver granites. The Shaver and Kearsarge suites are part of a ~105-100 Ma magmatic event that appears to have favored granitic magma production relative to earlier and later magmatism in the batholith. High-silica granites such as these also appear to be compositionally appropriate end members for mixing with mafic magma to generate the voluminous granodioritic suites of the Sierra Crest magmatic event. Chapter three extends the analysis to extrusive rocks. The Grizzly Peak Tuff, an Eocene rhyolitic caldera-forming system in the central Colorado Mineral Belt, has a more enriched isotopic signature than older and younger igneous rocks adjacent to the caldera. Moreover, the tuff and its resurgent plutons are isotopically distinct from rocks throughout

the mineral belt. The tuff's isotopic composition suggests it was derived in from felsic Proterozoic lower crust, and thus represents a large degree of crustal recycling. In contrast, the relatively constant isotopic compositions of igneous rocks preceding and following eruption of the tuff imply a long-lived, voluminous source inferred to be either enriched lithospheric mantle or lower crust, or a combination of the two. With these studies, my dissertation seeks to demonstrate the utility high-silica rocks have for understanding deep magma sources and processes, including recycling of old crust and production of new crust.

CHAPTER 2: AGES AND SOURCES OF THE SHAVER INTRUSIVE SUITE: SNAPSHOTS OF CRUSTAL RECYCLING IN THE CENTRAL SIERRA NEVADA BATHOLITH, USA

INTRODUCTION

Resolving the hierarchy of magmatic processes leading to the assembly of plutons, intrusive suites, and batholiths is critical to deciphering the geodynamics of magmatic arcs. Studying these systems and subsystems in detail provides greater insight into the overarching tectonic controls of arc magmatism, the tempo and mode of magma transport, and the thermal and mass balance of arcs, which are loci of crustal growth and recycling. The Cordilleran batholiths of western North America record a protracted period of Mesozoic magmatism. Despite decades of study, the controls on magma production and emplacement, including the importance of tectonic controls (e.g. Glazner, 1991; Tikoff and Teyssier, 1992; Tobisch et al., 1995), particularly in the Cretaceous Sierra Nevada batholith of California (Bateman, 1992), remain poorly understood.

Recent studies have centered on the emplacement and hybridization of middle and upper crustal plutons. In particular, high-precision U-Pb zircon dating of intrusive suites belonging to the 98-86 Ma Sierra Crest magmatic event (Coleman and Glazner, 1997) has fueled debate about how mapped plutons may be built incrementally over ~10 Ma timescales, far longer than the thermal lifetime of magma bodies in the upper crust (Glazner et al., 2004; Annen, 2009). The Late Cretaceous suites comprise older mafic units, intermediate- to late-stage megacrystic granodiorites, and late stage granitic intrusions, with suites recording both mantle and crustal sources

(Gray et al., 2008) or simply an enriched mantle source (Coleman et al., 1992). In contrast, Early Cretaceous magmatism in the western parts of the batholith resulted in chemical and temporal variations that are not as well organized, with isotopic data suggesting an increase in crustal inputs over time (Lackey et al., 2012; Holland et al., 2013).

The centrally-located Shaver Intrusive Suite (SIS; Fig. 1) presents an opportunity to assess the transition between contrasting older and younger magmatic styles in the batholith because it superficially shares qualities of both Early and Late Cretaceous magmatism in the Sierra. The SIS is similar to the older suites in that it is not concentrically zoned, yet it is generally more felsic than the western suites (Bateman, 1992). Like many of the younger intrusive suites of the batholith, the SIS is predominantly composed of granodiorite. However, it contrasts with many of the Late Cretaceous suites because the granitic and dioritic plutons of the SIS are discrete intrusions lacking gradational contacts (Bateman and Wones, 1972a). It is also an intriguing location to study changing magmatic styles and sources because the SIS is at the nexus of several proposed geochemical provinces and boundaries, including the $^{87}Sr/^{86}Sr_i = 0.706$ line, the Panthalassan/North American lithospheric break, and the strongly contaminated and reduced zone (Kistler and Peterman, 1973; Ague and Brimhall, 1987, 1988; Kistler, 1990). Thus, it may represent a critical transition in the Cretaceous Sierran arc.

GEOLOGIC BACKGROUND

The SIS (Fig. 1) is located in the central Sierra Nevada batholith of California, flanked on the west by the 124–105 Ma Fine Gold Intrusive Suite (Lackey et al., 2012) and on the east by the 98–91 Ma Mount Givens Granodiorite (Frazer et al., 2014).

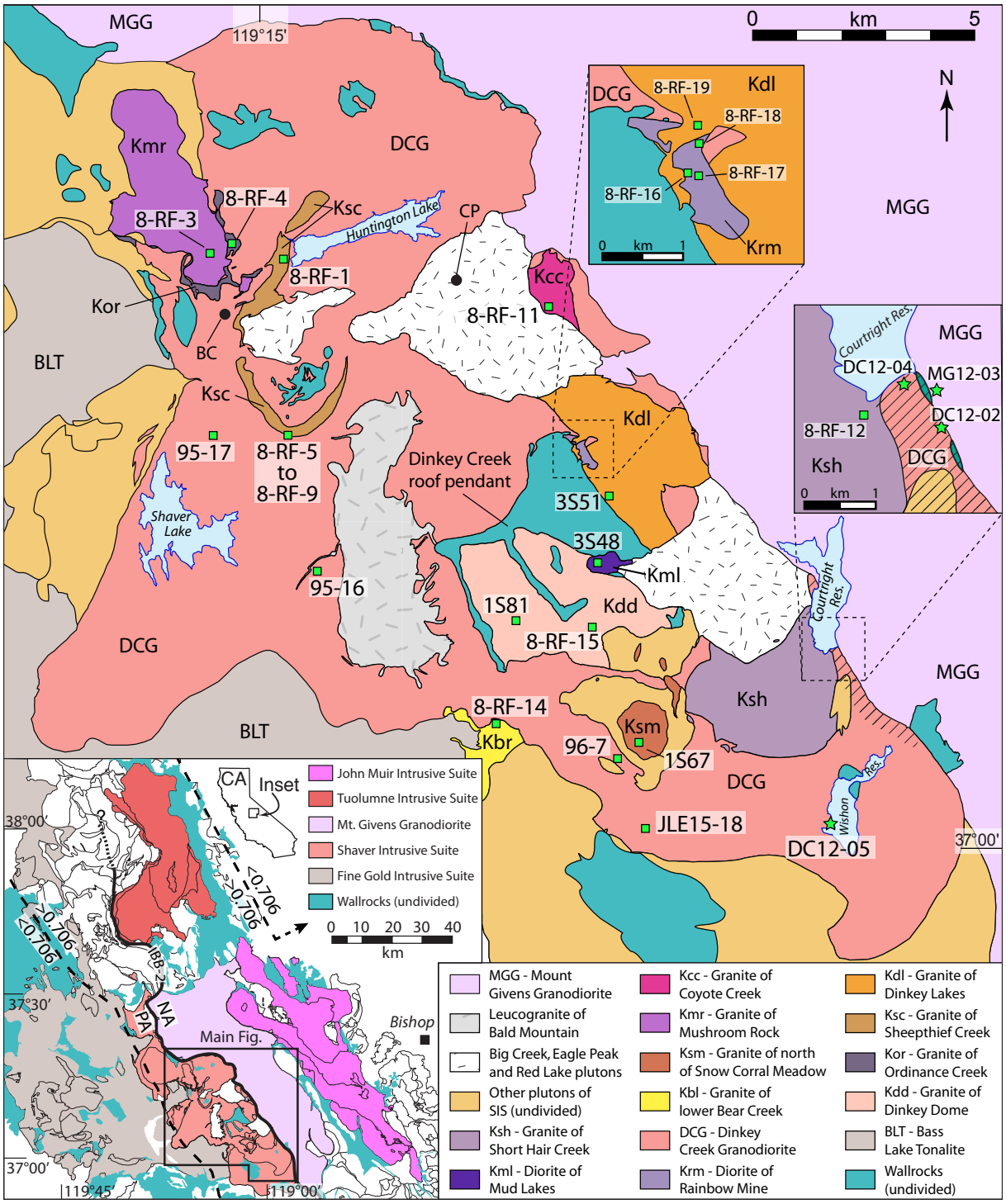

Figure 1. Generalized bedrock geologic map of the Shaver Intrusive Suite. Informal names of individual plutons are given in the legend and Table 1. Inset gives location of Shaver Intrusive Suite relative to other Cretaceous intrusive suites of the central Sierra Nevada as well as approximate locations of the $^{87}Sr/^{86}Sr_i = 0.706$ line, intrabatholithic break 2, and the PA-NA (Panthalassan-North American) boundary after Kistler and Peterman (1973), Kistler (1990, 1993), Saleeby and Busby (1993) and Lackey et al. (2008, 2012). Green symbols: samples analyzed in this study; green stars: samples dated by ID-TIMS; black circles: locations of Cenozoic volcanic pipes (BC – Big Creek; CP – Chinese Peak). Maps after Bateman (1965), Bateman et al. (1971), Bateman and Wones (1972a), Lockwood and Bateman (1976), Bateman (1992) and Lackey et al. (2008).

Wallrocks

Metamorphic wallrocks in and around the SIS are dominated by quartzite, with subordinate pelitic hornfels, schist, calc-silicate hornfels, and marble (Huber, 1968; Bateman et al., 1971; Bateman and Wones, 1972a; Lockwood and Bateman, 1976). The Dinkey Creek roof pendant is the most prominent wallrock mass exposed in the SIS, and it has been proposed to belong to terranes of various ages from the late Proterozoic to early Cambrian Snow Lake block (Lahren and Schweickert, 1989), to the Triassic-Jurassic Kings sequence (Kistler, 1993; Saleeby and Busby, 1993).

Shaver Intrusive Suite plutons

The SIS comprises numerous intermediate and felsic plutons plus scattered diorite bodies (Bateman, 1992). It is dominated by the Dinkey Creek Granodiorite (DCG), which ranges in composition from tonalite to granite, but is typically granodiorite in both equigranular and megacrystic facies (Bateman, 1992). The DCG contains abundant mafic enclaves that are hypothesized to result from magma mingling and stirring of a stratified magma chamber (Barbarin et al., 1989; Dorais et al., 1990; Cruden et al., 1999). Mafic orbs and comb layering are present near Deer Creek in a tonalitic portion of the DCG (Moore and Lockwood, 1973; Dodge and Kistler, 1990). Two shear zones are preserved at the DCG's margins, including the Kaiser shear zone in the north and the Courtright shear zone in the southeast (Tobisch et al., 1995). The Courtright shear zone is particularly well studied and records a two-stage strain history of weak extension followed by contraction, around 90 Ma (Tobisch et al., 1993; Renne et al., 1993). The DCG has previously been dated by isotope dilution thermal ionization mass spectrometry (ID-TIMS) at 104 Ma in its southwestern lobe (Stern et al., 1981) and 102 ± 1 Ma in the Courtright shear zone

(Fig. 1; Tobisch et al., 1993). Beck (2013) reported chemically abraded (CA) ID-TIMS data for single-zircon fractions in two samples from the DCG ranging from 101.4–100.6 Ma. Using laser ablation multi collector inductively coupled plasma mass spectrometry (LA-MC-ICP-MS), Lackey et al. (2012) dated a mafic enclave and its granodiorite host from the southern portion of the DCG, yielding indistinguishable ages of 99.4 ± 1.3 Ma and 101.5 ± 1.2 Ma, respectively.

This study focuses only on plutons within and adjacent to the DCG; additional large plutons of the SIS of Bateman (1992), including the granodiorites of McKinley Grove, Whiskey Ridge, Stevenson Creek, and the granite of Shuteye Peak, extend to the north and south of the DCG and are not considered here in part because of their uncertain ages. For example, the granite of Shuteye Peak west of Shaver Lake was dated by Stern et al. (1981) at 102 Ma, whereas Lackey et al. (2012) dated a different exposure of the same pluton at ~114 Ma.

Previous field studies proposed that the DCG is intruded by the all of the areally subordinate plutons in the SIS, including the granites of Dinkey Dome, Short Hair Creek, Sheepthief Creek, lower Bear Creek, Mushroom Rock, north of Snow Corral Meadow, and Ordinance Creek (Hamilton, 1956; Bateman et al., 1971; Bateman and Wones, 1972a; Lockwood and Bateman, 1976; Guy, 1980; Bateman, 1992; Cruden et al., 1999). This group of high-silica plutons will hereafter be informally referred to as the Shaver granites. Bateman (1992) interpreted the DCG foliations that parallel the Shaver granites to suggest that the smaller felsic plutons postdate the DCG, deforming the DCG as they were emplaced. However, beyond field relationships, little work has been done on the Shaver granites.

The Shaver granites are discontinuous and feature at least six plutons as defined by Bateman and Wones (1972a; 1972b) using texture and mineralogy (Fig. 1). Several plutons have separate exposures or are previously unnamed. Herein each exposure is informally named after

a landmark within it or nearby. Some of the Shaver granites are associated with small bodies of diorite, of unknown age (Bateman, 1992). Two of the Shaver granites are nested: the Mushroom Rock pluton is mantled by the slightly more mafic Ordinance Creek pluton, and the granite north of Snow Corral Meadow is surrounded by the granodiorite of McKinley Grove.

Shaver Intrusive Suite petrology and geochemistry

Past geochemical analyses of the Shaver granites show they are more siliceous (73–78 wt% SiO_2) than the DCG (48–71 wt% SiO_2; average is 65 wt% SiO_2). Moreover, some of the granites have magmatic garnet and muscovite (Fig. 2), and more unusual accessory mineral assemblages locally that include andalusite, sillimanite, molybdenite, and/or urananite (Hamilton, 1956; Bateman and Wones 1972b; Guy, 1980; Ague and Brimhall, 1988; Hinke, 2002, Lackey et al. 2006). Cordierite, a key indicator of S-type granites, is not recognized in the SIS (Ague and Brimhall, 1987). Ague and Brimhall (1988) assigned the SIS to a belt of "strongly contaminated and reduced" plutons on the basis of mineralogy and mineral compositions, particularly the greater amounts of ilmenite over magnetite, the relative lack of titanite, and the presence of Fe-rich biotite.

Isotopically, the DCG has relatively high initial $^{87}Sr/^{86}Sr$ ($^{87}Sr/^{86}Sr_i$) values compared to nearby suites (Dodge et al., 1986; Kistler, 1990). The SIS is east of the $^{87}Sr/^{86}Sr_i = 0.706$ line, inferred to be an expression of the premagmatic boundary between Proterozoic North American continental lithosphere to the east and accreted arc terranes to the west (Fig. 1; Kistler and Peterman, 1973). There are no published isotopic data for the Shaver granites.

Sub-arc xenolith suites

Cenozoic alkali basalt lavas of the San Joaquin volcanic field erupted through the SIS

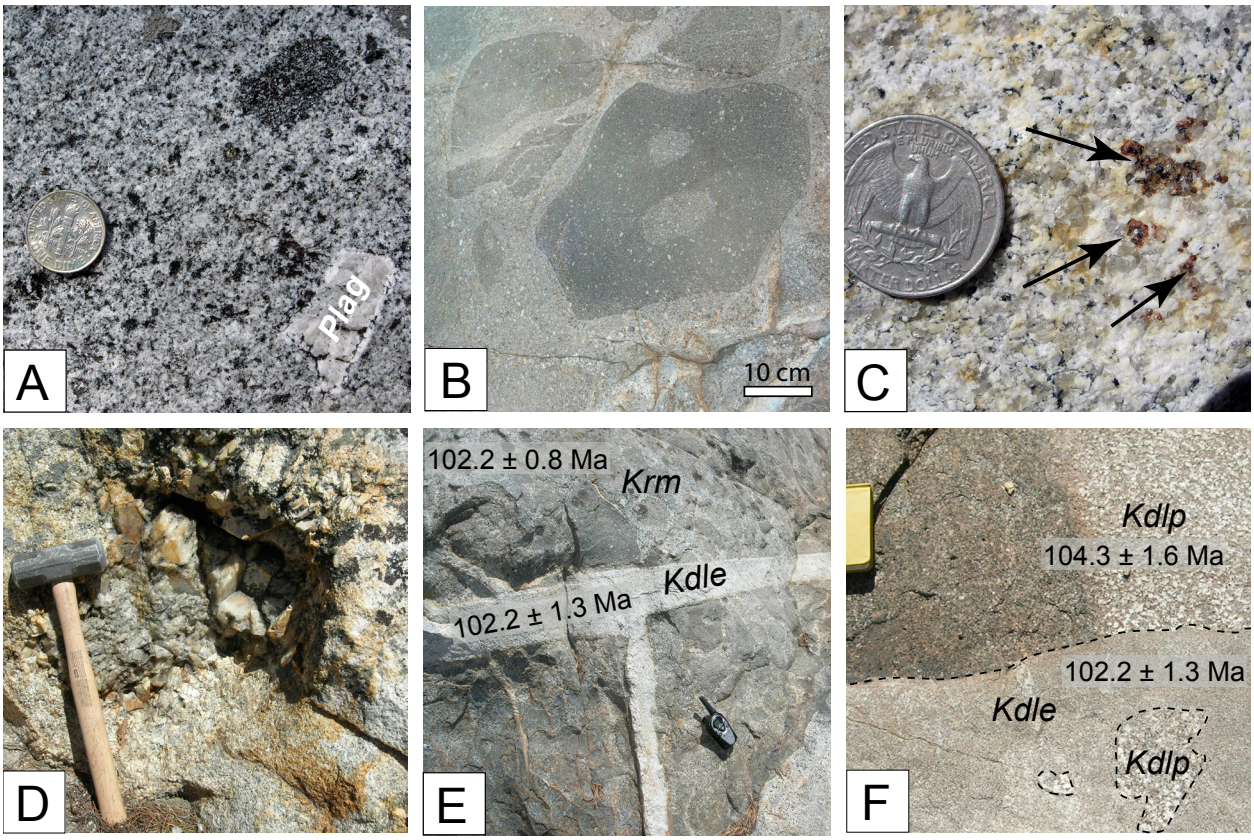

Figure 2. Field relations in the SIS. (A) Ordinance Creek pluton showing rapakivi rims on feldspar. (B) Mafic magmatic enclaves within the diorite of Mud Lakes. (C) Red garnet glomerocrysts in the Coyote Creek pluton. (D) Large miarolitic cavity in the Coyote Creek pluton with inward radiating euhedral K-feldspar and quartz crystals. Hammer handle length approximately 30 cm. (E) Dike of the equigranular facies of the Dinkey Lakes pluton intruding the diorite of Rainbow Mine. Laser ablation weighted mean ages shown were not acquired on this outcrop. Radio length approximately 15 cm. (F) Field relationships between porphyritic and equigranular facies of the Dinkey Lakes pluton. Laser ablation weighted mean ages shown were not acquired on this outcrop. Length of side of field notebook approximately 12 cm.

host nearly all known xenoliths of lower crustal and upper mantle origin from the Sierran arc (Fig. 1; Dodge et al. 1986, 1988), including Cretaceous-aged samples (Ducea and Saleeby, 1998). These xenolith suites provide understanding of the dynamics of magma formation and extraction in the Sierran arc (Mukapadahay and Manton, 1994, Ducea, 2001; 2002; Chin et al., 2014). Thus, the SIS is one of the few locations in the Cordillera where the connectivity of the petrogenetic record between coeval granitoids and xenoliths from the base of the arc can be evaluated.

METHODS

Sample collection and preparation

Samples from the SIS were collected for zircon separation and whole rock chemical analyses. In addition, samples of the Mount Givens Granodiorite corresponding to those dated by Frazer et al. (2014) were analyzed for their whole rock isotopic compositions.

Geochronology aliquots were crushed using standard techniques and zircon was isolated by gravimetric (water table and methylene iodide) and magnetic concentration methods. Analyzed zircons were hand-picked under a binocular microscope from the non-magnetic split on a Frantz magnetic separator. Grains were selected to be clean, inclusion-free, unbroken and typical of the population. Whole rock geochemical aliquots were pulverized to powder using standard crushing techniques outlined below.

U-Pb geochronology

LA-MC-ICP-MS

Most of the geochronologic data were collected at the University of Arizona LaserChron Center by LA-MC-ICP-MS. Zircon grains were mounted along with chips of Sri Lankan zircon standard SL-2 (Gehrels et al., 2008) in 1" epoxy rounds. Most mounts were initially characterized by scanned color cathodoluminescence (CL) at California State University, Bakersfield on a Hitachi S-3400N SEM at 10.0 kV.

Laser ablation analyses of all samples except those from the DCG and the Courtright shear zone were performed with a New Wave/Lambda Physik DUV193 Excimer laser operating at a wavelength of 193 nm using a spot diameter of 25-35 microns. The ablated material was carried with helium gas into the plasma source of a GV Instruments Isoprobe, which was equipped

with a flight tube of sufficient width that U, Th, and Pb isotopes were measured simultaneously. All measurements were made in static mode, using Faraday detectors for ^{238}U and ^{232}Th, an ion-counting channel for ^{204}Pb, and either faraday collectors or ion counting channels for ^{208}Pb-^{206}Pb. Ion yields were ~1 mv per ppm. Each analysis consisted of one 20-second integration on peaks with the laser off (for backgrounds), 20 one-second integrations with the laser firing, and a 30 second delay to purge the previous sample and prepare for the next analysis. The ablation pit was ~15 microns in depth.

Zircon U-Pb isotopic data from samples 95-16, 95-17 and 96-7 from the DCG were collected using a New Wave 193 nm ArF laser ablation system coupled to a Nu Plasma HR inductively-coupled plasma mass spectrometer (ICP-MS) at the University of Arizona following the methods of Gehrels et al. (2008) and Lackey et al. (2012). See http://sites.google.com/a/laserchron.org/laserchron/ for additional information.

For all laser ablation samples, inter-element fractionation of Pb/U is generally ~20%, whereas fractionation of Pb isotopes is generally less than 2%. In-run analysis every fifth measurement of fragments of SL-2, a Sri Lankan zircon crystal with known age of 564 ± 4 Ma (2σ error), is used to correct for this fractionation (Gehrels et al., 2008). The uncertainty resulting from the calibration correction is generally ~1% (2σ) for both $^{206}Pb/^{207}Pb$ and $^{206}Pb/^{238}U$ ages. The analytical data are reported in Appendix 1. Uncertainties shown in these tables are at the 2σ level, and include only measurement errors. The systematic error, which includes contributions from the standard calibration, age of the calibration standard, composition of common Pb, and U decay constants, is generally 1–2% (2σ). Common Pb correction was accomplished using the measured ^{204}Pb and assuming an initial Pb composition using the model of Stacey and Kramers (1975) with uncertainties of 1.0% for $^{206}Pb/^{204}Pb$ and 0.3% for $^{207}Pb/^{204}Pb$.

ID-TIMS

Four samples (DC12-02, MG12-03, DC12-04, and DC12-05) were analyzed by CA-ID-TIMS on a VG Sector 54 in the Department of Geological Sciences at the University of North Carolina at Chapel Hill following the sample preparation and analytical methods of Frazer et al. (2014). Data processing and age calculations were completed in the applications Tripoli and ET_Redux (Bowring et al., 2011; McLean et al., 2011). Corrections for initial Th/U disequilibrium (Mattinson, 1973; Schmitz and Bowring, 2001) were made in ET_Redux assuming the measured whole rock Th/U value (Table 3) for each sample approximates the magmatic value; this adjustment increased the ages of individual analyses by up to 100 ka.

$\delta^{18}O$ analysis

Bulk aliquots of zircon (4–5 mg) were picked and cleaned with HNO_3, HCl, and HF acid, with the latter removing radiation-damaged material from the zircon grains, which can alter $\delta^{18}O$ (Valley, 2003). Zircon crystals were powdered with a tungsten carbide mortar and pestle to facilitate fluorination (Lackey et al., 2008). Oxygen isotopes were analyzed by laser fluorination at the Stable Isotope Lab at the University of Oregon using a 35W New Wave CO_2 IR laser in a reagent atmosphere of bromine pentafluoride to liberate O_2 with the F^- anion. Liberated O_2 was passed through a hot Hg pump to remove excess F, then converted to CO_2 by reaction with a hot graphite rod. CO_2 gas was analyzed for $\delta^{18}O$ with a Finnigan MAT 253 mass spectrometer. Values are reported as $\delta^{18}O$ in ‰ relation to Vienna Standard Mean Ocean Water (VSMOW). Unknowns were corrected to Gore Mountain garnet (accepted value = 5.80‰; Valley et al., 1995) analyzed throughout the analytical session.

Whole rock elemental geochemistry

Whole rock powders of all samples except DC12-02, MG12-03, DC12-04, and DC12-05 were prepared in a Rocklabs® tungsten carbide head and mill. Powdered sample and flux were mixed at a 2:1 ratio, typically 3.5 g powder to 7.0 g dilithium tetraborate. The vortexer-blended mixture was fused to a glass bead in a graphite crucible at 1000°C for 10 minutes, reground, fused a second time, polished on diamond laps, and analyzed. Major oxides and 17 trace elements (Ba, Ce, Cr, Cu, Ga, Nb, Ni, Pb, Rb, Sc, Sr, Th, U, V, Y, Zn, Zr) are analyzed on the same fused bead using a 3.0 kW Panalytical Axios WD-XRF at Pomona College equipped with PE, LiF 200, LiF 220, GE, and PX1 crystals. Concentrations were determined using reference calibration curves defined by fifty-five certified reference materials that span a range of natural igneous, metamorphic, and sedimentary rock compositions. Oxides (in wt%) are totaled pre-normalization based on iterating analysis after determination of initial loss on ignition in the first analysis. Total Fe is reported as Fe_2O_3. Typical analytical uncertainties for major elements in absolute wt%, determined by fusion of duplicate powders, are ± 0.15% (SiO_2); 0.06–0.07% (Fe_2O_3, Al_2O_3); 0.02–0.05% (Na_2O, K_2O, MgO, CaO); <0.004% (TiO_2, MnO, P_2O_5). Trace element uncertainties at ±2σ vary, with most trace elements reproducible at better than 2 ppm: (Cu, Ga, Nb, Pb, Rb, Th, U, Y, Zr). Others are reproducible at 3 ppm (Cr, Sc, Sr, V), and a handful have higher uncertainties, in parentheses in ppm: Zn (6); Ni (7); Ba (40). Rare earth elements for samples 8-RF-1, 8-RF-3, 8-RF-19, 1S67, 1S81, 3S48, and 3S51 were measured by ICP-MS at Vrije University using the methods of Klaver et al. (2015).

Whole rock aliquots of samples DC12-02, MG12-03, DC12-04, and DC12-05, plus the samples of Frazer et al. (2014), were crushed to powder in a SPEX Shatterbox® alumina swing mill and analyzed at Actlabs (Ontario, Canada). Samples were dissolved by fusion in a lithium

metaborate/tetraborate mixture. Major elements and Ba, Sr, Y, Zr, Sc, Be and V were analyzed by inductively coupled plasma-optical emission spectroscopy (ICP-OES), with remaining trace elements and REE analyzed by ICP-MS. Relative uncertainties (±2σ) for major elements were less than 2% for all oxides except MgO (3%), MnO (5%), and P_2O_5 (16%). Trace elements analyzed at Actlabs that are reproducible (±2σ) at better than 2 ppm include Ag, Be, Cs, Ge, Hf, Sb, Sn, Ta, Th, Tl, U, and W. Other elements are reproducible within 3 ppm (Co, Mo, Nb, Sc), 4 ppm (Ga, Y) and others have higher uncertainties, in parentheses in ppm: Pb (9); Cu (14); Rb and Zr (15); V (19); Ni (23); Sr (25); Ba (31); Zn (42); Cr (49). Rare earth elements reproducible (±2σ) at 0.2 ppm or better are Eu, Ho, Lu, Tb, and Tm; REE reproducible at 0.2–0.5 ppm or better are Dy, Er, Gd, Pr, Sm, and Yb; others are reproducible at higher uncertainties, in ppm: Nd (1.2); La (1.5); Ce (2.1).

Strontium and neodymium isotopic analyses

Whole rock powders of samples 8-RF-1, 8-RF-3, 8-RF-19, 1S67, 1S81, 3S48, and 3S51 were dissolved in Teflon® bombs and separated using column chromatography following standard procedures outlined in Heumann and Davies (2002). Both Sr and Nd isotope ratios were measured in static mode on a ThermoElectron Triton Plus TIMS at Vrije University. The Sr fractions were loaded onto Re filaments using a TaF_5 activator to enhance ionization. Strontium isotope ratios were measured using a static multi-collection routine. An analysis consisted of 20 blocks of 10 cycles with an integration time of 8 s per cycle. Ratios of $^{87}Sr/^{86}Sr$ and $^{84}Sr/^{86}Sr$ were corrected for mass fractionation using an exponential law and $^{86}Sr/^{88}Sr$ ratio of 0.1194. Replicate analyses (n = 58) of the Sr standard NBS 987 on load sizes of 100 ng yielded average $^{87}Sr/^{86}Sr$ and $^{84}Sr/^{86}Sr$ ratios of 0.710242 ± 0.000008 (2σ) and 0.056492 ± 0.000004 (2σ). Neodymium

isotopes were measured on double Re filaments and were corrected for mass fractionation using an exponential law and $^{146}Nd/^{144}Nd$ ratio of 0.7219. Analyses of the standard BHVO-2 (n = 9) yielded $^{143}Nd/^{144}Nd = 0.512982 \pm 0.000005$ (2σ) and $^{145}Nd/^{144}Nd = 0.348405 \pm 0.000003$ (2σ); analyses of the standard BCR-2 (n = 4) yielded $^{143}Nd/^{144}Nd = 0.512636 \pm 0.000004$ (2σ) and $^{145}Nd/^{144}Nd = 0.348406 \pm 0.000004$ (2σ).

Whole rock powders of samples 8-RF-4, 8-RF-6 through -9, 8-RF-11, 8-RF-12, 8-RF-14, 8-RF-16, 8-RF-17, 8-RF-19, DC12-02, MG12-03, DC12-04, and DC12-05, and those of Frazer et al. (2014) were dissolved in HF and HNO_3 in Teflon® (Parr) bombs at 180°C for 48 hours. Following dissolution, samples were dried down to release Si, then immediately fluxed in concentrated HCl for 4-8 hours. Samples were subsequently aliquoted for Sr and Nd chemistry. Strontium was purified using Sr-spec cation exchange resin after the methods of Lundblad (1994) and loaded on single Re filaments with TaF_5. Neodymium was purified using a three-stage column chemistry procedure after Harvey and Baxter (2009) and loaded on single Re filaments in a Ta_2O_5-H_3PO_4 slurry. Strontium isotopic analyses were accomplished on a VG Sector 54 TIMS and Nd isotopes were analyzed on an Isotopx Phoenix TIMS, both housed at the University of North Carolina at Chapel Hill. Strontium was analyzed as a metal in dynamic multicollector mode with $^{88}Sr = 3V$. Neodymium was analyzed as an oxide in dynamic multicollector mode with $^{142}Nd^{16}O = 1V$. Isotope ratios for both elements were corrected for mass fractionation using an exponential law. Strontium isotopic ratios were normalized to $^{86}Sr/^{88}Sr = 0.1194$; Nd isotopic ratios were normalized to $^{146}Nd/^{144}Nd = 0.7219$. Replicate analyses of the NBS 987 Sr standard yielded $^{87}Sr/^{86}Sr = 0.710265 \pm 0.000015$ (2σ; n = 26). Replicate analyses of the Nd standard JNdi yielded $^{143}Nd/^{144}Nd = 0.512098 \pm 0.000012$ (2σ; n = 18).

All isotopic data are corrected to initial values using concentration and geochronologic

data presented in this study. Strontium data from the two labs are related by correcting present-day $^{87}Sr/^{86}Sr$ ratios of unknowns measured in each lab by the deviation of each lab's NBS 987 measurement from $^{87}Sr/^{86}Sr = 0.710250$, then corrected for decay to initial values. Neodymium data for the two labs are related to the La Jolla Nd standard, then corrected for decay to initial values. UNC Nd unknowns are corrected using a value of 0.999967, based on the difference between JNdi measurements in this study and La Jolla-normalized measurements of JNdi by Tanaka et al. (2000). Vrije University Nd unknowns are corrected using a value of 0.999997, based on the average difference between BCR-2 and BHVO-2 measurements in this study and the La Jolla-normalized measurements of the same standards by Weis et al. (2006). For age corrections of samples dated by LA-ICP-MS, the weighted mean age is used; for samples dated by ID-TIMS, the midpoint of the stated age range is used.

RESULTS

Cathodoluminescence

Cathodoluminescence reveals that most zircons have typical magmatic zonation, varying in style from sample to sample (Fig. 3; cf. Corfu et al., 2003). Many samples have oscillatory zonation, typified by the Sheepthief Creek and north of Snow Corral Meadow plutons. Sector zonation is present in more mafic samples, such as the two diorite plutons. Because no systematic pattern of U-Pb age is discernible with CL, images are shown without age spot locations. Laser ablation spots were typically placed midway through grains in order to cover the most representative domain (e.g., sample 8-RF-5 shows laser spots on the grains).

Figure 3. Cathodoluminescence (CL) images of representative zircons from dated samples. Most zircons have oscillatory or sector zoning, indicative of typical magmatic growth. Some notable features, such as inclusions or obvious inherited cores, are labeled. Images for all samples except 8-RF-5 are color CL collected at California State University – Bakersfield. Sample 8-RF-5 analyzed with black and white CL at Pomona College. Images for all samples are at the same scale.

U-Pb analyses

LA-MC-ICP-MS

Laser ablation data are reported as weighted mean ages with uncertainty given at the 95% confidence level after Ludwig (2003). Analyses were excluded from age interpretations in cases where grains were evidently inherited or antecrystic (Miller et al., 2007), or showed signs of obvious Pb-loss. Age interpretations are conservative and omit few analyses so as to not discount geologic complexities in the data. For samples 8-RF-4 and 8-RF-12, two age interpretations are provided because several high-precision analyses have significant weight on calculated weighted

mean ages. However, the preferred ages are those that include more analyses, yielding higher mean squares of weighted deviates (MSWD), thus reflecting potential zircon spectra complexity.

Zircon U-Pb data from most LA-MC-ICP-MS samples are concordant. Two age groups are evident: the Dinkey Dome pluton at 119-117.5 Ma, and the bulk of the SIS from ca. 106.5–98 Ma (Fig. 4; Table 1; Appendix 1). Three SIS samples (8-RF-4, 8-RF-5, and 3-S-51) are older than the DCG outside of uncertainty; one sample (8-RF-12) was younger than the DCG. Sample 1S81 of the Dinkey Dome pluton yielded the largest spectrum of ages. Three xenocrystic analyses include an analysis with a $^{207}Pb/^{206}Pb$ age of 2784 ± 63 Ma, a normally discordant analysis with a $^{207}Pb/^{206}Pb$ age of 979 ± 88 Ma, and a concordant analysis with a $^{206}Pb/^{238}U$ age of 140 ± 4 Ma. Several other fractions are subtly normally discordant near 120 Ma and have Proterozoic $^{207}Pb/^{206}Pb$ ages (Appendix 1). In addition, four analyses are 66–60 Ma, and likely reflect Pb-loss. Sample 8-RF-5 of the Sheepthief Creek pluton yielded an inherited zircon with a $^{207}Pb/^{206}Pb$ age of 1427 ± 62 Ma.

The Dinkey Lakes and Coyote Creek plutons, originally mapped as parts of the granite of Dinkey Dome (Bateman and Wones, 1972a), are instead coeval with the rest of the SIS. Two samples of the Dinkey Lakes pluton yield ages of 104.3 ± 1.6 and 102.2 ± 1.3 Ma, with the younger age overlapping the DCG. The $^{206}Pb/^{238}U$ weighed mean age of 100.1 ± 1.9 Ma for the Coyote Creek pluton (8-RF-11) also overlaps the DCG; however, most individual analyses were slightly normally discordant so it is not considered as robust as the other U-Pb data.

ID-TIMS

Three samples from the DCG and one sample of the adjacent Mount Givens Granodiorite were dated by ID-TIMS (Figs. 1, 5). All ages are concordant within 2σ analytical uncertainty

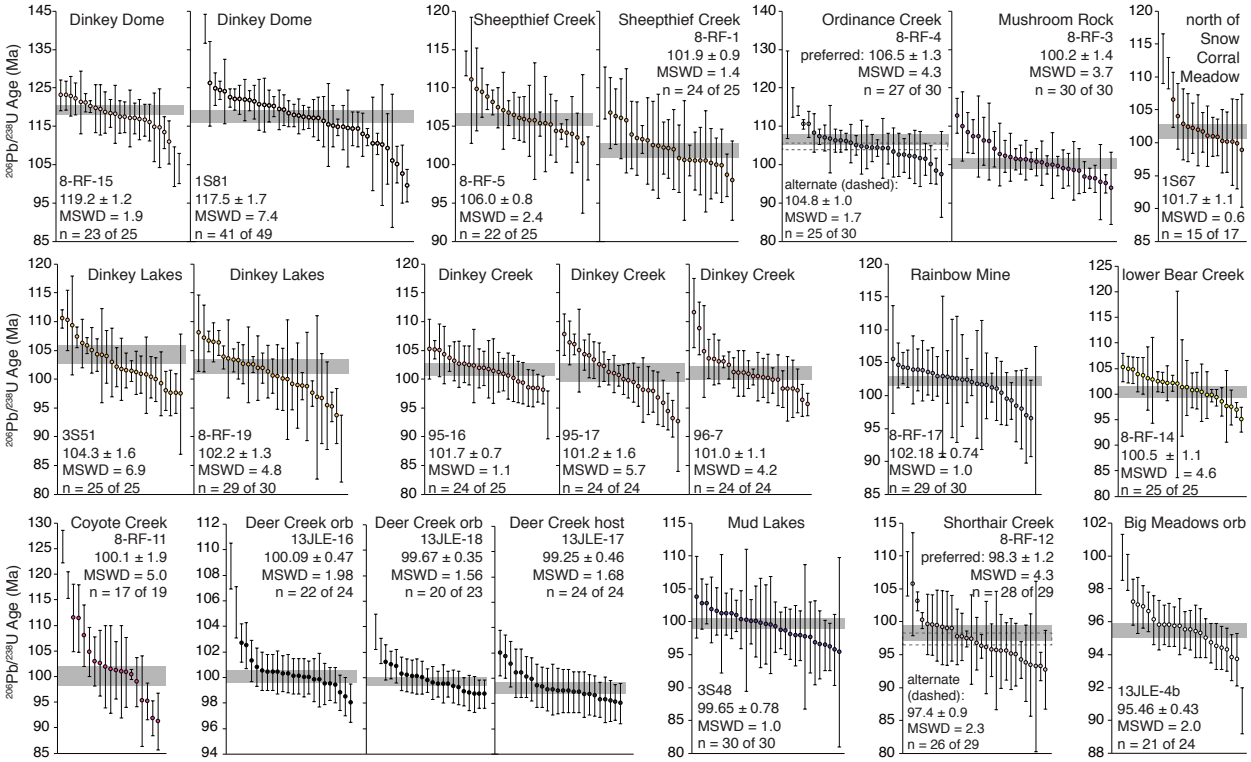

Figure 4. Results of laser ablation geochronology shown for each sample as $^{206}Pb/^{238}U$ age-sorted spectra. Analyses that are either obviously xenocrystic or affected by Pb-loss are omitted here; see Supplemental File for complete data. Note different ordinate age scales. Samples that are from same pluton (e.g., Dinkey Lakes) or similar locations (e.g., Ordinance Creek and Mushroom Rock) are shown at same scale. Individual analyses shown with corresponding 2σ analytical uncertainty; analyses not included in weighted mean calculations are shown as error bars only. Preferred weighted mean age interpretations and uncertainties at 95% confidence level (after Ludwig, 2003) shown by horizontal gray bars for each sample. Alternative interpretations of weighted mean ages and uncertainties for two samples given by dashed boxes; analyses omitted from alternative interpretations indicated by empty circles. Data for Deer Creek and Big Meadows (Eisenberg, 2014) included for comparison.

(Appendix 2). Preferred ages for ID-TIMS data are given as ranges due to the increasing difficulty of interpreting high-precision zircon data without corroborating compositional information (Samperton et al., 2015). Subsequent interpretations do not depend on precise crystallization ages. Note the age ranges provided here may not capture the full crystallization history of the samples (Glazner and Sadler, 2016), assuming all analyses are free from inheritance and Pb-loss. For several samples, weighed mean ages and 2σ analytical uncertainties are provided for comparison.

Sample DC12-02, collected in the DCG in the most mylonitized portion of the Courtright shear zone ~45 meters from the contact with the Mount Givens Granodiorite, yields 6 zircons

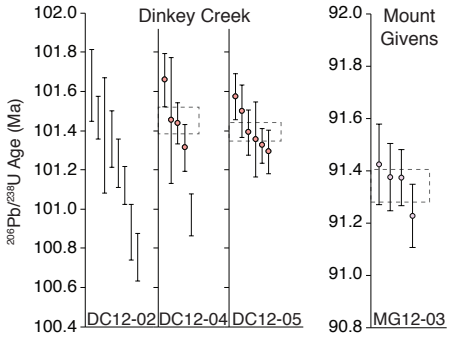

Figure 5. Results of ID-TIMS geochronology from the Courtright shear zone, shown as $^{206}Pb/^{238}U$ age-sorted spectra. Note different age scales on ordinates. All analyses are concordant and corrected for initial Th-disequilibrium using the whole rock Th/U measured for each sample. Preferred age interpretations are the age range of each sample including 2σ analytical uncertainties. Alternative age interpretations (dashed boxes) are weighted mean ages and corresponding 2σ analytical uncertainties calculated using analyses indicated by circles; see text for ages and explanation. Note that the Mount Givens Granodiorite is not part of the Shaver Intrusive Suite.

spread along concordia from 101.8–100.6 Ma (Fig. 5). Sample DC12-04 was collected in the further from the contact with the Mount Givens pluton and was less deformed. Four of five zircons yield an age range of 101.8-101.2 Ma, with a weighted mean age of 101.45 ± 0.07 Ma (MSWD = 4.9). One younger zircon is likely affected by Pb-loss. Sample DC12-05, collected several km west of the mapped shear zone, did not appear deformed in hand sample. Five zircons range from 101.7–101.2 Ma and yield a weighted mean age of 101.39 ± 0.05 Ma (MSWD = 3.5). A sample of the Mount Givens Granodiorite collected 20 m east of the shear zone and the DCG yields four zircons from 91.6-91.1 Ma and a weighted mean age of 91.34 ± 0.06 Ma (MSWD = 1.8). This is slightly older than other samples of the pluton from the northern end of Courtright Reservoir (Frazer et al., 2014). Samples DC12-02 and DC12-04 are within uncertainty of the 102 ± 1 Ma age of Tobisch et al. (1993).

Bulk geochemistry

Most samples from the SIS follow linear trends on Harker diagrams (Fig. 6; Table 2), except for the Deer Creek orbs and host, which appear to be relatively depleted in oxides such as TiO_2 and Al_2O_3 (Eisenberg, 2014). The Shaver granites follow the similar trends on Hark-

er diagrams, and most have greater than 70 wt% SiO_2. The A/CNK index (molar ratio Al_2O_3/[$CaO+Na_2O+K_2O$]), indicates the SIS is mostly metaluminous (A/CNK < 1), with some samples, including some of the Shaver granites, reaching mildly peraluminous values (A/CNK = 1.0 – 1.1). Magnesium number ($MgO/[MgO+FeO_{(tot)}]100$) decreases linearly with increasing SiO_2 in the SIS, except in the Shaver granites, which are depleted in MgO relative to $FeO_{(tot)}$. Magnesium number in the Deer Creek locality follows a positive trend with SiO_2, counter to the rest of the SIS (Eisenberg, 2014).

Trace element data generally follow linear trends relative to SiO_2 with some scatter (Tables 3, 4; Fig. 7). Elements including Sr, Sc, V, and the middle REEs decrease with increas-

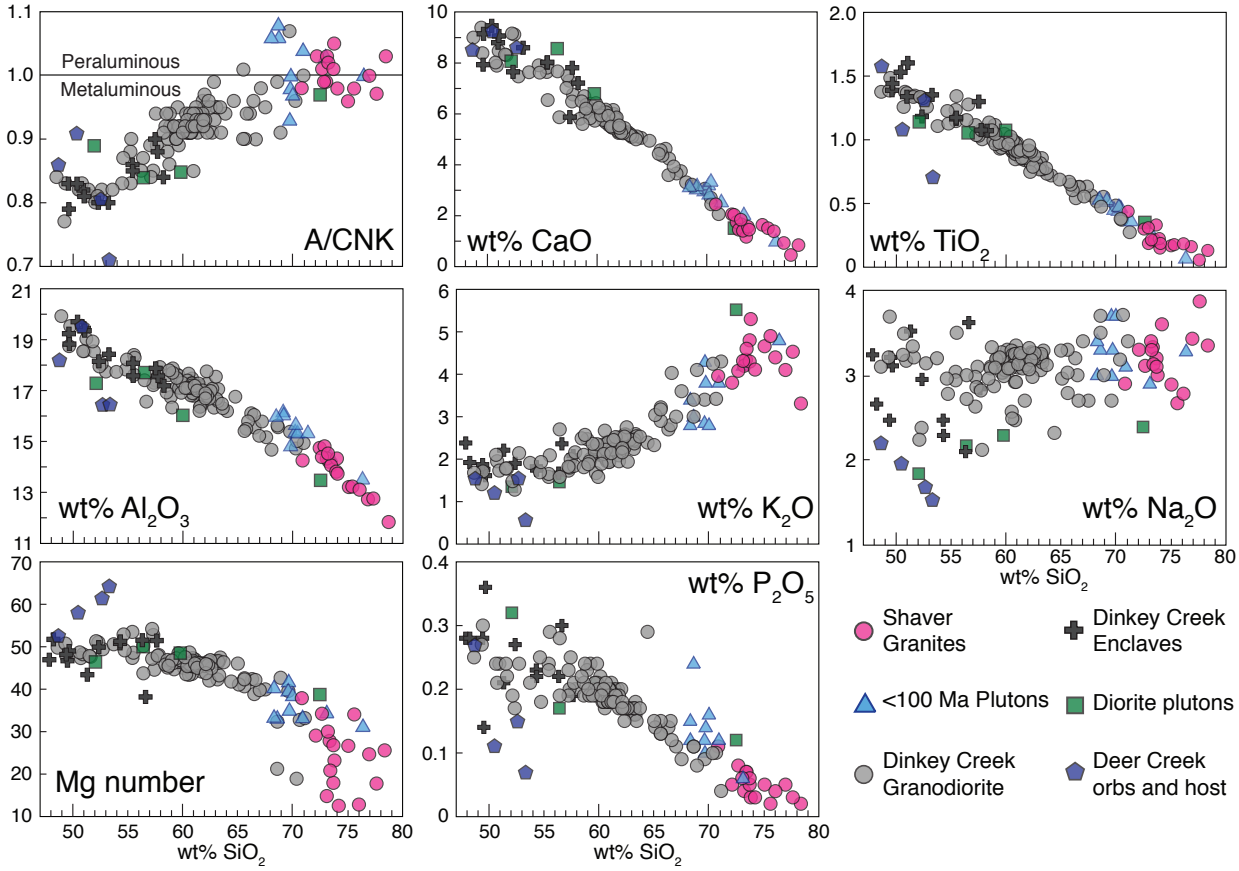

Figure 6. Representative Harker diagrams of whole rock analyses from the Shaver Intrusive Suite. Samples mostly follow linear trends, although there is general scatter in Na_2O, and there is significant scatter in P_2O_5 data in mafic compositions. Data are from this study, Barbarin et al. (1989), Lackey et al. (2008), and Hahm et al. (2014). The ratio A/CNK is calculated as the molar ratio $Al_2O_3/(CaO+Na_2O+K_2O)$; Mg number calculated as $MgO/(MgO+Fe_2O_3 \cdot 0.89981)$. Plutons designated as "<100 Ma" include Shorthair Creek (this study) and the leucogranite of Bald Mountain (Hahm et al., 2014).

ing SiO_2, whereas Ba, Rb, and Pb generally increase with increasing SiO_2. Niobium and Cs also appear to increase with increasing SiO_2, but with more scatter. Zirconium, Th, and U increase until approximately 65–70 wt% SiO_2, then decrease. The light and heavy REEs and Y show no apparent pattern with SiO_2. The SIS exhibits a wide range of REE concentrations, with the Shaver granites being most variable (Fig. 8). Limited data for the DCG suggest it has similar REE characteristics to the adjacent Mount Givens Granodiorite (Fig. 8). Europium anomalies ($Eu/Eu^* = Eu_N/(Sm_N \cdot Gd_N)^{1/2}$, where subscript "N" indicates the element normalized to chondrite values of McDonough and Sun, 1995), mostly fall in the range 1.4–0.6 and become more negative as SiO_2 content increases. The granite north of Snow Corral Meadow is an exception, with positive Eu/Eu* of 2.5 and 75.6 wt% SiO_2. Negative Ce anomalies as low as $Ce/Ce^* = 0.4$, where $Ce/Ce^* = Ce_N/(La_N \cdot Pr_N)^{1/2}$, are present in several of the Shaver granites. Cerium anomalies in the Shaver granites do not correlate with SiO_2, but do correlate with $^{87}Sr/^{86}Sr_i$, εNd_i, and $\delta^{18}O(Zrc)$ (Fig. 14).

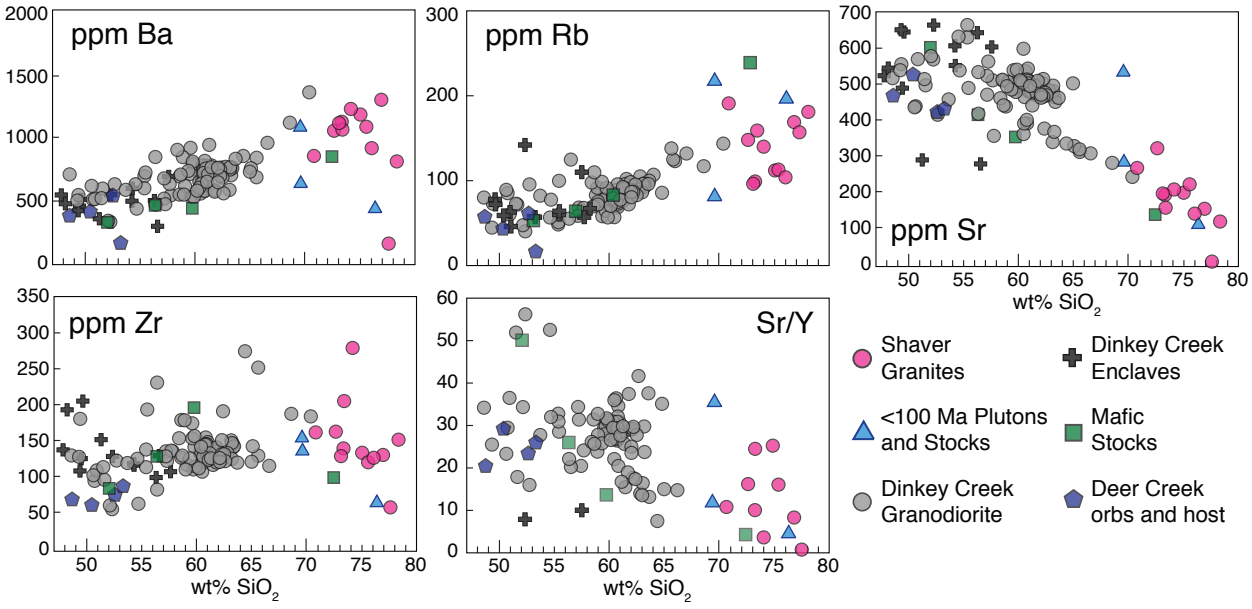

Figure 7. Harker diagrams for selected trace elements measured in this study. Trends are broadly linear across silica compositions. Note that the Shaver granites mostly have similar Zr concentrations to the DCG. Additional data sources as in Fig. 6.

Oxygen isotope ratios in zircon

Values of $\delta^{18}O$(Zrc) vary by 1.40‰ (Table 5), with the lowest $\delta^{18}O$(Zrc) (6.60‰) in a sample from the Dinkey Lakes pluton (8-RF-19) and the highest (8.00‰) from the Mushroom Rock pluton (8-RF-3). All of the $\delta^{18}O$(Zrc) values are above those for mantle-derived zircon (5.3 ± 0.3‰; Valley et al., 1998). Additional $\delta^{18}O$(Zrc) data from the SIS are reported by Lackey et al. (2006, 2008) and Eisenberg (2014). Including those data show the Dinkey Lakes pluton has the greatest $\delta^{18}O$(Zrc) range in the suite. Its two samples, collected 3 km apart, yield $\delta^{18}O$(Zrc) = 6.60‰ and 8.03‰. In contrast to the Dinkey Lakes pluton, many of the Shaver granites that are spatially associated have similar $\delta^{18}O$(Zrc) values, such as the nested Mushroom Rock (8.00‰) and Ordinance Creek (7.91‰) plutons, and two samples from the Sheepthief Creek pluton (7.15–7.18‰). In addition, diorite $\delta^{18}O$(Zrc) values are similar to the peraluminous plutons and the DCG (Fig. 9; Lackey et al., 2008).

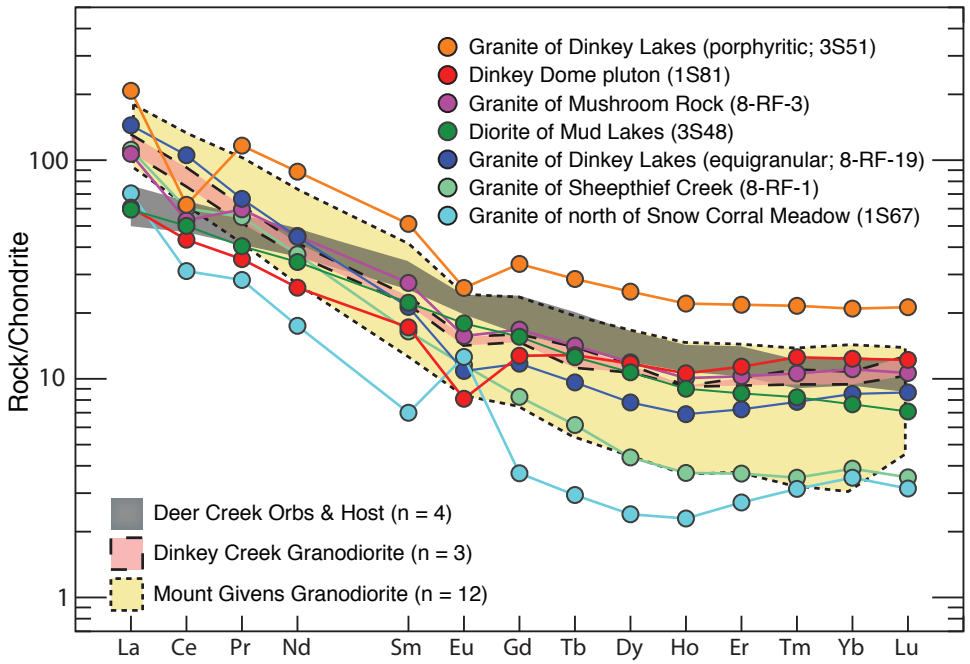

Figure 8. Rare earth element abundances for samples analyzed in this study normalized to chondritic composition of McDonough and Sun (1995). Individual analyses for each of the Shaver granites and the diorite of Mud Lakes are shown; granite REE concentrations span the entire range of concentrations measured in the Mount Givens Granodiorite. Note that field for the Dinkey Creek Granodiorite represents analyses of only three samples. Field for Mount Givens pluton includes sample MG12-03 of this study and plus data for samples from Frazer et al. (2014).

Radiogenic Isotopes

Most SIS samples have $^{87}Sr/^{86}Sr_i$ above 0.707; these are the highest $^{87}Sr/^{86}Sr_i$ values recognized in this part of the Sierra Nevada batholith (Figs. 9, 10; Table 6). The highest $^{87}Sr/^{86}Sr_i$ (0.7106) is from a leucocratic portion of the diorite of Rainbow Mine. The lowest value (0.6878) from the Coyote Creek pluton is reported for completeness, but will not be considered further because it is below that of basaltic achondrites (Papanastassiou and Wasserburg, 1968). Sample 8-RF-19 of the Dinkey Lakes pluton has the lowest likely robust $^{87}Sr/^{86}Sr_i$ (0.7054). In contrast, the other Dinkey Lakes pluton sample yields $^{87}Sr/^{86}Sr_i = 0.7087$. There is no clear trend in $^{87}Sr/^{86}Sr_i$ with SiO_2. The Sr isotopic data broadly agree with those of Dodge and Kistler (1990).

Neodymium isotopic data negatively correlate with $^{87}Sr/^{86}Sr_i$. Whereas the Sr isotopic data are the most radiogenic in the central part of the batholith, the Nd isotopic data are approximately equivalent to data from the Tuolumne and Whitney intrusive suites (Fig. 10). As with

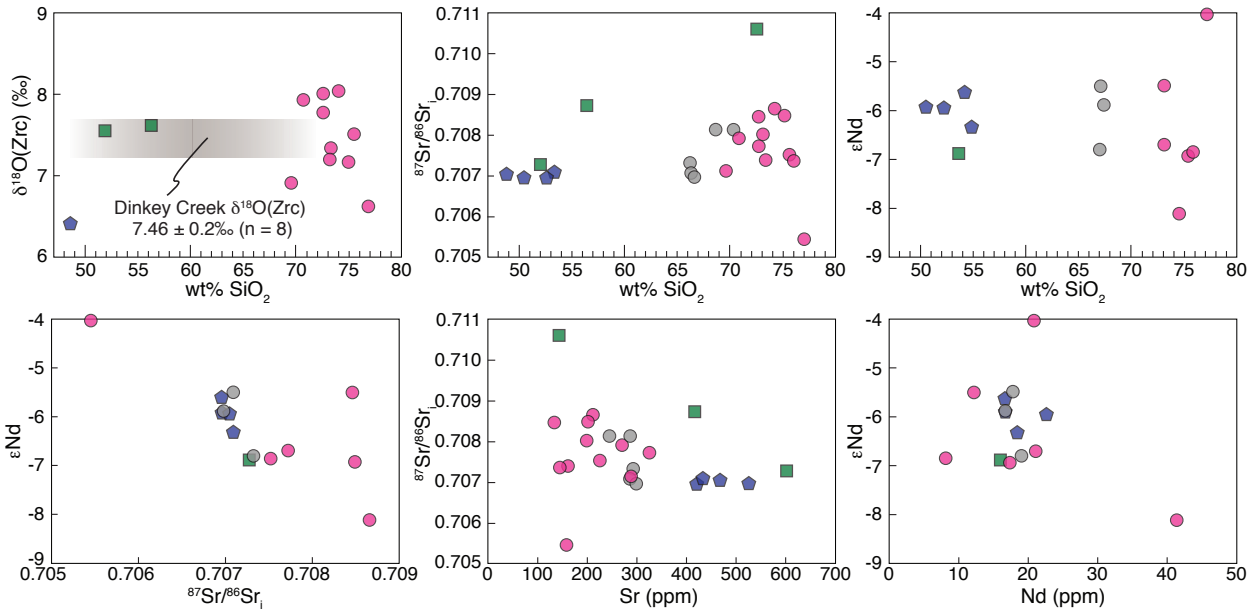

Figure 9. Results of isotopic analyses of the Shaver Intrusive Suite. Symbols as in Figures 6 and 7. Note the general scatter of the Shaver granites in all isotope systems relative to other SIS rocks. Radiogenic isotopic data are initial values corrected for decay using the corresponding age of the sample. Plot of $\delta^{18}O$(Zrc) also includes results from Lackey et al. (2006, 2008). Samples of Dinkey Creek Granodiorite analyzed for $\delta^{18}O$(Zrc) (Lackey et al., 2008) do not have corresponding SiO_2 data and thus the field for that pluton is shown as gradational in wt% SiO_2.

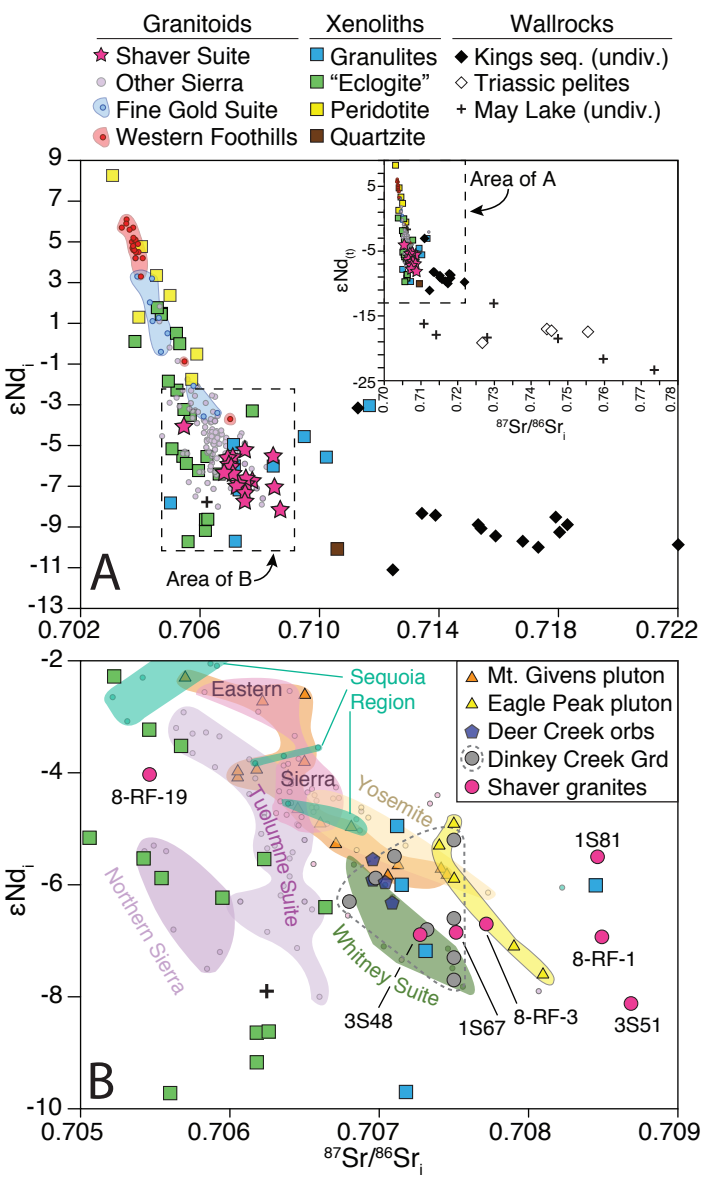

Figure 10. Results of Sr and Nd isotopic analyses for the Shaver Intrusive Suite. All data are shown as initial values corrected for decay using the corresponding age of the sample; xenolith and wallrock data are corrected to 100 Ma. (A) Data for the Shaver Intrusive Suite (pink stars) relative to published data for the Sierra Nevada batholith. Inset shows full extent of wallrock analyses. (B) Results for the Shaver Intrusive Suite relative to the Cretaceous batholith and some xenolith and wallrock analyses as in (A). Data for other suites and regions are from: Eagle Peak (Hill et al., 1988); Eastern Sierra (Coleman et al., 1992; Wenner and Coleman, 2004); Fine Gold (Truschel, 1996); Mount Givens (this study); Northern Sierra (Cecil et al., 2012); Sequoia (Holland et al., 2013); Shaver (Barbarin et al., 1989; Kistler and Fleck, 1994; this study); Tuolumne (Kistler et al., 1986; Gray et al., 2008); Western Foothills (Clemens-Knott, 1992); Whitney (Hirt and Glazner, 1995; Hirt, 2007); Yosemite (Ratjeski et al., 2001). Data for xenoliths are from: Domenick et al. (1983), Dodge et al. (1986), Mukhopadhyay and Manton (1994), and Ducea and Saleeby (1998), and Ducea (2001, 2002). Data for wallrocks are from: Kings sequence (Zeng et al., 2005); May Lake (Mills et al., 2009), and Triassic pelites (Zeng et al., 2005).

$^{87}Sr/^{86}Sr_i$, the Dinkey Lakes pluton has very heterogeneous Nd isotopic composition (εNd_i =–4.03 to –8.12). There is no correlation between εNd_i and SiO_2 (Fig. 9).

DICUSSION

Geochronology in the Shaver Intrusive Suite

Geochronologic data document emplacement of the SIS over ~8 Ma, from 106.5 to 98.3 Ma, although taking uncertainty into account permits emplacement duration from 7–11 Ma (Fig.

11). With an exposed area of ~670 km^2 and relief of ~2.2 km, the SIS has an approximate volume of 1500 km^3. Therefore, the average magma flux over the lifespan of the suite ranges from 0.0001–0.0002 km^3/a. This magma flux is similar to those calculated for other plutons and intrusive suites in the Sierra Nevada and elsewhere (Mills and Coleman, 2013; Frazer et al., 2014). Although there is debate about how plutonic volumes are calculated, particularly in regards to their apparent thicknesses (e.g., Lipman and Bachmann, 2015), field evidence suggests the SIS is tabular (Cruden et al., 1999).

The new geochronology indicates the Shaver granites were emplaced throughout the history of the SIS (Fig. 11). These data preclude past field interpretations that called for the Shaver granites to be significantly younger than the DCG (Bateman, 1992). However, the uncertainties in the LA-ICP-MS data permit all but two of the Shaver granites to be contemporaneous with

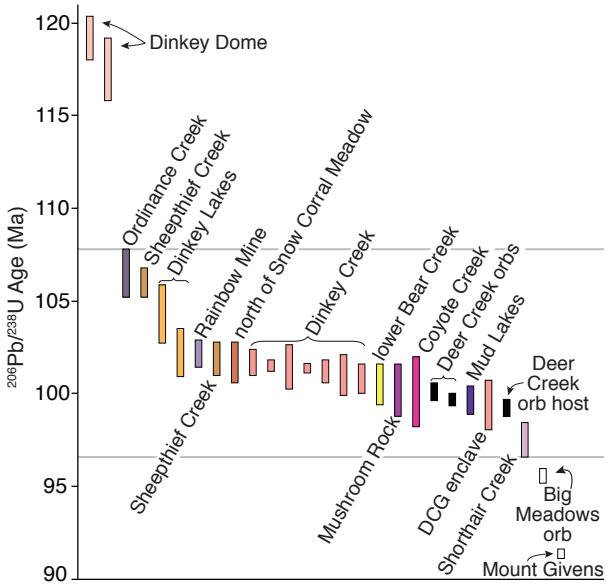

Figure 11. Compilation of zircon U-Pb geochronology in the Shaver Intrusive Suite ordered by age (laser ablation data: weighted means and 95% confidence interval; TIMS data: total age range with 2s analytical uncertainties). Interpreted age range of the Shaver Intrusive Suite indicated by horizontal gray lines. The uncertainties of the data permit only the Ordinance Creek and sample 8-RF-5 of Sheepthief Creek to be considered distinctly older than the DCG. Laser ablation ages for a mafic enclave and its host Dinkey Creek Granodiorite, as well as the Deer Creek orbicular locality, are also included (Lackey et al., 2012; Eisenberg, 2014). Ages for a Big Meadows orb (Eisenberg, 2014) and Mount Givens Granodiorite (sample MG12-03, this study) are included for comparison but are not part of the SIS.

or slightly younger than the DCG (Fig. 11). Samples 8-RF-4 from the Ordinance Creek pluton (106.5 ± 1.3 Ma) and 8-RF-5 from the Sheepthief Creek pluton (106.4 ± 1.2 Ma) are older, including uncertainty, than any dated sample of the DCG. The DCG adjacent to the Ordinance Creek pluton is undated, whereas the Sheepthief Creek sample is at minimum 2.5 Ma older than sample 95-17 of the DCG (101.2 ± 1.6 Ma), 2 km away (Fig. 1). Data for these two samples suggest, but do not require, that field relationships indicating the DCG has been cut by those plutons are inconclusive or incorrect.

The Dinkey Dome pluton (Kdd, Fig. 1) is a clear case where geochronologic data are at odds with previous field mapping, as it is some 15 Ma older than the DCG. The pluton's intimate association with the Dinkey Creek roof pendant is notable because the pendant is a part of the hypothesized Snow Lake block, which some have suggested was dextrally transported 400 km north in the Early Cretaceous (Lahren and Schweickert, 1989; Grasse et al., 2001). Recent LA-ICP-MS detrital zircon analyses of the Snow Lake pendant and others near the Tuolumne Intrusive Suite have cast doubt on the need for 400 km of displacement (Memeti et al., 2010b), but up to 200 km is still possible (Kistler, 1993; Saleeby and Busby, 1993; Lewis and Girty, 2001; Chapman et al., 2015). Memeti et al. (2010b) suggested movement on the hypothesized Mojave-Snow Lake fault must have occurred between 145 Ma and 102 Ma. Because of the chemical and isotopic similarities between the Dinkey Dome pluton and the 106-98 Ma Shaver granites, movement of the block may have been complete by the time of the pluton's emplacement ca. 119 Ma.

New CA-ID-TIMS U-Pb zircon data document emplacement of the DCG in the area of the Courtright shear zone ca. 102-101 Ma, with the Shorthair Creek pluton emplaced ca. 98 Ma. Both plutons are deformed, although deformation is most intense in the easternmost DCG where

it is in contact with the Mount Givens Granodiorite, which was emplaced ca. 91.3 Ma and does not appear deformed. Recalculated $^{40}Ar/^{39}Ar$ data from Tobisch et al. (1993) show that hornblende $^{40}Ar/^{39}Ar$ ages in and adjacent to Mount Givens Granodiorite overlap within uncertainty of its new zircon U-Pb age (Fig. 12). Biotite $^{40}Ar/^{39}Ar$ ages for all samples are synchronous and within ~2 Ma of the 91.3 Ma zircon U-Pb age of the Mount Givens Granodiorite. Renne et al. (1993) argued that the 160ºC/Ma cooling rate indicated by the data may have been the result of rapid uplift and/or exhumation ca. 90 Ma, when the Mount Givens pluton was emplaced and the shear zone was inferred to be active. However, the data permit an alternative interpretation. Cooling rates in non-deformed plutonic rocks are now routinely calculated to be >100ºC/Ma (Davis et al., 2012; Barboni et al., 2014; Samperton et al., 2015). Therefore, the $^{40}Ar/^{39}Ar$ data within and immediately adjacent to the Mount Givens Granodiorite may simply record the thermal effects of incremental emplacement and concomitant rapid cooling of small magma batches. This hypothesis raises the possibility that strain in the Courtright shear zone mostly accumulated prior to emplacement of the Mount Givens Granodiorite ca. 91.3 Ma.

Cerium anomalies and the source of the Shaver granites

Cerium anomalies occur when Ce^{3+} is oxidized to Ce^{4+}, thus decoupling the behavior of Ce relative to the trivalent REEs. Negative cerium anomalies are common in supracrustal rocks that have interacted with seawater, which has a large negative Ce anomaly (Elderfield and Greaves, 1982; Murray et al., 1990). Negative Ce anomalies as low as 0.85 are commonly measured in basalts erupted from arcs where the subducting sediment column also has a negative Ce anomaly (e.g., Hole et al., 1984; Plank and Langmuir, 1998). Such anomalies are rarely reported in plutonic or high-silica igneous rocks (Meen, 1990), and when present they are often attributed

to surficial weathering processes in part because they do not correlate with other geochemical or isotopic signatures (Sawka et al., 1986; Rooney et al., 2010; Lee et al., 2013). However, the correspondence of the most negative Ce anomalies with the highest $\delta^{18}O$(Zrc) values in the Shaver granites suggests a supracrustal source (Fig. 13). Furthermore, the high $^{87}Sr/^{86}Sr_i$ and low εNd_i values suggest the supracrustal source was likely not altered oceanic crust, as has been proposed for the Fine Gold Intrusive Suite (Lackey et al., 2012). Thus, a sedimentary source is plausible.

Metasedimentary wallrocks are common in the central Sierra Nevada, and could possibly have served as magma sources if similar rocks were present deep in the crust, where partial melting is more efficient (Annen and Sparks, 2002). For example, leucosomes and pelitic host rocks in a migmatite complex of the Kings sequence in the southern Sierra Nevada have Ce/Ce*

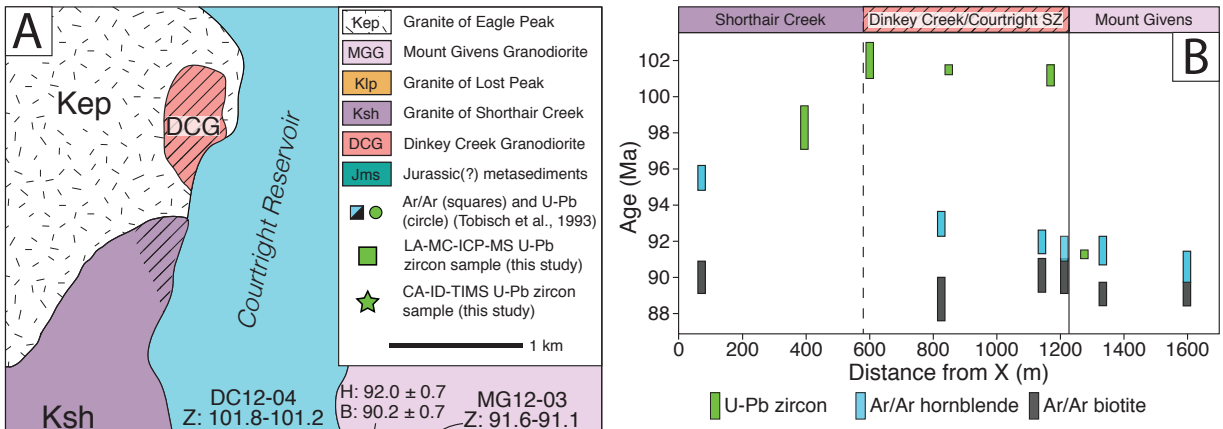

Figure 12. (A) Generalized geologic map of the Courtright shear zone in the area of Courtright Reservoir, after Tobisch et al. (1993). Area of shear zone indicated by hatched lines; deformation in shear zone is most intense on its eastern border with the Mount Givens Granodiorite. Location of boundary between Shorthair Creek pluton and Dinkey Creek Granodiorite in the area of the reservoir is uncertain. Geochronologic data are shown with 2σ uncertainties in Ma; $^{39}Ar/^{40}Ar$ data of Tobisch et al. (1993) are recalculated (see text). Cross section indicated by X-X' line. Z – zircon; H – hornblende; B – biotite. (B) Samples are projected onto cross section X-X' with age on the ordinate. Hornblende Ar/Ar dates for DCG samples collected closest to the Mount Givens pluton are within uncertainty of the Mount Givens pluton's zircon U-Pb age, suggesting the Ar system was reset in those samples. In contrast, the hornblende Ar/Ar date for the Shorthair Creek pluton appears unaffected by the Mount Givens pluton's thermal aureole. All biotite Ar/Ar data overlap ca. 90 Ma, suggesting that deformation in the shear zone was complete by that time. Jurassic(?) metasedimentary wallrocks are omitted from cross section for clarity.

of ~0.7 (Zeng et al., 2005). However, wallrocks in the SIS are dominated by quartzite, with little pelite (Bateman, 1992). There is also disagreement over the affinity of SIS wallrocks (e.g., Kistler and Bateman, 1966; Lahren and Schweickert, 1989; Kistler, 1993; Saleeby and Busby, 1993) making a genetic link between the Kings sequence and the Shaver granites tenuous.

The presence of Cenozoic volcanic pipes that have erupted through and near the SIS (Fig. 1) permits evaluation of connections to the deep crust. Common garnet pyroxenite xenoliths in the basalts may be residues complementary to the voluminous Cretaceous batholith, and have Ce/Ce* as low as 0.84 (Ducea, 2002). Rare metaquartzite xenoliths, which are interpreted as residues after melting of impure quartzite, have Ce/Ce* as low as 0.64 (Chin et al., 2013).

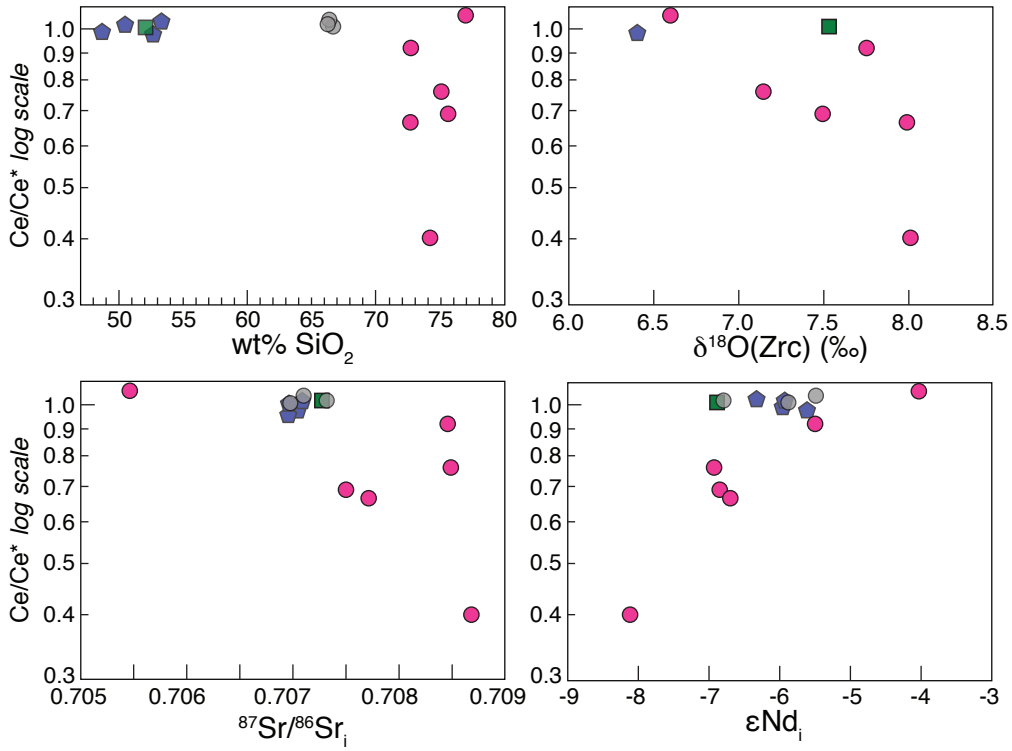

Figure 13. Cerium anomalies (Ce/Ce*) relative to compositional and isotopic parameters measured in this study. Cerium anomalies are restricted to the Shaver granites, but not all granites have an anomaly. Sample 8-RF-19 is the most silicic sample yet has the most positive anomaly (Ce/Ce* = 1.08). In contrast to silica, Ce anomalies correlate well with isotopic parameters. The correlation with $\delta^{18}O$(Zrc) is notable because it indicates the whole rock anomaly accords with crystal-scale isotopic compositions. Likewise, the correlation with εNd_i is notable because Ce and Nd are both light REEs and should therefore share a similar derivation. Symbols as in Fig. 9 and 10. See text for Ce anomaly calculation. Note that the ordinate is shown on a logarithmic scale.

Both xenolith types have mid-Cretaceous ages that overlap the SIS, and document the presence of negative Ce anomalies in the deep crust and/or upper mantle during assembly of the SIS. The metaquartzites in particular bear superficial similarity to exposed SIS wallrocks (Kistler and Bateman, 1966), and may also be isotopically appropriate matches for the Shaver granites, with one xenolith recording $^{87}Sr/^{86}Sr_{100\ Ma} = 0.710637$ and $\varepsilon Nd_{100\ Ma} = -10.3$ (Ducea and Saleeby, 1998). However, Sierran quartzites are infertile (Mills et al., 2009), and modeled melts complementary to the metaquartzite xenoliths are much more aluminous than the Shaver granites (Chin et al., 2013).

Lower crustal Ce-anomalous rocks could have been part of a fertile pre-existing wallrock terrane (Zeng et al., 2005), underthrust from the backarc (Ducea, 2001; Chin et al., 2013), or transported down the subduction zone with the Farallon slab (von Huene and Scholl, 1991). Lower Jurassic to mid-Cretaceous shales and cherts of the Franciscan assemblage on the Marin headlands have prominent negative Ce anomalies (Murray et al., 1990). If a similar package of mostly oceanic fertile sediments were thrust into the mantle wedge, it could have become a partial melting source. The variability of Ce anomaly magnitude in the Shaver granites, along with correlated isotopic compositions, may be attributed to entrainment of peritectic and accessory phases from the source (Villaros et al., 2009) and/or disequilibrium partial melting (Davies and Tommasini, 2000; Zeng et al., 2005). Variable Eu anomalies could perhaps be controlled by differing contributions of peritectic plagioclase (Clemens et al., 2011). A pelitic source for the Shaver granites is not ideal because the granites do not have cordierite or distinctly high A/CNK (e.g., Miller, 1985), but it is difficult to envision a scenario where non-sedimentary rocks form a significant part of the source because the Ce anomalies would be diminished by involvement of non-sedimentary rocks. Therefore, partial melting of a metasedimentary protolith and peritectic

assemblage entrainment (Clemens and Stevens, 2016) appear to be the simplest methods for generating the Shaver granites. This implies that the Shaver granites are mostly recycled supracrustal material.

Origins of diorites and the Dinkey Creek Granodiorite

In contrast to the Shaver granites, which have distinct mineralogy, Ce anomalies, and limited emplacement-level interaction with the rest of the SIS, the DCG and more mafic parts of the suite are superficially more similar to the large intrusive suites of the Sierra Crest. However, models for the origins of the mafic and intermediate parts of the SIS must account for their high $^{87}Sr/^{86}Sr_i$, low εNd_i, and high ^{18}O(Zrc) values relative to those parts of the batholith.

Some hypotheses call for a large component of primitive mantle to generate chemical and isotopic diversity in intrusive suites (DePaolo, 1981; Nelson et al., 2013). However, they cannot account for the heterogeneities in the SIS. Data for the SIS do not follow curvilinear mixing trends on isotope-silica and isotope-element plots, as would be expected from simple mixing of primitive mantle and Proterozoic crust. Lee and Bachmann (2014) hypothesized that relatively "flat" isotopic trends with varying silica content, which are suggested by the $\delta^{18}O$(Zrc) and εNd_i data for intermediate and mafic SIS rocks (Fig. 9), could be explained by mixing primitive mantle and lower crust followed by fractional crystallization. However, elements such as P_2O_5 and Zr have mostly linear trends on Harker diagrams and thus do not require a fractional crystallization origin (Figs. 6, 7). In addition, it would be difficult to achieve the evolved isotopic compositions in mafic end members of the SIS by assimilation and fractional crystallization processes. Following Nelson et al. (2013), and using high-alumina olivine tholeiite (Bacon et al., 1997) and average continental crust (Rudnick and Gao, 2003) for end members (Table 7), bulk assimilation

of 40–45% continental crust is necessary to achieve the isotopic compositions of most of the SIS (i.e., $^{87}Sr/^{86}Sr_i = 0.707$). Although such mixing would reproduce the suite's isotopic compositions, the new mafic end member would have ~53 wt% SiO_2 before subsequent fractional crystallization is taken into account, whereas the most mafic rocks present in the suite have 48 wt% SiO_2 (Fig. 9).

In contrast, others have suggested enriched mantle as an important component in the Sierra Nevada batholith, particularly in the well-studied Sierra Crest suites (Coleman et al., 1992; Wenner and Coleman, 2004). Enriched mantle is an appealing source for the mafic and intermediate parts of the SIS because it can account for its evolved radiogenic isotopic compositions. However, the SIS has elevated $\delta^{18}O$(Zrc) relative to the eastern Sierra (Lackey et al., 2008). This suggests that if enriched mantle played a role in the genesis of the SIS, it likely also interacted with supracrustal rocks in order to acquire the elevated $\delta^{18}O$ signature (Fig. 14). Both Kings sequence rocks and granulite xenoliths erupted through the Cenozoic Chinese Peak pipe are well-characterized and constitute plausible end members with high $\delta^{18}O$ values and appropriate $^{87}Sr/^{86}Sr$ (Fig. 1). Simple mixing arrays suggest incorporation of 0-40% crustal component into enriched mantle to account for the O isotope composition of mafic and intermediate parts of the SIS (Fig. 14). However, if Kings sequence rocks were involved in the production of the mafic and intermediate parts of the SIS, they must not have had Ce anomalies (Fig. 13; c.f. Zeng et al., 2005).

The Shaver Intrusive Suite and transitions in the Sierra Nevada batholith

The underlying causes for the structure, chemical and isotopic compositions of the SIS are enigmatic. Tobisch et al. (1995) showed that the SIS was emplaced during a period of dy-

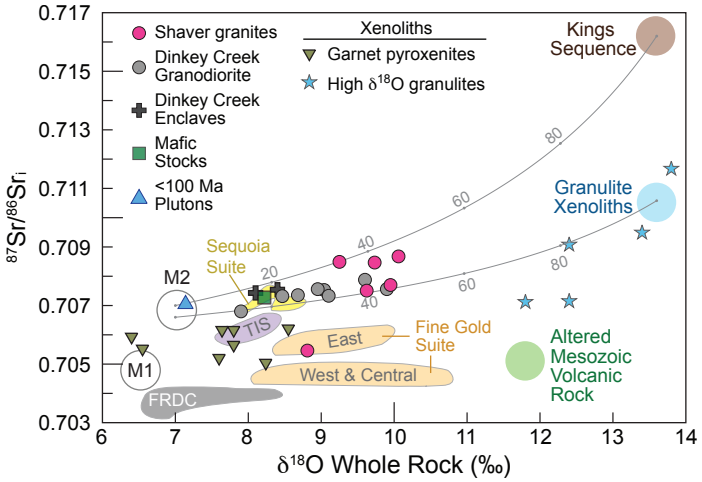

Figure 14. Strontium and oxygen isotope sources for the Shaver Intrusive Suite. M1 and M2 are postulated mantle reservoirs. M1 was suggested as a reservoir for the Dinkey Creek Granodiorite and Tuolumne Intrusive Suite by Lackey et al. (2012). However, the data presented here suggest the Shaver Intrusive Suite requires a more evolved source, designated M2. Simple mixing curves from M2 ($\delta^{18}O$ = 7‰, Sr_i = 0.7066-0.707, 550 ppm Sr) to high-$\delta^{18}O$ end-members of Kings Sequence ($\delta^{18}O$ =13.6‰ 0.7162, 190 ppm Sr) and granulite xenoliths ($\delta^{18}O$ =13.4‰ 0.71058, 190 ppm Sr) bound the Shaver Intrusive Suite array. Although the Sr and O isotopic data for the entire suite are satisfied by this mixing model, Ce anomaly data suggest alternative mechanisms for the generation of the Shaver granites. The mafic and intermediate members of the SIS require 0-40% crustal component similar to Kings sequence rocks and/or granulite xenoliths to acquire their high $\delta^{18}O$ values. Kings sequence source is a composite of $\delta^{18}O$ data from Lackey et al. (2006) and Sr concentration and isotopic data from Zeng et al. (2005a). Granulite xenolith data are a composite from Dodge et al. (1986), corrected to 100 Ma. Data for the Sequoia Intrusive Suite are from this study, with additional $\delta^{18}O$ data from Lackey et al. (2008) and Sr data from Chen and Tilton (1991). Additional Sierran data are from Masi et al. (1981), Clemens-Knott (1992), Kistler and Fleck (1994), and Truschel (1996). FRDC – Foothills ring dike complexes; TIS – Tuolumne Intrusive Suite. Altered Mesozoic volcanic rock field from Lackey et al. (2012), after Staudigel et al. (1995).

namic tectonic activity in the Sierra Nevada batholith, as recorded by ductile shear zones preserved in and near the suite. In a review of global geodynamics that included data from Tobisch et al. (1995), Matthews et al. (2012) noted a variety of tectonic markers that may have recorded a worldwide tectonic reorganization at 105–100 Ma, perhaps triggered by the cessation of subduction to the east of Australia and New Zealand. However, it is unclear how or why such an event would influence the compositions and emplacement dynamics of magmas in the SIS. Whereas other suites of similar age also feature high-silica granites (Holland et al., 2013; Putnam et al., 2015; Frazer et al., in prep.), none preserve voluminous granodiorites like the DCG.

The distinct composition of the SIS, particularly the Shaver granites, may have arisen from a fortuitous combination of prolonged magmatism and a preexisting metasedimentary

framework. All Cretaceous U-Pb zircon ages in the Sierra Nevada from 36.5°N to 38.15°N using data acquired on zircon pre-treated by air- or chemical-abrasion when dated by TIMS, or zircon dated by LA-ICP-MS were compiled (Fig. 15). Limiting the dataset to these modern techniques allows for better recognition of zircons affected by inheritance or Pb-loss. The compilation reveals that rather than a smoothly migrating magmatic arc from west to east as past work has indicated (Chen and Moore, 1982; Nadin and Saleeby, 2008), magmatism in the central Sierra Nevada progressed step-wise, with the temporal step coincident with the location of the Courtright shear zone and other proposed intrabatholithic faults (Lahren and Schweickert, 1989; Kistler, 1990, 1993; Saleeby and Busby, 1993). Magmatism began at 124-120 Ma west of the intrabatholithic divide, and began ca. 98-95 Ma east of the divide. The 103-100 Ma Kearsarge intrusive suite is an exception whose eastward location may have been controlled by the presence of pre-existing fractures (Frazer et al., in prep.) Whereas the magmatic front did not migrate smoothly as previously suggested, the cessation of magmatism did progress steadily eastward throughout the Cretaceous. A line fit by eye across the batholith suggests the trailing magmatic cessation migrated at a rate of 2.7 mm/a (Fig. 15), agreeing with the rate determined by Chen and Moore (1982).

The data suggest that locations in the farthest eastern reaches of each magmatic "step" (i.e., the SIS in western half of the batholith, and the Sierra Crest suites in the eastern half) may have been the loci of prolonged magmatic activity. For the SIS, this may have led to up to 15–20 Ma of thermal priming leading to the subsequent melting of metasedimentary rocks interpreted to have been metamorphosed under the SIS at 103 ± 10 Ma (Chin et al., 2013). This hypothesis predicts that similar thermal priming could have occurred on the eastern margin of the eastern "step" in the suites of the Sierra Crest magmatic event (Coleman and Glazner, 1997), though perhaps to

a lesser degree due to the shorter period of magmatism recorded there. It is also notable that the location of the eastern margin of each step coincides with the presence of well-documented shear zones (Tikoff and Teyssier, 1992; Tobisch et al., 1993, 1995; Tikoff and de Saint Blanquat, 1997; Nadin et al., 2016).

Despite the stepwise function of magmatism at current exposure levels, it is possible the magma generation zone in the asthenosphere progressed gradually inboard of the subduction zone due to slab flattening or subduction erosion (Coney and Reynolds, 1977; van Huene and Scholl, 1991). However, instead of ascending magmas migrating along with the generation zone, they continued to make use of the area of the intrabatholithic divide as a conduit to the mid- and upper crust in the west. By the end of magmatism in the SIS (~98 Ma), the conduit became untenable because the magma generation front was too far east; after 98 Ma, magmas made use of other pathways to begin building the Sierra Crest intrusive suites. This model is analogous to

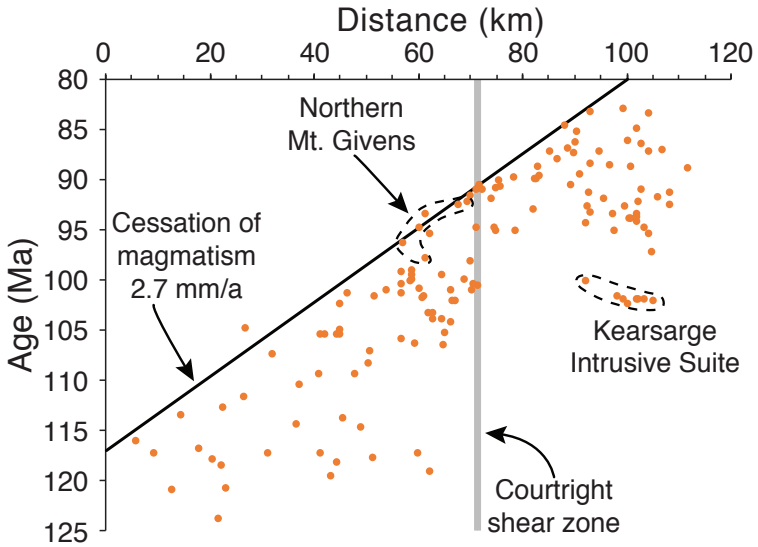

Figure 15. Data compilation of zircon U-Pb ages from the Cretaceous central Sierra Nevada batholith (36.5°N to 38.15°N) relative to their distance from a batholith-parallel line in the Central Valley oriented N35°W. Only samples dated by LA-ICP-MS, SIMS, SHRIMP, or ID-TIMS (using small fractions of pre-treated zircons) are included in this analysis. The results indicate that the 2.7 mm/a trend of Chen and Moore (1982) is present, but it tracks the eastward cessation of magmatism. The magmatic "front" appears to move across the batholith in a stepwise manner ca. 98 Ma, approximately demarcated by the location of the Courtright shear zone. Exceptions to this pattern include the northern part of the Mount Givens Granodiorite, which is younger than 98 Ma where the northern part of the pluton extends to the west. In addition, the location of the Kearsarge intrusive suite is enigmatic, and may have been controlled by pre-existing fractures (Frazer et al., in prep.).

hot spot volcanic chains, where the spacing between volcanoes may be controlled by lithospheric thickness and fractures that capture magma ascending from the source until the overriding plate has moved too far away (Vogt, 1974).

CONCLUSIONS

New U-Pb zircon geochronology shows that the Shaver Intrusive Suite was emplaced over an ~8 Ma period, from 106–98 Ma. Within the uncertainty of the laser ablation data, emplacement of granites, granodiorites, and diorites was essentially contemporaneous, although the only significant evidence for interactions between magmas of different compositions at emplacement level is the presence of mafic magmatic enclaves in the Dinkey Creek Granodiorite that dominates the suite. Prominent negative Ce anomalies in several of the peraluminous granites, coupled with the presence of Ce-anomalous metasedimentary xenoliths in Cenozoic volcanic rocks that erupted through the suite, suggest the granites are the products of partial melting of a metasedimentary source. It is hypothesized that the granites' variable REE concentrations and Ce anomaly magnitudes were governed by peritectic assemblage entrainment. Thus, the granites represent nearly 100% recycling of previously existing crustal material. In contrast, the bulk of the suite besides the granites was likely mostly derived from enriched mantle lithosphere with varying amounts of a supracrustal component such as Kings sequence-type rocks, or granulite. The contrasting mantle and crustal contributions to the SIS may be due to prolonged magmatism in the area of the SIS, which until ~98 Ma was the easternmost portion of the Cretaceous central Sierra Nevada batholith. If magmatism occurred in the area of the SIS since ~122 Ma, then the lower crust may have become thermally and chemically primed to partially melt metasedimentary rocks of varying fertility (impure quartzite to pelites) to generate the Shaver granites.

TABLE 1. SAMPLE SUMMARY

Sample	IGSN*	Name/Description	Rock type†	Analyses performed§	UTM-N#	UTM-E	Age ± 2σ**
8-RF-1	P4700000J	Sheepthief Creek	granite	Zrc, $\delta^{18}O$-Sr_i-εNd, WR	4122494	301547	101.9 ± 0.9
8-RF-3	P4700000K	Mushroom Rock	granite	Zrc, $\delta^{18}O$-Sr_i-εNd, WR	4122957	298625	100.2 ± 1.4
8-RF-4	P4700000L	Ordinance Creek	granite	Zrc, $\delta^{18}O$-Sr_i, WR	4123156	299198	106.5 ± 1.3
8-RF-5	P4700000M	Sheepthief Creek	granite	Zrc, $\delta^{18}O$, WR	4115181	301322	106.0 ± 0.8
8-RF-6	P47000018	Sheepthief Creek	granite	Sr_i, WR	4115056	301347	ND
8-RF-7	P47000019	Sheepthief Creek	granite	Sr_i, WR	4115089	301349	ND
8-RF-8	P4700001A	Dinkey Creek	granodiorite	Sr_i, WR	4114995	301316	ND
8-RF-9	P4700001B	Dinkey Creek	granodiorite	Sr_i, WR	4114966	301296	ND
8-RF-11	P4700000N	Coyote Creek††	granite	Zrc, Sr_i, WR	4120042	312716	100.1 ± 1.9
8-RF-12	P4700000O	Shorthair Creek	granite	Zrc, $\delta^{18}O$-Sr_i, WR	4105142	324281	98.3 ± 1.2
8-RF-14	P4700000P	Lower Bear Creek	granite	Zrc, $\delta^{18}O$-Sr_i, WR	4102479	309971	100.5 ± 1.1
8-RF-15	P4700000Q	Dinkey Dome	granite	Zrc, Sr_i, WR	4106172	314037	119.2 ± 1.2
8-RF-16	P4700000R	Rainbow Mine††	leucodiorite	Sr_i, WR	4113986	313947	ND
8-RF-17	P4700000S	Rainbow Mine††	diorite	Zrc, $\delta^{18}O$-Sr_i, WR	4113953	314114	102.18 ± 0.74
8-RF-18	P4700000T	Rainbow Mine††	diorite	WR	4114384	314160	ND
8-RF-19	P4700000U	Dinkey Lakes††	granite	Zrc, $\delta^{18}O$-Sr_i-εNd, WR	4114626	314158	102.2 ± 1.3
1S67§§	P4700000V	North of Snow Corral Meadow	granite	Zrc, $\delta^{18}O$-Sr_i-εNd, WR	4102088	315437	101.7 ± 1.1
1S81§§	P4700000W	Dinkey Dome	granite	Zrc, $\delta^{18}O$-Sr_i-εNd, WR	4106978	311033	117.5 ± 1.7
3S48§§	P4700000X	Mud Lakes††	diorite	Zrc, $\delta^{18}O$-Sr_i-εNd, WR	4109522	315054	99.63 ± 0.76
3S51§§	P4700000Y	Dinkey Lakes††	granite	Zrc, $\delta^{18}O$-Sr_i-εNd, WR	4111836	315339	104.3 ± 1.6
95-16##	P4700000Z	Dinkey Creek	granodiorite	Zrc, $\delta^{18}O$	4107269	300768	101.7 ± 0.7
95-17##	P47000010	Dinkey Creek	granodiorite	Zrc, $\delta^{18}O$	4114386	298468	101.2 ± 1.6
96-7##	P47000011	Dinkey Creek	granodiorite	Zrc, $\delta^{18}O$	4100640	315668	101.0 ± 1.1
13JLE-4a	P47000012	Big Meadows host	gabbro	Sr_i-εNd, WR	4067046	340330	ND
13JLE-4b	P47000013	Big Meadows orb core	gabbro	Zrc, Sr_i-εNd, WR	4067046	340330	95.57 ± 0.40
13JLE-15	P47000014	Deer Creek orb core	gabbro	Sr_i-εNd, WR	4097406	315964	ND
13JLE-16	P47000015	Deer Creek orb core	gabbro	Zrc, Sr_i-εNd, WR	4097406	315964	100.09 ± 0.47
13JLE-17	P47000016	Dinkey Creek (Deer Creek orb host)	gabbro	Zrc, $\delta^{18}O$-Sr_i-εNd, WR	4097406	315964	99.25 ± 0.46
13JLE-18	P47000017	Deer Creek orb core	gabbro	Zrc, Sr_i-εNd, WR	4097406	315964	99.67 ± 0.35
DC12-02	P4700000D	Dinkey Creek	granodiorite	Zrc, Sr_i-εNd, WR	4104697	325337	101.8-100.6
MG12-03	P4700000E	Mount Givens	granodiorite	Zrc, Sr_i-εNd, WR	4105368	325121	91.6-91.1
DC12-04	P4700000F	Dinkey Creek	granodiorite	Zrc, Sr_i-εNd, WR	4105322	324680	101.8-101.2
DC12-05	P4700000G	Dinkey Creek	granodiorite	Zrc, Sr_i-εNd, WR	4097808	324206	101.7-101.2

*IGSN: International Geo Sample Number. Access sample metadata at www.geosamples.org.
†*Sensu lato*
§Analysis abbreviations: Zrc – zircon U-Pb geochronology; $\delta^{18}O$ – $\delta^{18}O$ in zircon; Sr_i – whole rock $^{87}Sr/^{86}Sr$; εNd – whole rock $^{143}Nd/^{144}Nd$; WR – whole rock elemental composition
#Sample locations given in NAD 83, UTM zone 11 north
**Preferred age and uncertainty given in Ma. ND: not dated. Note age ranges given for DC12-02 through DC12-05. See text for geochronologic methods used
††Informal pluton name used in this paper
§§$\delta^{18}O$ and WR data from Lackey et al. (2006)
##$\delta^{18}O$ data from Lackey et al. (2008)

TABLE 2. MAJOR ELEMENT DATA

Sample	SiO_2 wt%	TiO_2 wt%	Al_2O_3 wt%	Fe_2O_3 wt%	MnO wt%	MgO wt%	CaO wt%	Na_2O wt%	K_2O wt%	P_2O_5 wt%	Total
8-RF-1*	75.06	0.18	13.14	1.69	0.03	0.31	1.59	2.89	4.66	0.05	99.60
8-RF-3*	72.66	0.32	14.32	2.40	0.04	0.63	2.09	3.11	4.08	0.08	99.73
8-RF-4*	70.83	0.47	14.17	3.67	0.06	1.13	2.45	2.90	3.96	0.11	99.75
8-RF-5*	73.36	0.22	14.15	2.16	0.03	0.42	1.71	3.33	4.34	0.07	99.79
8-RF-6*	73.12	0.21	14.51	2.11	0.03	0.33	1.84	3.29	4.29	0.06	99.79
8-RF-7*	76.05	0.18	13.12	1.65	0.02	0.22	1.38	2.78	4.39	0.04	99.82
8-RF-8*	70.35	0.38	15.02	3.27	0.06	0.68	2.45	3.18	4.25	0.10	99.73
8-RF-9*	68.59	0.47	15.59	3.89	0.07	0.95	3.20	3.49	3.39	0.11	99.75
8-RF-11*	77.63	0.06	12.75	0.55	0.02	0.06	0.45	3.87	4.53	0.03	99.95
8-RF-12*	69.63	0.45	14.75	3.38	0.07	1.22	2.94	2.99	4.29	0.10	99.82
8-RF-14*	73.42	0.23	13.98	2.41	0.04	0.32	1.44	3.13	4.60	0.07	99.64
8-RF-16*	72.47	0.35	13.43	3.04	0.06	0.97	1.49	2.39	5.52	0.12	99.84
8-RF-17*	56.37	1.05	17.67	8.18	0.13	4.13	8.52	2.17	1.46	0.17	99.85
8-RF-18*	59.76	1.07	16.01	7.74	0.12	3.68	6.75	2.29	2.19	0.21	99.82
8-RF-19*	76.96	0.17	12.69	1.21	0.05	0.20	0.92	3.43	4.10	0.05	99.78
13JLE-4a*	56.93	0.84	19.19	6.55	0.10	2.37	6.58	3.06	1.60	3.06	100.28
13JLE-4b*	52.78	1.27	17.62	9.33	0.15	4.46	7.73	2.81	1.33	2.81	100.29
13JLE-15*	53.30	0.70	16.47	8.27	0.14	7.42	10.96	1.55	0.54	0.07	99.42
13JLE-16*	50.46	1.08	19.53	7.74	0.11	5.35	9.19	1.95	1.18	0.11	96.70
13JLE-17*	48.66	1.58	18.20	9.95	0.17	5.55	8.52	2.19	1.51	0.27	96.60
13JLE-18*	52.64	1.31	16.45	8.04	0.11	6.39	8.60	1.67	1.52	0.15	96.88
DC12-02§	66.34	0.506	14.72	4.82	0.077	1.46	3.83	3.01	3.37	0.10	98.23
MG12-03§	64.45	0.608	15.90	5.60	0.082	1.74	4.46	4.08	2.18	0.20	99.30
DC12-04§	66.64	0.543	15.04	4.87	0.079	1.56	3.99	3.12	3.38	0.12	99.34
DC12-05§	66.22	0.573	15.01	5.49	0.083	1.64	4.13	3.10	3.37	0.11	99.72

*Data acquired by X-ray fluorescence at Pomona College
§Data acquired by inductively coupled plasma optical emission spectroscopy at Actlabs (Ontario, Canada)

TABLE 3. TRACE ELEMENT DATA

Sample	Sc ppm	V ppm	Ba ppm	Sr ppm	Y ppm	Zr ppm	Cr ppm	Co ppm	Ni ppm	Cu ppm	Zn ppm	Ga ppm	As ppm	Rb ppm	Nb ppm	Mo ppm	Cs ppm	Hf ppm	Ta ppm	Pb ppm	Th ppm	U ppm
8-RF-1*	BDL[†]	9	1176	202	8	134	4	NA[§]	BDL	5	46	15	NA	112	10	NA	5	NA	NA	21	11	3
8-RF-3*	5	29	1049	324	20	163	5	NA	BDL	49	84	18	NA	148	14	NA	6	NA	NA	23	12	4
8-RF-4*	8	48	851	270	25	162	6	NA	BDL	5	83	19	NA	191	17	NA	12	NA	NA	21	19	8
8-RF-5*	5	15	1119	196	8	140	4	NA	BDL	4	58	16	NA	100	11	NA	7	NA	NA	21	13	4
8-RF-6*	8	48	1119	285	31	189	9	NA	4	BDL	69	20	NA	117	13	NA	BDL	8	NA	18	15	3
8-RF-7*	5	35	1351	245	26	185	8	NA	2	BDL	64	18	NA	144	14	NA	9	6	NA	18	16	3
8-RF-8*	BDL	11	918	145	5	128	9	NA	3	BDL	31	14	NA	104	8	NA	BDL	4	NA	16	6	BDL
8-RF-9*	4	20	1106	199	7	131	7	NA	5	BDL	42	16	NA	96	9	NA	BDL	5	NA	18	12	BDL
8-RF-11*	BDL	5	163	13	17	59	BDL	NA	BDL	4	49	14	NA	157	10	NA	5	NA	NA	31	13	4
8-RF-12*	6	59	638	287	24	137	11	NA	BDL	6	69	17	NA	218	16	NA	12	NA	NA	33	32	18
8-RF-14*	4	12	1058	161	16	205	6	NA	BDL	6	78	18	NA	159	18	NA	6	NA	NA	23	20	5
8-RF-16*	11	44	846	143	33	100	7	NA	BDL	5	61	17	NA	239	18	NA	14	NA	NA	28	30	15
8-RF-17*	25	226	463	416	16	129	24	NA	BDL	13	89	19	NA	64	10	NA	8	NA	NA	13	7	5
8-RF-18*	24	164	440	355	26	196	30	NA	5	14	87	18	NA	83	14	NA	7	NA	NA	17	16	9
8-RF-19*	BDL	5	1292	158	19	131	6	NA	BDL	4	53	14	NA	169	15	NA	8	NA	NA	27	23	7
13JLE-4a*	11.2	172.4	477.8	588.3	11.6	60.3	12.4	58.3	-0.30	16.7	99.7	20.1	14.7	72.1	11.4	2.5	4.6	2.6	9.2	1.7	12.4	2.6
13JLE-4b*	19.2	228.9	401.9	534.3	17.3	93.6	29.5	155.1	4.30	31.5	128.8	19.9	24.0	46.7	11.5	3.9	2.5	2.6	7.9	0.2	9.3	4.1
13JLE-15*	30.6	210.8	161.2	432.6	17.4	86.7	198.2	171.8	22.7	9.4	95.6	15.8	-5.0	15.4	7.0	2.7	5.3	2.4	NA	-4.7	4.6	0.9
13JLE-16*	24.9	285.6	408.8	525.3	17.6	62.0	62.8	137.3	21.6	17.2	91.4	19.5	4.8	43.7	6.4	1.8	2.5	1.4	NA	-1.7	2.6	1.5
13JLE-17*	32.9	251.4	372.8	466.3	22.9	68.8	32.3	154.9	14.0	34.7	131.1	20.1	9.1	58.2	12.9	3.4	4.6	2.8	NA	-0.6	6.0	0.2
13JLE-18*	31.5	312.0	530.0	420.6	17.8	75.2	87.2	115.6	34.8	16.9	99.2	18.7	4.7	61.1	6.7	2.1	9	1.8	NA	-0.7	3.4	2.2
DC12-02[#]	8	74	633	285	13	115	260	9	BDL	20	60	16	BDL	138	7	4	5	3.3	1.7	19	22.7	6.3
MG12-03[#]	7	91	418	579	8	137	40	13	30	40	90	21	BDL	95	8	BDL	4.1	3.7	0.9	16	10.0	5.6
DC12-04[#]	9	79	611	298	13	132	230	10	BDL	20	70	17	BDL	153	8	4	6.9	3.8	1.4	19	26.0	9.1
DC12-05[#]	9	84	590	292	15	127	40	11	BDL	10	60	17	BDL	154	9	3	3.5	3.5	1.3	18	23.1	5.6

*Data measured by X-ray fluorescence at Pomona College
[§]NA = element not analyzed
[†]BDL = below detection limit
[#]Data for Sc, V, Ba, Sr, Y, and Zr measured by inductively coupled plasma optical emission spectrometry at Actlabs (Ontario, Canada). All other elements measured by inductively coupled plasma mass spectrometry at Actlabs

TABLE 4. RARE EARTH ELEMENT DATA

Sample	La ppm	Ce ppm	Pr ppm	Nd ppm	Sm ppm	Eu ppm	Gd ppm	Tb ppm	Dy ppm	Ho ppm	Er ppm	Tm ppm	Yb ppm	Lu ppm	Ce/Ce*	Eu/Eu*
8-RF-1§	26.45	36.82	5.22	17.34	2.52	0.67	1.70	0.23	1.11	0.21	0.61	0.09	0.66	0.09	0.76	0.99
8-RF-3§	25.32	32.46	5.66	21.03	4.20	0.91	3.45	0.53	3.02	0.57	1.70	0.27	1.88	0.27	0.66	0.73
8-RF-19§	34.22	64.49	6.32	20.82	3.26	0.63	2.41	0.36	1.98	0.39	1.20	0.20	1.45	0.22	1.06	0.68
1S67§	16.71	19.03	2.69	8.16	1.07	0.73	0.76	0.11	0.61	0.13	0.45	0.08	0.60	0.08	0.69	2.48
1S81§	14.37	26.48	3.35	12.19	2.63	0.47	2.62	0.48	2.98	0.60	1.88	0.32	2.10	0.31	0.92	0.55
3S48§	14.08	30.63	3.84	15.98	3.41	1.04	3.20	0.47	2.72	0.51	1.42	0.21	1.30	0.18	1.01	0.96
3S51§	49.21	38.24	11.07	41.36	7.82	1.51	6.89	1.07	6.36	1.25	3.61	0.55	3.56	0.54	0.40	0.63
13JLE-4a†	30.80	54.26	5.47	18.45	2.79	1.06	2.03	0.29	1.51	0.31	0.89	0.13	0.94	0.13	1.01	1.36
13JLE-4b†	18.59	37.94	4.81	19.40	4.19	1.16	3.56	0.53	3.07	0.60	1.63	0.22	1.63	0.24	0.97	0.92
13JLE-15†	14.17	33.75	4.45	18.42	3.85	1.26	3.51	0.52	3.06	0.60	1.70	0.24	1.71	0.24	1.03	1.04
13JLE-16†	11.76	28.63	3.91	16.71	4.03	1.22	3.31	0.52	3.00	0.61	1.69	0.23	1.63	0.22	1.02	1.02
13JLE-17†	18.00	39.62	5.23	22.63	5.30	1.43	4.96	0.75	4.17	0.82	2.35	0.31	2.15	0.30	0.99	0.85
13JLE-18†	12.58	28.37	3.87	16.64	3.95	1.12	3.57	0.53	3.21	0.64	1.72	0.24	1.57	0.23	0.98	0.91
DC12-02#	30.2	54.4	5.32	17.8	3.4	0.79	2.9	0.4	2.6	0.5	1.5	0.23	1.7	0.26	1.04	0.77
MG12-03#	26.2	51.6	5.73	20.2	3.5	0.93	2.7	0.4	1.9	0.3	0.9	0.14	0.9	0.13	1.02	0.92
DC12-04#	25.3	46.0	4.78	16.7	3.2	0.86	2.9	0.4	2.7	0.5	1.5	0.24	1.5	0.25	1.01	0.86
DC12-05#	30.9	56.4	5.75	19.0	3.5	0.86	3.1	0.5	2.8	0.5	1.6	0.27	1.7	0.31	1.02	0.80

*Ce and Eu anomalies calculated as $Ce_N/(La_N \times Pr_N)^{½}$ and $Eu_N/(Sm_N \times Gd_N)^{½}$, respectively, where subscript N denotes concentration normalized to chondritic values of McDonough and Sun (1995)
§Data measured by inductively coupled plasma mass spectrometry (ICP-MS) at Vrije University
†Data measured by ICP-MS at University of California – Santa Barbara
#Data measured by ICP-MS at Actlabs (Ontario, Canada)

TABLE 5. OXYGEN ISOTOPE VALUES FOR ZIRCON

Sample	Pluton	Rock type*	$\delta^{18}O$(Zrc) (‰)	$\pm 1\sigma$
8-RF-1	Sheepthief Creek	granite	7.15	0.03
8-RF-3	Mushroom Rock	granite	8.00	0.03
8-RF-4	Ordinance Creek	granite	7.91	0.03
8-RF-5	Sheepthief Creek	granite	7.19	0.03
8-RF-12	Shorthair Creek	granite	6.92	0.03
8-RF-14	Lower Bear Creek	granite	7.33	0.03
8-RF-17	Rainbow Mine	diorite	7.61	0.03
8-RF-19	Dinkey Lakes	granite	6.60	0.03
13JLE-4a	Big Meadows (orb core)	gabbro	6.97	0.10
13JLE-17	Dinkey Creek (Deer Creek orb host)	tonalite	6.40	0.10
1S67†	North of Snow Corral Meadow	granite	7.50	0.04
1S81†	Dinkey Dome	granite	7.76	0.04
3S48†	Mud Lakes	diorite	7.54	0.04
3S51†	Dinkey Lakes	granite	8.02	0.04
95-16§	Dinkey Creek	granodiorite	7.35	0.01
95-17§	Dinkey Creek	granodiorite	7.32	0.09
96-7§	Dinkey Creek	granodiorite	7.58	0.04

**Sensu lato*

†Oxygen isotope data from Lackey et al. (2006)

§Oxygen isotope data from Lackey et al. (2008)

TABLE 6. SR AND ND ISOTOPIC DATA

Sample	Rb ppm	Sr ppm	$^{87}Sr/^{86}Sr$	± 2σ abs*	$^{87}Sr/^{86}Sr_{norm}$	$^{87}Rb/^{86}Sr$	$^{87}Sr/^{86}Sr_i$	Sm ppm	Nd ppm	$^{143}Nd/^{144}Nd$	± 2σ abs*	$^{147}Sm/^{144}Nd$	$^{143}Nd/^{144}Nd_{norm}$	$^{143}Nd/^{144}Nd_i$	εNd_i
8-RF-1†	88	202	0.710318	0.000008	0.710326	1.261	0.708500	2.52	17.34	0.512210	0.000006	0.088	0.512211	0.512153	-6.91
8-RF-3†	100	324	0.708991	0.000007	0.708999	0.893	0.707727	4.20	21.03	0.512245	0.000007	0.121	0.512246	0.512167	-6.67
8-RF-4#	191	270	0.711013	0.000011	0.710998	2.047	0.707899								
8-RF-6#	96	199	0.710119	0.000010	0.710104	1.396	0.708001								
8-RF-7#	104	145	0.710504	0.000010	0.710489	2.076	0.707362								
8-RF-8#	144	245	0.710605	0.000009	0.710590	1.701	0.708124								
8-RF-9#	117	285	0.709856	0.000009	0.709841	1.188	0.708119								
8-RF-11#	157	13	0.738072	0.000010	0.738056	35.047	0.688205								
8-RF-12#	218	287	0.710192	0.000010	0.710177	2.198	0.707106								
8-RF-14#	159	161	0.711475	0.000013	0.711460	2.858	0.707378								
8-RF-16#	239	143	0.717620	0.000010	0.717605	4.840	0.710576								
8-RF-17#	64	416	0.709372	0.000009	0.709357	0.445	0.708711								
8-RF-19†	187	158	0.710426	0.000014	0.710434	3.425	0.705459	3.26	20.82	0.512363	0.000006	0.095	0.512364	0.512301	-4.01
1S67§	105	225	0.709472	0.000003	0.709480	1.350	0.707528	1.07	8.16	0.512209	0.000009	0.079	0.512210	0.512158	-6.82
1S81§	205	134	0.715860	0.000010	0.715868	4.430	0.708471	2.63	12.19	0.512305	0.000004	0.130	0.512306	0.512206	-5.47
3S48§	77	601	0.707798	0.000007	0.707806	0.371	0.707281	3.41	15.98	0.512241	0.000005	0.129	0.512242	0.512158	-6.86
3S51§	155	211	0.711807	0.000011	0.711815	2.123	0.708663	7.82	41.36	0.512166	0.000007	0.114	0.512167	0.512089	-8.08
DC12-02††	138	285	0.709103	0.000009	0.709088	1.401	0.707053	3.4	17.8	0.512303	0.000005	0.116	0.512320	0.512244	-5.16
MG12-03††	95	579	0.707223	0.000010	0.707208	0.475	0.706592	3.5	20.2	0.512332	0.000006	0.105	0.512349	0.512286	-4.57
DC12-04††	153	298	0.709119	0.000010	0.709104	1.490	0.706961	3.2	16.7	0.512283	0.000004	0.116	0.512283	0.512223	-5.55
DC12-05††	154	292	0.709519	0.000010	0.709504	1.526	0.707304	3.5	19.0	0.512233	0.000004	0.111	0.512250	0.512176	-6.47
MG10-01††	165	370	0.708802	0.000011	0.708802	1.290	0.707045	4.4	23.1	0.512289	0.000004	0.115	0.512306	0.512234	-5.49
MG10-02††	192	217	0.709531	0.000011	0.709516	2.560	0.706165	1.9	13.2	0.512370	0.000005	0.087	0.512387	0.512335	-3.61
MG10-03††	198	103	0.713377	0.000010	0.713362	5.565	0.706030	0.6	4.5	0.512357	0.000005	0.081	0.512374	0.512325	-3.78
MG10-04††	241	284	0.709278	0.000009	0.709263	2.456	0.706039	2.1	12.5	0.512377	0.000004	0.102	0.512394	0.512536	-3.64
MG10-05††	121	388	0.708687	0.000009	0.708672	0.902	0.707448	3.2	19.1	0.512281	0.000005	0.101	0.512298	0.512235	-5.47
MG10-07††	137	400	0.707989	0.000008	0.707974	0.991	0.706694	2.5	14.8	0.512313	0.000005	0.102	0.512330	0.512269	-4.91
MG10-08††	194	352	0.708873	0.000010	0.708858	1.595	0.706795	3.8	25.0	0.512321	0.000004	0.092	0.512338	0.512283	-4.64
MG11-01††	130	470	0.707556	0.000012	0.707541	0.800	0.706452	6.1	33.2	0.512347	0.000004	0.111	0.512364	0.512294	-4.30
MG11-02††	139	388	0.708527	0.000010	0.708512	1.037	0.707108	3.6	21.0	0.512291	0.000004	0.104	0.512308	0.512243	-5.31
MG11-03††	129	495	0.707401	0.000009	0.707386	0.754	0.706383	3.4	18.7	0.512376	0.000004	0.110	0.512393	0.512535	-3.75
MG11-04††	137	288	0.708125	0.000010	0.708110	1.376	0.706195	3.7	18.3	0.512450	0.000005	0.122	0.512467	0.512389	-2.41
MG12-01††	139	445	0.708638	0.000009	0.708623	0.904	0.707398	4.6	25.0	0.512291	0.000006	0.111	0.512308	0.512239	-5.40

Note: Subscript "norm" indicates ratio normalized to facilitate interlaboratory comparison. See text for rationale. Initial isotopic values calculated using normalized ratios and U-Pb zircon ages given in Table 1. For ID-TIMS age ranges, the midpoint was used. Ages used for undated samples are: 8-RF-6 and 8-RF-7 (106 Ma); 8-RF-8 and 8-RF-9 (102 Ma); 8-RF-16 (102.18 Ma)

*Analytical uncertainty only. See text for reproducibility of standards at Vrije University (VU) and University of North Carolina at Chapel Hill (UNC)

†Rb concentration by isotope dilution (ID) at VU; Sr concentration by X-ray fluorescence (XRF) at Pomona College (PC); Sm, Nd concentrations by ICP-MS at VU; isotopic ratios by TIMS at VU

#Rb, Sr concentrations by XRF at PC; isotopic ratios by TIMS at UNC

§Rb concentration by ID at VU; Sr concentration from Lackey et al. (2006); Sm, Nd concentrations by ICP-MS at VU; isotopic ratios by TIMS at VU

††Rb, Sm, Nd concentrations by ICP-MS at Actlabs (Ontario, Canada); Sr by ICP-optical emission spectroscopy at Actlabs; isotopic ratios by TIMS at UNC

CHAPTER 3: THE ALABAMA HILLS GRANITE AND IMPLICATIONS FOR DEXTRAL OFFSETS IN OWENS VALLEY, MID-CRETACEOUS SIERRAN MAGMATISM, AND THE GENESIS OF GRANODIORITES

INTRODUCTION

Understanding the origins of the Alabama Hills, in Owens Valley, CA, and their relationship to the adjacent Sierra Nevada has been a goal of geologists since Josiah Whitney described them as "forming a sort of detached outlier of the Sierra, and composed of similar granitic and metamorphic rocks" (Whitney, 1872, p. 137). Their composition (Lee, 1906; Knopf, 1918) and well-documented historical seismic activity (Whitney, 1872; Gilbert, 1884; Hobbs, 1910) typify the geology of eastern California. Coupled with their ease of access between the Sierra Nevada and Inyo Range, they are an intriguing target for study.

The Quaternary history of the Alabama Hills is well-documented due to interest in modern activity on the Lone Pine fault, including the 1872 earthquake (M_w 7.8-7.9; Hough and Hutton, 2008) that devastated Lone Pine and produced a dramatic and well-preserved fault scarp near the eastern base of the hills. This has led to a wealth of study on the Lone Pine and Owens Valley faults (Lubetkin and Clark, 1988; Beanland and Clark, 1994; Lee et al., 2001) and their relationships to larger-scale tectonic systems (e.g., Wesnousky and Jones, 1994; Unruh et al., 2003; Le et al., 2007; Stevens et al., 2013). The Alabama Hills have also proven fruitful for the application of cosmogenic nuclides to understand bedrock erosion rates, earthquake recurrence, and debris flow deposition (Bierman et al., 1995a, 1995b; Nichols et al., 2006).

Pre-Quaternary study of the Alabama Hills has mostly been limited to the Jurassic metavolcanic and metasedimentary rocks that comprise the eastern half of the hills (Dunne and Walker, 1993; Dunne et al., 1998; Sorensen et al., 1998), as well as the Independence dike swarm that intrudes those units (e.g., Moore and Hopson, 1961; Chen and Moore, 1979; Bartley et al., 2007). Relatively little work has been done on the granite pluton that comprises the western half of the hills. A zircon U-Pb age of 85 Ma (Chen and Moore, 1982) is similar to the youngest parts of the Sierra Crest magmatic event, including the adjacent Whitney Intrusive Suite (Coleman and Glazner, 1997; Davis, 2010), and has led some to speculate the Alabama Hills are a down-dropped block from the Whitney suite (Ali et al., 2009).

High-precision U-Pb zircon geochronology, whole rock elemental and radiogenic isotopic data are used to test the links between the Alabama Hills Granite and the main Sierra Nevada batholith. These data demonstrate the Alabama Hills Granite is mid-Cretaceous in age and belongs to a suite of plutons of similar ages and isotopic compositions that lies to the north of the Whitney Intrusive Suite. The data permit evaluation of the relationship of the Alabama Hills block to the Sierra Nevada, and the extent of high-silica granite in the mid-Cretaceous batholith. Finally, the significance of high-Zr, high-silica granite for the generation of both voluminous granitoids and high-silica rhyolites is explored.

GEOLOGIC BACKGROUND

The Alabama Hills are a low range located in Owens Valley, west of the town of Lone Pine, CA and east of the Sierra Nevada range front (Figs. 1, 2). The range was first mapped in reconnaissance by Knopf (1918) and includes the Jurassic volcanic complex of the Alabama Hills (Dunne et al., 1998; Stone et al., 2000) and the Cretaceous Alabama Hills Granite (Stone et

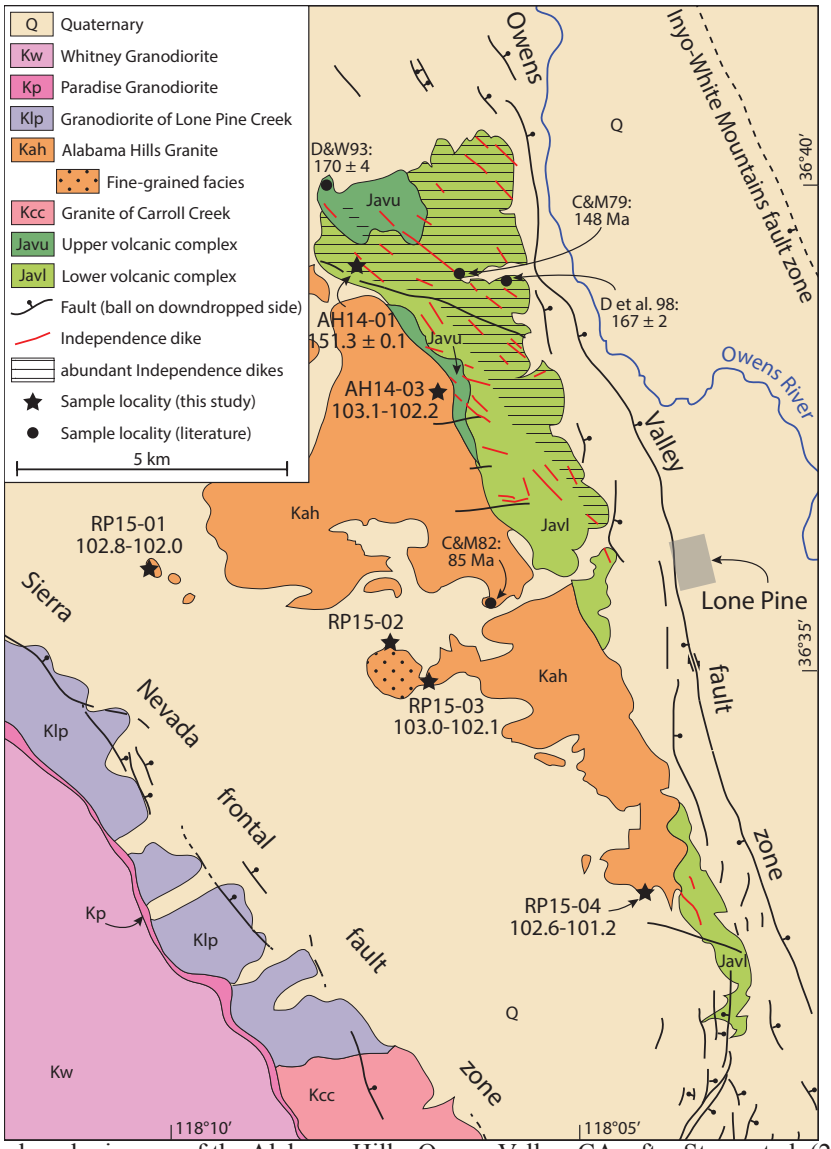

Figure 1. Generalized geologic map of the Alabama Hills, Owens Valley, CA, after Stone et al. (2000). Zircon U-Pb ages given in Ma as weighted means with 2σ uncertainty, or as age ranges (see text for discussion). Note that wheras all individual Independence dikes are mapped, two samples (AH14-01 and literature data of C&M79) were specifically collected from Independence dikes. Literature age prefixes: C&M79 – Chen and Moore (1979); C&M82 – Chen and Moore (1982); D&W93 – Dunne and Walker (1993); D et al. 98 – Dunne et al. (1998).

al., 2000). The volcanic complex of the Alabama Hills is also pervasively invaded by the Jurassic Independence dike swarm (Chen and Moore, 1979; Carl et al., 1998).

The western part of the Alabama Hills is dominated by the Alabama Hills Granite (Stone et al., 2000). The granite is exposed as distinctive inselbergs and ridges over an area of approximately 30 km^2. The pluton is mostly equigranular granite, although textures range from mildly porphyritic to fine-grained (Stone et al., 2000). Color index is below 10%, with accessory min-

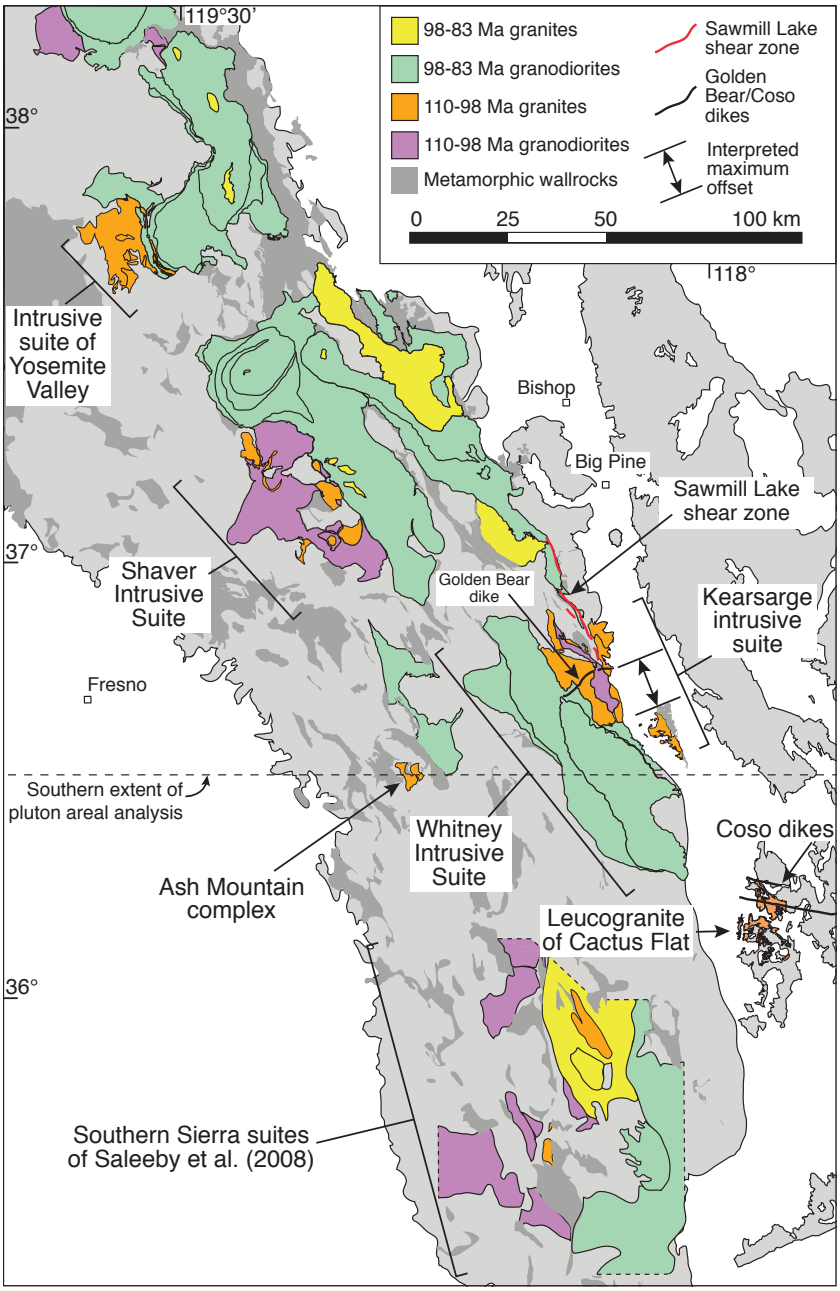

Figure 2. Generalized bedrock geologic map of the central Sierra Nevada batholith indicating localities mentioned in the text. The Alabama Hills Granite is grouped with the Kearsarge intrusive suite, which includes the Bullfrog, Independence, and Dragon plutons in the main batholith, and may also include the leucogranite of Cactus Flat in the Coso Range. Maximum interpreted offset of Alabama Hills relative to the main batholith is approximately 10 km based on the distance to the Golden Bear dike. Mid- and Late Cretaceous plutons shown in color are those considered "well-dated" in Figure 8. Horizontal dashed line indicates southern extent of plutons included in analysis of Figure 8. Only those parts of the intrusive suites that have been reliably dated are shown. For example, the intrusive suite of Yosemite Valley is limited to the map units that are dated by Ratajeski et al. (2001) and Putnam et al. (2015). The western part of the El Capitan Granite of Bateman (1992) is omitted due to a 114 Ma age (Putnam et al., 2015). Light gray part of batholith indicates plutonic rock undivided by age or composition. Bedrock geology after Moore (1963, 1978, 1981), Huber (1983), Moore and Sisson (1987), Bateman (1992), Moore and Nokleberg (1992), Sisson and Moore (1994), Stone et al. (2000), Wahrhaftig (2000), Lackey et al. (2008), and Saleeby et al. (2008). Evolution Basin Alaskite modified after Wenner and Coleman (2003) and Davis et al. (2012). Tuolumne Intrusive Suite modified after Memeti et al. (2010b). Sawmill Lake shear zone after Bartley et al. (2012).

erals including biotite, magnetite, ilmenite, and titanite (Richardson, 1975; Ague and Brimhall, 1988a; Stone et al., 2000). Ague and Brimhall (1988a) assigned the Alabama Hills Granite to their I-SC (strongly contaminated I-type) group of plutons. Lackey et al. (2008) measured $\delta^{18}O$ in two bulk zircon aliquots from a single sample, finding $\delta^{18}O$ in zircon = 6.41 ± 0.08 ‰ (2σ). Chen and Moore (1982) dated a sample from the central part of the pluton using TIMS U-Pb geochronology on bulk zircon aliquots (~10 mg each), yielding a concordant age of 85 Ma.

METHODS

Six samples were collected from the Alabama Hills for geochronological and geochemical analyses. Sample AH14-01 was collected from a diabase dike in the northern part of the volcanic complex of the Alabama Hills. Samples AH14-03, RP15-01, RP15-03, and RP15-04 were taken from the main body of the Alabama Hills Granite with the aim of maximizing spatial distribution. Samples were equigranular, although RP15-03 and RP15-04 featured some alkali feldspar crystals up to 1 cm in length with rapakivi texture. Sample RP15-02 was collected from a prominent hill mapped as a fine-grained facies of the Alabama Hills Granite (Stone et al., 2000). Only fresh, unweathered samples were selected for whole rock geochemical and isotopic analyses.

Whole rock elemental and isotopic geochemistry

Whole rock aliquots of samples RP15-01 through RP15-04 were crushed to powder in a SPEX Shatterbox® alumina swing mill and analyzed at Actlabs (Ontario, Canada). Samples were dissolved by fusion in a lithium metaborate/tetraborate mixture; major elements and Ba, Sr, Y, Zr, Sc, Be and V were analyzed by inductively coupled plasma-optical emission spectroscopy (ICP-OES), with remaining trace elements and REE analyzed by ICP-MS. Uncertainties (±2σ

relative) for major elements were less than 2% for all oxides except MgO (3%), MnO (5%), and P_2O_5 (16%). Trace elements analyzed at Actlabs that are reproducible (±2σ absolute) at better than 2 ppm include Ag, Be, Cs, Ge, Hf, Sb, Sn, Ta, Th, Tl, U, and W. Other elements are reproducible within 3 ppm (Co, Mo, Nb, Sc), 4 ppm (Ga, Y) and others have higher uncertainties, in parentheses in ppm: Pb (9); Cu (14); Rb and Zr (15); V (19); Ni (23); Sr (25); Ba (31); Zn (42); Cr (49). Rare earth elements reproducible (±2σ) at 0.2 ppm or better are Eu, Ho, Lu, Tb, and Tm; REE reproducible at 0.2-0.5 ppm or better are Dy, Er, Gd, Pr, Sm, and Yb; others are reproducible at higher uncertainties, in ppm: Nd (1.2); La (1.5); Ce (2.1).

For isotope geochemistry analyses, whole rock powders were dissolved in HF and HNO_3 in Teflon® (Parr) bombs at 180°C for 48-72 hours. Following dissolution, samples were dried down then immediately fluxed in 6M HCl for 16 hours. Samples were subsequently aliquoted for Sr and Nd purification by ion exchange column chromatography. Strontium was purified using Sr-spec cation exchange resin after the methods of Lundblad (1994) and loaded on single Re filaments with TaF_5. Neodymium was purified through a three-stage column chemistry procedure after Harvey and Baxter (2009) and loaded on single Re filaments in a Ta_2O_5-H_3PO_4 slurry. Strontium isotopic analyses were accomplished on a VG Sector 54 TIMS and Nd isotopes were analyzed on an Isotopx Phoenix TIMS at the University of North Carolina at Chapel Hill. Strontium was analyzed as a metal in dynamic multicollector mode with $^{88}Sr = 3V$; Nd was analyzed as an oxide in dynamic multicollector mode with $^{142}Nd^{16}O = 1V$. Strontium and Nd isotope ratios were corrected for mass fractionation using an exponential law; Sr isotopic ratios were normalized to $^{86}Sr/^{88}Sr = 0.1194$; Nd isotopic ratios were normalized to $^{146}Nd/^{144}Nd = 0.7219$. Replicate analyses of the NBS 987 Sr standard yielded $^{87}Sr/^{86}Sr = 0.710265 \pm 0.000015$ (2σ; n = 26). Replicate analyses of the Nd standard JNdi yielded $^{143}Nd/^{144}Nd = 0.512098 \pm 0.000012$ (2; n = 18). All

isotopic data are corrected to initial values using elemental concentration values from this study and a crystallization age of 102 Ma.

Geochronology

Geochronology was performed by CA-ID-TIMS on either a VG Sector 54 or Isotopx Phoenix-X62 in the Department of Geological Sciences at the University of North Carolina at Chapel Hill following the sample preparation and analytical methods of Frazer et al. (2014). Zircons for each sample were thermally annealed for 48 hours at 900ºC and then chemically abraded in HF and HNO_3 acids for 16 hours at 220ºC (Mundil et al., 2004; Mattinson, 2005). Individual grains were then selected under a binocular microscope for dissolution and isotope dilution using a mixed ^{205}Pb-^{233}U-^{236}U tracer after Parrish and Krogh (1987). Dissolution and chemical purification methods for U and Pb were modified after Krogh (1973) and Parrish (1987). Data processing and age calculations were completed using the applications Tripoli and ET_Redux, developed as part of the EARTHTIME initiative (Bowring et al., 2011; McLean et al., 2011), and include 2σ analytical uncertainties only. Corrections for initial Th/U disequilibrium (Mattinson, 1973; Schmitz and Bowring, 2001) were made in ET_Redux. Corrections for samples RP15-01 through RP15-04 were made assuming the measured whole rock Th/U value for each respective sample approximates the magmatic value; this adjustment increased the ages of individual analyses by up to 100 ka. Samples without corresponding whole rock concentration data used the following Th/U values and rationales: AH14-01: 3.5 (average of Independence dike samples AH95-8B, AH95-8C, and ID95-11 of Glazner et al., 2008a); AH14-03: 4.4 (average of samples RP15-01, RP15-03, and RP15-04 from this study).

RESULTS

Whole rock chemical analyses

Samples of Alabama Hills Granite have 73-77 wt% SiO_2 and small ranges of major element concentrations except sample RP15-02 from the fine-grained facies, which has slightly lower Fe_2O_3, MnO, MgO, CaO, and TiO_2, and higher K_2O (Fig. 3). Trace element concentrations are variable (Fig. 4). Samples RP15-01 and RP15-03 have higher Zr and Cr concentrations than other samples (Table 2). Sample RP15-02 is depleted in Ba, Sr, Y, and Zr relative to the equi-granular facies, whereas it has higher Rb and U concentrations. All samples contain at least 13 ppm Nb and Y/Sr ratios above 0.1 (Fig. 4).

Samples from the equigranular facies have La_N/Lu_N ratios near 10, and Gd_N/Lu_N near 1, indicating a "flat" chondrite-normalized heavy rare earth element (REE) pattern (subscript "N" indicates concentration normalized to chondritic values of McDonough and Sun, 1995). The same samples also have Eu/Eu* (calculated as $Eu_N/(Sm_N \cdot Gd_N)^{½}$) near 0.4, whereas sample RP15-02 has no discernable Eu anomaly (Fig. 5). Sample RP15-02 has low REE concentrations and a distinct REE pattern with low La_N/Lu_N and Gd_N/Lu_N.

Radiogenic isotopic analyses

There is a wide range of $^{87}Sr/^{86}Sr_i$ ratios among the samples analyzed, from 0.7030 to 0.7058. The equigranular samples have more restricted $^{87}Sr/^{86}Sr_i$ values (0.7052-0.7058), whereas RP15-02, with Rb/Sr = 11.75, yielded $^{87}Sr/^{86}Sr_i = 0.7030$. Neodymium isotopic compositions are restricted; calculated εNd at 102 Ma for the four Alabama Hills Granite samples ranges -2.4 to -3.1 (Table 2; Fig. 6).

Zircon geochronology

As modern high-precision zircon U-Pb data for intrusive rocks have become difficult to

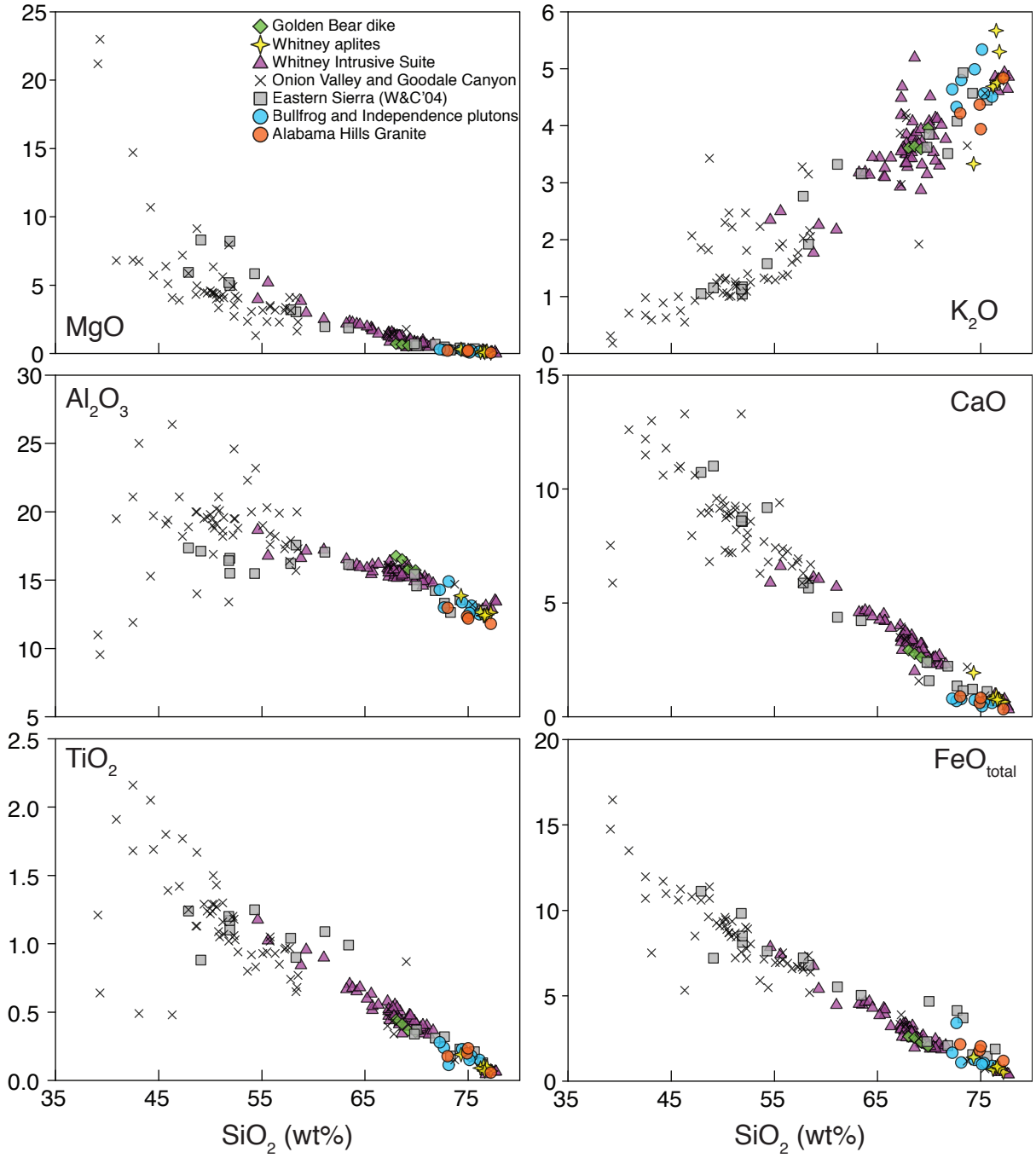

Figure 3. Major element data for the Alabama Hills Granite and other plutonic rocks of the eastern Sierra Nevada batholith. Ordinate units are wt% of the oxide indicated. The Alabama Hills Granite cannot be distinguished from other high-silica rocks, including aplites and leucogranites from the Whitney Intrusive Suite, and the Bullfrog and Independence plutons. Literature data from Bradford (1995), Sisson et al. (1996), Wenner and Coleman (2004), Kylander-Clark et al. (2005), Hirt (2007), Glazner et al. (2008b), and Coleman et al. (2012). W&C'04 – Wenner and Coleman (2004).

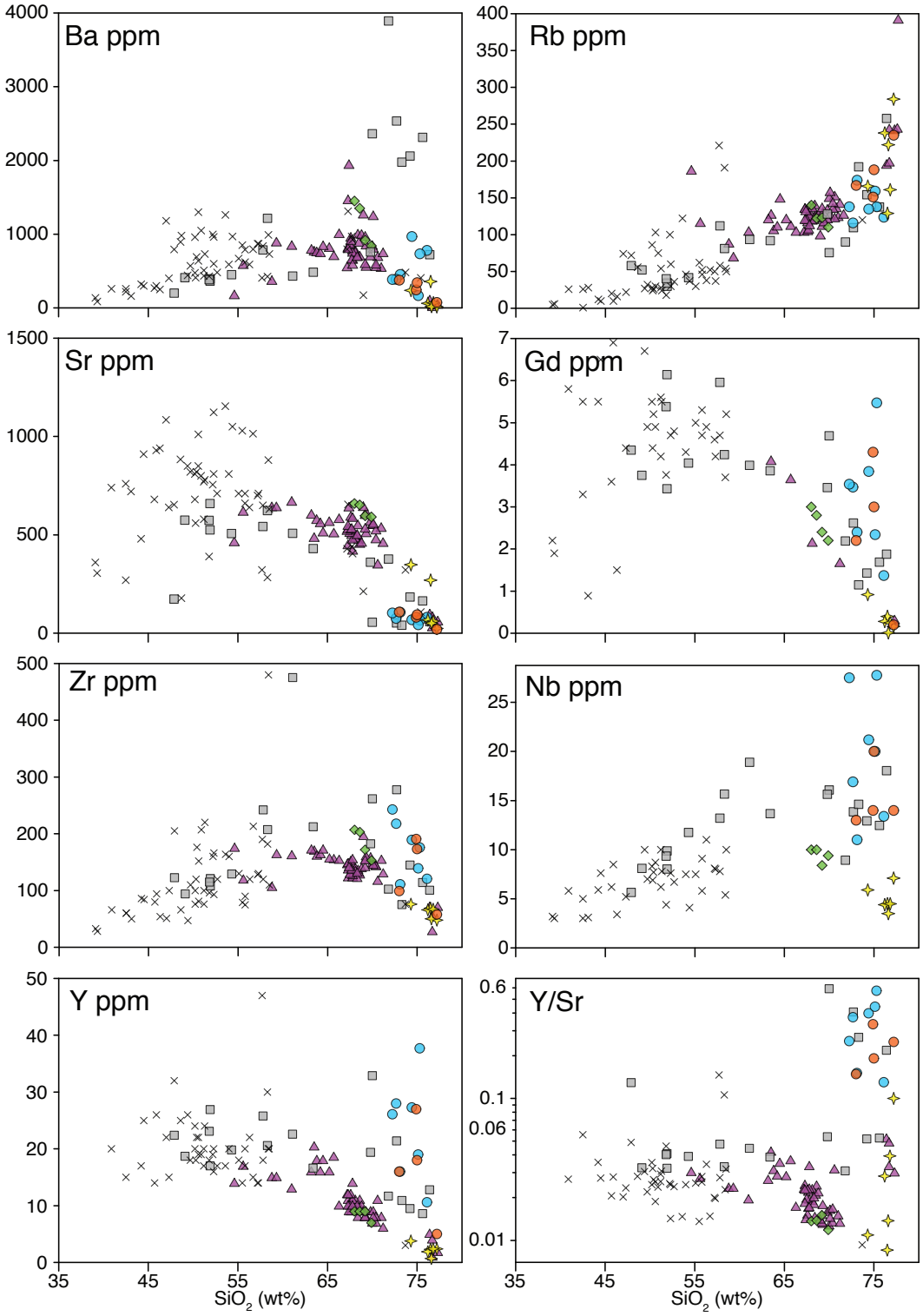

Figure 4. Trace element data for the Alabama Hills Granite and other plutonic rocks in the eastern Sierra Nevada. Data for the main facies of the Alabama Hills Granite are distinct from Whitney Intrusive Suite data with enrichments in HFSEs including Zr, Y, and Nb, as well as middle REEs including Gd. Sample RP15-02 from the fine-grained facies tracks high-silica rocks of the Whitney suite except for Y/Sr, where it plots with the Alabama Hills Granite and Bullfrog and Independence plutons. Symbols and data sources as in Fig. 3.

interpret geologically (Miller et al., 2007; Samperton et al., 2015; Schaltegger et al., 2015), and because the interpretations do not depend on precise relationships between samples, weighted mean ages are not assigned to the Alabama Hills Granite samples (Table 3; Fig. 7). Instead, the range of the 2σ analytical uncertainties for individual analyses from each sample is provided. A weighted mean age is calculated for dike sample AH14-01, which likely had a simpler thermal history.

Sample AH14-01 was collected from a diabase dike in the northern Alabama Hills metavolcanic complex. Four concordant zircon analyses yield Th-corrected $^{206}Pb/^{238}U$ ages spanning 1.3 Ma from 152.0-150.7 Ma. They yield a weighted mean age of 151.34 ± 0.13 Ma with a mean square of weighted deviates (MSWD) of 8.0.

Samples AH14-03, RP15-01, RP15-03, and RP15-04 are all concordant within uncertain-

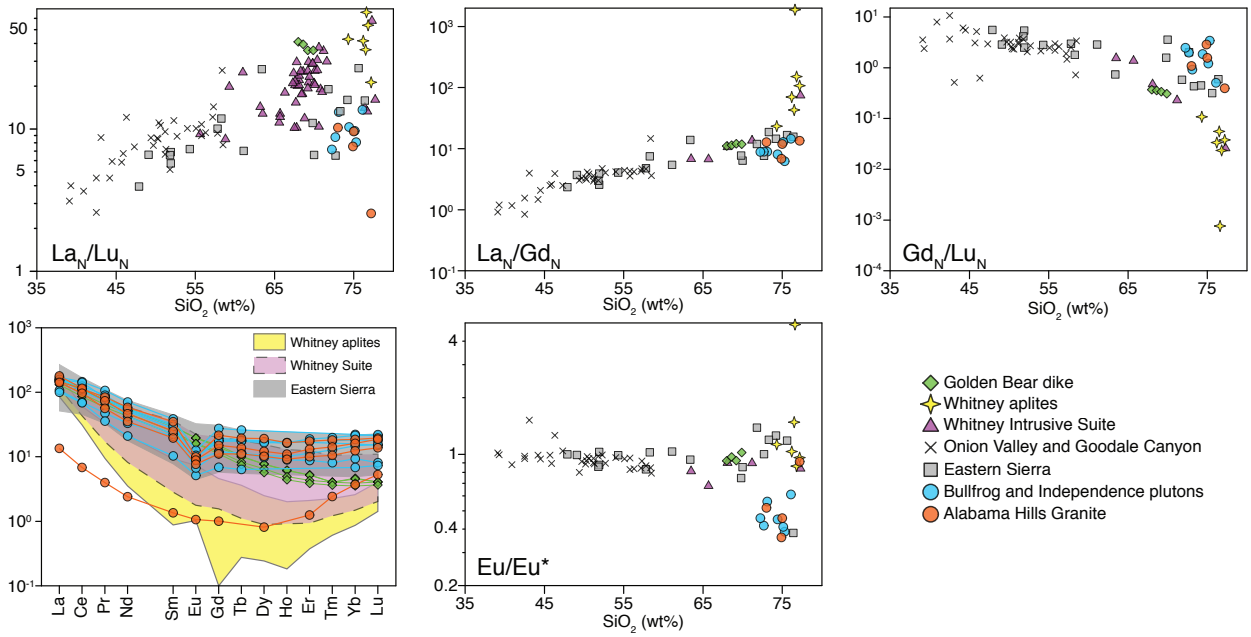

Figure 5. Rare earth element for the Alabama Hills Granite and other plutonic rocks in the eastern Sierra Nevada. Except for sample RP15-02, the Alabama Hills Granite has flatter REE patterns, with lower La_N/Lu_N and higher Gd_N/Lu_N, than Whitney Intrusive Suite rocks of similar silica concentrations. In addition, main facies Alabama Hills Granite samples are distinguished from Whitney suite rocks by having Eu/Eu* near 0.4. In contrast to the Whitney Intrusive Suite, REE data for the Bullfrog and Independence plutons match the Alabama Hills Granite well. The low light REE concentrations in sample RP15-02 are likely a primary feature, as suggested by εNd_i values similar to the other Alabama Hills Granite samples. Data sources as in Fig. 3.

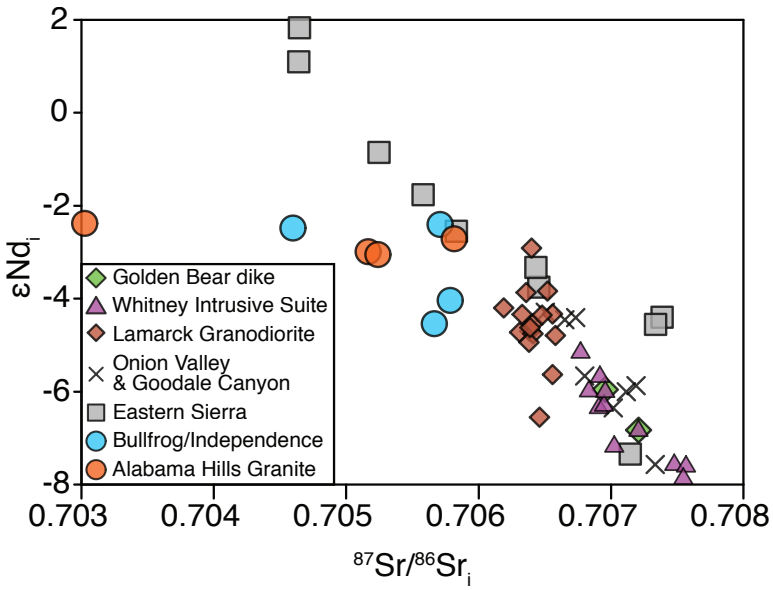

Figure 6. Strontium and Nd isotopic data corrected to initial values for the Alabama Hills Granite and other plutonic rocks of the eastern Sierra Nevada. Strontium is less radiogenic and Nd is more radiogenic in the Alabama Hills Granite compared to the Whitney Intrusive Suite. In addition, the Alabama Hills Granite data are matched well by Sr-Nd data for the Bullfrog and Independence plutons. Note that we interpret the lowest $^{87}Sr/^{86}Sr_i$ datum for the Alabama Hills Granite (sample RP15-02) to be compromised by post-crystallization open system processes, though the Sm-Nd system is considered robust (see text). Data sources as in Fig. 3, except: Lamarck Granodiorite (Coleman et al., 1992); Whitney Intrusive Suite (Hirt, 2007).

ty. Sample AH14-03 gave the oldest age spectrum, with seven individual zircons ranging 103.1-102.2 Ma. Seven zircons from sample RP15-03 yielded a nearly identical spectrum from 103.0-102.1 Ma. Four zircons each were dated in samples RP15-01 and RP15-04. Sample RP15-04 gave an age range of 102.8-102.0 Ma. Three zircons from RP15-01 overlap in age from 102.6-101.2 Ma, although the total range is encompassed by one zircon with high analytical uncertainty due to a relatively poor Pb isotopic analysis (Fig. 7). One younger grain has an age of 99.5 ± 0.3 Ma. Excluding the two youngest grains from sample RP15-01, 20 individual zircon analyses from the Alabama Hills Granite span 1.3 Ma from 103.1-101.8 Ma.

DISCUSSION

Interpretation of new geochronology

The 151.34 ± 0.13 Ma age for a mafic dike from the northern Alabama Hills metavolca-

nic complex suggests it is correlative with the Late Jurassic Independence dike swarm. To our knowledge, this is the most precise date yet for any dikes from the swarm. Although it is older than the nominal ~148 Ma age of the Late Jurassic portion of the swarm (Chen and Moore, 1979), the swarm may contain dikes as old as 152 ± 3 Ma (unpub. data by J.M. Mattinson, E.R. Schermer, and C.J. Busby cited in Schermer and Busby, 1994).

New data for the Alabama Hills Granite indicate it was assembled from 103-102 Ma; one grain with an age of 99.5 ± 0.3 Ma from sample RP15-01 is interpreted to reflect Pb-loss that was incompletely mitigated by chemical abrasion pre-treatment (Fig. 7). Although this study did not analyze the same outcrop dated by Chen and Moore (1982; precise location indicated in Stone et al., 2000), the samples dated here are likely representative of zircon crystallization ages throughout the pluton because of their spatial distribution. Note that the full zircon age range in the pluton may be 60% longer than what we have measured due to undersampling (Glazner and Sadler, 2016).

The 17-18 Ma difference between these new data and the 85 Ma age of Chen and Moore

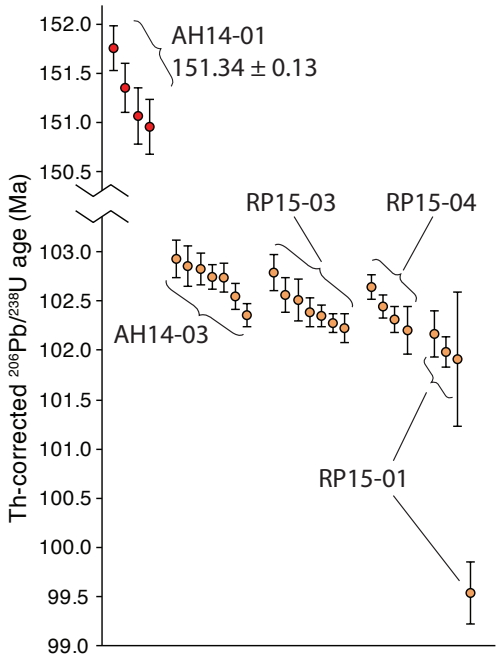

Figure 7. New CA-ID-TIMS age-sorted data for a mafic dike (interpreted as a member of the Independence dike swarm) from the Jurassic volcanic complex of the Alabama Hills (AH14-01) and the Alabama Hills Granite (four other samples). Each filled circle represents a single zircon analysis; vertical bars indicate 2σ analytical uncertainty. Note change in scale on ordinate. Weighted mean and 2σ analytical uncertainty provided for sample AH14-01 (see text for other sample age interpretations). Youngest zircon from sample RP15-01 interpreted to reflect Pb-loss.

(1982) is likely due to pervasive Pb-loss in the large fractions they dated (10 mg zircon each). These data suggest that geochronology performed on bulk zircon fractions, often without physical or chemical pre-treatment to remove Pb-loss zones, should be interpreted with caution because the data may not accurately reflect zircon crystallization ages. Large discrepancies (more than 5 Ma) between older and modern U-Pb dating techniques have also been documented nearby in the Independence pluton (Kylander-Clark et al., 2005), in the northern Mount Givens Granodiorite (Frazer et al., 2014), in the eastern Bass Lake Tonalite (Lackey et al., 2012), and in the Mineral King pendant (Klemetti et al., 2014).

Relationship of the Alabama Hills Granite to the Sierra Nevada batholith

Whitney Intrusive Suite

Chen and Moore's (1982) geochronology for the Alabama Hills pluton (85 Ma) and Whitney Intrusive Suite (87-83 Ma) led some workers to suggest they were originally contiguous and shared a genetic history (Ali et al., 2009), although Stone et al. (2000) considered the two bodies to be separate due to their dissimilar mineralogy. New zircon data for the Whitney suite (90.6-84.8 Ma; Davis, 2010) and geochronologic and geochemical data for the Alabama Hills Granite permit reevaluation of the links between the two. The age data demonstrate the Alabama Hills pluton is 12-17 Ma older than Whitney Intrusive Suite, precluding a genetic link between them. In addition, trace element and REE data are distinctive. The main body of the Alabama Hills Granite is enriched in HFSE as well as middle and heavy REEs relative to high-silica rocks of the Whitney Intrusive Suite (Figs. 4, 5). Europium anomalies are also more pronounced in the Alabama Hills samples. The adjacent intrusive complexes also appear to have different sources, as the Alabama Hills Granite is isotopically more primitive than the Whitney Intrusive Suite (Fig.

6), except in $\delta^{18}O$ in zircon (Lackey et al., 2008). These data, in sum, suggest different petrogenetic processes led to the high-silica granites in the Alabama Hills and the Whitney suite.

The fine-grained facies of the Alabama Hills Granite (sample RP15-02) appears to be a late-stage differentiate. The scoop-shaped REE pattern is similar to Sierra Nevada aplites interpreted to have been removed from titanite-bearing sources (Glazner et al., 2008), but it differs in having an enigmatic depletion in light REEs (Fig. 5). The REE pattern is probably a primary feature because the sample yielded εNd_i similar to other Alabama Hills samples (Table 2, Fig. 6). Although the Sm-Nd systematics are likely robust, the Rb-Sr system was apparently disturbed by open-system processes, yielding unrealistic $^{87}Sr/^{86}Sr_i$ near 0.703.

Mid-Cretaceous plutons near the Sierra crest: the Kearsarge intrusive suite

Several plutons north of the Alabama Hills along the Sierran crest and range front appear to be plausible temporal and geochemical matches for the Alabama Hills Granite (Fig. 6). These include the high-silica Bullfrog and Independence plutons, which are bisected by the more mafic Dragon pluton (Moore, 1963, 1981; Stone et al., 2000), and the smaller Sardine and Diamond plutons. Modern zircon geochronology indicates the Independence pluton is 102.5 ± 0.2 Ma, and the Bullfrog pluton has an age of ~100 Ma (Kylander-Clark et al., 2005; Davis, 2010). Bulk zircon geochronology mostly agrees with the modern techniques, and suggests the Dragon, Sardine, and Diamond plutons may have also been emplaced in the period 106-102 Ma (Chen and Moore, 1982; Saleeby et al., 1990), overlapping the Alabama Hills Granite. Compositional and isotopic analyses of the Sierran plutons also bear similarity to the Alabama Hills Granite, and strengthen the significance of those only dated by bulk zircon techniques. The Bullfrog and Independence plutons are enriched in HFSE, middle and heavy REEs, have high Y/Sr, and comparable Eu

anomalies to the main Alabama Hills pluton (Figs. 4, 5; Wenner and Coleman, 2004; Kylander-Clark et al., 2005; Coleman et al., 2012). Isotopic data for the plutons range from $^{87}Sr/^{86}Sr_i$ = 0.7045 to 0.7058 and εNd_i = -2.4 to -4.5 (Fig. 6; Saleeby et al., 1990; Wenner and Coleman, 2004; Kylander-Clark et al., 2005). The plutons also have relatively homogeneous $\delta^{18}O$(Zrc), ranging 4.79-5.40‰ (Lackey et al., 2008). Collectively, the isotopic data suggest all of these plutons were derived from an enriched mantle source or juvenile mantle derivative with mantle-like O, $^{87}Sr/^{86}Sr_i$ = 0.705-0.706, and $\varepsilon Nd_i \approx$ -2.5 to -4.5. These enriched mantle characteristics are slightly less evolved than those proposed for the nearby Lamarck Granodiorite (Coleman et al., 1992).

On the basis of robust chemical, isotopic, and age similarities between the Bullfrog, Independence, and Alabama Hills plutons, we hereafter group them into the informal Kearsarge intrusive suite, after numerous geographic features in the suite that bear the name Kearsarge. The Dragon, Diamond, and Sardine plutons are also included based on their isotopic similarities to the Alabama Hills, Bullfrog, and Independence plutons, although additional geochronological analyses are required to confirm such an assignment. The McGann pluton, a quartz-poor quartz monzonite to the north of the Independence pluton (Moore, 1963), could also be correlative but has no age or chemical data to test the relationship.

Intrusive rocks of the Kearsarge intrusive suite are intimately associated with the Oak Creek metavolcanic pendant. The pendant exposes mostly Middle Jurassic rocks, but also includes subordinate mid-Cretaceous metavolcanic rocks dated to ~110-109 Ma by bulk zircon geochronology (Saleeby et al., 1990). The rhyolite sill has $^{87}Sr/^{86}Sr_i$ similar to the Kearsarge intrusive suite, of 0.7052, whereas two analyses of the ash-flow tuff yielded $^{87}Sr/^{86}Sr_i$ = 0.7070 and

0.7062. These data suggest that mid-Cretaceous volcanic rocks in the pendant may have a similar source to the Kearsarge intrusive suite, and perhaps a close temporal history.

Tectonic origins of the Alabama Hills block

The Alabama Hills block is highly dilated by the Independence dike swarm; realignment of the Alabama Hills with similar high-dilation zones in the Sierra Nevada batholith could require 55 km of dextral offset between them (Bartley et al., 2007). Because isotopic data suggest the Alabama Hills Granite is part of the Kearsarge intrusive suite, such hypothesized dextral offset would have had to accumulate between the emplacement of highly-dilating Independence dikes in the Alabama Hills (~151.3 Ma) and emplacement of the Alabama Hills Granite ca. 103 Ma. Although a large amount of offset is possible, it is unnecessary. First, the swarm strikes across Owens Valley at a low angle, so correlations are subject to considerable uncertainty (Bartley et al., 2007). Second, there is no preserved evidence for Late Jurassic-Early Cretaceous dextral shear zones in the eastern Sierra, although such shear zones could have been obliterated by Cretaceous magmatism or covered by sediments in Owens Valley. Third, only the southern limit of the high dilation zone of the Independence dikes is exposed in the Alabama Hills. There, dilation values drop from 29% in the northern Alabama Hills to 4% just west of Lone Pine (Bartley et al., 2007). A similar southerly decrease in dilation values occurs in the Woods Lake basin (44% to 2%), approximately along strike of the dike swarm from the Alabama Hills (Bartley et al., 2007). Glazner et al. (2008a) also noted compositional similarities between dikes in the Alabama Hills and Woods Lake basin, suggesting these areas may have been in close proximity when the swarm was emplaced. Altogether, it appears large amounts of offset between the Ala-

bama Hills and the Sierra Nevada batholith are not necessary. Smaller amounts of offset may be possible.

The relationship between the Kearsarge intrusive suite exposed in the Sierra Nevada, proper, and the Alabama Hills Granite suggests the pluton could have originally been emplaced further north, adjacent to the range-front Independence pluton. Such a scenario must account for the distinctive ~15-20 m wide, ~83.4 Ma Golden Bear dike, which is not present in the Alabama Hills (Kylander-Clark et al., 2005). If the Alabama Hills Granite was emplaced adjacent to the rest of the Kearsarge intrusive suite, it must have been displaced dextrally by at least 10 km, and perhaps over 30 km, prior to emplacement of the Golden Bear dike 30 Ma later. However, another possibility is that the Alabama Hills Granite was always south of the latitude of the Golden Bear dike, permitting at most ~10 km of dextral offset of the block to its current location. This small amount of offset is preferred because it is simplest, and because there are no structures in the Alabama Hills Granite, the other Kearsarge intrusive suite plutons, or younger Whitney Intrusive Suite plutons that suggest range-front dextral shear. It is also possible the Alabama Hills Granite extends further north than its current exposure; numerous workers using have recognized a shallowly buried bedrock ridge extending north from the Alabama Hills approximately 12 km to the northeast, truncating near Independence (Kane and Pakiser, 1961; Pakiser et al., 1964; Stevens et al., 2013; Chaulk, 2016).

If the Alabama Hills have moved little relative to the main Sierra Nevada batholith since the Late Jurassic, it suggests the block is a suitable piercing point for areas highly-dilated by the Independence dike swarm, which is estimated to be offset by 75 km across Owens Valley (Bartley et al., 2007). Dextral offset of 65 km inferred by Kylander-Clark et al. (2005) is also strengthened by the recognition of the Kearsarge intrusive suite. Kylander-Clark et al. (2005) originally

correlated the leucogranite of Cactus Flat in the Coso Range with only the Bullfrog and Independence plutons. The addition of the Alabama Hills Granite and other small, isotopically similar granitoids from Sierran range front makes this mid-Cretaceous suite more prominent (Fig. 2). Thus, the leucogranite of Cactus Flat, which has a low negative Eu anomaly (Eu/Eu* = 0.44) and similar $^{87}Sr/^{86}Sr_i$ (0.7060), may have also been part of the Kearsarge intrusive suite, which was subsequently dismembered by dextral (Kylander-Clark et al., 2005; Bartley et al., 2007) and normal (Moore, 1963, 1981; Stone et al., 2000; Ali et al., 2009) faulting.

The Enigmatic mid-Cretaceous central Sierra Nevada

For the purposes of the following discussion, the Cretaceous batholith is broken into three intervals of time: the Early Cretaceous, from 124-110 Ma; the mid-Cretaceous, from 110-98 Ma; and the Late Cretaceous, from 98-83 Ma. The latter period includes the Sierra Crest magmatic event of Coleman and Glazner (1997), extended to slightly younger ages due to new geochronology (Kylander-Clark et al., 2005). These temporal groups broadly correspond to the western, axial, and eastern batholithic belts of Nadin and Saleeby (2008), although recognition of the Kearsarge intrusive suite in the eastern Sierra suggests that east-west spatial patterns require additional consideration.

Controls on the location of the Kearsarge intrusive suite

Workers have long recognized that plutons of the Cretaceous Sierra Nevada batholith become progressively younger towards the east through intrusive relationships and isotopic dating (e.g., Calkins, 1930; Stern et al., 1981), with Chen and Moore (1982) calculating eastward magmatic front migration at 2.7 mm/a. These early hypotheses predict mid-Cretaceous plutons to be located in the axial part of the batholith, between Early Cretaceous and Late Cretaceous

rocks. Numerous suites dated by modern methods follow this prediction (Fig. 2), and additional geochronology for plutons between those suites may strengthen the relationship. The Kearsarge intrusive suite stands in contrast to this pattern, as it is 45-60 km inboard of the Ash Mountain complex when measured perpendicular to the ~N20W trend of the Cretaceous batholith (Fig. 2).

The migrating magmatic front has commonly been attributed to flattening of an eastward-subducting Farallon slab, although the mechanisms causing flattening are debated (Coney and Reynolds, 1977; Chen and Moore, 1982; Tobisch et al., 1995; Nadin et al., 2016). The recently-proposed westward-dipping subduction hypothesis is intriguing, where slab rollback causes the migrating pattern of ages (e.g., Hildebrand, 2009, 2013). However, westward-dipping subduction requires the Kearsarge suite to have been emplaced close to the trench, where water supply would be limited to low P-T sediment dewatering reactions (Kerrick and Connolly, 2001; Rüpke et al., 2004). Trenchward emplacement is also problematic as it calls for little interaction with the mantle wedge, which is difficult to reconcile with the mantle-like isotopic data for the suite (Fig. 6; Lackey et al., 2008).

Another explanation for the Kearsarge intrusive suite's location is that it is an expression of backarc magmatism over an eastward-dipping subduction zone. The Central Andes backarc may serve as an analog. There, magmatism has been documented as far as 300 km east of the active Western Cordillera in association with strike-slip systems or lineaments (Riller et al., 2001; Chernicoff et al., 2002; Gioncada et al., 2010). These examples are intriguing because the Sierra Nevada may share some commonalities with them. For example, the Kearsarge intrusive suite is located near the southernmost recognized portion of the Sawmill Lake shear zone, which deforms Jurassic plutonic and metavolcanic rocks of the Oak Creek pendant (Fig. 2; Bartley et al., 2012) and was active through ~95 Ma (Mahan et al., 2003; Stearns and Bartley, 2014). The shear

zone is apparently not present in the larger plutons of the Kearsarge intrusive suite. However, the small Sardine pluton appears to be deformed along with mid-Cretaceous metavolcanic wallrocks of the Oak Creek pendant (Saleeby et al., 1990). Thus, the Sawmill Lake shear zone, or some correlative deeper structure, could have served to focus magmas of the Kearsarge intrusive suite; a similar process has been invoked for the crack-seal assembly of the 95 Ma late synkinematic McDoogle pluton (Mahan et al., 2003; Bartley et al., 2008; Stearns and Bartley, 2014).

The Independence dike swarm suggests an alternative to the Sawmill Lake shear zone for focusing the Kearsarge intrusive suite. Coleman et al. (2000) documented 94-90 Ma dikes in the swarm that superficially resemble Jurassic dikes in composition and orientation. The similarities between Cretaceous dikes and Jurassic dikes despite significant changes in convergence direction (i.e., sinistral to dextral; Engebretson et al., 1985; Glazner, 1991) suggests that regional strain may not be a major factor controlling the orientation of intrusive rocks in the batholith. Coleman et al. (2000) hypothesized that the common orientation of Jurassic and Cretaceous dikes may be controlled by fractures in pre-existing (i.e., Middle Jurassic or older) rocks, or by the orientation of the North American margin as realized by a relative lack of coupling between North America and the subducting Farallon plate, causing extension perpendicular to the plate's margin (Tobisch et al., 1986). Thus, the Kearsarge intrusive suite may have taken advantage of similar pre-existing fractures that led it to intrude inboard of other mid-Cretaceous rocks. If Jurassic fractures or the orientation of the continental margin were controlling factors for the inboard extension of ~105-100 Ma magmatism, this hypothesis predicts that undiscovered mid-Cretaceous plutons may be present along a similar trend (i.e., N30°W to N40°W; Tikoff and Teyssier, 1992; Coleman et al., 2000) between the Kearsarge intrusive suite and the ~105-100 Ma arc in the central

part of the batholith. Therefore, plutons from the Marion Peak quadrangle (Moore, 1978) make intriguing targets to test this hypothesis.

Are mid-Cretaceous plutonic rocks different from the rest of the batholith?

The new geochronology and geochemistry presented here adds to a growing high-quality dataset documenting mid-Cretaceous magmatism in the Sierra Nevada batholith, including the 106.6-103.5 Ma intrusive suite of Yosemite Valley (Ratajeski et al., 2001; Nelson et al., 2013; Putnam et al., 2015), the 106.5-98 Ma Shaver Intrusive Suite (Frazer et al., in prep.) and the 105.5-102.5 Ma Ash Mountain complex in Sequoia National Park (Holland et al., 2013). These intrusive suites superficially appear to be more felsic than the preceding and following magmatism in the batholith (Clemens-Knott and Saleeby, 1999; Lackey et al., 2012; Coleman and Glazner, 1997). The Dinkey Creek Granodiorite of the Shaver Intrusive Suite is the only well-dated voluminous granodiorite in the mid-Cretaceous batholith (Frazer et al., in prep.). However, the suite also includes numerous texturally and chemically distinct granite plutons (Frazer et al., in prep.).

To test whether the mid-Cretaceous batholith is more felsic than the Early or Late Cretaceous, a simple analysis of the areal extent and composition of Cretaceous plutons in the central Sierra Nevada batholith was performed. Plutons were categorized by their USGS compositional designations (Bateman, 1992). A more optimal methodology for investigating spatio-temporal compositional trends would involve regular sampling on a grid pattern to avoid biasing, as has been carried out in the Peninsular Ranges batholith (Baird et al., 1979; Lee et al., 2007; Lee and Morton, 2015). Unfortunately, despite thousands of geochemical analyses in the central Sierra Nevada, a structured sampling regimen has not been undertaken. The method used here is obvi-

ously a crude measure, but the large time bins used and the stark results make the analysis illustrative of broad compositional trends.

Two sets of analyses were performed in the Cretaceous batholith from 36.5-38.25°N (Fig. 8). The first included only plutons considered to be "well-dated". As demonstrated in the Alabama Hills and elsewhere, older geochronologic data may be compromised by unresolved Pb-loss or inheritance due to the use of large fractions or a lack of physical or chemical pre-treatment (e.g., Krogh, 1982; Mattinson, 2005). Therefore, in the "well-dated" analysis, only plutons dated by LA-ICP-MS, secondary ion mass spectrometry, sensitive high resolution ion microprobe, or ID-TIMS on pre-treated zircons were used. One exception was the inclusion of mafic ring dike complexes in the western Sierra (Clemens-Knott and Saleeby, 1999) because such mafic rocks are unlikely to contain inherited zircon, and if affected by Pb-loss, the rocks would be older and would not affect the younger age groups. The second analysis performed was "complete", and tentatively assigns all mapped plutons from 36.5-38.25°N to age groups based on pluton location, field data from USGS mapping, and cautious interpretation of existing geochronologic data. The well-dated analysis is considered more robust, although the complete analysis is useful in determining whether plutons dated by modern geochronology are biased toward particular compositions.

The compositions of the Early and Late Cretaceous parts of the batholith accord with conventional wisdom (Fig. 8). The Early Cretaceous batholith is the most mafic, with more than 70 area% comprising tonalite in both the well-dated and the complete datasets, and the remaining areas taken up by mafic ring dike complexes and smaller proportions of more felsic rocks including granodiorite, trondhjemite, and granite. The Late Cretaceous batholith is dominated by the granodiorites of the Sierra Crest magmatic event (Coleman and Glazner, 1997), covering

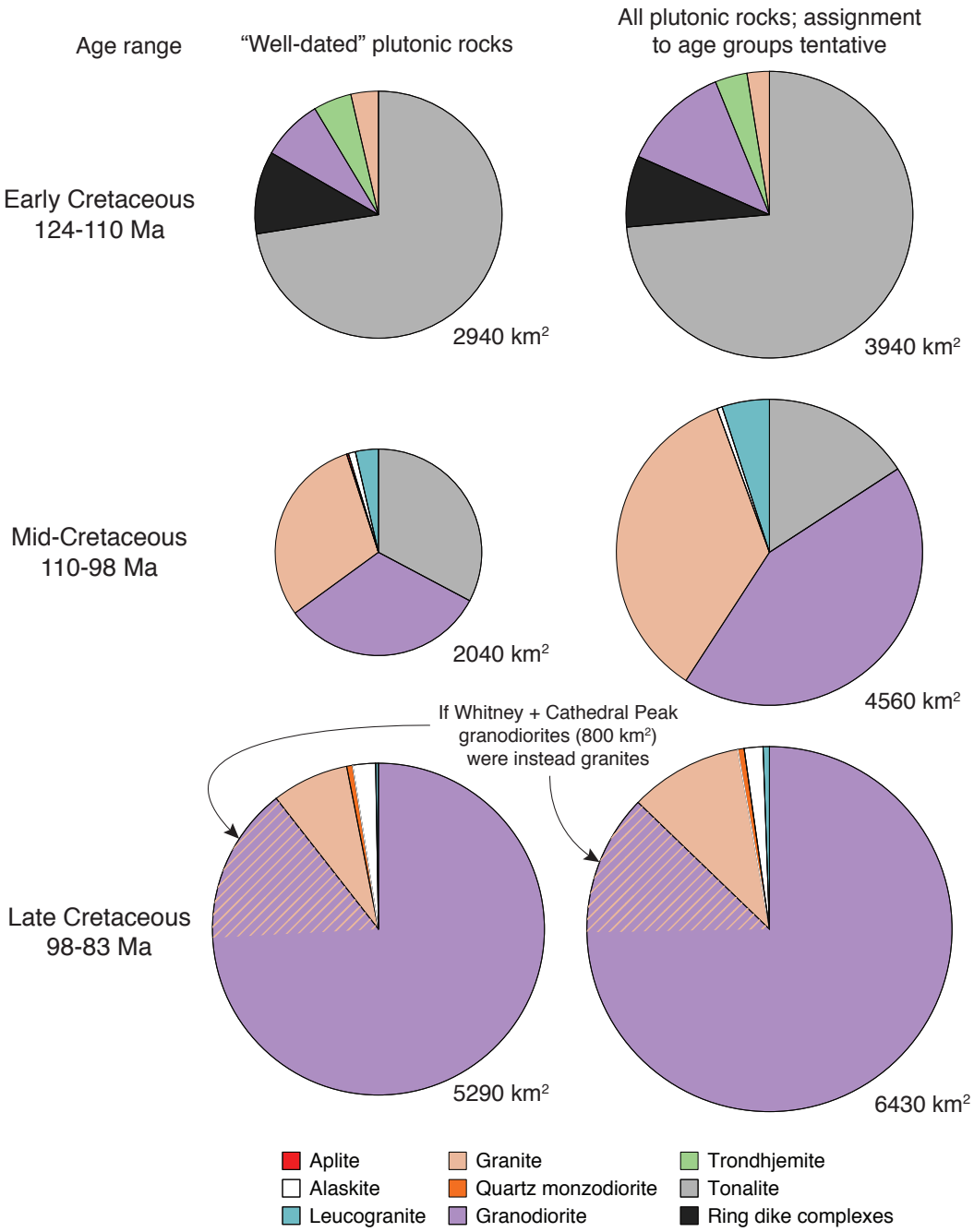

Figure 8. Areal analyses of Cretaceous intrusive rocks of the Sierra Nevada by age grouping. Rock compositional type taken from descriptions in USGS publications where available. Rationale for age ranges given in text. In left column, "well-dated" plutonic rocks are those dated by U-Pb zircon using LA-ICP-MS, SIMS, SHRIMP, or TIMS on single or several zircons pretreated by air- or chemical abrasion such that the effects of Pb-loss and inheritance are minimized compared to bulk fractions. For the right column, plutons were assigned to age groups using USGS-defined intrusive relationships and cautiously-interpreted legacy age data. The relatively similar compositional breakdowns between well-dated and complete areal analyses for each age group suggests there is little compositional bias in the rocks that have been dated, and that granites are more common in the mid-Cretaceous (110-98 Ma) compared to the Late Cretaceous (98-83 Ma). In the Late Cretaceous group, hatched lines show the effects of changing the designations of the Cathedral Peak and Whitney plutons from granodiorite to granite. In both cases, granodiorite dominates granite in the Late Cretaceous. Diorites and gabbros are not included in the analyses due to a general lack of age control.

more than 85 area% in both datasets. Granites are also somewhat common in the Late Cretaceous, comprising 7.5 area% and 10 area% in the well-dated and complete datasets, respectively. Therefore, granodiorite:granite ratios by area in the Late Cretaceous are ~11:1 to ~8.5:1. Because plutons commonly extend across compositional fields in QAP diagrams (e.g., many analyses of the Cathedral Peak Granodiorite fall in the granite field; Bateman, 1992), the effect of changing the designation of the Cathedral Peak and Whitney plutons to granite was also tested. Despite a combined area of 800 km^2 in the two plutons, the results show that Late Cretaceous granodiorites comprise nearly 75 area% in both datasets and still dwarf granites by a ratio of ~3:1 by area (Fig. 8).

In contrast to the Early and Late Cretaceous, the mid-Cretaceous has subequal amounts of granite and granodiorite by area (Fig. 8). If leucogranites are included with granites, then the more silicic rocks are areally superior. This result is at odds with the common notion that the youngest parts of the batholith are the most felsic (e.g., Bateman et al., 1963; Bateman, 1992; Nadin and Saleeby, 2008). The relatively small areal extent of the "well-dated" mid-Cretaceous batholith does not appear to bias the analysis toward granitic compositions; the "complete" mid-Cretaceous dataset contains subequal amounts of granodiorite and granites + leucogranites. Note that the large amount of "well-dated" tonalite in the mid-Cretaceous is due to the inclusion of the Bass Lake Tonalite's "eastern domain" from Lackey et al. (2012).

We suggest that the large differences in granodiorite:granite areal ratios between the mid-Cretaceous (~1:1) and Late Cretaceous (~11:1) overcome the uncertainties inherent in the use of general pluton compositions. Even if undated granodiorites and granites were apportioned to the mid- or Late Cretaceous "complete" datasets in error, unrealistic scenarios are required to make the areal ratios comparable between the time periods. For example, if all granites of

unknown age are added to "well-dated" Late Cretaceous, and all granodiorites of unknown age are added to the "well-dated" mid-Cretaceous, granodiorite:granite areal ratios would remain larger in the Late Cretaceous, at ~3.7:1, than the mid-Cretaceous, ~2.9:1. Therefore, the granites exposed in the mid-Cretaceous batholith are greater in area than granites of the Late Cretaceous Sierra Crest magmatic event.

These results are broadly similar to the more robust measurements made in the Peninsular Ranges batholith. There, high-silica granites comprise a larger area in the western batholith (37%) than the eastern batholith (16%), perhaps because the western batholith is a relatively shallower exposure (Ague and Brimhall, 1988b; Lee and Morton, 2015). However, high-silica granites of the Sierran mid-Cretaceous appear to be abundant at both shallow and mid-crustal levels. For example, the Kearsarge intrusive suite was emplaced at low pressures (20-200 MPa; Richardson, 1975; Ague and Brimhall, 1988b; Sorensen et al., 1998), whereas the axial mid-Cretaceous suites were emplaced at higher pressures (230-400 MPa; Ague and Brimhall, 1988b; Tobisch et al., 1993; Putnam et al., 2015). Furthermore, if depth is a controlling factor in the expression of granites in the Sierra Nevada, more granites would be expected in the areas of the shallowly-emplaced Late Cretaceous Tuolumne (~150 MPa; Gray et al., 2008; Challener and Glazner, 2017) and Whitney intrusive suites (20-350 MPa; Ague and Brimhall, 1988b). Therefore, some other factor likely controls the genesis and expression of high-silica granites in the Sierra Nevada.

There are leucogranites, and there are leucogranites

Recent debate on the origins of high-silica granite has centered around whether high-silica magmas are distilled from batholith-scale crystal mushes in the mid- to upper crust (e.g.,

Bachmann and Bergantz, 2004; Hildreth, 2004; Gualda and Ghiorso, 2013; Lee and Morton; 2015) or are partial melts of deeper sources, including the crust and/or mantle (e.g., Wenner and Coleman, 2004; Sisson et al., 2005; Stevens et al., 2007; Clemens et al., 2010; Villaros et al., 2009; Tappa et al., 2011; Coleman et al., 2012). Here we comment on how new data for high-silica granites from the Sierra Nevada may bear on this lively and ongoing conversation.

There is little doubt that one class of high-silica granites—aplites—is the product of shallow-level crystal-liquid separation from a crystalline mush (Eichelberger et al., 2006; Glazner et al., 2008b). Low pressure haplogranitic compositions and trace element enrichments or depletions strongly support such an origin (Glazner et al., 2008b; Putnam et al., 2015). Aplites separated from titanite-bearing mushes have "scoop-shaped" REE patterns and Y depletions (Glazner et al., 2008b), whereas those derived from titanite-free sources do not (Bachmann and Bergantz, 2008; Putnam et al., 2015).

Evidence also suggests high-silica melt segregation occurs cyclically on scales of a km or less in large, incrementally-emplaced granodiorites, with trends toward similar trace element enrichments and depletions as aplites at high SiO_2 contents (Economos et al., 2010; Coleman et al., 2012). These high-silica magmas ("cycles") may have segregated from a granodiorite mush, leading to gradational field and chemical relationships, but became trapped at the structural discontinuity of previously solidified granodiorite (Coleman et al., 2012).

The high-silica granite plutons studied here stand in sharp contrast to aplites and cycles, in some cases quite literally. In the field, many of the granite plutons of the Sierra Nevada are noted for their sharp intrusive contacts (e.g., Bateman, 1992; Holland et al, 2013). In places where contacts are gradational over scales of less than a meter, they are interpreted to reflect coeval emplacement of discrete magma batches rather than a genetic relationship where one

magma was derived from the other (Ratajeski et al., 2001; Putnam et al., 2015). The common absence of gradational contacts between high-silica granite plutons and granodiorites in the Sierra makes it difficult to envision a process through which the former is derived from the latter at emplacement level (e.g., Bachmann and Bergantz, 2004, 2008; Lee and Morton, 2015).

Whereas field evidence appears to contradict hypotheses that call for the generation of granites from granodiorites, perhaps the current exposures of the batholith are structurally biased (Lee and Morton, 2015). However, the chemical evidence against derivation of the high-silica granites from granodiorites in the Sierra Nevada is also compelling. For example, the Shaver Intrusive Suite (Frazer et al., in prep.) is the only well-dated mid-Cretaceous suite that comprises a large granodiorite pluton and discrete, largely coeval granites. Despite a temporal link, the granite plutons have more variable O, Sr, and Nd isotopic compositions than the granodiorite and other mafic rocks, precluding a scenario in which the granites were derived from the granodiorite.

High-silica granite plutons throughout the Sierra Nevada, regardless of age, are chemically distinct from aplites and cycles. Sierran high-silica granite plutons are enriched in HFSEs, Y, and middle REEs relative to aplites and cycles at similar SiO_2 concentrations, suggesting the plutons' magmas evolved in the absence of titanite, in contrast to cycles and many aplites (Coleman et al., 2012). Coleman et al. (2012) suggested three possible mechanisms for the titanite-absent signature in high-silica granite plutons. The first two occur at emplacement level. First, titanite could be absent from the crystallization sequence because of hot and reducing magmatic conditions (Bachmann and Bergantz, 2008). Although reducing conditions have been inferred in parts of the central Sierra (e.g., Shaver Intrusive Suite), many high-silica suites were emplaced under oxidizing conditions that typify most of the batholith (Ague and Brimhall, 1988a). Despite the

differing conditions, high-silica granites throughout the Sierra are enriched in middle REE like Gd (Fig. 9), suggesting the varying redox states did not affect titanite. Another possibility is that titanite crystallization was suppressed until after extraction of the high-silica granites (Colombini et al., 2011). However, titanite is present in the Fish Canyon Tuff (Bachmann et al., 2002), and is not uncommon in other Cordilleran-type dacites and rhyolites (see compilation in Glazner et al., 2015). This suggests titanite can appear before magmas are 50% crystalline. In addition, if high-silica plutons owe their high Gd contents to extraction prior to extremely late titanite crystallization (e.g., if titanite saturation occurs at 76 wt% SiO_2; Colombini et al., 2011), such a scenario predicts there should be slightly less silicic complementary cumulates that are depleted in Gd. However, a data compilation for the Sierra Nevada does not reveal the putative cumulates (Fig. 9).

If shallow fractionation does not satisfy the requirements for the generation of these high-silica granites, perhaps a deeper genesis is possible (Coleman et al., 2012). Experimental and isotopic data have been used to suggest Sierran granites were derived from partial melting in the lower crust, particularly juvenile, amphibole-bearing mafic rocks that were themselves derived from variably enriched mantle (e.g., Coleman et al., 1992; Sisson et al., 2005; Hollande et al., 2013). Alternatively, it has been suggested that the chemical variation in granitic plutons is controlled by the composition of the source, and heterogeneities are thus linked to source heterogeneity (e.g., Clemens et al., 2010; Clemens and Stevens, 2016). Specifically, Clemens et al. (2011) suggested that the sources of I-type granites are likeliest to be intermediate-to-mafic arc volcanic rocks.

It is difficult to envision a unifying model for the generation of the high-silica granite plutons in the Sierra Nevada in light of their varied isotopic compositions. The Kearsarge intrusive

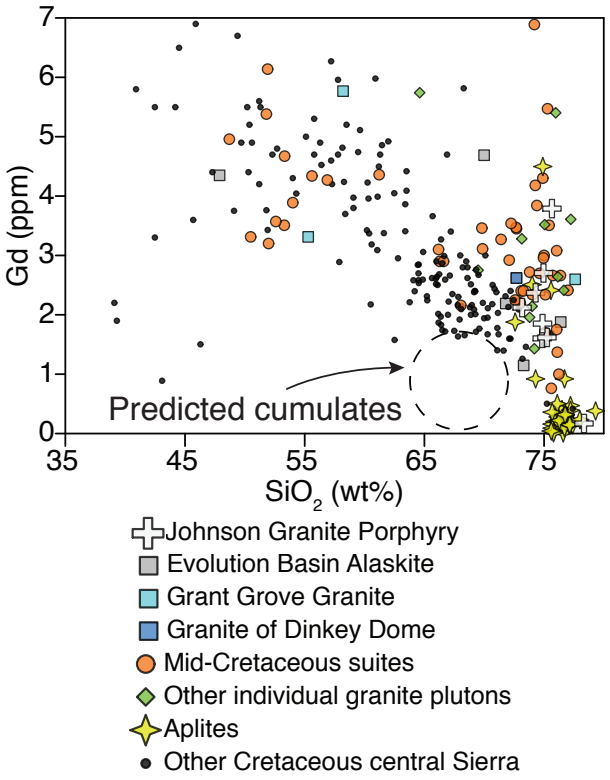

Figure 9. Plot of Gd concentration against silica concentration for Cretaceous plutonic rocks in the central Sierra Nevada. Data for notable granite plutons (Johnson Granite, Evolution Basin, Grant Grove, Dinkey Dome) plotted with separate symbols. Dashed circle indicates predicted composition of cumulates complementary to high-SiO_2 plutons if the high-Gd, high-SiO_2 plutons were separated from a mush prior to saturation of titanite (e.g., Colombini et al., 2011). The lack of the predicted cumulates suggests late saturation of titanite was was uncommon in the Sierra Nevada. Data from Sisson et al. (1996), Truschel (1996), Ratajeski et al. (2001), Wenner and Coleman (2004), Kylander-Clark et al. (2005), Hirt (2007), Glazner et al. (2008b), Gray et al. (2008), Coleman et al. (2012), Holland et al. (2013), Putnam et al. (2015), Gaynor and Glazner (2016), Frazer et al. (in prep.), Frazer (unpub. data), and this study.

suite has mostly mantle-like isotopic compositions, including $\delta^{18}O$(Zrc) (Lackey et al., 2008), precluding an arc volcanic source as envisioned by Clemens et al. (2011). In contrast, the granites of the Shaver Intrusive Suite (Frazer et al., in prep.) have variable isotopic compositions and whole rock Ce anomalies suggesting they may have been derived from a variable metasedimentary source (e.g., Villaros et al., 2012). Yet both of these suites have high-silica granites that are enriched in HFSEs, Y, and middle REEs, with generally negative Eu anomalies. Thus, more work is necessary to identify the sources and mechanisms that led to the generation of these plutons and their distinct geochemical signatures.

High-silica granites and the genesis of granodiorites

Some workers have recently cast doubt on the possibility of a magma mixing origin for granodiorites based on the presence of curvilinear trends on Harker diagrams (Lee and Bachmann, 2014; Keller et al., 2015). For example, Lee and Bachmann (2014) suggested that mixing

processes are not significant in the generation of intermediate magmas because data compilations fail to show linear mixing trends between felsic and mafic rocks in P_2O_5 and Zr. However, data from large Sierran suites are equivocal (Fig. 10). Data for P_2O_5 in the Tuolumne and Whitney suites are nearly linear, particularly if the mafic end member is similar in composition to mafic enclaves. The Zr data for the Sierra Crest suites do follow a subtle curvilinear trend, with a peak between 60-65 wt% SiO_2 and a noted decrease in Zr at high silica concentrations (Fig. 10). If the putative magma mixing end members considered were only those compositions present in the Sierra Crest suites, then the Zr data appear to preclude a mixing origin.

However, the Sierran high-silica granites have similar or sometimes higher Zr concentrations to the Sierra Crest suites (100-200 or greater ppm Zr). Since the granodioritic intrusive

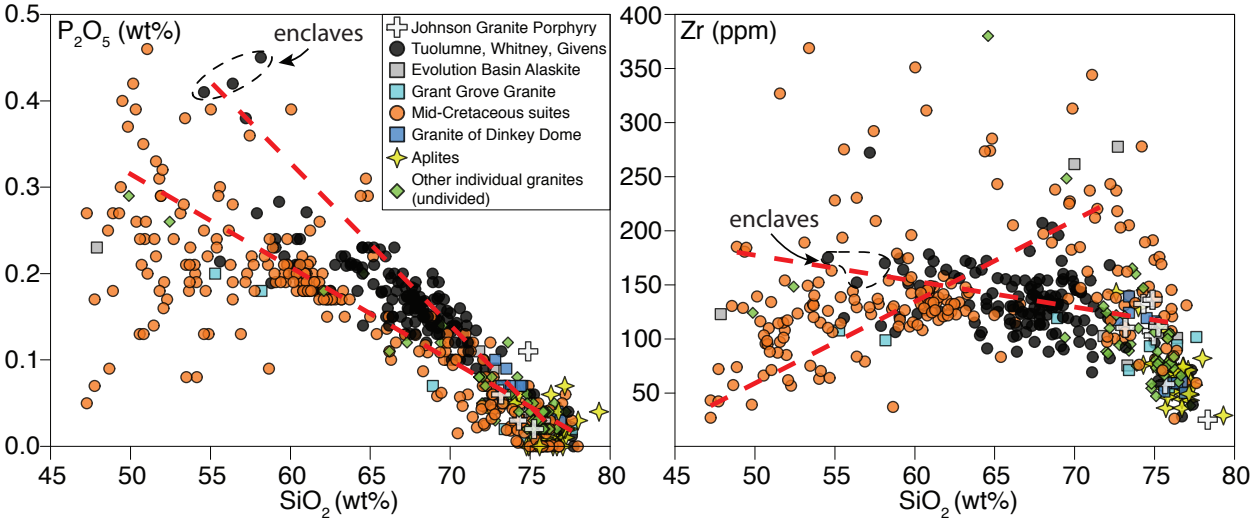

Figure 10. Plots of P_2O_5 and Zr against SiO_2 for three representative Sierra Crest intrusive suites (black circles; Tuolumne, Whitney, Mount Givens), as well as data for aplites from those intrusive suites (yellow stars), and other individual granite plutons as in Fig. 9. Phosphorus data for the Sierra Crest suites are approximately linear and do not appear to require an origin by fractional crystallization. Linear mixing trends between low- and high-SiO_2 parts of the mid-Cretaceous suites would produce granodiorite with lower P_2O_5 than the Sierra Crest suites, although if the mafic endmember is similar to enclaves, the pattern is reproduced. Note that the low-P_2O_5, low SiO_2 rocks are subsets of the data of Holland et al. (2013) and Nelson et al. (2013). Zirconium data for the Sierra Crest suites are subtly curvilinear, with a noted decrease in Zr at high SiO_2 shown in the Sierra Crests intusive suites and their aplites (black circles, yellow stars). Data for the mid-Cretaceous suites (orange circles) and the individual granite plutons (green diamonds) are highly scattered, although two hypothetical mixing trends (red dashed lines) between low- and high-SiO_2 components of those suites can reproduce the Zr concentrations of most Sierra Crest granodiorites. Note in particular that the high-SiO_2 granites have similar Zr concentrations (100-200 ppm) to granodioritic compositions. In contrast, the aplites and other low-Zr, high-SiO_2 intrusive rocks of the Sierra Crest suites are interpreted to be the products of shallow crystal-liquid separation (e.g., Glazner et al., 2008b; Coleman et al., 2012).

suites have largely flat Zr patterns with SiO_2 until the most felsic compositions, the high-Zr, high-silica granite plutons appear to be plausible end members for magma mixing scenarios. The low-Zr, high-silica parts of the intrusive suites are relatively small volume, generated at emplacement level by late crystal-liquid separation (e.g., Glazner et al., 2008b; Coleman et al., 2012). If magmas similar to the high-silica granite plutons were indeed end members in mixing to produce the voluminous Late Cretaceous suites, it may also explain the paucity of Late Cretaceous granites relative to the mid-Cretaceous (Fig. 8). Production of the Late Cretaceous suites would require large volumes of high-silica granitic magmas to mix with mafic magmas in order to generate the voluminous granodiorites. Perhaps high-silica magmas were produced at similar rates and volumes in the Late Cretaceous and the mid-Cretaceous, but in the Late Cretaceous Sierra Crest magmatic event, those high-silica magmas were largely consumed as mixing end members.

High-silica granites and volcano-pluton connections

Miller et al. (2003) noted a dichotomy in granitoids, grouping them into "hot" and "cold" classes on the basis of zircon inheritance and Zr saturation temperatures. Their hot granites lacked inherited zircon and averaged Zr saturation temperatures of 837°C Zr, whereas the cold granites had more than 10% "premagmatic" zircons and averaged 766°C (calculated using the calibration of Watson and Harrison, 1983). Such a dichotomy may also apply to the different types of high-silica rocks in the Sierra Nevada due to their contrasting Zr concentrations (Fig. 10). None of these rocks have more than 10% "premagmatic" zircon, although some of the Sierra Crest suites have antecrystic and/or xenocrystic zircon (e.g., Coleman et al., 2004; Miller et al., 2007; Frazer et al., 2014).

Zircon saturation temperatures were calculated for samples over 70 wt% SiO_2 from

individual high-silica granite plutons, Sierra Crest suites, and aplites using the updated parameterization of Boehnke et al. (2013). The results show that high-silica granite plutons have median zircon saturation temperatures of 721°C, with lower median saturation temperatures in high-silica parts of Sierra Crest suites (693°C) and aplites (661°C) (Fig. 11). The significance lies in the contrasts between the rock types, rather than their precise temperatures, which may not accurately reflect when most zircon in these rocks crystallized (Harrison et al., 2007). Broadly, it is logical that aplites would yield the lowest calculated temperatures, as they are interpreted as late-stage differentiates at shallow crustal levels (Eichelberger et al., 2006; Glazner et al., 2008b; Bachmann and Bergantz, 2008). More importantly, the data suggest that discrete high-silica granite plutons may have been slightly hotter as magmas than high-silica parts of Sierra Crest suites. After Miller et al. (2003), it follows that the individual granite plutons would have also been more eruptible than the high-silica members of the Sierra Crest or aplites. This supports the interpretations of Glazner et al. (2008b) and Coleman et al. (2012) that aplites and leucocratic cycles of the Sierra Crest suites resulted from emplacement level crystal-liquid separation. Those rock types are also poor matches for erupted high-silica rocks such as rhyolites (Glazner et al., 2015). In contrast, if the discrete high-silica granites were once relatively hot, crystal-poor (Miller et al., 2003) and eruptible, they may represent suitable intrusive equivalents to high-silica erupted rocks. It is also intriguing that the youngest volcanic rocks preserved in the Sierra Nevada batholith, such as the those at the Boyden Cave, Cinko Lake, Oak Creek, and Strawberry Mine pendants (Saleeby et al. 1990; Memeti et al., 2010b), and ash-flow tuffs and caldera collapse deposits in the Ritter Range (Fiske and Tobisch, 1994) are approximately mid-Cretaceous in age, when many high-silica granite plutons were emplaced (Fig. 8). Perhaps the distinct composition

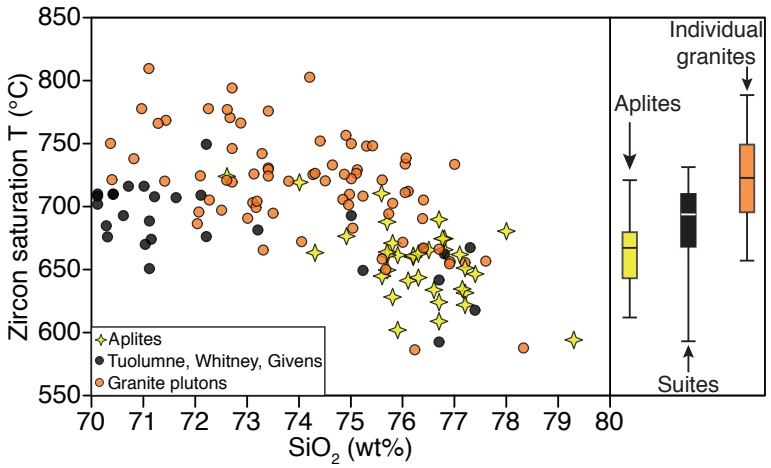

Figure 11. Compilation of calculated zircon saturation temperatures (Boehnke et al., 2013) for high-silica rocks of Sierra Crest intrusive suites (Tuolumne, Whitney, Mount Givens), individual granite plutons (Kearsarge, Ash Mountain, Shaver, Yosemite Valley, Evolution Basin, Dinkey Dome, Johnson Granite), and aplites. The pattern shows that individual granite plutons have higher zircon saturation temperatures than large intrusive suites or aplites at similar silica concentrations, suggesting that the individual granites may have been hotter as magmas than aplites or the high-silica portions of intrusive suites. Box-and-whisker plots in right panel elucidate the differences between the rock types; 1st and 3rd quartiles are contained in boxes; horizontal line indicates the median value. Whiskers extend to 95th and 5th percentiles. Data from Ratajeski et al. (2001), Wenner and Coleman (2004), Kylander-Clark et al. (2005), Hirt (2007), Lackey et al. (2006), Glazner et al. (2008b), Gray et al. (2008), Coleman et al. (2012), Holland et al. (2013), Putnam et al. (2015), Gaynor and Glazner (2016), Frazer et al. (in prep.), Frazer (unpub. data), and this study.

of mid-Cretaceous magmatism resulted in a more voluminous volcanic expression than the Late Cretaceous Sierra Crest magmatic event.

CONCLUSIONS

New geochronologic data indicate the Alabama Hills Granite is 103-102 Ma, about 17 Ma older than previously recognized. Although its individual outcrop area is relatively small, the recognition of this granite as mid-Cretaceous has implications for the Sierra Nevada batholith from Jurassic through Recent time. The data suggest the Alabama Hills Granite belongs to the heretofore unrecognized Kearsarge intrusive suite, which is characterized by its ~103-100 Ma age, silicic plutons, and mantle-like isotopic compositions ($^{87}Sr/^{86}Sr_i \approx 0.7045$-$0.7060$, $\varepsilon Nd_i \approx -2$ to -5) relative to nearby Late Cretaceous rocks of the Sierra Crest. Without a link to the Whitney Intrusive Suite, the Alabama Hills block may have moved dextrally relative to the main Sierra Nevada batholith. However, it is likely it moved no more than 10 km dextrally since the

mid-Cretaceous, and perhaps since the intrusion of the ~151-148 Ma Independence dike swarm. As such, the Alabama Hills serve as a suitable piercing point for reconstructing dextral offset across Owens Valley, which previous workers have estimated at 65-75 km. The location of the Kearsarge intrusive suite some 60 km east of other mid-Cretaceous Sierran plutons suggests it may represent backarc magmatism that was focused along a pre-existing shear zone or fractures, similar to that observed in the Andes. The Kearsarge intrusive suite and other mid-Cretaceous intrusive complexes in the axial part of the Sierra Nevada batholith comprise approximately sub-equal amounts of granite and granodiorite, in contrast to the large suites of the Late Cretaceous Sierra Crest magmatic event, which are dominated by granodiorite. Unlike aplites and high-silica segregations in granodiorites, individual Sierran high-silica granite plutons appear to lack a titanite-removal signature, and it is suggested this is due to their origins deep in the crust. In addition, high-silica granite plutons are enriched in Zr relative to high-silica granites of the Late Cretaceous suites, suggesting the individual plutons: 1) may represent suitable end members for mixing with mafic melts to produce the voluminous granodiorites of the batholith; 2) may have once been hot, crystal-poor magmas that would have been capable of eruption, in contrast to the high-silica granites segregated from the Late Cretaceous suites at emplacement level.

TABLE 1. ALABAMA HILLS SAMPLE SUMMARY

Sample	Description	Age (Ma)	UTM-E*	UTM-N*	IGSN†
AH14-01	Independence dike (mafic)	151.34 ± 0.13	399189	4057055	P4700001C
AH14-03	Alabama Hills Granite	103.1-102.2	400282	4054245	P4700001E
RP15-01	Alabama Hills Granite	102.6-101.2	395073	4051373	P4700001F
RP15-02	Alabama Hills Granite (fine-grained facies)	Not dated	399492	4049916	P4700001G
RP15-03	Alabama Hills Granite	103.0-102.1	400230	4049235	P4700001H
RP15-04	Alabama Hills Granite	102.8-102.0	404115	4045307	P4700001I

Note: See text for zircon U-Pb age interpretations. Sample RP15-02 was not dated

*UTM coordinates given in NAD 83 datum, zone 11S

†IGSN – International Geo Sample Number. Additional sample metadata available at www.geosamples.org

TABLE 2. MAJOR AND TRACE ELEMENT DATA

Sample	RP15-01	RP15-02	RP15-03	RP15-04
Major element analyses* by ICP-OES				
SiO_2	74.91	77.22	74.97	72.97
Al_2O_3	12.34	11.81	12.19	12.98
Fe_2O_3	2.00	1.32	2.27	2.40
MnO	0.061	0.017	0.076	0.056
MgO	0.15	0.06	0.22	0.21
CaO	0.62	0.34	0.83	0.89
Na_2O	3.96	3.31	3.79	4.05
K_2O	4.37	4.84	3.94	4.22
TiO_2	0.199	0.059	0.236	0.178
P_2O_5	0.07	0.06	0.05	0.05
LOI	0.72	0.61	0.55	0.58
Total	99.4	99.64	99.13	98.6
Trace element analyses† by ICP-OES				
Sc	2	2	3	2
Be	3	6	3	4
V	13	10	17	14
Ba	244	73	343	378
Sr	81	20	94	108
Y	27	5	18	16
Zr	191	58	173	99
Trace element analyses† by ICP-MS				
Cr	250	BDL	310	20
Co	2	BDL	2	2
Ni	BDL	BDL	BDL	BDL
Cu	10	BDL	20	BDL
Zn	40	BDL	40	BDL
Ga	16	17	16	17
Ge	1	3	2	2
Rb	151	235	188	167
Nb	14	14	20	13
Mo	4	BDL	5	BDL
Ag	0.8	BDL	0.6	BDL
Sn	2	BDL	2	2
Sb	0.6	BDL	0.8	0.6
Cs	1.2	2.3	2.6	1.6
La	34.9	3.2	42.6	33.5
Ce	68.6	4.2	70.5	59.3
Pr	7.86	0.37	6.85	5.24
Nd	26.6	1.1	21.2	16.1
Sm	5.2	0.2	3.7	2.9
Eu	0.56	0.06	0.5	0.43
Gd	4.3	0.2	3.0	2.2
Tb	0.7	BDL	0.5	0.4
Dy	4.7	0.2	3.0	2.5
Ho	0.9	BDL	0.6	0.5
Er	2.8	0.2	2.1	1.6
Tm	0.45	0.06	0.35	0.26
Yb	3.0	0.6	2.6	2.0
Lu	0.48	0.13	0.46	0.34
Hf	5.1	2.5	5.4	3.2
Ta	1.7	1.7	2.3	1.7
W	3	5	2	2
Tl	0.6	0.9	0.7	0.6
Pb	13	12	17	13
Th	11.5	14.8	30.1	19.3
U	3.2	14.9	9.2	3.0

Note: LOI = loss on ignition; BDL = below detection limit
*Major element data in wt%
†Trace element data in ppm

TABLE 3. SR AND ND ISOTOPIC DATA FOR THE ALABAMA HILLS GRANITE

Sample	Rb ppm	Sr ppm	$^{87}Rb/^{86}Sr$	$^{87}Sr/^{86}Sr$	± 2σ abs*	$^{87}Sr/^{86}Sr_i$	Sm ppm	Nd ppm	$^{147}Sm/^{144}Nd$	$^{143}Nd/^{144}Nd$	± 2σ abs*	$^{143}Nd/^{144}Nd_i$	εNd_i
RP15-01	151	81	5.397	0.713639	0.000010	0.705816	5.2	26.6	0.118	0.512447	0.000004	0.512368	-2.71
RP15-02	235	20	34.146	0.752518	0.000012	0.703025	0.2	1.1	0.110	0.512385	0.000006	0.512385	-2.38
RP15-03	188	94	5.790	0.713559	0.000010	0.705167	3.7	21.2	0.106	0.512354	0.000005	0.512354	-2.99
RP15-04	167	108	4.476	0.711725	0.000010	0.705238	2.9	16.1	0.109	0.512423	0.000006	0.512350	-3.05

Note: All isotopic data corrected for decay since 102 Ma.

*Analytical uncertainty only. See text for reproducibility of standards

TABLE 4. U-PB ZIRCON ISOTOPIC DATA FOR ROCKS FROM THE ALABAMA HILLS

	Composition				Isotopic Ratios							Ages (Ma)					
Fraction	U (ppm)	Pb (pg)[a]	Th/U[b]	Total common Pb (pg)[c]	$^{206}Pb/^{204}Pb$[d]	$^{206}Pb/^{238}U$[e]	Error (2σ%)	$^{207}Pb/^{235}U$[e]	Error (2σ%)	$^{207}Pb/^{206}Pb$[e]	Error (2σ%)	$^{206}Pb/^{238}U$[fg]	Error (2σ abs.)	$^{207}Pb/^{235}U$[g]	Error (2σ abs.)	$^{207}Pb/^{206}Pb$[g]	Error (2σ abs.)	Corr. coef.
AH14-01, mafic Independence dike																		
F-1	123	24	0.99	1.3	1044	0.0238075	0.15	0.161912	1.24	0.049325	1.14	151.75	0.23	152.38	1.75	163.3	26.6	0.690
F-5	172	18	0.84	2.7	382	0.0236732	0.18	0.154235	3.11	0.047253	2.97	150.91	0.27	145.64	4.22	62.0	70.7	0.806
F-6	170	14	0.97	1.8	451	0.0236811	0.19	0.161554	2.45	0.049478	2.32	150.96	0.28	152.06	3.46	170.6	54.1	0.734
F-7	152	13	1.09	1.0	678	0.0236991	0.19	0.160700	1.80	0.049179	1.69	151.07	0.29	151.32	2.53	156.4	39.5	0.597
F-8	370	20	1.23	1.8	582	0.0237450	0.17	0.157259	2.85	0.048033	2.77	151.35	0.25	148.30	3.93	100.9	65.6	0.459
AH14-03, Alabama Hills Granite																		
F-1	193	36	1.34	1.1	1687	0.0160233	0.12	0.106515	0.89	0.048212	0.84	102.55	0.13	102.77	0.87	109.7	19.7	0.518
F-2	414	26	0.74	1.0	1479	0.0159911	0.12	0.105264	0.86	0.047742	0.80	102.36	0.12	101.62	0.84	86.5	18.9	0.612
F-3	440	29	0.98	1.1	1525	0.0160523	0.14	0.106896	0.88	0.048297	0.78	102.74	0.14	103.12	0.87	113.8	18.3	0.799
F-4	409	20	0.96	0.9	1231	0.0160816	0.19	0.106887	1.36	0.048205	1.17	102.93	0.20	103.11	1.33	109.4	27.6	0.972
F-5	174	35	1.08	1.9	985	0.0160533	0.12	0.106837	1.18	0.048268	1.11	102.75	0.12	103.07	1.16	112.4	26.1	0.626
F-7	313	23	0.96	2.5	507	0.0160652	0.16	0.105207	2.28	0.047496	2.17	102.82	0.16	101.57	2.20	74.2	51.7	0.686
F-8	247	18	0.84	2.9	366	0.0160708	0.20	0.106798	3.11	0.048198	2.97	102.86	0.20	103.03	3.05	109.0	70.2	0.703
RP15-01, Alabama Hills Granite																		
F-1	355	43	0.77	2.1	1171	0.0159218	0.67	0.103772	2.14	0.047291	1.66	101.91	0.68	100.25	2.04	62.9	39.5	0.796
F-2	337	15	0.84	1.4	589	0.0159624	0.23	0.103743	2.56	0.047158	2.37	102.17	0.23	100.23	2.44	56.2	56.6	0.819
F-3	383	44	0.72	2.8	926	0.0155474	0.32	0.102192	2.05	0.047692	1.79	99.54	0.32	98.80	1.93	83.0	42.5	0.827
F-5	412	36	0.79	2.6	802	0.0159322	0.15	0.104697	1.55	0.047681	1.44	101.98	0.16	101.10	1.49	82.4	34.1	0.764
RP15-03, Alabama Hills Granite																		
F-1	561	21	0.67	2.1	588	0.0159714	0.14	0.105472	1.89	0.047895	1.80	102.23	0.14	101.82	1.83	94.1	42.7	0.659
F-5	464	24	0.76	0.8	1730	0.0159911	0.11	0.106029	0.79	0.048089	0.73	102.35	0.11	102.33	0.77	103.7	17.1	0.620
F-6	363	49	0.65	1.2	2399	0.0159794	0.10	0.105842	0.60	0.048039	0.54	102.28	0.10	102.15	0.58	101.2	12.8	0.625
F-7	344	22	0.87	1.0	1306	0.0159978	0.14	0.106391	1.00	0.048233	0.93	102.39	0.15	102.66	0.98	110.7	21.9	0.575
F-8	244	10	0.79	1.1	551	0.0160252	0.18	0.105673	2.11	0.047826	2.01	102.57	0.18	102.00	2.05	90.7	47.7	0.615
F-9	378	16	0.78	1.4	666	0.0160600	0.18	0.106256	1.98	0.047985	1.85	102.79	0.19	102.53	1.93	98.5	43.8	0.742
F-10	197	18	0.89	1.3	781	0.0160168	0.21	0.105731	1.86	0.047877	1.70	102.51	0.21	102.05	1.81	93.2	40.2	0.809
RP15-04, Alabama Hills Granite																		
F-1	200	33	0.79	1.2	1533	0.0160048	0.11	0.106477	0.82	0.048251	0.75	102.45	0.12	102.74	0.80	111.6	17.8	0.653
F-2	331	26	0.85	1.0	1404	0.0159834	0.13	0.106109	0.87	0.048148	0.81	102.31	0.14	102.40	0.85	106.6	19.2	0.495
F-3	445	26	0.72	1.8	858	0.0160344	0.12	0.106412	1.39	0.048132	1.30	102.64	0.12	102.68	1.35	105.8	30.8	0.686
F-4	357	33	0.65	2.1	942	0.0159657	0.23	0.105836	1.69	0.048078	1.59	102.20	0.24	102.15	1.65	103.1	37.6	0.506

Note: All analyses performed on chemically abraded single zircon grains

[a]Total mass of radiogenic Pb.

[b]Th contents calculated from radiogenic ^{208}Pb and ^{230}Th-corrected $^{206}Pb/^{238}U$ date of the sample, assuming concordance between U-Pb and Th-Pb systems.

[c]Total mass of common Pb.

[d]Measured ratio corrected for fractionation and spike contribution only.

[e]Measured ratios corrected for fractionation, tracer and blank. Pb blank ratios: $^{206}Pb/^{204}Pb = 18.687 \pm 0.25$; $^{207}Pb/^{204}Pb = 15.658 \pm 0.25$; and $^{208}Pb/^{204}Pb = 38.258 \pm 0.5$ (1σ abs.)

[f]Corrected for initial Th/U disequilibrium using radiogenic ^{208}Pb and $Th/U_{[magma]}$, which is assumed to be approximated by the measured whole rock Th/U ratio.

[g]Isotopic dates calculated using $\lambda_{238} = 1.55125E^{-10}$ (Jaffey et al. 1971) and $\lambda_{235} = 9.8485E^{-10}$ (Jaffey et al. 1971).

CHAPTER 4: TRACKING THE CENTRAL COLORADO MINERAL BELT THROUGH TIME: NEW ISOTOPIC DATA FOR THE GRIZZLY PEAK CALDERA AND TWIN LAKES PLUTON WITH IMPLICATIONS FOR PLUTON-VOLCANO CONNECTIONS AND MAGMA SOURCES

INTRODUCTION

The Colorado Mineral Belt is an important Cenozoic magmatic feature that extends from the Colorado Front Range to the Four Corners region (Fig. 1; Tweto and Sims, 1963; Chapin, 2012). Many of the region's largest economic metal deposits are located in the mineral belt (Wilson and Sims, 2003). Persistent magmatism in the belt coupled with its economic prominence has led to much study regarding the nature and style of magmatism there, particularly to understand the sources and mechanisms that concentrated deposits of Mo, Pb, Zn, Cu, Au, and Ag (e.g., Simmons and Hedge, 1978; Farmer and DePaolo, 1984; Stein and Hannah, 1985; Mutschler et al., 1987; Bookstrom et al., 1988; Stein and Crock, 1990; Shannon et al., 2004).

Past studies have focused on elucidating the histories of individual magmatic centers (e.g., Shannon, 1988; Mills and Coleman, 2013) or tracking regional patterns that vary in space and time (e.g., Stein, 1985; Stein and Crock, 1990). Understanding the spatiotemporal patterns of magmatism is important because the mineral belt developed through different tectonic regimes, including compression during the Laramide orogeny and extension during Rio Grande rifting (Chapin, 2012). Moreover, significant F-rich, high-grade porphyry Mo deposits ("Climax-type") at Urad-Henderson, Climax, and Mount Emmons, were emplaced in the northern, central, and

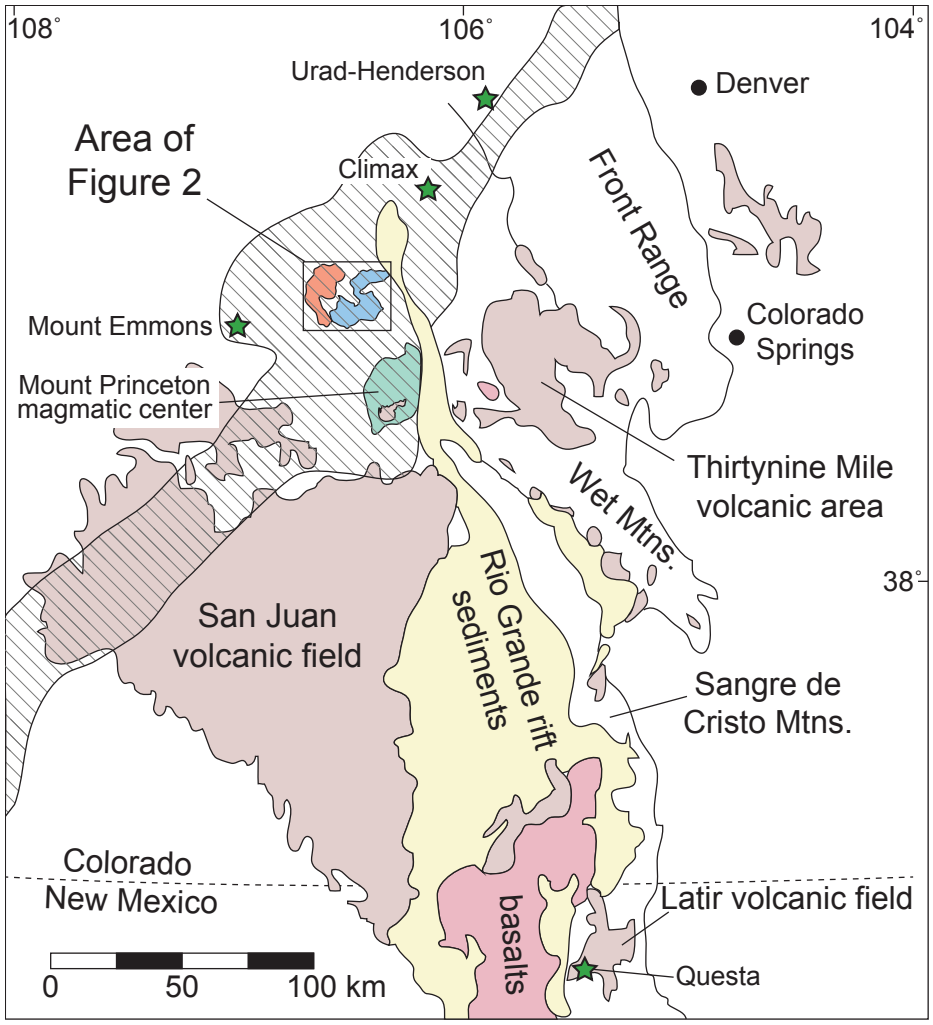

Figure 1. Generalized geologic map of central Colorado and northern New Mexico showing geologic features and locations discussed in the text. Grizzly Peak caldera (orange) and Twin Lakes pluton (blue) are noted by box. Locations of important fluorine-rich porphyry Mo deposits indicated by green stars; note the Grizzly Peak caldera is nearly equidistant between the Climax and Mount Emmons deposits. Location of Colorado Mineral Belt indicated by hatched lines, after Tweto and Sims (1963). Map after Lipman (2000) and McIntosh and Chapin (2004).

southern parts of the mineral belt, with differing isotopic compositions suggesting that lower crustal sources vary laterally (Stein, 1985; Stein and Crock, 1990).

This chapter aims to contribute to the understanding of temporal patterns in the Colorado Mineral Belt through study of the central Colorado Mineral Belt in the Sawatch Range (Fig. 1). This part of the mineral belt is well-suited to tracking secular changes in magma sources and styles because magmatism there occurred over at least 30 Ma, and includes both plutonic and volcanic episodes. This includes the Twin Lakes pluton (Fig. 2), a large granodiorite whose

63-39 Ma emplacement mirrors the Laramide history of the mineral belt (Feldman et al., 2012). Adjacent to the Twin Lakes pluton is the Grizzly Peak magmatic center, which comprises the well-characterized 300-600 km^3 Grizzly Peak Tuff, plus resurgent plutons that intruded the intracaldera tuff soon after its eruption ca. 34.3 Ma (Fig. 2; Fridrich et al., 1991; McIntosh and Chapin, 2004). Through new geochemical, isotopic, and geochronological analyses, this chapter investigates the postulated links between the Grizzly Peak Tuff and its resurgent plutons, as well as the Grizzly Peak magmatic center's relationship to the adjacent Twin Lakes pluton and the Colorado Mineral Belt as a whole. The data also permit speculation about the lack of Mo deposits in the Grizzly Peak caldera and the ultimate source of Mo in the lower crust and/or mantle.

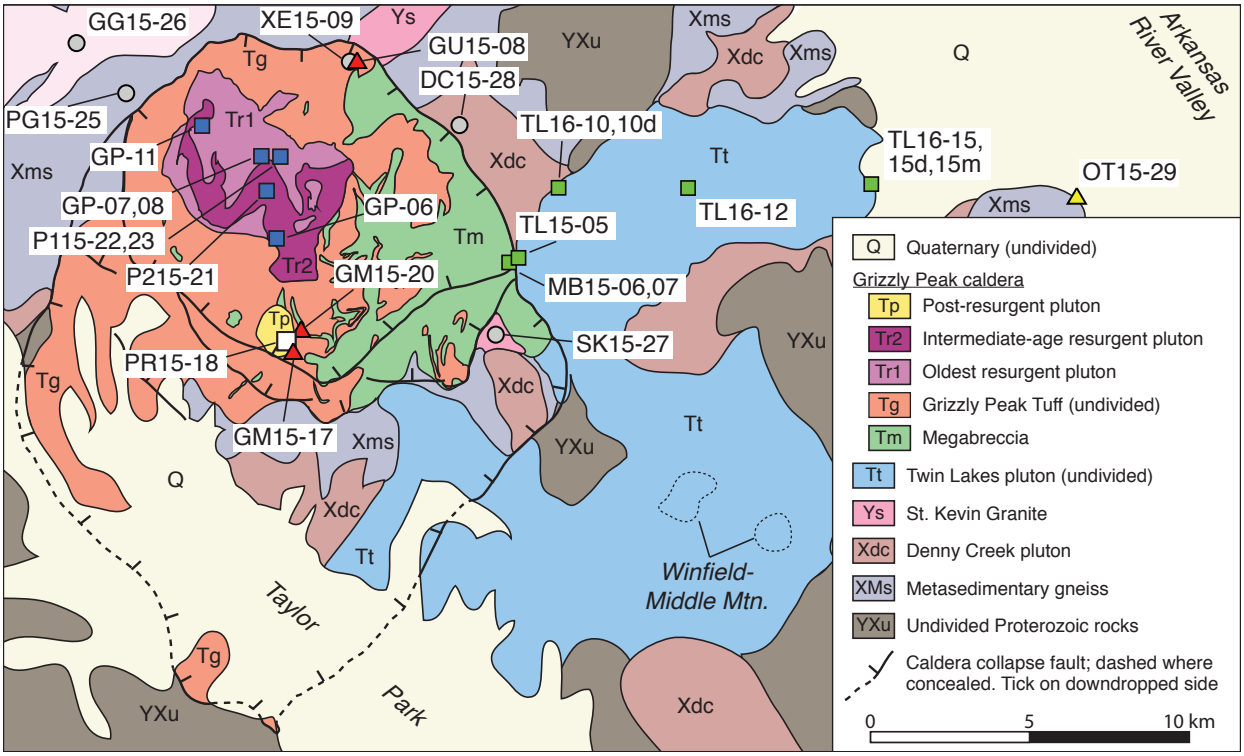

Figure 2. Generalized bedrock geologic map of the Grizzly Peak caldera and Twin Lakes pluton, northern Sawatch Range, Colorado. Locations of samples analyzed in this study indicated by symbols used in later geochemical figures. Outcrop area of tuff in Arkansas River Valley (sample OT15-29) is smaller than the symbol used. Locations of Mo-rich deposits at Winfield-Middle Mountain (Ranta, 1974; Stein and Crock, 1990) noted by dotted lines. Map after Fridrich et al. (1998).

GEOLOGICAL BACKGROUND

Proterozoic wallrocks

Proterozoic units dominate the wallrocks to the Twin Lakes pluton and Grizzly Peak caldera. Major units include metasedimentary gneisses that may be as young as 1701 Ma (Jones and Thrane, 2012), the deformed 1672-1656 Ma Denny Creek Granodiorite (Bickford and Boardman, 1984; Baker and Jones, 2008), and Mesoproterozoic plutons including the Grottos pluton and the ~1.4 Ga St. Kevin Granite (Nyman et al., 1994; Fridrich et al., 1998). Isotopic data for these rocks are limited. Feldspar Pb isotopic compositions for the Denny Creek and St. Kevin plutons are similar to each other (Aleinikoff et al., 1993). Present-day whole rock $^{87}Sr/^{86}Sr$ ratios for the St. Kevin Granite 40 km northeast of Grizzly Peak caldera range from 0.754 to 0.869 (Pearson et al., 1966).

Twin Lakes Granodiorite

The Twin Lakes pluton is an equigranular to porphyritic granodiorite with alkali feldspar megacrysts up to 15 cm long. The main body is gradational into leucocratic and mafic facies that dominate the southwestern portion of the pluton, including parts within the mapped extent of the Grizzly Peak caldera (Fridrich et al., 1998). The pluton is cut by numerous aplite dikes and contains modally layered zones interpreted to have resulted from shear segregation processes (Wilshire, 1969; Fridrich et al., 1998). The southeastern part, near Middle Mountain, comprises ~38 Ma rhyolites and granites that have been prospected for molybdenum as part of the Winfield mining district (Fridrich et al., 1998). A zircon U-Pb laser ablation-inductively coupled plasma-mass spectrometry (LA-ICP-MS) survey across the pluton indicates it was constructed from 63-39 Ma, with a gap from 57-43 Ma (Feldman, 2010). The gap mirrors the timing of a lull

in Laramide plutonism throughout the Colorado Mineral Belt (Feldman et al., 2012). Thermochronology by $^{40}Ar/^{39}Ar$ in K-feldspar suggests possible younger unexposed magmatism from 37-32 Ma (Feldman, 2010). Biotite $^{40}Ar/^{39}Ar$ ages are largely concordant with U-Pb zircon ages acquired from the same samples, except for the area of Middle Mountain where biotite ages are several Ma younger than zircon ages (Feldman, 2010). Initial Sr and Nd isotopic compositions include $^{87}Sr/^{86}Sr_i$ = 0.7062-0.7072 and εNd = -5.4 to -10.1 (Farmer and DePaolo, 1984; Stein and Crock, 1990). A sample of mineralized granite at Winfield yielded $\varepsilon Nd_{38\ Ma}$ = -8.0 and $^{87}Sr/^{86}Sr_{38\ Ma}$ = 0.7073 (Stein and Crock, 1990).

Grizzly Peak caldera

The Grizzly Peak Tuff is largely preserved as intracaldera fill in the 600 km^3 Grizzly Peak caldera. Fridrich et al. (1991) estimated the pre-erosion volume of the intracaldera tuff to be 300 km^3. Outflow tuff may have also had an original volume of 300 km^3, but only two small remnants interpreted as outflow tuff are preserved (Fridrich et al., 1991). One remnant is located 20 km east in the Arkansas River Valley (Fig. 2; Fridrich et al., 1998). Pumice fiamme define a compositional range from from 72-77 wt% SiO_2, grading from high-silica rhyolite at its stratigraphic base to low-silica rhyolite at the highest exposures (Fridrich and Mahood, 1987). Two small horizons in the Grizzly Peak Tuff contain more diverse pumice fiamme of seven distinct compositional groups (Fridrich and Mahood, 1987). Pumice groups 1-3 are equivalent to the rhyolitic pumice present throughout the intracaldera tuff. More mafic pumice compositions in the horizons range down to 57 wt% SiO_2 in group 7. The non-rhyolitic pumices comprise 5-10% of these horizons (Fridrich and Mahood, 1987).

Several plutons are interpreted as resurgent into the caldera. The Lincoln Gulch stock, in

the northern part of the caldera, includes three of the largest resurgent plutons, which are generally zoned from felsic granodiorite at their margins to mafic granodiorite at their cores (Fridrich and Mahood, 1984; Fridrich et al., 1998). Dike-like intrusions similar to the Lincoln Gulch stock are also preserved along the southeastern caldera ring fault (Fridrich et al., 1998). Following the main phase of resurgent intrusions, a series of small "post-resurgent" intrusions were emplaced in the central part of the caldera (Fridrich et al., 1991). Some of the dikes entrained large (up to 5 m diameter) boulders of pink, medium-grained granite interpreted to be a crystallized portion of the Grizzly Peak magma chamber carried from depth during resurgence (Fridrich et al., 1991).

Published isotopic analyses are limited to the Grizzly Peak Tuff. Johnson and Fridrich (1990) measured O, Sr, Nd, and Pb isotopic compositions for the compositionally diverse pumice fiamme groups. Oxygen, Sr, and Pb isotopic data are complicated and do not define simple trends from one fiamme group to another. Overall, $^{87}Sr/^{86}Sr_i$ in whole rock samples ranges from 0.7099 to 0.7111. Lead isotopic data are not corrected for decay but still fall in the field of Pb isotopic compositions defined by other central Colorado Mineral Belt rocks (Stein, 1985). Neodymium isotopic data change gradationally from group to group, but do not vary systematically with composition. The most mafic fiamme have $\varepsilon Nd_i = -13.0$, whereas the most radiogenic fiamme are in group 3 (low-silica rhyolite), at $\varepsilon Nd_i = -11.3$. The most felsic fiamme, in group 1, have $\varepsilon Nd_i = -12.1$. The chemical and isotopic variability in the tuff has been attributed to primitive basalt that underwent fractional crystallization and assimilation of 20-40% Proterozoic crust (Johnson and Fridrich, 1990). Recent isotopic work in the K/Ca system shows that the Grizzly Peak Tuff possesses $^{40}Ca/^{44}Ca$ ratios higher than mantle values (Mills et al., 2013). Excess ^{40}Ca occurs in

reservoirs with high K/Ca ratios over time, such as Proterozoic continental crust. Therefore, Mills et al. (2013) suggested the Grizzly Peak Tuff has 40-70% ancient crustal component.

Sanidine $^{40}Ar/^{39}Ar$ geochronology indicates the Grizzly Peak Tuff erupted at 34.31 ± 0.12 Ma (2σ; McIntosh and Chapin, 2004). Biotite K-Ar ages on the resurgent and post-resurgent plutons ranges from 36.8 ± 2.8 Ma to 32.9 ± 2.2 Ma (Kennecott, unpub. data recalculated by Fridrich et al., 1991; Fridrich et al., 1991). Biotite K-Ar data for a deposit interpreted as outflow Grizzly Peak Tuff in Arkansas River Valley yielded an age of 33.3 ± 2.0 Ma (2σ; Fridrich et al., 1991).

Colorado Mineral Belt

The Colorado Mineral Belt is an enigmatic NE-SW feature comprising plutonic and volcanic rocks emplaced throughout its 500-km length from Laramide time (75-43 Ma) through the Miocene (Tweto and Sims, 1963; Chapin, 2012). Although there are different definitions for the extent of the mineral belt, the Twin Lakes pluton and Grizzly Peak caldera are centrally located in all of them (Tweto and Sims, 1963; Mutschler et al., 1987; Stein and Crock, 1990). The central part of the mineral belt also includes the 36-30 Ma Mount Princeton magmatic center to the southeast (Zimmerer and McIntosh, 2012; Mills and Coleman, 2013) and Mount Emmons and the Elk Mountains to the west (Fig. 1).

There are numerous hypotheses for the origins of the Colorado Mineral Belt that attempt to account for its economic importance, its orientation cutting across the "geologic grain" of Colorado (Tweto and Sims, 1963), and its unique spatiotemporal characteristics. The belt represents the only magmatism within an otherwise 1200-km-wide gap in Cordilleran magmatism during the Laramide (75-43 Ma; Chapin, 2012). Some workers have posited that mineral belt magma-

tism was primarily controlled by the presence of Precambrian shear zones and other lithospheric discontinuities that are subparallel to the belt (Tweto and Sims, 1963; Karlstom and Humphreys, 1998; Wilson and Sims, 2003). Others have suggested the mineral belt is the result of a "leaky segment boundary" that may have been exploited as the exceptionally thick Wyoming craton and North American continental interior created an impediment to a flatly-subducting Farallon plate (Barker and Stein, 1990; Chapin, 2012). Isotopic work on the Colorado Mineral Belt has shown that magmatism related to Climax-type molybdenum mineralization is characterized by less radiogenic Nd (εNd_i = -8 to -14) than other mineral belt rocks (εNd_i = -1 to -10.6). Mineralizing rocks also have $^{87}Sr/^{86}Sr_i$ from 0.7095 to 0.740, whereas non-Climax type mineral belt rocks range from 0.705 to 0.710 (Stein, 1985; Stein and Crock, 1990). In contrast, Pb isotopic characteristics for mineralizing rocks are not distinct. Lead isotopic compositions vary regionally in all belt rocks, regardless of mineralization. Stein (1985) first demonstrated the northern mineral belt has the highest $^{208}Pb/^{204}Pb$ ratios, which progressively decrease in the central and southern mineral belt. Subsequent Pb isotopic work has largely corroborated the spatial pattern (Johnson and Fridrich, 1990; Mills, 2012).

METHODS

Samples selected for geochronological and geochemical analyses (Table 1) were chosen to limit altered zones as much as possible. Outer rinds affected by surficial weathering were removed on the outcrop using a hammer and chisel. A tile saw was used to remove additional weathered zones, if present. All samples were crushed using a jaw crusher. Crushed aliquots of bulk Grizzly Peak Tuff were picked by hand before further processing to avoid incorporation of weathered zones or lithic fragments. Aliquots of crushed samples selected for U-Pb zircon

geochronology were further disaggregated in a steel disc mill. Zircon was isolated using standard density (water table, methylene iodide) and magnetic (Frantz) techniques. Samples analyzed for elemental and isotope geochemistry were pulverized to powder in a SPEX 8530 Shatterbox alumina swing mill.

Whole rock powders of all samples were analyzed at Actlabs (Ontario, Canada). Samples were dissolved by fusion in a lithium metaborate/tetraborate mixture; major elements and Ba, Sr, Y, Zr, Sc, Be and V were analyzed by inductively coupled plasma-optical emission spectroscopy (ICP-OES), with remaining trace elements and REE analyzed by ICP-MS. Uncertainties are dependent on the abundances of the oxides and elements analyzes and for these samples are generally as follows: major elements uncertainties are less than 2% (±2σ relative) for all oxides except MgO (3%), MnO (5%), and P_2O_5 (16%). Trace elements analyzed at Actlabs that are reproducible (±2σ absolute) at better than 2 ppm include Ag, Be, Cs, Ge, Hf, Sb, Sn, Ta, Th, Tl, U, and W. Other elements are reproducible within 3 ppm (Co, Mo, Nb, Sc), 4 ppm (Ga, Y) and others have higher uncertainties, in parentheses in ppm: Pb (9); Cu (14); Rb and Zr (15); V (19); Ni (23); Sr (25); Ba (31); Zn (42); Cr (49). Rare earth elements reproducible (±2σ absolute) at 0.2 ppm or better are Eu, Ho, Lu, Tb, and Tm; REE reproducible at 0.2-0.5 ppm or better are Dy, Er, Gd, Pr, Sm, and Yb; others are reproducible at higher uncertainties, in ppm: Nd (1.2); La (1.5); Ce (2.1).

Whole rock isotopic analyses were prepared by weighing a mass of powder sufficient to provide aliquots of 1 µg Sr, 200 ng Nd, and 100 ng Pb for each sample. Whole rock powders were digested in HF and HNO_3 in Teflon® (Parr) bombs at 180°C for 48 hours. Following digestion, samples were dried down then immediately fluxed in concentrated HCl on a 180°C hot plate for 16 hours. Samples were subsequently aliquoted for Sr, Nd, and Pb purification by ion exchange column chromatography. Strontium was purified using Sr-spec cation exchange resin

after the methods of Lundblad (1994) and loaded on single Re filaments with TaF_5. Neodymium was purified through a three-stage column chemistry procedure after Harvey and Baxter (2009) and loaded on single Re filaments in a Ta_2O_5-H_3PO_4 slurry. Lead was purified in a two-stage hydrobromic-hydrochloric column procedure modified after Krogh (1973). Strontium isotopic analyses were accomplished on a VG Sector 54 TIMS at the University of North Carolina at Chapel Hill. Strontium was analyzed as a metal in dynamic multicollector mode with $^{88}Sr = 3V$. Neodymium isotopes were analyzed on an Isotopx Phoenix TIMS at the University of North Carolina at Chapel Hill, and was analyzed as an oxide in dynamic multicollector mode with $^{142}Nd^{16}O = 1V$. Strontium and Nd isotope ratios were corrected for mass fractionation using an exponential law, with Sr isotopic ratios normalized to $^{86}Sr/^{88}Sr = 0.1194$ and Nd isotopic ratios normalized to $^{146}Nd/^{144}Nd = 0.7219$. Lead isotopic analyses were completed on the VG Sector 54. Lead was analyzed as a metal in static multicollector mode with $^{208}Pb = 1V$. Lead isotope ratios for most samples were corrected for mass fractionation using a value of 0.165%/amu following replicate analyses of the NBS 981 Pb standard. A batch of samples analyzed at a later date on the same instrument was corrected for mass fractionation using a value of 0.150%/amu (see Table 4 for samples). Replicate analyses of the NBS 987 Sr standard yielded $^{87}Sr/^{86}Sr = 0.710265 \pm 0.000015$ (2σ; n = 26). Replicate analyses of the Nd standard JNdi yielded $^{143}Nd/^{144}Nd = 0.512098 \pm 0.000012$ (2σ; n = 18). All isotopic data for Cenozoic samples are corrected to initial values (i.e., values at the time of crystallization or eruption) using ages indicated in Table 1. Ages used are from this study or are approximated based on the LA-ICP-MS data of Feldman (2010). Isotopic data for Proterozoic samples are corrected for radiogenic ingrowth since 35 Ma to approximate their isotopic compositions at the time of the eruption of the Grizzly Peak Tuff.

Geochronology was performed by chemical abrasion-isotope dilution-thermal ionization

mass spectrometry (CA-ID-TIMS) on either a VG Sector 54 or Isotopx Phoenix-X62 in the Department of Geological Sciences at the University of North Carolina at Chapel Hill following the sample preparation and analytical methods of Frazer et al. (2014). Zircons for each sample were thermally annealed for 48 hours at 900ºC, then chemically abraded in HF and HNO_3 acids for 16 hours at 220ºC (Mundil et al., 2004; Mattinson, 2005). Individual grains free of cracks, obvious cores, or mineral inclusions were selected under a binocular microscope for dissolution. Dissolution and chemical purification methods for U and Pb were modified after Krogh (1973) and Parrish (1987), used the mixed ^{205}Pb-^{233}U-^{235}U EARTHTIME tracer (Condon et al., 2015). Data processing and age calculations were completed using the applications Tripoli and ET_Redux, developed as part of the EARTHTIME initiative (Bowring et al., 2011; McLean et al., 2011), and include 2σ analytical uncertainties only. Corrections for initial Th/U disequilibrium (Mattinson, 1973; Schmitz and Bowring, 2001) were made in ET_Redux assuming the measured whole rock Th/U value for each sample approximates the magmatic value; this adjustment increased the ages of individual analyses by up to 100 ka. All subsequent zircon U-Pb data discussed in this chapter will be Th-corrected.

RESULTS

Grizzly Peak Tuff and resurgent plutons

Samples of bulk Grizzly Peak Tuff yielded SiO_2 concentrations from 69-73 wt%. Sample GU15-08, from the upper subunit of the Grizzly Peak Tuff near Independence Pass (Fridrich et al., 1998), was the most silicic, whereas bulk tuff samples from the structurally lower middle subunit in the central part of the caldera were slightly less silicic. Resurgent pluton samples ranged from 61-69 wt% SiO_2. One mafic enclave (sample GP-08) collected from the oldest

resurgent pluton has 56 wt% SiO_2. Samples of bulk tuff and resurgent plutons follow broadly linear trends on major element Harker diagrams (Fig. 3), with two exceptions. Sample P115-22 was collected from the oldest resurgent pluton is strongly foliated, unlike other resurgent pluton samples. It is distinguished from other resurgent pluton and tuff samples by having higher K_2O, and lower CaO, TiO_2, and P_2O_5. Sample GP-08, a mafic enclave from the resurgent pluton, falls below the linear trend on plots of Al_2O_3 and CaO (Fig. 3).

Trace element data for the tuff and resurgent plutons also follow broadly linear trends for most elements (Fig. 4). However, resurgent pluton sample P115-22 has higher Rb and lower Zr and Y concentrations than other tuff and resurgent pluton samples, and mafic enclave sample GP-08 has relatively low Sr compared to other resurgent pluton samples. Zirconium and Hf trends are also non-linear, with the Zr and Hf concentrations peaking at 61.5 wt% SiO_2. Samples of Grizzly Peak Tuff and the resurgent plutons have approximately chondritic Zr/Hf ratios (~37; McDonough and Sun, 1995) across the SiO_2 spectrum (Fig. 5). Ratios of Th/U are generally greater than 6 (Fig. 5). Chondrite-normalized REE patterns indicate that all samples are enriched in light REEs, with La_N/Lu_N ratios from 16-36 (subscript "N" denotes concentration normalized to chondritic values of McDonough and Sun, 1995), although Grizzly Peak Tuff samples have slightly lower ratios than similarly siliceous resurgent plutons (Fig. 5). Sample P115-22, which has distinctly lower REE concentrations than other tuff and resurgent pluton samples (Fig. 6). Bulk Grizzly Peak Tuff has negative Eu anomalies (where $Eu/Eu^* = Eu_N/(Sm_N \cdot Gd_N)^{1/2}$) of 0.72 to 0.89, whereas resurgent pluton samples (except P115-22) have Eu/Eu* of 0.92 to 1.04 (Fig. 5).

Most tuff and resurgent pluton samples have $^{87}Sr/^{86}Sr_i$ between 0.7098 and 0.7108, except sample P115-22 with $^{87}Sr/^{86}Sr_i = 0.732$ (Fig. 7). Initial $^{87}Sr/^{86}Sr$ in the tuff is positively correlated with SiO_2 content, whereas the resurgent plutons have a negative correlation with SiO_2

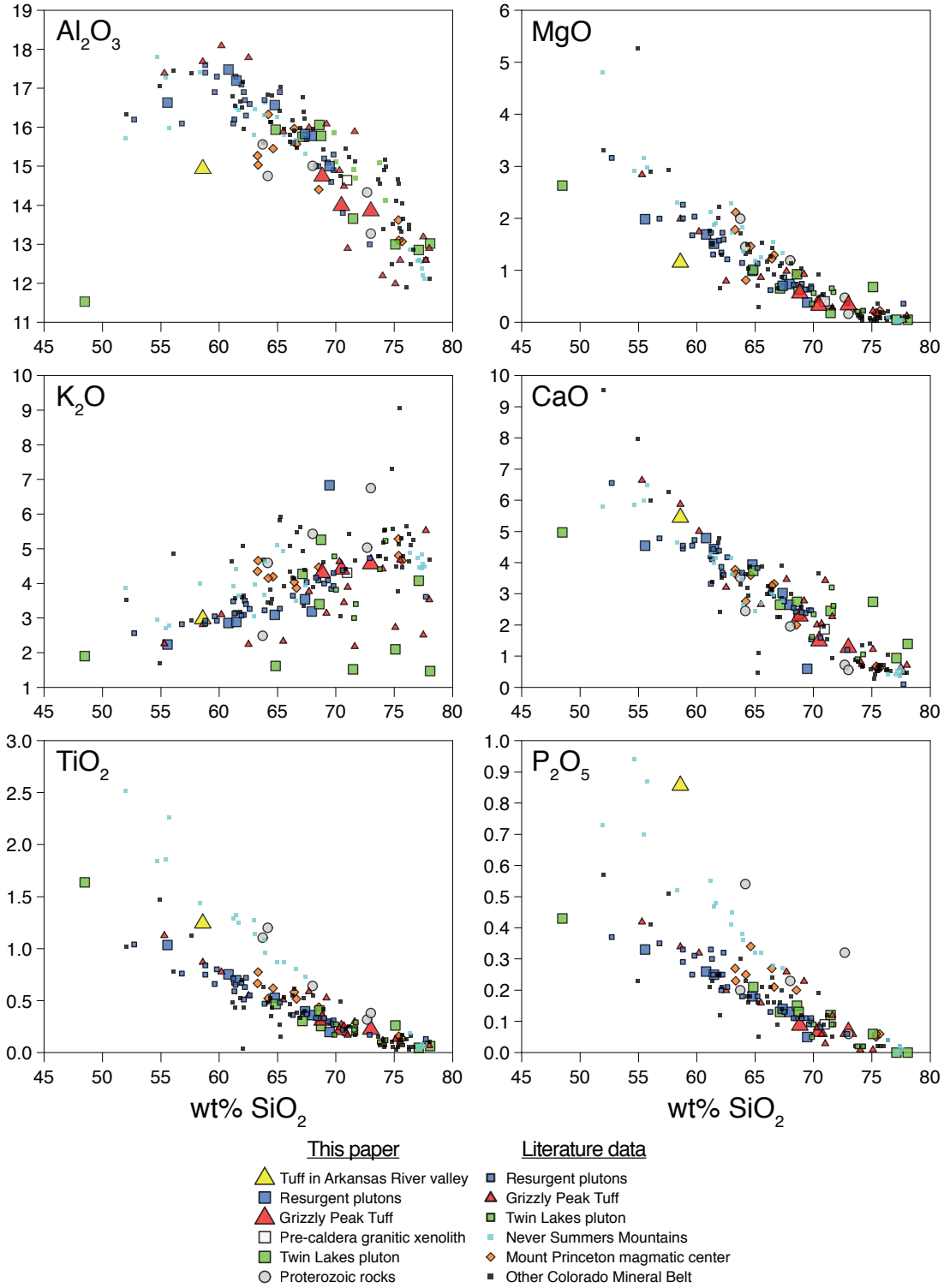

Figure 3. Major element Harker diagrams for samples analyzed in this study (large symbols) and the literature. Concentrations given in wt%. Most data for Cenozoic rocks from this study form linear trends and are similar to literature values for the same units. Exceptions include low-K_2O samples of the Twin Lakes pluton, a modally layered sample from the Twin Lakes pluton with low Al_2O_3, CaO, and MgO, and the tuff in the Arkansas River Valley with low Al_2O_3, MgO, and high P_2O_5. Literature data sources are: Grizzly Peak Tuff and resurgent plutons – Fridrich (1987); Twin Lakes pluton and other Colorado Mineral Belt – Stein (1985); Neversummers – Jacob et al. (2015); Princeton area – Mills and Coleman (2013).

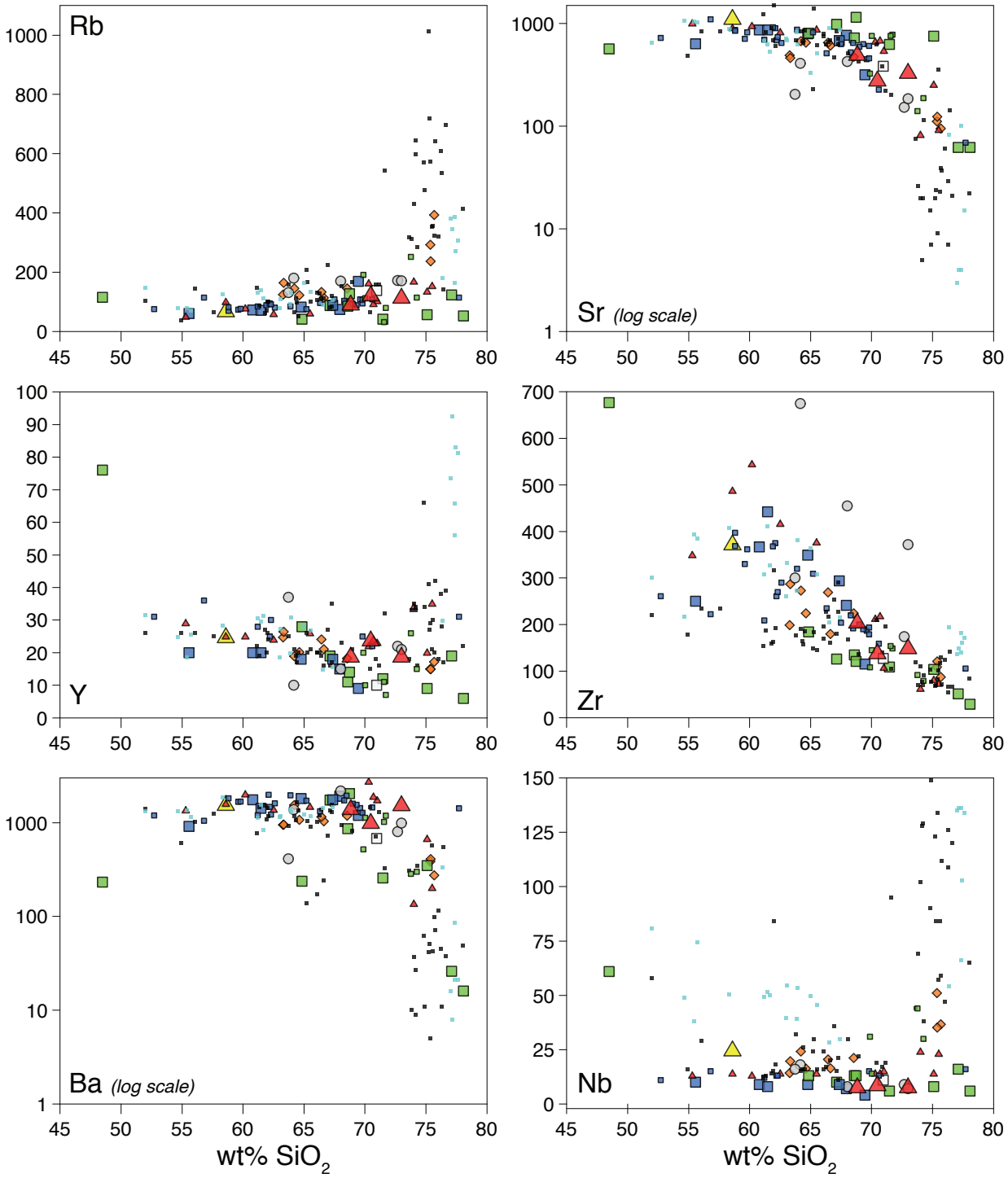

Figure 4. Trace element variation diagrams for samples from this study (large symbols) and other Cenozoic igneous rocks in Colorado. Trace element concentrations in ppm. Note log scale is used for ordinates for Ba and Sr. Symbols as in Figure 3. High-silica samples of Grizzly Peak Tuff (Fridrich, 1987; this study) do not have the extreme trace element enrichments or depletions as similarly-siliceous samples of the Colorado Mineral Belt (Stein, 1985) or Never Summer Mountains (Jacob et al., 2015). Twin Lakes pluton is distinct from Grizzly Peak Tuff with generally lower Rb, Zr, Y, and Ba, and has higher Sr at similar SiO_2 concentrations (except for aplite dikes). Note also the distinct off-trend trace element concentrations of the modally-layered sample of the Twin Lakes pluton, including very high concentrations of Y and Nb.

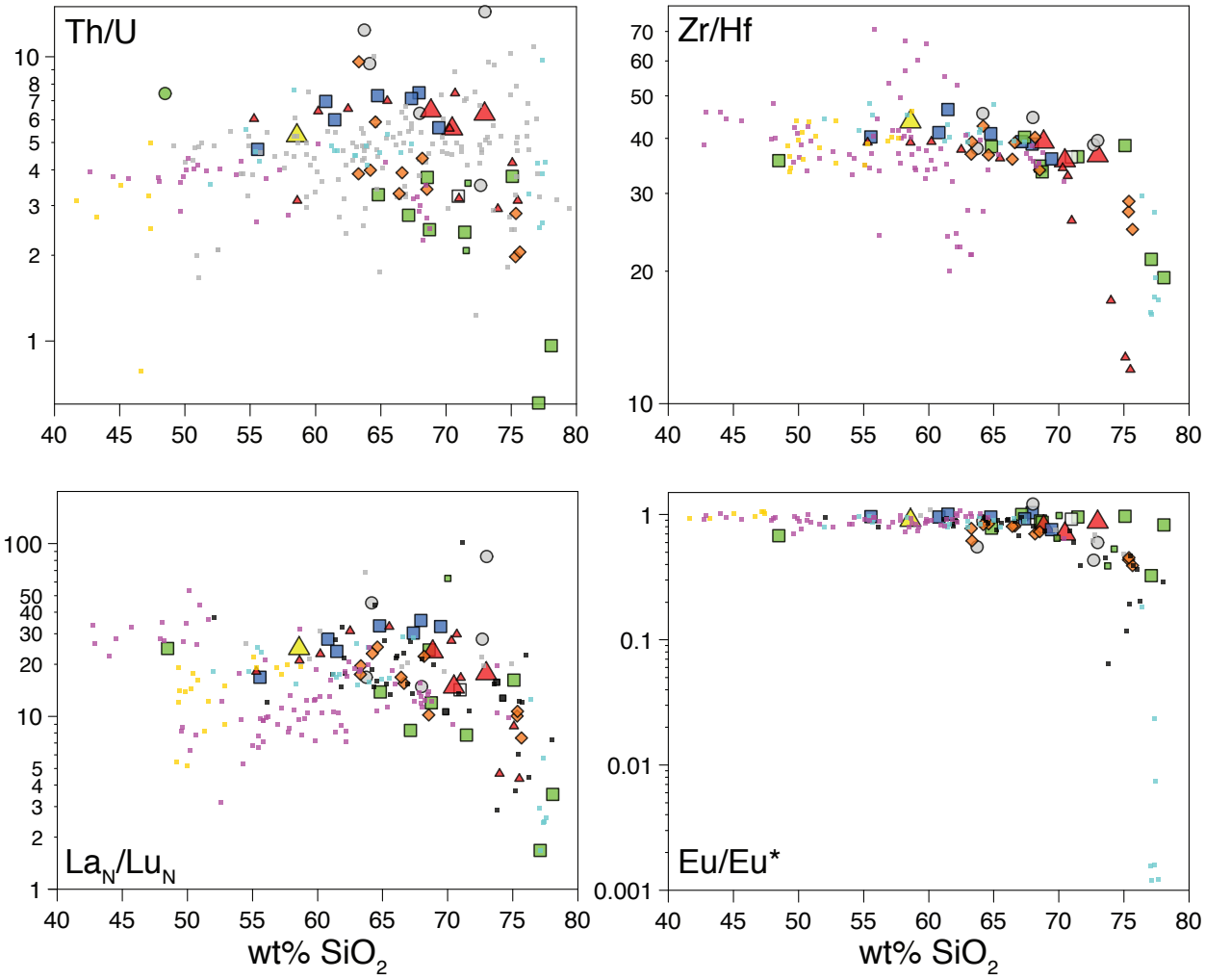

Figure 5. Trace element and REE ratios versus silica concentrations for samples from this study (large symbols) and other Cenozoic igneous rocks in Colorado. All ordinates are log scales. Samples of Grizzly Peak Tuff and resurgent plutons have high Th/U relative rocks from this study and most literature analyses in Colorado. Granitic xenolith (white square) plots with Twin Lakes data rather than Grizzly Peak data in Th/U. High-SiO_2 pumice fiamme analyses of Fridrich (1987) have sub-chondritic Zr/Hf ratios (chondrite Zr/Hf = 37; McDonough and Sun, 1995), whereas bulk tuff at same silica contents is approximately chondritic. Twin Lakes aplite dike samples have low Th/U, Zr/Hf, and La_N/Lu_N. See text for definition of normalized ratios and Eu/Eu* calculation. Symbols as in Figure 3. Additional symbols are purple squares: San Juan volcanic field (Bachmann et al., 2002; Parat et al., 2005; Parker et al., 2005; Lake and Farmer, 2015; Sliwinski et al., 2017); yellow squares: Rio Grande rift (Thompson et al., 1991; Cosca et al., 2014); gray squares: Thirtynine Mile volcanic field (Campbell, 1994).

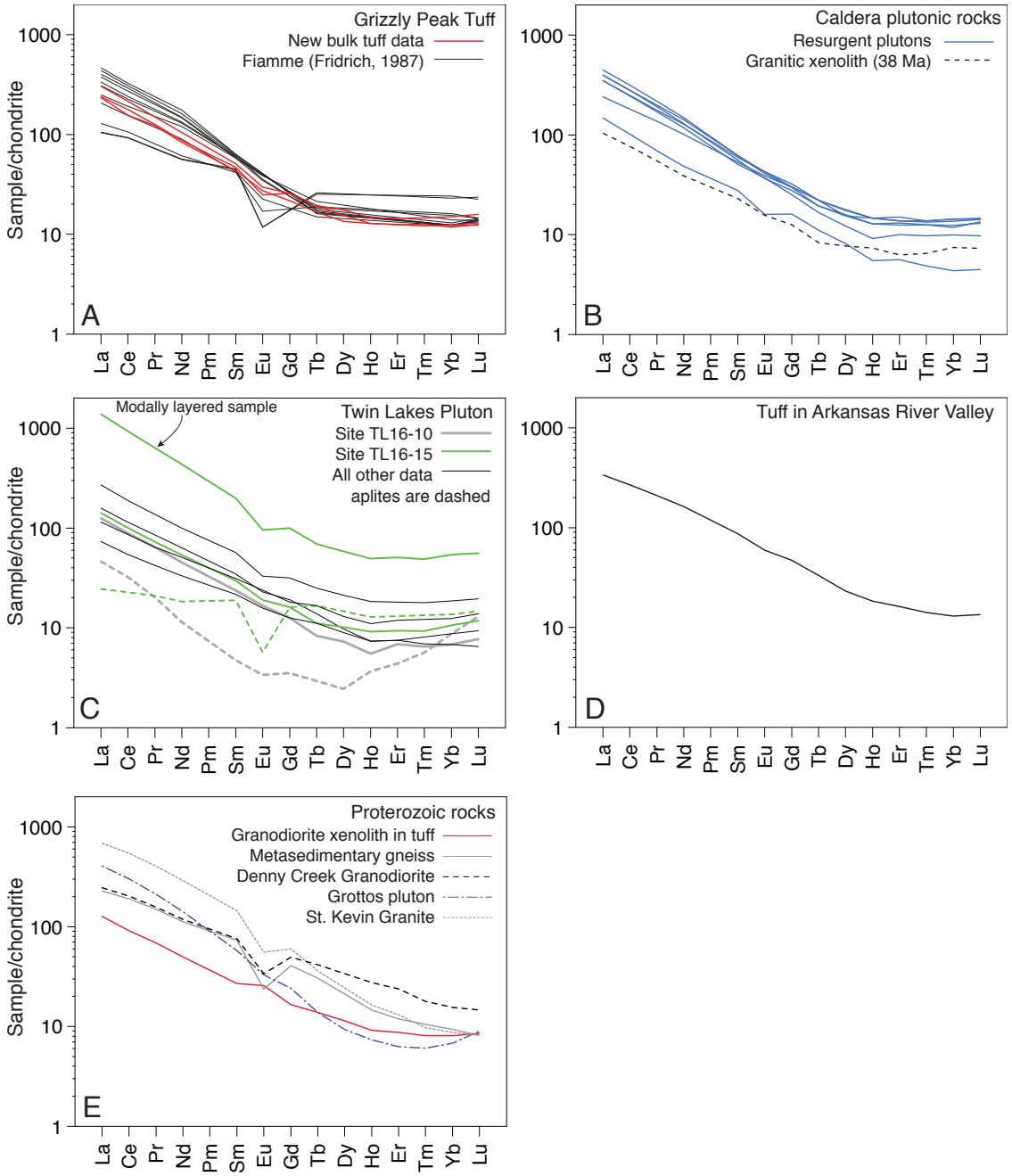

Figure 6. Rare earth element plots with concentrations normalized to chondritic values of McDonough and Sun (1995). (A) Grizzly Peak Tuff data include pumice fiamme of Fridrich (1987). High-silica fiamme have deeper negative Eu anomalies and higher heavy REE concentrations than bulk tuff. (B) Resurgent pluton samples have consistent REE concentrations and patterns. Only the REE-depleted sample P115-22 has an Eu anomaly. The 38 Ma granitic xenolith also has lower REE concentrations and is similar to Twin Lakes samples. (C) Twin Lakes pluton REE data vary widely within the main map unit, and local features (aplites and modal layering) extend the range of REE patterns. We interpret the aplite at site TL16-10 (scoop-shaped patter) to have been locally derived, whereas the distinct "seagull" type pattern and isotopic compositions of aplite from site TL16-15 suggest that it may have been derived from a source different than its host granodiorite. (D) REE data for the tuff in the Arkansas River Valley are similar to the Grizzly Peak Tuff. However, isotopic and geochronologic data indicate it is a separate unit. (E) Proterozoic REE data vary widely. St. Kevin Granite has high light REE concentrations and a steep pattern, similar to other 1.4 Ga plutons in central Colorado (Stein and Crock, 1990). The granodiorite xenolith in the tuff has the only positive Eu anomaly (Eu/Eu* = 1.22) in this study.

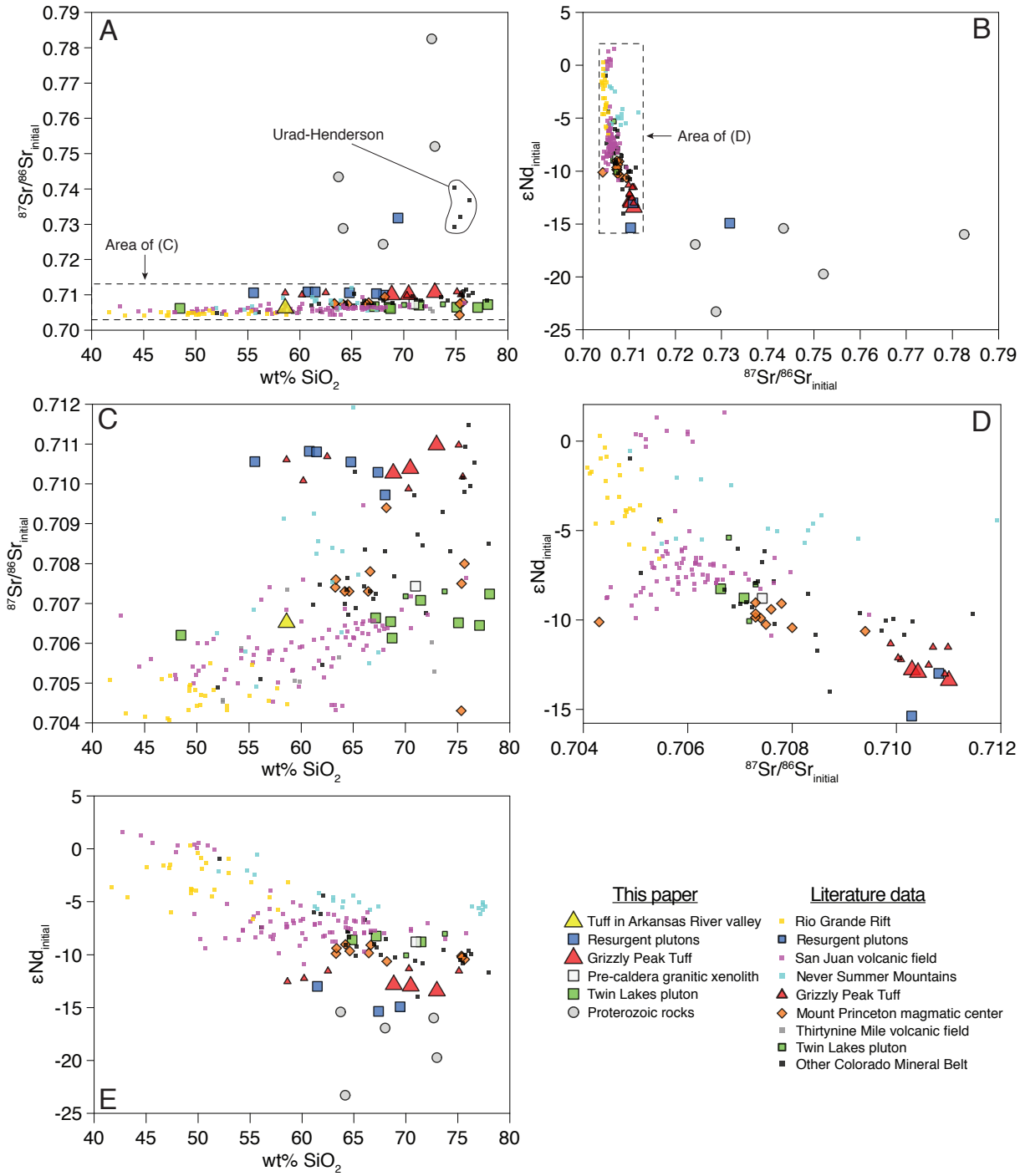

Figure 7. Strontium and Nd isotope data for samples from this study and other Cenozoic igneous rocks in Colorado. Panels (A), (C), and (E) are isotope-SiO_2 diagrams, with (C) showing broad positive correlation of $^{87}Sr/^{86}Sr_i$ with SiO_2 across all rocks, whereas (E) demonstrates that εNd_i and silica are negatively correlated. Although such patterns may suggest a mixing origin between primitive mantle and Proterozoic crust (Johnson, 1991) isotopic data for individual magmatic centers (Grizzly Peak, Twin Lakes, Mount Princeton, Never Summer Mountains) do not show correlations (panels C and E). (B) and (D) show that the Grizzly Peak Tuff and resurgent plutons have amongst the most radiogenic Sr and unradiogenic Nd in Cenozoic Colorado rocks, although Sr data for the Henderson deposit are a notable exception (panel A). Data sources as in Figure 3 and Figure 5, with additional data for Grizzly Peak (Johnson and Fridrich, 1990), Rio Grande rift (Johnson and Thompson, 1991), San Juan volcanic field (Riciputi et al., 1995), and Thirtynine Mile volcanic field (Campbell, 1994).

content. Grizzly Peak Tuff samples have εNd_i ranging from -12.7 to -13.3, and the resurgent plutons range -13.0 to -15.5 (Fig. 7). All samples have slightly less radiogenic εNd_i at higher SiO_2 concentrations. Lead isotopic compositions for all samples except P115-22 are restricted to $^{206}Pb/^{204}Pb_i$ = 17.93-18.10, $^{207}Pb/^{204}Pb_i$ = 15.55-15.57, and $^{208}Pb/^{204}Pb_i$ = 38.41-38.68 (Fig. 8). Sample P115-22 has more radiogenic $^{206}Pb/^{204}Pb_i$ and $^{207}Pb/^{204}Pb_i$, and less radiogenic $^{208}Pb/^{204}Pb_i$.

One zircon from the middle subunit of the Grizzly Peak Tuff (sample GM15-20) yielded a concordant $^{206}Pb/^{238}U$ age of 35.05 ± 0.15 Ma (Fig. 9). In contrast, six of seven zircons dated from three resurgent pluton samples (P215-21, P115-22, P115-23) are reversely discordant. Two zircons from resurgent pluton 1 (sample P115-23) are closest to concordia. A concordant grain yields an age of 34.85 ± 0.10 Ma, and a second grain is discordant and slightly younger. All three zircons from sample P115-21 of resurgent pluton 2 are reversely discordant. The range of their $^{206}Pb/^{238}U$ ages and 2 uncertainties are encompassed by one fraction measured at 34.43 ± 0.39 Ma. Sample P115-22 from resurgent pluton 1 yielded the most reversely discordant data in two zircons, which range in age from 34.47-33.90 Ma including 2σ uncertainties (Fig. 9).

Twin Lakes Granodiorite

Samples of typical Twin Lakes pluton range from 65-75 wt% SiO_2. Two aplites are 77-78 wt% SiO_2, and a modally layered sample has 48 wt% SiO_2 (Fig. 3). Excluding the modally layered sample, samples plot on linear trends on Harker diagrams for all major elements except K_2O and Na_2O, which are highly scattered. Trace element data are also typically linear, except for scatter in Ba and Rb (Fig. 4). The aplites are depleted in Sr and enriched in U and Pb relative to the granodiorite. The modally layered sample (TL16-15m) has high concentrations of V, Y, Zr, and Th, and low concentrations of Sr and Ba relative to its host granodiorite (TL16-15). Ratios

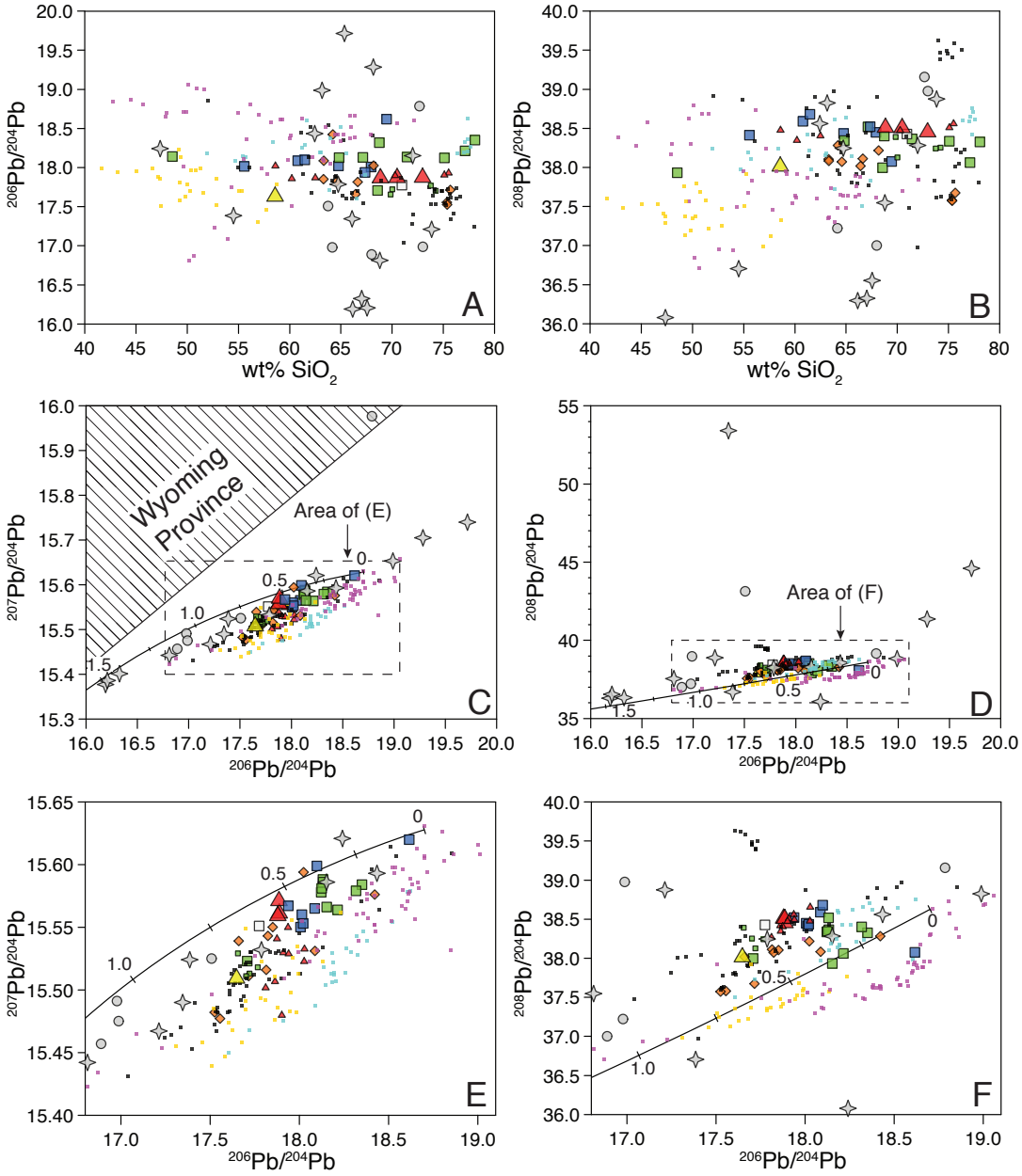

Figure 8. Lead isotope data for samples from this study and other Cenozoic igneous rocks from Colorado. (A) and (B) show there is no correlation of Pb isotope composition and silica. Panel (C) shows all $^{207}Pb/^{204}Pb$-$^{206}Pb/^{204}Pb$ data, and panel (D) shows all $^{208}Pb/^{204}Pb$-$^{206}Pb/^{204}Pb$ data. Isotopic data for Proterozoic rocks (Stein, 1985 – gray crosses; this study – gray circles) vary widely. High $^{207}Pb/^{204}Pb$ sample in panel (C) is metasedimentary gneiss sample PG15-25. Its uranogenic Pb composition is similar to Archean rocks of the Wyoming Province (hatched area; Wooden and Mueller, 1988). Panels (E) and (F) focus on Pb isotope data of Cenozoic samples. (E) Twin Lakes samples (green squares) with low $^{207}Pb/^{204}Pb$-$^{206}Pb/^{204}Pb$ ratios are from Eocene parts of the pluton, whereas high $^{207}Pb/^{204}Pb$-$^{206}Pb/^{204}Pb$ ratios are from older samples. (F) Samples from this study largely plot with $^{208}Pb/^{204}Pb$-$^{206}Pb/^{204}Pb$ data of central Colorado Mineral Belt samples of Stein (1985). Solid black lines on Pb-Pb diagrams are Pb isotope growth curves of Stacey and Kramers (1975); curve ages are given in Ga; tick marks are every 0.25 Ga. Data from this study, Mills (2012), Cosca et al. (2014), and Jacob et al. (2015) are whole rock data corrected to initial values. Colorado Mineral Belt data of Stein (1985) are feldspar compositions that are not corrected for decay but are interpreted to represent initial values. Cenozoic whole rock data of Johnson and Fridrich (1990), Johnson and Thompson (1991), Riciputi et al. (1995), Parat et al. (2005), and Lake and Farmer (2015), and Proterozoic whole rock data of Stein (1985), are not corrected for decay.

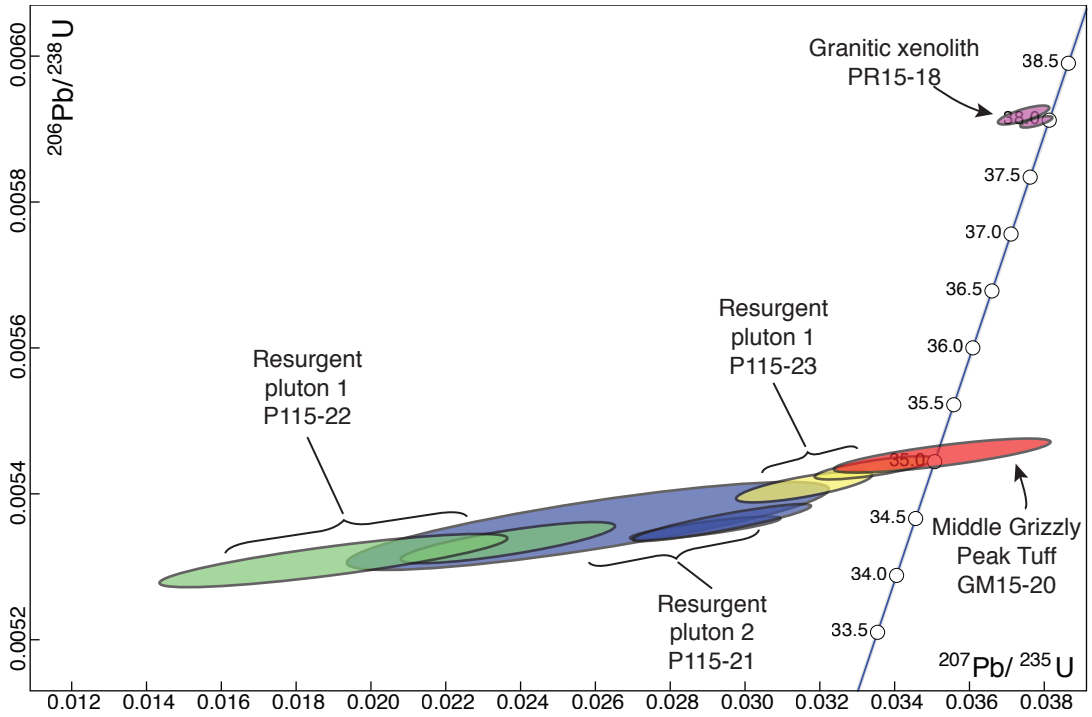

Figure 9. Zircon U-Pb concordia diagram of selected samples dated by CA-ID-TIMS in this study. The oldest analysis of resurgent pluton sample P115-23 is concordant and is indistinguishable within uncertainty of a concorant analysis of the Grizzly Peak Tuff, and suggests the pluton was emplaced very soon after eruption. We interpret the reversely discordant data of the other resurgent pluton samples to suggest they were likely also emplaced shortly after eruption. Data for the mafic tuff in the Arkansas River Valley (sample OT15-29), which includes one concordant and one reversely discordant analysis both near 24.5 Ma, not shown for clarity. One normally discordant zircon analysis from sample PR15-18 with a $^{207}Pb/^{206}Pb$ age of 1353 ± 10 Ma is not shown; see Table 5 for data. Ages along concordia are given in Ma.

of Th/U decrease with increasing SiO_2, with markedly decreased ratios in the aplite dike samples (Fig. 5). Aplites also have sub-chondritic Zr/Hf ratios near 20. Typical Twin Lakes granodiorite samples have La_N/Lu_N between 8-25 and minor to absent negative Eu anomalies (Figs. 5, 6). The aplites follow very different patterns to the main pluton and to each other. Sample TL16-10d has a scoop-shaped pattern, whereas TL16-15d has a flat "seagull"-type pattern characterized by very low La_N/Lu_N and a negative Eu anomaly of 0.33 (Figs. 5, 6). The modally layered sample has elevated REE concentrations relative to its host granodiorite (Fig. 6), and a more pronounced negative Eu anomaly.

Initial $^{87}Sr/^{86}Sr$ in the Twin Lakes pluton ranges from 0.7061 to 0.7072. There does not appear to be any correlation with SiO_2 concentrations, although the aplite dikes have slightly

higher $^{87}Sr/^{86}Sr_i$ than their host rocks (Fig. 7). Neodymium isotopic data from three samples collected in close proximity to each other near the caldera margin (Fig. 2) show little variation around εNd_i = -8.6. Lead isotopic data for all samples except TL15-12 fall in the range $^{206}Pb/^{204}Pb_i$ = 18.13-18.35, $^{207}Pb/^{204}Pb_i$ = 15.56-15.59, and $^{208}Pb/^{204}Pb_i$ = 38.06-38.52. Uranogenic Pb data are distinct from the Grizzly Peak Tuff and resurgent plutons (Fig. 8). Sample TL15-12, collected from a ~42 Ma part of the Twin Lakes pluton (Feldman, 2010), has less radiogenic Pb isotopic compositions than all other Twin Lakes samples (Fig. 8).

Other Cenozoic rocks

Sample PR15-18 was collected from a large granite outcrop in the post-resurgent pluton map unit of Fridrich et al. (1998). It is a porphyritic biotite granite with pink alkali feldspar megacrysts up to 4 cm long. The granite has similar major and trace element abundances as felsic samples of the Twin Lakes pluton and resurgent plutons (Figs. 3, 4). Rare earth element abundances are similar to the Twin Lakes pluton, but lower than most of the resurgent pluton samples. The sample has $^{87}Sr/^{86}Sr_i$ = 0.7074 and εNd_i = -8.8, and initial Pb isotopic compositions that are intermediate between sample TL15-12 and all other Twin Lakes samples (Fig. 8). One zircon yielded a concordant $^{206}Pb/^{238}U$ age of 37.985 ± 0.083 Ma, with a second zircon slightly reversely discordant at 38.046 ± 0.050 Ma. A third zircon is normally discordant and has a $^{207}Pb/^{206}Pb$ age of 1353 ± 10 Ma. Regression of a chord through the data yields a lower intercept age of 38.32 ± 0.33 Ma and an upper intercept age of 1410 ± 11 Ma.

Sample OT15-29 was collected near Twin Lakes Reservoir in the Arkansas River Valley from an outcrop mapped as an outflow deposit of the upper subunit of the Grizzly Peak Tuff (Fridrich et al., 1998). Pumice extracted from the red-weathered tuff yielded 59 wt% SiO_2 and

major element concentrations distinct from the all other analyzed Cenozoic rocks in this study (Fig. 3). Trace element concentrations are similar to mafic samples from the Grizzly caldera resurgent plutons, although it has slightly elevated Nb (Fig. 4). This tuff has $^{87}Sr/^{86}Sr_i$ = 0.7065, with Pb isotopic compositions similar to sample TL15-12 (Figs. 7, 8). Geochronologic data include one concordant fraction with a $^{206}Pb/^{238}U$ age of 24.46 ± 0.37 Ma and a reversely discordant zircon at 24.34 ± 0.22 Ma (Table 5).

Proterozoic rocks

Samples of four different wallrock units adjacent to the Grizzly Peak caldera, as well as a large (1 m diameter) granodioritic xenolith in the upper subunit of the tuff, were analyzed (Fig. 1). Silica contents range from 64-73 wt%; major elements scatter about the linear trends defined by Cenozoic samples in this study. In general, Proterozoic rocks have lower CaO, and higher TiO_2 and P_2O_5, than Cenozoic samples at the same silica concentration. Trace elements are also relatively scattered, with high Zr concentrations in several samples (Fig. 4). Proterozoic rocks collected around the caldera generally have high La_N/Lu_N ratios and negative Eu anomalies (Figs. 5, 6). In contrast, the granodiorite xenolith has relatively low REE concentrations and a small positive Eu anomaly (Eu/Eu* = 1.22). Isotopic compositions (corrected to 35 Ma) vary widely (Figs. 7, 8). Initial $^{87}Sr/^{86}Sr$ ranges 0.724-0.783 and εNd_i from -15.4 to -23.3. In all samples except the metasedimentary gneiss, $^{206}Pb/^{204}Pb_i$ ranges from 16.89-17.51 and $^{207}Pb/^{204}Pb_i$ from 15.46-15.53. In contrast, the metasedimentary gneiss (sample PG15-25) has higher $^{206}Pb/^{204}Pb_i$ and $^{207}Pb/^{204}Pb_i$ ratios (18.79 and 15.98). Thorogenic Pb is variable, from $^{208}Pb/^{204}Pb_i$ = 37.00-43.14.

DISCUSSION

Interpretation of new geochronology

Many of the geochronologic data are reversely discordant, and were acquired on both instruments used in this study. One possible cause for the discordant data is that zircon populations may have lost U-rich "parent" zones by hydrothermal or metamorphic processes after crystallization (Mattinson et al., 1996). Indeed, many of the zircons in this study have relatively high Th/U (Table 5). However, the reversely discordant data in this study are likely a result of preparation and/or analytical issues because: 1) some zircons with high Th/U are concordant; 2) some zircons with low Th/U are reversely discordant; 3) the whole rocks themselves also have high Th/U, suggesting the high Th/U of the zircons is primary (Table 2). Regardless of the origin of reverse discordance, the geochronologic data are interpreted with caution.

Rocks in Grizzly Peak caldera

The 35.05 ± 0.15 Ma age for a zircon from the Grizzly Peak Tuff is some 750 ka older than its 34.3 ± 0.12 Ma sanidine $^{40}Ar/^{39}Ar$ age (McIntosh and Chapin, 2004). Discrepancies between the U-Pb and Ar/Ar systems often occur in volcanic rocks, although they typically differ by less than 500 ka (Costa, 2008). For example, the weighted mean zircon U-Pb age of the Badger Creek Tuff from the Mount Princeton magmatic center (Fig. 1), is ~210 ka older than the 34.26 ± 0.06 Ma sanidine $^{40}Ar/^{39}Ar$ age (Zimmerer and McIntosh, 2012; Mills and Coleman, 2013). Recalculation of the Grizzly Peak Tuff Ar/Ar data using updated K decay constant and Fish Canyon sanidine age (Renne et al., 2011) yields an updated sanidine age of 34.87 ± 0.12 Ma, which is within uncertainty of the new zircon U-Pb age before taking into account decay

constant uncertainties. More zircon geochronology on the Grizzly Peak Tuff is required to confirm that the single zircon age is robust.

Geochronology for the resurgent plutons are difficult to interpret due to reverse discordance. However, a zircon from resurgent pluton 1 is concordant within uncertainty and overlaps with the zircon U-Pb age for the tuff. This suggests the pluton was emplaced shortly after eruption of the tuff. The rest of the discordant data for the resurgent plutons also suggest crystallization ages shortly following eruption. Short timespans between zircon U-Pb ages for the tuff and resurgent plutons are supported by field relationships (Fridrich et al., 1991) and are also observed in other Cenozoic calderas in the Rockies (Tappa et al., 2011; Mills and Coleman, 2013; Rosera et al., 2013).

Fridrich et al. (1991) speculated that granitic xenoliths similar to sample PR15-18 may represent completely solidified parts of the Grizzly Peak magma chamber that were subsequently entrained during resurgent magmatism. The concentration data largely corroborate the similarities between the tuff and granitic xenoliths, although sample PR15-18 has lower Ba and Th/U than the tuff (Figs. 4, 5). However, U-Pb zircon data for the granitic xenolith suggest a crystallization age approximately 3 Ma older than the Grizzly Peak Tuff (Fig. 9). One explanation for this discrepancy is that the zircon data are compromised by inheritance. If Grizzly Peak magma assimilated or otherwise interacted with slightly older granitoids, the Cenozoic data for sample PR15-18 could represent recycling of slightly older zircons, or mixing between inherited and autocrystic growth (Miller et al., 2007).

Whole rock isotopic data more clearly elucidate the relationship between the xenolith and the Grizzly Peak system. Sample PR15-18 has distinctly less radiogenic Sr and Pb, and more radiogenic Nd, than the tuff (Figs. 7, 8). Thus, the xenolith cannot represent a crystallized portion

of the Grizzly Peak magma chamber, and therefore the zircon U-Pb data likely reflect magmatism in the area before the Grizzly Peak system was established. The granitic xenolith appears to share numerous similarities to the Twin Lakes pluton. The interpreted crystallization age (38 Ma) is similar to the youngest parts of the Twin Lakes pluton (39 Ma; Feldman, 2010) and the Winfield-Middle Mountain area (38 Ma; Fridrich et al., 1998). In addition, inherited zircon characteristics are similar. The Twin Lakes pluton commonly has a 1400 Ma inherited component (Feldman, 2010), and a chord regressed through the granitic xenolith's concordant and normally discordant data yields an upper intercept age of 1410 ± 11 Ma. Combined with similar whole rock isotopic compositions (Figs. 7, 8; Stein, 1985; Stein and Crock, 1990), we suggest that this xenolith and others like it in the post-resurgent intrusions (Fridrich et al., 1998) may represent a western extension of the Twin Lakes pluton that was disrupted by the eruption of the Grizzly Peak Tuff and subsequent resurgent magmatism.

Outflow tuff in Arkansas River Valley

Two zircons from the tuff in the Arkansas River Valley suggest a crystallization age ca. 24.5 Ma, whereas K/Ar in biotite yielded an age of 33.1 ± 1.0 Ma (Fridrich, 1987). The discrepancy could be due to inherited Ar in the biotite, Pb-loss in the zircons, or a combination of the two. However, the U-Pb data to are likely more robust because the zircons were chemically abraded (Mundil et al., 2004; Mattinson, 2005), and it is unlikely that two zircons of different sizes would record the same apparent age after experiencing Pb-loss. Therefore, the age of this tuff outcrop is best approximated by the zircon U-Pb data.

Significance of chemical and isotopic data for Proterozoic basement rocks

Lead isotopic data for the metasedimentary gneiss (sample PG15-25) are intriguing

because of its high uranogenic Pb isotope ratios (Fig. 8). Although the $^{206}Pb/^{204}Pb$ ratio is similar to the ~1800 Ma Idaho Springs Formation (Stein, 1985), sample PG15-25 also has a $^{207}Pb/^{204}Pb$ ratio near 16, which is much higher than data for Proterozoic whole rocks from northern and southern Colorado (Fig. 8; Aleinikoff et al., 1993; McLennan et al., 1995). High $^{207}Pb/^{204}Pb$ ratios relative to $^{206}Pb/^{204}Pb$ are reported in the Archean Wyoming Province, where 2.79 Ga rocks in the eastern Beartooth Mountains have similar present-day Pb isotopic compositions to the metasedimentary gneiss (Wooden and Mueller, 1988; Frost et al., 1998; Mueller and Frost, 2006; Mueller et al., 2010). Many of the Wyoming Archean rocks also have radiogenic Sr isotopic compositions similar to sample PG15-25 (Wooden and Mueller, 1988).

Lead isotopic and U-Pb zircon evidence suggests there is only minor influence of Archean material in Paleoproterozoic rocks in the northern Colorado, closest to the Wyoming province (Aleinikoff et al., 1993). However, more recent zircon and whole rock isotopic work has revealed Archean-aged zircons and the involvement of older crust in the genesis of Paleoproterozoic rocks in central Colorado (Hill and Bickford, 2001; Bickford and Hill, 2007; Bickford et al., 2008; Jones and Thrane, 2012). One Archean-aged zircon was also identified in LA-ICP-MS analyses of the Twin Lakes pluton (Feldman, 2010). Therefore, it is plausible that the metasedimentary gneiss, which is at least 1701 Ma (Jones and Thrane, 2012), acquired its Pb (and possibly Sr) from Archean rocks during the Paleoproterozoic.

A newly recognized tuff in the Arkansas River Valley

The data presented here indicate that the small tuff outcrop in the Arkansas River Valley cannot be a remnant of extracaldera Grizzly Peak Tuff. Significantly, the isotopic data do not permit a link because the tuff in the Arkansas River Valley has lower $^{87}Sr/^{86}Sr$, $^{206}Pb/^{204}Pb$,

$^{207}Pb/^{204}Pb$, and $^{208}Pb/^{204}Pb$ ratios (Figs. 7, 8). Moreover, U-Pb zircon geochronology yields consistent ages ca. 24.5 Ma, some ~10 Ma younger than the Grizzly Peak Tuff.

It is difficult to determine the significance of this unit. Outcrops are poorly exposed over only 0.03 km^2 and are deeply weathered (Fridrich et al., 1998). It erupted after initiation of Rio Grande rifting in this area, which began ~30-28 Ma and is characterized by bimodal magmatic compositions (Shannon, 1988; Chapin and Cather, 1994; Mills and Coleman, 2013; Ricketts et al., 2016). Its location on rift flank makes it difficult to determine if the small outcrop area is due to small-volume eruption, or to weathering and poor preservation as a consequence of rifting. The lack of volcanic rocks with similar ages in this part of Colorado (McIntosh and Chapin, 2004) suggests this eruptive unit may have been a local phenomenon. Around the same time, the youngest leucogranites in the Climax porphyry Mo system were emplaced ~35 km to the northeast (24 Ma; Bookstrom et al., 1988), and the small Raspberry Gulch rhyolite dome erupted in the Mount Princeton area (22 Ma; Campbell, 1994; Zimmerer and McIntosh, 2012).

Sources and magmatic processes in the Twin Lakes pluton

Magma sources

The restricted Sr isotopic range for the Twin Lakes pluton, from $^{87}Sr/^{86}Sr_i$ = 0.7061-0.7071 in rocks from 63-42 Ma (Feldman, 2010), suggests either a persistent and homogenous magma source(s), or that efficient and fortuitous mixing of different sources occurred throughout the pluton's diachronous history. The Pb and Nd data suggest the latter scenario is more likely, as they are variable in time and space. Three samples from the northwestern portion of the pluton have $\varepsilon Nd_i \approx -8.6$, whereas Farmer and DePaolo (1984) measured a more radiogenic value of -5.4 in the northeastern part of the pluton. A sample of ~41 Ma Twin Lakes pluton from near

Winfield/Middle Mountain has εNd_i = -10.1 (Stein and Crock, 1990; Feldman, 2010). The Pb isotopic data are more straightforward. All Paleocene samples have $^{206}Pb/^{204}Pb_i$ greater than 18.1, whereas Eocene samples have $^{206}Pb/^{204}Pb_i \approx 17.7$, suggesting a switch to a source with lower U/Pb ratios (Fig. 8). Thorogenic Pb data are more difficult to distinguish, but $^{208}Pb/^{204}Pb_i$ ratios appear slightly lower in younger samples.

The Pb isotopic data are intriguing because of recent hypotheses for the genesis of Mo-rich deposits. Pettke et al. (2010) suggested that Mo deposits are characterized by low uranogenic Pb ratios relative to otherwise similar Mo-poor intrusions, due to sourcing from ancient metasomatized subcontinental lithospheric mantle. In the case of the Twin Lakes pluton, the young, unradiogenic samples of Stein (1985) come from the Winfield/Middle Mountain area, which may be an eroded Climax-type Mo deposit (Ranta, 1974; Stein and Crock, 1990). Metasomatized subcontinental lithospheric mantle is also hypothesized to be enriched in light REE and large-ion lithophile elements, leading to low Sm/Nd and moderate Rb/Sr ratios (Kessel et al., 2005; Pettke et al., 2010). If the Eocene parts of the pluton were derived from such a source, it suggests that 1) the Paleocene Twin Lakes pluton was derived from a different source than the Eocene parts; 2) the similar Sr isotopic compositions between the Eocene and Paleocene parts of the pluton are coincidental.

Emplacement level processes

Isotopic data demonstrate that the modally layered sample (TL16-15m) has the same source as its host rock (TL16-15; Table 3; Figs. 7, 8). The modal layering's REE pattern is also parallel to the host rock's, but with a more pronounced negative Eu anomaly. It has previously been suggested that modal layering in the Twin Lakes resulted from flow sorting and deformation

processes that effectively segregated mafic minerals from the main granodiorite (Wilshire, 1969). However, the high viscosities of silicic magmas preclude sedimentary-type mechanisms for generating such features (Glazner, 2014). An alternative explanation that would satisfy the chemical data, including REE enrichment, and Al_2O_3, K_2O, CaO, Na_2O, Ba, Sr, and Eu depletion relative to its host rock (Figs. 3, 4), is that it was once relatively "normal" granodiorite from which felsic liquid was removed (e.g., Coleman et al., 2011).

Two aplites collected from opposite ends of the northern part of the Twin Lakes pluton have starkly different REE patterns (Fig. 6). Sample TL16-10d, collected at the northwestern margin of the pluton (Fig. 2), has a scoop-shaped REE pattern and negligible Eu anomaly characteristic of aplites interpreted to have been separated from a titanite-bearing granodioritic mush (Glazner et al., 2008). In contrast, aplite TL16-15d was collected from a similarly-aged outcrop on the far eastern margin of the pluton, and has a flat REE pattern and a large negative Eu anomaly. Compared to the Oligocene-Miocene granites of Stein and Crock (1990), which also have prominent negative Eu anomalies, this aplite has low REE concentrations. Such a flat pattern in a pluton that contains titanite throughout (Fridrich et al., 1998; Feldman, 2010) is enigmatic. One possibility is that aplitic liquid was separated from a granodiorite mush prior to titanite crystallization (Colombini et al., 2011). However, it is plausible that this aplite dike was not derived from the granodiorite it intrudes. The $^{208}Pb/^{204}Pb$ data in particular permit the aplite to have been derived from a different source than the host rock (Fig. 8). Thus, the aplite on the eastern part of the Twin Lakes pluton could have been derived from a separate, titanite-free source from depth.

Source and history of the Grizzly Peak magmatic system

Hypotheses for the chemical and isotopic diversity of the Grizzly Peak Tuff have focused

on the heterogeneous tuff horizons that contain compositionally diverse pumice fiamme (Fridrich and Mahood, 1987; Johnson and Fridrich, 1990). For example, Zr-TiO_2 plots of pumice samples follow a liquid line of descent, allowing the possibility that the tuff resulted from fractional crystallization of a large magma chamber prior to eruption (Fig. 10; Fridrich and Mahood, 1987). Isotopic diversity may have been generated by assimilation of diverse Proterozoic rocks at emplacement level (Johnson and Fridrich, 1990). In addition, the resurgent plutons are interpreted to have been derived from the same magma as the tuff (Fridrich and Mahood, 1984).

Analyses of resurgent pluton samples fill the compositional space between all tuff compositions on the Zr-TiO_2 plot, suggesting that after eruption of the tuff, some portions of compositionally diverse melts could have remained in the chamber and mixed in varying proportions to produce the resurgent pluton compositions (Fig. 10). However, the isotopic data preclude such a scenario. At comparable SiO_2 concentrations, the resurgent plutons have less radiogenic Nd and more radiogenic Pb than the tuff (Figs. 7, 8). Alternatively, perhaps the leftover tuff magmas were modified by assimilation of Proterozoic wallrocks to generate the resurgent pluton isotopic compositions (e.g., Johnson and Fridrich, 1990). However, this is unlikely because assimilation is thermally limited in the upper crust (Glazner, 2007). Furthermore, if ancient rocks were the assimilant, the Sr isotopic compositions of the resurgent plutons should also diverge from that of the tuff.

In light of new compositional and isotopic data, we propose that the Grizzly Peak Tuff and the resurgent plutons were derived in large part from partial melting of felsic Proterozoic hydrous lower crust (e.g., Stein and Crock, 1990). The volumetrically minor mafic pumices in the tuff (57 wt% SiO_2) and mafic enclaves in the plutons could have been derived from small-scale compositional heterogeneities in the source, such as metasomatized amphibolite (e.g., Rapp and

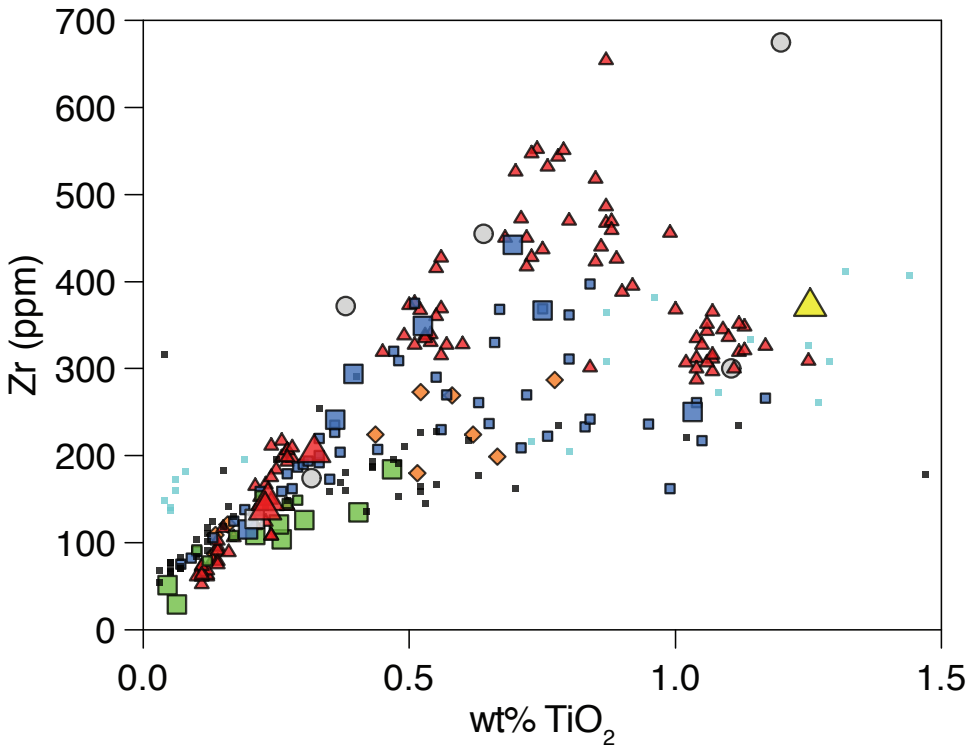

Figure 10. Plot of Zr-TiO_2 data for samples from this study (large symbols) and Cenozoic igneous rocks of Colorado. Data for the resurgent plutons fill in compositional gaps between pumice fiamme groups, suggesting the possibility that the plutons represent mixtures of unerupted Grizzly Peak magmas. However, Nd isotopic data for the plutons are less radiogenic than the tuff, making a mixing hypothesis untenable. Symbols and data sources as in Figure 3. Large amount of additional literature data for Grizzly Peak Tuff (small red triangles) due to inclusion of pressed powder X-ray fluorescence analyses of Fridrich (1987). Data presentation after Fridrich (1987) and Fridrich and Mahood (1987).

Wilson, 1995). A lower crustal source is supported by the high Th/U contents of in tuff and resurgent pluton whole rocks and zircons dated here (Fig. 5; Table 5). In addition, the source must have been ancient and felsic in order to generate high $^{40}Ca/^{44}Ca$ ratios (Mills et al., 2013). This model benefits from being simpler than calling upon coupled assimilation-fractional crystallization of primitive basalts, followed by a second stage of assimilation and fractional crystallization in the upper crust to generate the observed compositions (Johnson and Fridrich, 1990). In addition, partial melting can produce variable isotopic compositions such as those observed within the tuff and resurgent plutons (Figs. 7, 8; Stevens et al., 2007; Clemens et al., 2011; Villaros et al., 2012).

Relationships to the Colorado Mineral Belt

The Grizzly Peak Tuff represents an excursion in Sr and Nd isotopic compositions relative to the Colorado Mineral Belt and other rocks from the central Colorado volcanic field, including the Thirtynine Mile and San Juan volcanic fields, and Rio Grande rift magmatism (Fig. 11). Neodymium isotopic data for the tuff are distinctly unradiogenic compared to the dataset except for two much younger samples from the southern mineral belt (Stein and Crock, 1990). Strontium isotopic data for the tuff are relatively evolved, but are exceeded by a few mineral belt plutons (Simmons and Hedge, 1978; Stein and Crock, 1990), and the Never Summer Mountains outside the mineral belt (Jacob et al., 2015). In contrast, there is no distinction between the Grizzly Peak Tuff and other Cenozoic igneous rocks from Colorado in Pb isotopic compositions, including thorogenic Pb, which are similar to other central mineral belt rocks (Stein, 1985; Fig. 11).

Although temporal and spatial isotopic trends have been recognized in the Colorado Mineral Belt (Stein, 1985; Stein and Crock, 1990; Chapin, 2012), the long magmatic history of the central part of the mineral belt appears to be characterized by relatively stable isotopic compositions if the Grizzly Peak Tuff is considered an anomalous crustal melting event. For example, all Sr isotopic data from the 63-39 Ma Twin Lakes pluton, the ~38 Ma granitic xenolith in Grizzly Peak caldera, and the ~24.5 Ma mafic tuff in the Arkansas River Valley fall in the range $^{87}Sr/^{86}Sr_i$ = 0.7061 to 0.7072. Limited Nd isotopic data for the same rocks fall in the range εNd_i = -5 to -10; although the radiogenic end of the range in Sr data is anchored by just one sample (Farmer and DePaolo, 1984). Cenozoic rocks in the nearby Mount Princeton magmatic center have similar isotopic compositions (Figs. 7, 8; Mills, 2012). The data suggest a common source(s) was tapped continually over Cenozoic time in the central Colorado Mineral Belt, occasionally punc-

tuated by eruption of voluminous, isotopically anomalous tuffs (Grizzly Peak and Wall Mountain) that are rich in ancient crustal components (Johnson and Fridrich, 1990; Mills, 2012; Mills et al., 2013; this study).

In contrast to the relatively persistent Sr (and Nd?) isotopic compositions over time in the central mineral belt, Pb isotopic data in the central mineral belt show temporal trends, particularly in $^{206}Pb/^{204}Pb_i$. Stein (1985) attributed the broad decrease in uranogenic Pb ratios with time to

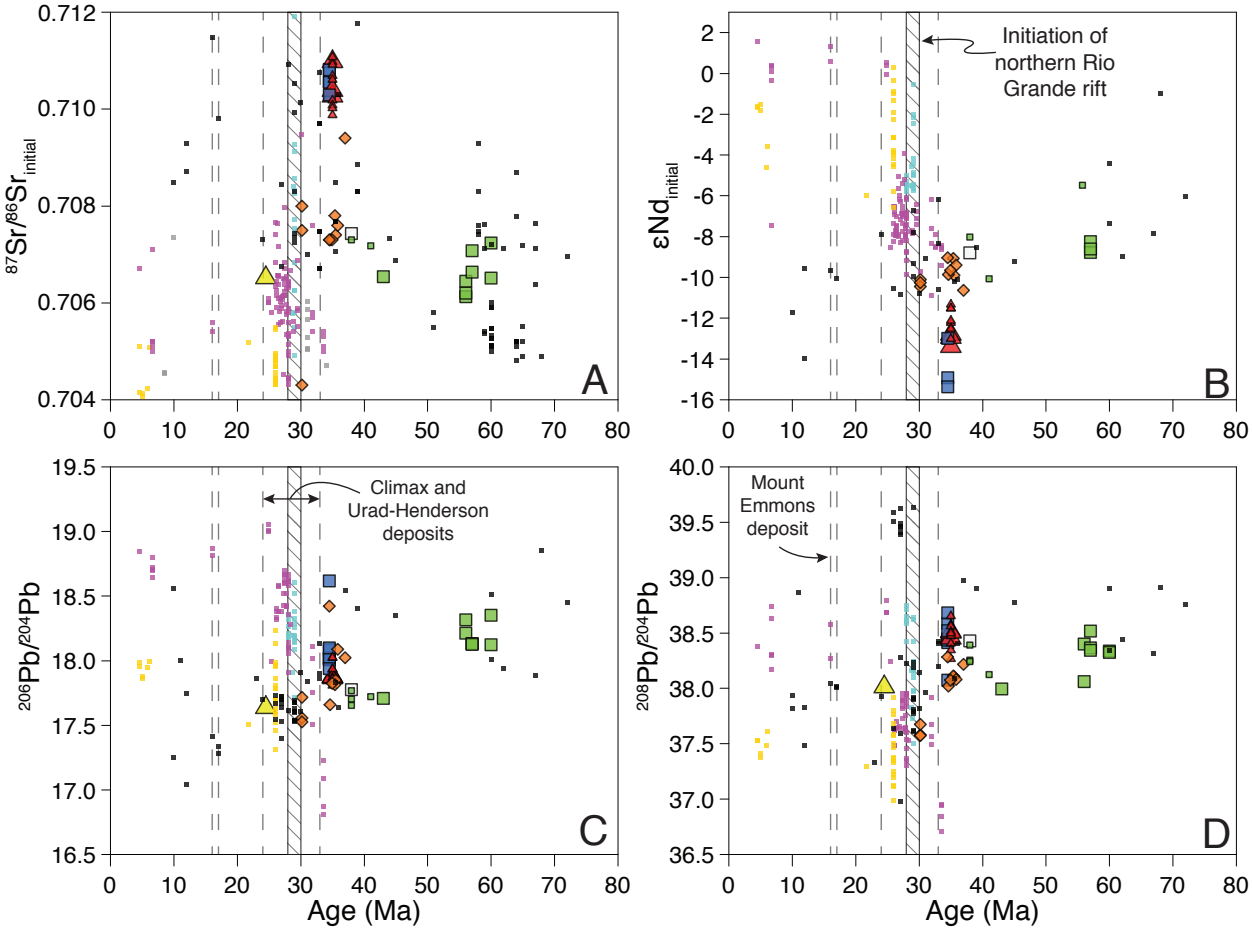

Figure 11. Diagrams showing variations through time in Colorado igneous rocks for (A) $^{87}Sr/^{86}Sr_i$; (B) εNd_i; (C) $^{206}Pb/^{204}Pb$; (D) $^{208}Pb/^{204}Pb$. Grizzly Peak Tuff and resurgent plutons are distinct in Sr and Nd isotopic compositions (panels A and B). Secular trends in Colorado Mineral Belt data are apparent in all plots except (D) $^{208}Pb/^{204}Pb$. Mineral belt rocks have more radiogenic Sr, and less radiogenic Nd and $^{206}Pb/^{204}Pb$ through time. In the central Colorado Mineral Belt, there are no apparent trends in the Sr or Nd data (excluding the Grizzly Peak magmatic center), whereas uranogenic Pb mirrors trends in the mineral belt as a whole towards less radiogenic compositions, including Grizzly Peak data. Data symbols and sources as in Figures 3, 7, and 8. Colorado Mineral Belt dataset (small black squares) also includes data of Simmons and Hedge (1978). Ages of Mo deposits from Bookstrom et al. (1988), Stein and Crock (1990), and Shannon et al. (2004). Timing of northern Rio Grande rift initiation from Zimmerer and McIntosh (2004), Mills and Coleman (2013), and Ricketts et al. (2016).

the spatial distribution of mineral belt magmatism, as the youngest rocks are in the southwest and have the lowest $^{206}Pb/^{204}Pb_i$ ratios. Stein (1985) suggested the regional trend may be due to spatial compositional variability in a lower crustal source, or due to different melting depths. In contrast, the data presented here show that $^{206}Pb/^{204}Pb_i$ ratios may also vary secularly in a relatively restricted area (Fig. 11), as in the Twin Lakes pluton. These data suggest that early magmatism in the central Colorado Mineral Belt preferentially tapped sources with high U/Pb ratios, whereas lower U/Pb source(s) predominated later, although it is not clear why such a change occurred.

The relatively consistent Sr data coupled with the systematic changes in uranogenic Pb ratios through time in the central Colorado Mineral Belt (Grizzly Peak and Wall Mountain tuffs excepted) may be explained by several scenarios: 1) primitive mantle is the primary control on isotopic composition of the rocks, with assimilation-fractional crystallization producing the consistent Sr isotopic compositions. Lead isotopic compositions are controlled by the lower crust due to its much higher Pb contents relative to mantle melts (Johnson and Fridrich, 1990; Johnson, 1991). 2) Rocks are derived from metasomatized, relatively mafic lower crust of varying composition, with perhaps some metasomatized mantle playing a role (Stein and Crock, 1990; Jacob et al., 2015). 3) Isotopic compositions are largely controlled by enriched subcontinental lithospheric mantle (Coleman et al., 1992). The first scenario is probably least likely in the central part of the mineral belt, because it requires similar compositions and amounts of assimilant to be incorporated into primitive basalts, which must then differentiate to a similar degree repeatedly over a nearly 40 Ma interval. Production of isotopically homogeneous granitoids after assimilating isotopically heterogeneous Proterozoic rocks would be fortuitous.

The data cannot distinguish between the latter two models. Although the Grizzly Peak Tuff may have been derived from metasomatized felsic lower crust, that does not preclude other

rocks in the area from being derived from mafic lower crust as well (Stein, 1985; Stein and Crock, 1990). Indeed, the lower crust in Colorado is inferred to be isotopically heterogeneous (Lake and Farmer, 2015). If such heterogeneity existed vertically and laterally, derivation of most central Colorado Mineral Belt rocks by anatexis of lower crust is plausible, provided there was a sufficient volume of source rocks with the appropriate compositions. The possibility of an enriched lithospheric mantle source for the central part of the mineral belt is also intriguing because the lithospheric mantle is inferred to also be laterally heterogeneous. Enriched mantle under some parts of the Rocky Mountains reaches $^{87}Sr/^{86}Sr_i = 0.705$, $\varepsilon Nd_i = -5$, and $^{206}Pb/^{204}Pb_i = 20.0$ (Roden et al., 1990; Bailley, 2010; Gonzales et al., 2010). The simplest scenario in the central mineral belt would involve a parcel of enriched subcontinental lithospheric mantle with isotopic characteristics similar to those analyzed here ($^{87}Sr/^{86}Sr_i = 0.706$, $\varepsilon Nd_i = -8$, and $^{206}Pb/^{204}Pb_i = 17.6$). It is also possible that some combination of enriched lithospheric mantle and metasomatized mafic Proterozoic lower crust served as the source(s) for most of the Twin Lakes Granodiorite and other igneous rocks in this area (e.g., Stein and Crock, 1990).

Why is there not a large Mo deposit at Grizzly Peak?

The location and composition of the Grizzly Peak magmatic system are enticing because of their apparent similarities to nearby Climax-type deposits, including Climax, Urad-Henderson, and Mount Emmons (Fig. 1; Ludington and Plumlee, 1999). Numerous mining claims and workings for Mo, Au, Pb, Zn, and other metals in and around the caldera attest to the appeal of the Grizzly Peak magmatic system's economic potential (Wilson and Sims, 2003; Mineral Resources Data System, USGS, 2005). The existing geochemical dataset for the Grizzly Peak caldera (Fig. 4; Table 2; Fridrich, 1987) also appears similar to Climax-type deposits in most respects except,

critically, it lacks concentrated Mo. The 38 Ma granitic xenolith and some resurgent pluton samples analyzed here have Mo concentrations up to 9 ppm, or ~10 times the continental crust average (0.8 ppm; Rudnick and Gao, 2003), but samples of bulk Grizzly Peak Tuff have Mo below the detection limit (<2 ppm), and Fridrich (1987) did not analyze pumice fiamme for Mo.

One explanation for the lack of concentrated Mo assumes the magmatic system had a similar genesis to other Climax-type Mo systems, particularly the Questa deposit that was preceded by a 500 km^3 rhyolitic tuff (Tappa et al., 2011; Zimmerer and McIntosh, 2012). If that was the case, it is possible that the current level of exposure in the Grizzly Peak system does not permit observation of deeper high-grade ore zones, which are typically restricted to 100-200 m of mineralizing intrusions (Ludington and Plumlee, 2009). Such a lack of exposure could be due to the preservation of intracaldera Grizzly Peak Tuff, or because the caldera has not been disrupted and tilted like the Questa magmatic system (Johnson et al., 1989; Rosera et al., 2013). Another possibility is that the Grizzly Peak system was not permitted to concentrate Mo, whether through low degree partial melting (Rosera et al., 2013) or extensive fractional crystallization (Johnson et al., 1989; von Quadt et al., 2011), and therefore Mo is "diluted" in the tuff and resurgent plutons. However, because Mo behaves incompatibly in silicate systems (Candela and Holland, 1986), both partial melting and fractional crystallization would be expected to concentrate Mo above crustal averages in the silicic rocks of the Grizzly Peak magmatic system, which is not observed.

Another explanation for the lack of exposed, concentrated Mo in the Grizzly Peak magmatic system is that despite its size and location, its timing did not allow it to produce significant Mo-rich fluids. Climax-type deposits are associated with extensional environments that may permit thermal and/or chemical interaction with the underlying mantle (Stein and Crock, 1990; Ludington and Plumlee, 2009; Chapin, 2012), and the Grizzly Peak system predates Rio Grande

rift extension (Ricketts et al., 2016). However, the nearby Climax deposit began developing during "tectonic relaxation" ca. 33 Ma, and thus a similar tectonic regime should also apply to the Grizzly Peak system (Bookstrom et al., 1988).

The distinct isotopic compositions of the Grizzly Peak Tuff and the resurgent plutons suggest source characteristics may be an important factor (Figs. 7, 11). Past isotopic surveys of the Colorado Mineral Belt sought out rocks associated with ores and important mining or prospecting activity (Stein, 1985; Stein and Crock, 1990). Therefore, the lack of Colorado Mineral Belt rocks with similar Nd and Sr isotopic compositions to the Grizzly Peak system is significant and suggests that source rocks with those isotopic compositions are not economically important. Since the isotopic compositions of the Grizzly Peak Tuff and its resurgent plutons are interpreted to have been inherited from a felsic Proterozoic lower crustal source, it suggests that felsic lower crust in this part of the mineral belt was not an important source of Mo. This is in contrast to proposals for derivation of Mo-rich deposits by anatexis of felsic lower crust elsewhere in the mineral belt (Stein and Crock, 1990). Some recent models that call for hybridized lower crust as the source Mo may offer an explanation (Richards, 2009, 2011; Rosera et al., 2013). Rosera et al. (2013) suggested that high-flux mantle inputs to the lower crust in the Questa magmatic system in northern New Mexico (Fig. 1) generated the 500 km^3 Amalia Tuff and also constructed a hybridized lower crust rich in mantle-derived volatiles and metals such as Mo. Subsequent partial melting of the volatile-rich hybridized crust scavenged those metals and concentrated them in small volume, high-silica magmas that yielded a Climax-type porphyry system upon crystallization (Rosera et al., 2013). Indeed, the Sr and Nd isotopic compositions of mineralizing intrusions at Questa are more juvenile than the Amalia Tuff or earlier magmatism (Gaynor et al., 2015). However, there is no exposed evidence for a juvenile isotopic component after eruption of the

Grizzly Peak Tuff (Fig. 11). This suggests the Grizzly Peak magmatic system was either derived by mechanisms that did not generate a volatile-hybridized lower crust, or volatile-hybridized lower crust was generated but was not incorporated into the exposed Grizzly Peak magmatic system.

CONCLUSIONS

New isotopic and geochemical data in the central Colorado Mineral Belt demonstrate: 1) a Proterozoic metasedimentary gneiss adjacent to the Grizzly Peak caldera has Pb (and possibly other isotopic components) similar to the those found in the Archean Wyoming Province; 2) Cenozoic rocks adjacent to the Grizzly Peak caldera record broadly consistent Sr and Nd isotopic compositions over a 40 Ma period that spans the eruption of the Grizzly Peak Tuff; 3) the Grizzly Peak Tuff and its resurgent plutons are chemically and isotopically distinct relative to nearby Cenozoic igneous rocks including the Twin Lakes pluton, a granitic xenolith ~3 Ma older than the tuff, and an Oligocene mafic tuff exposed 20 km away in the Arkansas River Valley. The radiogenic Sr and highly unradiogenic Nd isotopic compositions of the Grizzly Peak Tuff and resurgent plutons, coupled with trace element indicators such as high Th/U, suggest they may have been generated by anatexis of Proterozoic lower crust. The resurgent plutons have slightly more enriched Sr, Nd, and Pb isotopic compositions than the tuff, precluding a complementary relationship between the two; the data imply compositional heterogeneities were inherited from the source. Preliminary zircon U-Pb geochronology on the tuff and reinterpretation of high-quality $^{40}Ar/^{39}Ar$ data suggest the Grizzly Peak Tuff erupted ca. 35 Ma; additional U-Pb zircon data suggest the resurgent plutons were emplaced shortly after eruption. We infer the broadly similar isotopic compositions present in the Cenozoic rocks of the central Colorado Mineral Belt to be

derived from a different lower crustal source(s) than the Grizzly Peak Tuff, or from enriched subcontinental lithospheric mantle. The lack of Mo enrichment in the Grizzly Peak Tuff and its resurgent plutons, despite their compositions and location in the mineral belt, suggests either that Mo-rich deposits are not exposed, or that the isotopically-enriched lower crustal source was not an important source of Mo.

TABLE 1. SUMMARY OF SAMPLES FROM CENTRAL COLORADO MINERAL BELT

Sample	Map unit	Description	Age	Age source	UTM-E*	UTM-N*	IGSN†
TL15-05	Tt	Twin Lakes pluton	57	1	368022	4323340	P4700001J
MB15-06	Tm	Twin Lakes megabreccia	57	1	367990	4323299	P4700001K
MB15-07	Tm	Twin Lakes megabreccia	57	1	367994	4323253	P4700001L
GU15-08	Tg	Upper Grizzly Peak Tuff	35	2	363360	4329185	P4700001M
XE15-09	Tg	Granodiorite xenolith in tuff	pЄ?	2	363360	4329185	P4700001N
GM15-17	Tg	Middle Grizzly Peak Tuff	35	2	360802	4320610	P4700001V
PR15-18	Tp	Granite xenolith in resurgent pluton	38	2	360898	4320589	P4700001W
GM15-20	Tgm	Middle Grizzly Peak Tuff	35	2	361190	4320835	P4700001Y
P215-21	Tr2	Intermediate age resurgent pluton	34.5	2	360216	4325534	P4700001Z
P115-22	Tr1	Oldest resurgent pluton	34.5	2	360634	4326478	P47000020
P115-23	Tr1	Oldest resurgent pluton	34.5	2	360629	4326480	P47000021
PG15-25	Xms	Metasedimentary gneiss	pЄ	3	356140	4328593	P47000023
GG15-26	Yg	Grottos pluton	pЄ	3	354416	4330144	P47000024
SK15-27	Ys	St. Kevin Granite	pЄ	3	367129	4321084	P47000025
DC15-28	Xdc	Leucocratic Denny Creek pluton	pЄ	3	366809	4326996	P47000026
OT15-29	Tav	Mafic tuff in Arkansas River valley	24.5	2	385541	4324606	P47000027
TL16-10	Tt	Twin Lakes pluton	60	1	369277	4325526	P4700002G
TL16-10d	Tt	Aplite in Twin Lakes pluton	60	1	369277	4325526	P4700002H
TL16-12	Tt	Twin Lakes pluton	43	1	373395	4325775	P4700002K
TL16-15	Tt	Twin Lakes pluton	56	1	378796	4324886	P4700002N
TL16-15d	Tt	Aplite in Twin Lakes pluton	56	1	378796	4324886	P4700002O
TL16-15m	Tt	Modally layered Twin Lakes pluton	56	1	378796	4324886	P4700002P
GP-06	Tr2	Intermediate age resurgent pluton	34.5	2	360334	4324228	
GP-07	Tr1	Oldest resurgent pluton	34.5	2	360125	4326646	
GP-08	Tr1	Oldest resurgent pluton	34.5	2	360125	4326646	
GP-11	Tr2	Intermediate age resurgent pluton	34.5	2	358220	4327733	

Note: Ages for Cenozoic samples given in Ma. Age sources are: 1 – Feldman (2010); 2 – this study; 3 – Fridrich et al. (1998). Ages for Twin Lakes samples are estimates based on proximity to dated samples of Feldman (2010). Ages for Grizzly Peak Tuff and resurgent pluton samples dated in this study are applied to non-dated samples of those same units

*UTM coordinates for samples in NAD 83 datum, zone 13S

†IGSN – International Geo Sample Number. Additional sample metadata available at www.geosamples.org. Samples GP-06 through GP-11 are courtesy of M. Zimmerer

TABLE 2. MAJOR AND TRACE ELEMENT ANALYSES

Sample	TL15-05	MB15-06	MB15-07	GU15-08	XE15-09	GM15-17	PR15-18	GM15-20	P215-21
Description	Twin Lakes pluton	(Twin Lakes) Mbreccia	(Twin Lakes) Mbreccia	Upper GPT	Grano-diorite xenolith	Middle GPT	Xeno. in resurgent pluton	Middle GPT	Middle resurgent pluton
Major element analyses* by ICP-OES									
SiO_2	67.14	71.46	64.83	72.98	68.00	68.84	70.96	70.47	61.47
Al_2O_3	15.76	13.66	15.94	13.88	15.01	14.77	14.64	14.02	17.2
Fe_2O_3	3.11	2.66	5.24	1.91	3.52	3.02	2.53	2.2	5.53
MnO	0.095	0.055	0.132	0.026	0.038	0.050	0.053	0.058	0.073
MgO	0.65	0.18	1.01	0.35	1.19	0.58	0.40	0.34	1.51
CaO	2.65	2.45	3.74	1.31	1.95	2.32	1.86	1.52	4.43
Na_2O	3.77	4.45	4.44	2.95	2.67	3.35	3.87	3.38	3.43
K_2O	4.27	1.52	1.62	4.59	5.43	4.34	4.31	4.44	2.89
TiO_2	0.303	0.21	0.467	0.234	0.64	0.321	0.209	0.229	0.695
P_2O_5	0.13	0.12	0.21	0.07	0.23	0.09	0.09	0.07	0.25
LOI	1.33	1.98	1.74	1.55	1.21	1.23	0.51	2.05	2.85
Total	99.21	98.74	99.38	99.85	99.91	98.90	99.43	98.78	100.30
Trace element analyses† by ICP-OES									
Sc	4	3	6	5	12	6	3	5	9
Be	1	2	2	1	3	1	2	2	1
V	31	23	54	14	56	23	19	15	69
Ba	1748	258	238	1561	2178	1425	679	1012	1423
Sr	983	628	805	337	427	504	385	283	866
Y	19	12	28	19	15	19	10	24	20
Zr	126	109	184	151	455	206	127	140	442
Trace element analyses† by ICP-MS									
Cr	190	30	170	20	190	20	210	20	90
Co	4	3	6	2	6	3	3	2	8
Ni	BDL	BDL	BDL	BDL	20	BDL	BDL	BDL	BDL
Cu	10	BDL	50	BDL	20	BDL	10	BDL	20
Zn	70	50	120	50	60	80	50	100	80
Ga	21	18	25	16	19	18	20	17	21
Ge	2	1	2	1	1	1	1	1	1
Rb	87	42	42	116	170	93	138	124	71
Nb	10	6	13	8	8	8	11	9	8
Mo	3	BDL	3	BDL	3	BDL	4	BDL	9
Ag	BDL	BDL	BDL	BDL	1.3	BDL	BDL	BDL	BDL
Sn	2	1	2	1	2	1	2	1	2
Sb	0.7	0.6	0.6	0.7	0.7	0.6	0.6	0.7	BDL
Cs	1.2	1.8	1.3	3.6	5.7	2.8	1.3	2.7	2.1
La	27.2	17.3	63.9	55.5	30.1	72.1	24.7	56.6	82.6
Ce	52.9	33.3	116.0	95.7	55.9	132.0	46.9	109.0	153.0
Pr	5.96	3.92	12.7	11.4	6.37	13.9	5.07	11.7	16.4
Nd	23.2	15.1	45.7	38.1	22.8	47.8	17.7	39.6	58.2
Sm	4.6	3.2	8.4	6.4	4.0	7.5	3.4	6.9	8.8
Eu	1.34	0.89	1.86	1.54	1.45	1.67	0.88	1.40	2.40
Gd	3.6	2.5	6.3	4.3	3.3	5.1	2.5	5.1	6.0
Tb	0.6	0.4	0.9	0.6	0.5	0.7	0.3	0.7	0.8
Dy	3.2	2.2	5.2	3.3	2.8	3.8	1.9	4.3	3.8
Ho	0.6	0.4	1.0	0.7	0.5	0.7	0.4	0.8	0.8
Er	1.9	1.2	2.9	2.0	1.4	2.0	1.0	2.3	2.2
Tm	0.30	0.20	0.44	0.30	0.20	0.31	0.16	0.36	0.34
Yb	2.0	1.4	3.0	2.0	1.3	1.9	1.2	2.4	2.3
Lu	0.34	0.23	0.48	0.32	0.21	0.31	0.18	0.39	0.36
Hf	3.2	3.0	4.8	4.1	10.2	5.2	3.5	3.9	9.5
Ta	1.1	0.8	1.5	0.9	0.7	0.8	1.3	1.1	0.4
W	2	2	2	2	3	2	2	3	4
Tl	0.4	0.2	0.2	0.5	0.7	0.5	0.6	0.8	0.4
Pb	34	17	24	23	27	49	41	57	20
Th	7.2	5.8	15.7	17.2	9.5	18.3	16.8	19.2	13.8
U	2.6	2.4	4.8	2.7	1.5	2.8	5.2	3.4	2.3

TABLE 2 (CONTINUED). MAJOR AND TRACE ELEMENT ANALYSES

Sample	P115-22	P115-23	PG15-25	GG15-26	SK15-27	DC15-28	OT15-29	TL16-10	TL16-10d
Description	Oldest resurgent pluton	Oldest resurgent pluton	Metased gneiss	Grottos pluton	St. Kevin Granite	Denny Creek pluton	Tuff in Ark. Valley	Twin Lakes pluton	Twin Lakes aplite
Major element analyses* by ICP-OES									
SiO_2	69.45	67.36	72.67	64.16	72.99	63.73	58.59	75.09	78.08
Al_2O_3	15.00	15.83	14.33	14.75	13.27	15.56	14.97	13.00	13.02
Fe_2O_3	2.23	3.13	3.45	6.47	2.89	8.03	7.88	2.49	0.60
MnO	0.022	0.073	0.034	0.073	0.034	0.085	0.086	0.069	0.017
MgO	0.38	0.70	0.47	1.45	0.16	1.99	1.17	0.68	0.05
CaO	0.60	3.02	0.72	2.45	0.56	3.53	5.48	2.74	1.39
Na_2O	3.48	3.56	1.54	3.06	1.95	3.18	3.36	3.28	5.19
K_2O	6.83	3.54	5.03	4.59	6.75	2.49	3.00	2.10	1.47
TiO_2	0.197	0.395	0.316	1.199	0.380	1.105	1.253	0.260	0.063
P_2O_5	0.05	0.14	0.32	0.54	0.06	0.20	0.86	0.06	BDL
LOI	0.63	2.26	1.29	0.87	1.23	0.85	2.14	0.67	0.39
Total	98.87	100	100.2	99.6	100.3	100.8	98.79	100.4	100.3
Trace element analyses† by ICP-OES									
Sc	2	6	5	8	5	22	13	3	2
Be	1	1	BDL	3	2	2	2	1	3
V	16	32	20	80	16	112	94	27	BDL
Ba	1199	1753	805	1385	992	413	1577	350	16
Sr	317	684	153	411	186	205	1127	756	62
Y	9	18	22	10	21	37	25	9	6
Zr	115	294	174	675	372	300	374	104	29
Trace element analyses† by ICP-MS									
Cr	30	100	30	190	30	230	80	BDL	BDL
Co	3	4	5	12	3	20	15	3	BDL
Ni	BDL	BDL	BDL	30	BDL	40	30	BDL	BDL
Cu	BDL	BDL	BDL	40	10	30	20	BDL	BDL
Zn	BDL	70	50	140	50	110	80	60	BDL
Ga	18	19	16	23	16	23	21	18	21
Ge	BDL	1	1	1	1	2	1	1	3
Rb	169	88	172	180	171	131	70	57	53
Nb	4	9	9	18	7	16	25	8	6
Mo	BDL	2	BDL	3	BDL	3	BDL	BDL	BDL
Ag	BDL	0.6	BDL	1.7	0.7	BDL	1.3	BDL	BDL
Sn	2	2	2	4	3	5	2	1	BDL
Sb	0.6	0.6	0.5	0.6	0.7	0.6	BDL	BDL	BDL
Cs	0.9	0.9	3.2	2.0	3.0	1.9	0.7	1.7	1.1
La	35.0	93.5	53.9	96.0	162.0	58.4	79.9	29.7	10.9
Ce	62.2	172.0	117.0	185.0	335.0	124.0	165.0	54.2	19.8
Pr	6.43	17.80	13.90	19.60	37.40	14.60	19.50	5.95	1.87
Nd	22.1	59.3	51.1	64.9	132.0	54.3	74.4	20.6	5.2
Sm	4.1	8.3	10.8	8.5	21.4	11.2	12.9	3.5	0.7
Eu	0.90	2.05	1.33	1.86	3.13	1.90	3.34	0.94	0.19
Gd	3.2	5.5	8.1	4.8	11.9	9.8	9.4	2.5	0.7
Tb	0.4	0.7	1.1	0.5	1.3	1.5	1.2	0.3	BDL
Dy	2.0	3.8	5.2	2.3	6.0	8.3	5.7	1.8	0.6
Ho	0.3	0.7	0.8	0.4	0.9	1.5	1.0	0.3	0.2
Er	0.9	2.0	1.9	1.0	2.1	3.8	2.6	1.1	0.7
Tm	0.12	0.31	0.26	0.15	0.24	0.44	0.35	0.16	0.14
Yb	0.7	2.0	1.5	1.1	1.4	2.5	2.1	1.1	1.4
Lu	0.11	0.32	0.20	0.22	0.20	0.36	0.33	0.19	0.32
Hf	3.2	7.3	4.5	14.8	9.4	7.9	8.5	2.7	1.5
Ta	0.5	0.7	0.9	1.1	0.7	1.0	1.3	0.5	0.4
W	3	2	2	3	2	2	BDL	1	BDL
Tl	0.7	0.4	0.7	0.9	0.8	0.5	BDL	0.2	0.1
Pb	38	21	41	23	31	16	11	20	44
Th	16.3	17.8	19.4	10.4	24.5	17.4	11.2	7.6	43.9
U	2.9	2.5	5.5	1.1	1.7	1.4	2.1	2.0	45.6

TABLE 2 (CONTINUED). MAJOR AND TRACE ELEMENT ANALYSES

Sample	TL16-12	TL16-15	TL16-15d	TL16-15m	GP-06	GP-07	GP-08	GP-11
Description	Twin Lakes pluton	Twin Lakes pluton	Twin Lakes aplite	Modally layered Twin Lakes	Middle resurgent pluton	Oldest resurgent pluton	Mafic enclave in GP-07	Middle resurgent pluton
Major element analyses* by ICP-OES								
SiO_2	68.58	68.73	77.11	48.47	60.8	67.94	55.56	64.76
Al_2O_3	16.06	15.78	12.85	11.53	17.48	15.78	16.63	16.57
Fe_2O_3	3.41	2.7	0.84	23.09	5.27	3.07	7.74	3.94
MnO	0.050	0.090	0.029	0.465	0.099	0.062	0.146	0.086
MgO	0.92	0.63	0.05	2.63	1.69	0.73	1.98	0.99
CaO	2.74	2.34	0.94	4.97	4.79	2.65	4.54	3.94
Na_2O	3.92	3.42	3.76	2.74	3.2	3.66	3.75	3.55
K_2O	3.4	5.26	4.08	1.90	2.86	3.19	2.24	3.09
TiO_2	0.404	0.255	0.045	1.638	0.751	0.361	1.033	0.525
P_2O_5	0.15	0.13	BDL	0.43	0.26	0.13	0.33	0.18
LOI	0.37	0.3	0.2	2.49	2.41	1.06	4.74	2.67
Total	100.0	99.63	99.90	100.40	99.62	98.64	98.70	100.30
Trace element analyses† by ICP-OES								
Sc	4	4	2	23	10	6	18	8
Be	2	1	2	2	1	1	1	1
V	47	37	7	400	74	30	158	46
Ba	866	2048	26	232	1755	1923	918	1809
Sr	723	1155	62	566	867	772	634	794
Y	11	14	19	76	20	15	20	18
Zr	135	121	51	677	367	241	250	349
Trace element analyses† by ICP-MS								
Cr	BDL	BDL	BDL	30	BDL	BDL	30	BDL
Co	6	3	BDL	22	9	4	18	5
Ni	BDL	BDL	BDL	BDL	BDL	BDL	BDL	BDL
Cu	BDL	BDL	BDL	BDL	20	BDL	30	BDL
Zn	50	50	BDL	390	80	50	120	70
Ga	21	20	20	41	21	18	24	20
Ge	1	2	2	3	1	1	1	1
Rb	85	127	123	115	72	74	61	82
Nb	13	13	16	61	9	7	10	9
Mo	BDL	BDL	BDL	BDL	BDL	BDL	BDL	BDL
Ag	BDL	BDL	BDL	2.5	1.2	0.9	0.9	1.2
Sn	2	2	1	7	1	2	12	1
Sb	BDL	BDL	BDL	BDL	BDL	BDL	BDL	BDL
Cs	1.2	3.2	2.2	11.4	0.8	1.1	2.5	1.3
La	37.4	33.5	5.8	328.0	94.3	83.0	56.9	106.0
Ce	69.9	61.6	13.9	572	172	151	111	193
Pr	7.92	6.73	1.94	59.0	18.4	15.8	12.7	20.1
Nd	28.9	24.5	8.4	198.0	64.8	53.9	46.2	67.9
Sm	5.1	4.4	2.8	29.4	9.2	7.5	7.9	9.2
Eu	1.29	1.07	0.32	5.39	2.41	2.08	2.18	2.31
Gd	3.8	3.2	3.2	19.9	6.4	5.0	6.0	5.9
Tb	0.5	0.4	0.6	2.5	0.8	0.6	0.8	0.7
Dy	2.4	2.5	3.6	14.3	4.3	3.0	4.4	3.9
Ho	0.4	0.5	0.7	2.7	0.8	0.5	0.8	0.7
Er	1.2	1.5	2.1	8.1	2.2	1.6	2.4	2.1
Tm	0.17	0.23	0.33	1.20	0.33	0.24	0.34	0.31
Yb	1.1	1.7	2.2	8.7	2.2	1.6	2.3	1.9
Lu	0.16	0.29	0.36	1.38	0.35	0.24	0.35	0.33
Hf	3.9	3.6	2.4	19.0	8.9	6.2	6.2	8.5
Ta	1.0	0.9	1.2	3.9	0.5	0.5	0.5	0.5
W	BDL	1	BDL	3	BDL	1	BDL	BDL
Tl	0.2	0.5	0.5	0.6	0.3	0.3	0.2	0.2
Pb	17	33	52	23	14	35	12	18
Th	12.4	10.1	11.8	83.8	15.3	14.2	10.4	17.5
U	3.3	4.1	19.5	11.3	2.2	1.9	2.2	2.4

Note: LOI – loss on ignition; BDL – below detection limit; Mbreccia – megabreccia; GPT – Grizzly Peak Tuff; Xeno. – xenolith; Metased – metasedimentary; Ark. – Arkansas

*Major element data in wt%

†Trace element data in ppm

TABLE 3. SR AND ND ISOTOPIC ANALYSES

Sample	Age (Ma)	Rb ppm	Sr ppm	$^{87}Rb/^{86}Sr$	$^{87}Sr/^{86}Sr$	± 2σ abs*	$^{87}Sr/^{86}Sr_t$	Sm ppm	Nd ppm	$^{147}Sm/^{144}Nd$	$^{143}Nd/^{144}Nd$	± 2σ abs*	$^{143}Nd/^{144}Nd_i$	εNd_t
TL15-05	57	87	983	0.256	0.706840	0.000011	0.706633	4.6	23.2	0.1200	0.512186	0.000004	0.512142	-8.25
MB15-06	57	42	628	0.193	0.707237	0.000010	0.707080	3.2	15.1	0.1281	0.512162	0.000003	0.512115	-8.78
MB15-07	57							8.4	45.7	0.1111	0.512165	0.000004	0.512124	-8.60
GU15-08	35	116	337	0.996	0.711501	0.000010	0.711006	6.4	38.1	0.1016	0.511933	0.000004	0.511910	-13.32
XE15-09†	35	170	427	1.154	0.724901	0.000009	0.724327	4.0	22.8	0.1061	0.511748	0.000003	0.511724	-16.95
GM15-17	35	93	504	0.534	0.710564	0.000010	0.710299	7.5	47.8	0.0949	0.511963	0.000004	0.511941	-12.72
PR15-18	38	138	385	1.037	0.707989	0.000011	0.707429	3.4	17.7	0.1161	0.512168	0.000003	0.512139	-8.79
GM15-20	35	124	283	1.268	0.711046	0.000010	0.710416	6.9	39.6	0.1054	0.511958	0.000004	0.511935	-12.87
P215-21	34.5	71	866	0.237	0.710926	0.000010	0.710810	8.8	58.2	0.0914	0.511948	0.000003	0.511928	-12.99
P115-22	34.5	169	317	1.546	0.732528	0.000010	0.731770	4.1	22.1	0.1122	0.511854	0.000004	0.511829	-14.92
P115-23	34.5	88	684	0.372	0.710473	0.000010	0.710291	8.3	59.3	0.0846	0.511825	0.000004	0.511806	-15.37
PG15-25†	35	172	153	3.277	0.784155	0.000009	0.782526	10.8	51.1	0.1278	0.511802	0.000004	0.511773	-16.00
GG15-26†	35	180	411	1.270	0.729430	0.000012	0.728799	8.5	64.9	0.0792	0.511417	0.000003	0.511417	-23.30
SK15-27†	35	171	186	2.672	0.753408	0.000011	0.752080	21.4	132.0	0.0980	0.511604	0.000003	0.511582	-19.73
DC15-28†	35	131	205	1.856	0.744355	0.000009	0.743433	11.2	54.3	0.1247	0.511831	0.000004	0.511802	-15.43
OT15-29	24.5	70	1127	0.180	0.706610	0.000011	0.706547							
TL16-10	60	57	756	0.218	0.706695	0.000008	0.706509							
TL16-10d	60	53	62	2.474	0.709345	0.000011	0.707236							
TL16-12	43	85	723	0.340	0.706747	0.000008	0.706539							
TL16-15	56	127	1155	0.318	0.706382	0.000008	0.706129							
TL16-15d	56	123	62	5.742	0.711015	0.000010	0.706447							
TL16-15m	56	115	566	0.588	0.706666	0.000010	0.706198							
GP-06	34.5	72	867	0.240	0.710937	0.000010	0.710819							
GP-07	34.5	74	772	0.277	0.709837	0.000011	0.709701							
GP-08	34.5	61	634	0.278	0.710693	0.000010	0.710557							
GP-11	34.5	82	794	0.299	0.710696	0.000009	0.710550							

Note: Subscript "t" indicates $^{87}Sr/^{86}Sr$ and εNd values corrected for radiogenic ingrowth since the listed age. All ages are interpreted as approximate crystallization or eruption ages except where noted

*Analytical uncertainty only. See text for reproducibility of standards

†Sample interpreted as Proterozoic; isotopic values corrected to Grizzly Peak Tuff eruption at 35 Ma

TABLE 4. PB ISOTOPIC ANALYSES

Sample	Age (Ma)	U ppm	Th ppm	Pb ppm	$^{206}Pb/^{204}Pb$	2σ (abs.)*	$^{207}Pb/^{204}Pb$	2σ (abs.)*	$^{208}Pb/^{204}Pb$	2σ (abs.)*	$^{206}Pb/^{204}Pb_t$	$^{207}Pb/^{204}Pb_t$	$^{208}Pb/^{204}Pb_t$
TL15-05	57	2.6	7.2	34	18.175	0.010	15.590	0.008	38.558	0.022	18.132	15.588	38.519
MB15-06	57	2.4	5.8	17	18.212	0.010	15.589	0.008	38.430	0.019	18.133	15.586	38.367
MB15-07	57	4.8	15.7	24	18.237	0.009	15.586	0.008	38.466	0.020	18.125	15.581	38.345
GU15-08	35	2.7	17.2	23	17.928	0.012	15.563	0.012	38.550	0.037	17.887	15.562	38.466
XE15-09†	35	1.5	9.5	27	16.907	0.011	15.458	0.012	37.041	0.035	16.889	15.457	37.003
GM15-17	35	2.8	18.3	49	17.900	0.010	15.560	0.009	38.568	0.025	17.880	15.560	38.526
PR15-18	38	5.2	16.8	41	17.822	0.014	15.553	0.012	38.478	0.032	17.775	15.551	38.428
GM15-20	35	3.4	19.2	57	17.907	0.016	15.573	0.016	38.560	0.043	17.886	15.572	38.522
P215-21	34.5	2.3	13.8	20	18.137	0.018	15.601	0.015	38.789	0.034	18.098	15.599	38.681
P115-22	34.5	2.9	16.3	38	18.643	0.007	15.621	0.006	38.123	0.014	18.617	15.620	38.075
P115-23	34.5	2.5	17.8	21	17.978	0.015	15.570	0.014	38.616	0.034	17.938	15.567	38.522
PG15-25†	35	5.5	19.4	41	18.833	0.095	15.980	0.080	39.212	0.208	18.786	15.977	39.157
GG15-26†	35	1.1	10.4	23	16.994	0.011	15.492	0.011	37.272	0.027	16.978	15.491	37.222
SK15-27†	35	1.7	24.5	31	17.006	0.015	15.476	0.013	39.065	0.031	16.987	15.475	38.976
DC15-28†	35	1.4	17.4	16	17.540	0.014	15.526	0.012	43.266	0.032	17.508	15.525	43.136
OT15-29	24.5	2.1	11.2	11	17.693	0.008	15.512	0.007	38.108	0.018	17.647	15.510	38.028
TL16-10§	60	2.0	7.6	20	18.183	0.008	15.581	0.007	38.410	0.018	18.123	15.578	38.337
TL16-10d§	60	45.6	43.9	44	18.972	0.008	15.614	0.008	38.521	0.018	18.351	15.584	38.325
TL16-12§	43	3.3	12.4	17	17.790	0.008	15.527	0.008	38.097	0.022	17.708	15.523	37.996
TL16-15§	56	4.1	10.1	33	18.386	0.009	15.582	0.009	38.458	0.023	18.317	15.579	38.402
TL16-15d§	56	19.5	11.8	52	18.421	0.006	15.574	0.005	38.102	0.011	18.214	15.564	38.061
TL16-15m§	56	11.3	83.8	23	18.424	0.003	15.578	0.003	38.599	0.011	18.152	15.566	37.935
GP-06§	34.5	2.2	15.3	14	18.140	0.008	15.568	0.007	38.710	0.018	18.086	15.565	38.588
GP-07§	34.5	1.9	14.2	35	18.024	0.009	15.551	0.009	38.492	0.022	18.006	15.550	38.447
GP-08§	34.5	2.2	10.4	12	18.077	0.010	15.563	0.009	38.508	0.023	18.015	15.560	38.412
GP-11§	34.5	2.4	17.5	18	18.066	0.012	15.556	0.012	38.544	0.037	18.020	15.553	38.436

Note: Measured isotopic ratios corrected for fractionation using a value of 0.165%/amu except where noted. Subscript "t" indicates Pb ratio corrected for radiogenic ingrowth since the listed age. All ages are interpreted as crystallization or eruption ages except where noted

*Analytical uncertainty only

†Sample interpreted as Proterozoic; isotopic values corrected to Grizzly Peak Tuff eruption at 35 Ma

§Measured isotopic ratios corrected for fractionation using a value of 0.15%/amu. See text for explanation

TABLE 5. U-PB ZIRCON ANALYSES FOR SELECTED SAMPLES OF GRIZZLY PEAK TUFF, RESURGENT PLUTONS, AND TUFF IN ARKANSAS RIVER VALLEY

	Composition				Isotopic Ratios							Ages (Ma)						
Fraction	U (ppm)	Pb (pg)[a]	Th/U[b]	Total common Pb (pg)[c]	$^{206}Pb/^{204}Pb$[d]	$^{206}Pb/^{238}U$[e]	Error (2σ%)	$^{207}Pb/^{235}U$[e]	Error (2σ%)	$^{207}Pb/^{206}Pb$[e]	Error (2σ%)	$^{206}Pb/^{238}U$[fg]	Error (2σ abs.)	$^{207}Pb/^{235}U$[g]	Error (2σ abs.)	$^{207}Pb/^{206}Pb$[g]	Error (2σ abs.)	Corr. coef.
PR15-18, Granite xenolith in post-resurgent pluton. Sector 54																		
F-1		36	0.58	1.1	1961	0.005896	0.13	0.03776	1.1	0.04647	1.0	37.985	0.050	37.63	0.42	21	25	0.746
F-3		40	0.33	3.0	884	0.005904	0.22	0.03742	1.8	0.04598	1.7	38.046	0.083	37.30	0.67	-4	40	0.767
F-5		62	0.27	2.3	1748	0.069936	0.13	0.8355	0.57	0.08669	0.53	435.87	0.54	616.7	2.7	1353	10	0.445
GM15-20, Middle subunit Grizzly Peak Tuff. Phoenix X62																		
F-3		5	1.2	1.5	171	0.005439	0.43	0.0353	8.3	0.0470	7.9	35.05	0.15	35.2	2.8	50	190	0.800
P215-21, Intermediate age resurgent pluton. Sector 54																		
F-1		8	1.47	1.9	218	0.005340	0.30	0.0289	7.0	0.0393	6.7	34.42	0.10	28.9	2.0	-400	170	0.847
F-3		7	1.13	1.8	214	0.005347	0.48	0.0294	8.1	0.0398	7.7	34.46	0.16	29.4	2.4	-363	200	0.901
F-4		4	1.46	2.3	98	0.005343	1.1	0.0258	25	0.0350	24	34.43	0.39	25.8	6.4	-711	670	0.836
P115-22, Oldest resurgent pluton. Phoenix X62																		
F-1		6	0.71	1.9	211	0.005318	0.53	0.0236	12	0.0322	12	34.29	0.18	23.7	2.8	-944	340	0.804
F-2		5	1.18	3.0	111	0.005295	0.69	0.0190	25	0.0260	24	34.13	0.23	19.1	4.6	-1625	820	0.839
P115-23, Oldest resurgent pluton. Phoenix X62																		
F-1		10	1.70	1.9	275	0.005381	0.41	0.0313	6.0	0.0423	5.7	34.68	0.14	31.3	1.8	-211	140	0.775
F-2		6	1.42	1.2	277	0.005407	0.30	0.0333	4.9	0.0446	4.7	34.85	0.10	33.2	1.6	-75	110	0.759
OT15-29, Tuff in Arkansas River Valley. Sector 54																		
F-1		4	1.51	5.7	53	0.003789	1.5	0.0206	38	0.039	36	24.46	0.37	20.7	7.7	-390	950	0.897
F-2		2	1.66	1.2	112	0.003771	0.89	0.0197	19	0.0380	19	24.34	0.22	19.8	3.8	-488	500	0.878

Note: All analyses performed on chemically abraded single zircon grains. Instrument used indicated next to sample name.

[a]Total mass of radiogenic Pb.

[b]Th contents calculated from radiogenic ^{208}Pb and ^{230}Th-corrected $^{206}Pb/^{238}U$ date of the sample, assuming concordance between U-Pb and Th-Pb systems.

[c]Total mass of common Pb.

[d]Measured ratio corrected for fractionation and spike contribution only.

[e]Measured ratios corrected for fractionation, tracer and blank. Pb blank ratios: $^{206}Pb/^{204}Pb = 18.687 \pm 0.25$; $^{207}Pb/^{204}Pb = 15.658 \pm 0.25$; and $^{208}Pb/^{204}Pb = 38.258 \pm 0.5$ (1σ abs.)

[f]Corrected for initial Th/U disequilibrium using radiogenic ^{208}Pb and $Th/U_{[magma]}$, which is assumed to be approximated by the measured whole rock Th/U ratio.

[g]Isotopic dates calculated using $\lambda_{238} = 1.55125E^{-10}$ (Jaffey et al. 1971) and $\lambda_{235} = 9.8485E^{-10}$ (Jaffey et al. 1971).

APPENDIX 1: LA-ICP-MS ZIRCON U-PB DATA FOR THE SHAVER INTRUSIVE SUITE

				Isotope Ratios						error	Apparent ages (Ma)					
Analysis	U (ppm)	Th (ppm)	Th/U	$^{207}Pb/^{206}Pb$	±2σ (%)	$^{207}Pb/^{235}U$	±2σ (%)	$^{206}Pb/^{238}U$	±2σ (%)	corr.	$^{206}Pb/^{238}U$	±2σ (abs.)	$^{207}Pb/^{235}U$	±2σ (abs.)	$^{207}Pb/^{206}Pb$	±2σ (abs.)
8-RF-1, Sheepthief Creek pluton, IGSN: P4700000J																
8RF1-1	451	1082	0.42	0.0502	14.4	0.1105	14.8	0.0160	3.6	0.25	102.0	3.8	106.5	15.0	206	335
8RF1-2	436	916	0.48	0.0451	13.2	0.1033	13.8	0.0166	3.4	0.25	106.3	3.6	99.8	13.0	-52	323
8RF1-3	480	2400	0.20	0.0493	7.4	0.1087	10.0	0.0160	6.8	0.68	102.4	6.8	104.8	10.0	160	172
8RF1-4	1027	3389	0.30	0.0497	23.8	0.1113	24.2	0.0162	4.4	0.18	103.8	4.4	107.1	24.6	181	555
8RF1-5	293	938	0.31	0.0493	16.8	0.1086	17.2	0.0160	3.4	0.19	102.2	3.4	104.7	17.2	163	395
8RF1-6	378	756	0.50	0.0460	8.8	0.0996	9.6	0.0157	3.8	0.39	100.5	3.8	96.4	8.8	-3	211
8RF1-7	514	1696	0.30	0.0472	7.4	0.1053	8.8	0.0162	4.6	0.53	103.4	4.8	101.7	8.6	61	178
8RF1-8	356	1246	0.29	0.0472	10.8	0.1022	11.0	0.0157	2.0	0.19	100.5	2.0	98.8	10.4	57	257
8RF1-9	1582	6328	0.25	0.0481	2.6	0.1099	5.6	0.0166	5.0	0.89	106.0	5.2	105.9	5.6	103	60
8RF1-10	272	517	0.53	0.0474	10.2	0.1055	10.4	0.0161	1.8	0.17	103.3	1.8	101.9	10.2	70	245
8RF1-11	450	1485	0.30	0.0466	10.4	0.1010	12.2	0.0157	6.6	0.53	100.5	6.6	97.7	11.4	31	249
8RF1-12	390	1404	0.28	0.0480	11.4	0.1060	12.6	0.0160	5.8	0.45	102.5	5.8	102.3	12.4	97	268
8RF1-13	1578	5050	0.31	0.0490	5.4	0.1042	6.0	0.0154	2.8	0.47	98.6	2.8	100.7	5.8	149	124
8RF1-14	282	1156	0.24	0.0503	9.6	0.1082	10.8	0.0156	4.8	0.45	99.8	4.8	104.3	10.8	208	224
8RF1-15	366	769	0.48	0.0472	7.6	0.1019	8.8	0.0157	4.6	0.52	100.1	4.6	98.5	8.4	60	180
8RF1-16	281	787	0.36	0.0466	11.4	0.1072	12.2	0.0167	4.4	0.36	106.7	4.6	103.4	12.0	27	274
8RF1-17	372	818	0.45	0.0462	10.0	0.1016	11.4	0.0159	5.2	0.45	102.0	5.2	98.3	10.6	10	243
8RF1-18	388	1009	0.38	0.0987	14.6	0.2327	14.8	0.0171	3.0	0.21	109.3	3.4	212.4	28.4	1599	272
8RF1-19	360	792	0.45	0.0450	15.4	0.0975	16.2	0.0157	4.4	0.28	100.5	4.4	94.4	14.6	-56	378
8RF1-20	428	856	0.50	0.0489	7.8	0.1052	8.6	0.0156	3.6	0.42	99.9	3.6	101.6	8.4	142	184
8RF1-21	1405	4075	0.34	0.0485	1.4	0.1078	5.8	0.0161	5.6	0.97	103.1	5.6	104.0	5.6	124	33
8RF1-22	405	810	0.50	0.0480	7.0	0.1044	8.4	0.0158	4.4	0.54	100.8	4.4	100.8	8.0	101	167
8RF1-23	687	1099	0.63	0.0475	7.0	0.1001	8.8	0.0153	5.4	0.61	97.9	5.2	96.9	8.2	72	165
8RF1-24	221	508	0.43	0.0500	18.4	0.1083	20.0	0.0157	7.8	0.39	100.5	7.8	104.4	19.8	194	429
8RF1-25	817	1716	0.48	0.0482	3.6	0.1100	7.6	0.0165	6.6	0.88	105.7	6.8	106.0	7.6	111	85
8-RF-3, Mushroom Rock pluton, IGSN: P4700000K																
8RF3-1	233	489	0.48	0.0458	12.8	0.0985	13.0	0.0156	2.4	0.19	99.9	2.4	95.4	12.0	-15	311
8RF3-2	132	370	0.36	0.0554	26.4	0.1243	26.6	0.0163	4.4	0.17	104.0	4.6	119.0	30.0	429	589
8RF3-3	439	1624	0.27	0.0459	11.8	0.1003	12.0	0.0158	2.8	0.23	101.4	2.8	97.1	11.2	-7	285
8RF3-4	98	235	0.42	0.0484	48.0	0.1032	48.2	0.0155	5.2	0.11	98.9	5.0	99.8	45.8	119	1145
8RF3-5	132	304	0.43	0.0506	24.6	0.1037	24.6	0.0149	2.4	0.10	95.0	2.4	100.2	23.6	224	569
8RF3-6	136	326	0.42	0.0480	22.8	0.1041	23.2	0.0157	3.6	0.15	100.6	3.6	100.5	22.2	100	542
8RF3-7	216	432	0.50	0.0471	21.0	0.1041	22.4	0.0160	8.0	0.35	102.6	8.2	100.5	21.4	52	502
8RF3-8	98	206	0.48	0.0411	64.2	0.0883	64.2	0.0156	2.6	0.04	99.6	2.6	86.0	53.0	-279	1669
8RF3-9	215	946	0.23	0.0477	26.4	0.1103	26.8	0.0168	4.0	0.15	107.3	4.4	106.2	27.0	83	629
8RF3-10	148	400	0.37	0.0509	24.2	0.1110	24.8	0.0158	5.2	0.21	101.2	5.2	106.9	25.2	236	560
8RF3-11	130	247	0.53	0.0519	15.6	0.1101	17.4	0.0154	7.8	0.45	98.4	7.6	106.1	17.6	283	358
8RF3-12	351	562	0.63	0.0509	11.8	0.1189	12.6	0.0169	4.8	0.38	108.3	5.2	114.1	13.6	236	270
8RF3-13	217	521	0.42	0.0489	13.6	0.1132	16.8	0.0168	10.0	0.59	107.3	10.6	108.9	17.4	144	321
8RF3-14	502	1707	0.29	0.0507	14.4	0.1057	15.0	0.0151	4.2	0.28	96.8	4.0	102.0	14.6	226	333
8RF3-15	98	255	0.38	0.0485	31.4	0.1067	31.6	0.0160	4.2	0.13	102.2	4.2	103.0	31.0	122	742
8RF3-16	100	240	0.42	0.0418	28.4	0.0845	30.0	0.0147	10.0	0.33	93.8	9.4	82.3	23.8	-238	717
8RF3-17	89	249	0.36	0.0495	39.0	0.1132	39.4	0.0166	5.8	0.15	106.1	6.2	108.9	40.6	172	916
8RF3-18	163	619	0.26	0.0484	29.8	0.1176	30.2	0.0176	4.2	0.14	112.7	4.6	112.9	32.2	118	708
8RF3-19	184	497	0.37	0.0516	40.6	0.1093	41.0	0.0154	6.0	0.15	98.3	5.8	105.3	41.0	268	938
8RF3-20	305	1129	0.27	0.0482	14.6	0.0999	15.0	0.0151	3.8	0.25	96.3	3.6	96.7	13.8	107	344
8RF3-21	165	429	0.38	0.0442	21.4	0.0957	22.2	0.0157	5.8	0.26	100.4	5.8	92.8	19.6	-99	526
8RF3-22	168	302	0.56	0.0508	24.4	0.1056	24.6	0.0151	2.8	0.11	96.4	2.6	102.0	23.8	233	565
8RF3-23	361	1119	0.32	0.0476	6.2	0.1128	10.2	0.0172	8.2	0.80	109.9	9.0	108.5	10.6	79	148
8RF3-24	145	305	0.48	0.0456	23.4	0.1002	24.2	0.0159	6.2	0.25	101.9	6.2	96.9	22.4	-24	570
8RF3-25	191	344	0.56	0.0457	15.6	0.0972	16.2	0.0154	4.4	0.27	98.7	4.2	94.2	14.6	-18	378
8RF3-26	127	330	0.38	0.0560	20.8	0.1221	21.0	0.0158	2.2	0.11	101.0	2.2	116.9	23.2	454	463
8RF3-27	499	1098	0.45	0.0507	8.2	0.1157	12.6	0.0166	9.6	0.76	106.0	10.0	111.2	13.2	225	189
8RF3-28	315	599	0.53	0.0459	10.2	0.0942	14.6	0.0149	10.4	0.71	95.4	9.8	91.5	12.8	-10	246
8RF3-29	405	567	0.71	0.0473	16.6	0.1033	17.0	0.0158	3.8	0.22	101.3	3.8	99.8	16.2	63	397
8RF3-30	391	938	0.42	0.0481	7.6	0.1035	11.4	0.0156	8.6	0.75	99.8	8.6	100.0	11.0	106	180
8-RF-4, Ordinance Creek pluton, IGSN: P4700000L																
8RF4-1	113	203	0.56	0.0499	55.2	0.1124	55.6	0.0164	6.8	0.12	104.6	7.0	108.2	57.0	188	1305
8RF4-2	124	186	0.67	0.0486	32.2	0.1029	32.4	0.0154	3.6	0.11	98.3	3.4	99.5	30.8	129	762
8RF4-3	118	177	0.67	0.0412	30.2	0.0909	30.6	0.0160	4.4	0.14	102.4	4.4	88.3	25.8	-277	774
8RF4-4	153	168	0.91	0.0453	26.8	0.0998	27.4	0.0160	5.8	0.21	102.2	5.8	96.6	25.2	-39	652
8RF4-5	83	133	0.63	0.0365	53.6	0.0822	53.8	0.0163	3.6	0.07	104.3	3.6	80.2	41.4	-590	1475
8RF4-6	131	144	0.91	0.0404	33.8	0.0888	34.4	0.0159	6.8	0.20	102.0	7.0	86.4	28.6	-325	873
8RF4-7	44	88	0.50	0.0357	55.0	0.0802	55.4	0.0163	7.6	0.14	104.2	7.8	78.4	41.8	-654	1533
8RF4-8	79	119	0.67	0.0397	146.8	0.0869	147.0	0.0159	7.2	0.05	101.5	7.2	84.6	119.6	-369	4422
8RF4-9	62	99	0.63	0.0401	42.2	0.0864	42.6	0.0156	5.0	0.12	100.0	5.0	84.1	34.4	-344	1100
8RF4-10	119	179	0.67	0.0419	30.2	0.0966	30.4	0.0167	3.2	0.11	107.0	3.4	93.6	27.2	-235	767

8RF4-11	124	161	0.77	0.0440	21.0	0.1001	21.6	0.0165	4.8	0.22	105.5	5.0	96.9	20.0	-111	519
8RF4-12	94	103	0.91	0.0418	27.2	0.0931	28.0	0.0161	6.4	0.23	103.2	6.4	90.4	24.2	-237	690
8RF4-13	53	80	0.67	0.0972	42.0	0.2480	43.2	0.0185	9.8	0.23	118.2	11.4	224.9	87.2	1570	796
8RF4-14	462	878	0.53	0.0474	5.0	0.1190	6.0	0.0182	3.4	0.56	116.2	3.8	114.2	6.4	71	118
8RF4-15	51	87	0.59	0.0294	85.8	0.0617	86.6	0.0152	11.6	0.13	97.4	11.2	60.8	51.0	-1224	2774
8RF4-16	74	81	0.91	0.0391	79.6	0.0961	79.6	0.0178	1.0	0.01	114.0	1.2	93.2	71.0	-412	2154
8RF4-17	99	129	0.77	0.0414	41.8	0.0967	42.0	0.0169	4.6	0.11	108.2	5.0	93.8	37.6	-260	1069
8RF4-18	155	202	0.77	0.0459	22.6	0.1039	22.8	0.0164	2.6	0.11	105.0	2.6	100.4	21.8	-8	548
8RF4-19	64	70	0.91	0.0418	57.8	0.0914	57.8	0.0158	4.2	0.07	101.4	4.2	88.8	49.2	-237	1482
8RF4-20	229	412	0.56	0.0483	23.8	0.1105	23.8	0.0166	2.2	0.09	106.0	2.2	106.4	24.0	116	561
8RF4-21	104	114	0.91	0.0402	57.6	0.0920	57.6	0.0166	2.6	0.05	106.1	2.8	89.4	49.4	-337	1509
8RF4-22	76	84	0.91	0.0375	46.4	0.0829	46.8	0.0160	5.4	0.12	102.5	5.6	80.8	36.4	-521	1255
8RF4-23	71	78	0.91	0.0387	48.0	0.0872	48.2	0.0163	5.4	0.11	104.5	5.6	84.9	39.4	-436	1274
8RF4-24	80	72	1.11	0.0457	41.6	0.1027	41.8	0.0163	2.2	0.05	104.3	2.2	99.3	39.6	-19	1018
8RF4-25	147	132	1.11	0.0452	29.8	0.1040	31.0	0.0167	8.4	0.27	106.7	8.8	100.5	29.6	-46	729
8RF4-26	116	186	0.63	0.0434	32.6	0.1003	32.8	0.0168	2.0	0.06	107.2	2.0	97.0	30.2	-146	814
8RF4-27	76	106	0.71	0.0446	37.2	0.1020	37.4	0.0166	2.8	0.08	106.2	3.0	98.7	35.2	-79	918
8RF4-28	123	123	1.00	0.0421	40.4	0.1002	40.4	0.0173	1.0	0.03	110.5	1.2	97.0	37.4	-223	1024
8RF4-29	88	106	0.83	0.0386	45.2	0.0867	45.4	0.0163	4.0	0.09	104.2	4.0	84.4	36.8	-445	1204
8RF4-30	102	102	1.00	0.0433	31.0	0.1033	31.2	0.0173	3.0	0.10	110.5	3.4	99.8	29.6	-149	774
8-RF-5, Sheepthief Creek pluton, IGSN: P4700000M																
8RF5-1	441	970	0.45	0.0442	18.2	0.0992	18.4	0.0163	1.8	0.10	104.1	1.8	96.0	16.8	-101	450
8RF5-2	612	1346	0.45	0.0492	8.6	0.1069	9.0	0.0158	2.8	0.31	100.8	2.8	103.1	8.8	157	200
8RF5-3	276	635	0.43	0.0484	15.6	0.1103	16.2	0.0165	4.4	0.27	105.7	4.6	106.2	16.4	117	370
8RF5-4	375	1163	0.32	0.0442	19.0	0.0978	21.0	0.0161	8.8	0.42	102.7	9.0	94.8	19.0	-100	469
8RF5-5	441	1103	0.40	0.0473	9.4	0.1063	10.0	0.0163	3.8	0.38	104.3	4.0	102.5	9.8	63	222
8RF5-6	506	1518	0.33	0.0461	9.8	0.1028	10.4	0.0162	3.2	0.30	103.5	3.2	99.4	9.8	1	237
8RF5-7	264	581	0.45	0.0901	3.2	1.9594	4.2	0.1578	2.8	0.65	944.3	24.2	1101.7	28.6	1427	62
8RF5-8	706	1624	0.43	0.0522	11.0	0.1184	11.0	0.0165	1.6	0.14	105.3	1.6	113.6	12.0	293	251
8RF5-9	408	1102	0.37	0.0468	7.6	0.1105	8.2	0.0171	3.0	0.37	109.4	3.2	106.4	8.2	40	181
8RF5-10	363	944	0.38	0.0450	13.8	0.1007	14.6	0.0162	4.8	0.33	103.9	5.0	97.4	13.6	-58	338
8RF5-11	886	2215	0.40	0.0515	13.6	0.1192	13.8	0.0168	2.4	0.18	107.4	2.6	114.4	15.0	262	312
8RF5-12	800	2080	0.38	0.0485	9.6	0.1112	10.0	0.0166	2.8	0.28	106.4	3.0	107.1	10.2	122	226
8RF5-13	159	398	0.40	0.0484	16.6	0.1145	17.2	0.0172	5.0	0.29	109.8	5.4	110.1	18.0	117	391
8RF5-14	320	832	0.38	0.0483	11.8	0.1114	12.8	0.0167	4.8	0.37	107.0	5.0	107.2	13.0	113	278
8RF5-15	416	998	0.42	0.0504	20.2	0.1143	20.6	0.0165	3.8	0.19	105.2	4.0	109.9	21.4	212	468
8RF5-16	441	926	0.48	0.0466	8.0	0.1065	8.4	0.0166	2.8	0.32	106.0	2.8	102.8	8.2	29	192
8RF5-17	867	1647	0.53	0.0472	7.0	0.1061	7.2	0.0163	1.0	0.14	104.3	1.0	102.4	7.0	58	169
8RF5-18	522	1253	0.42	0.0483	4.8	0.1133	5.0	0.0170	1.6	0.30	108.8	1.6	109.0	5.2	113	114
8RF5-19	1053	2948	0.36	0.0472	5.8	0.1073	8.2	0.0165	5.8	0.72	105.3	6.2	103.5	8.0	61	136
8RF5-20	847	1609	0.53	0.0468	7.4	0.1076	7.6	0.0167	1.6	0.21	106.7	1.6	103.8	7.4	37	176
8RF5-21	446	1427	0.31	0.0484	14.0	0.1104	15.8	0.0165	7.2	0.46	105.7	7.6	106.3	15.8	120	329
8RF5-22	288	691	0.42	0.0495	14.8	0.1129	15.0	0.0166	2.8	0.19	105.9	3.0	108.6	15.4	169	344
8RF5-23	353	988	0.36	0.0452	13.6	0.1052	13.6	0.0169	1.4	0.11	108.1	1.6	101.6	13.2	-48	331
8RF5-24	399	1077	0.37	0.0735	40.2	0.1761	41.0	0.0174	7.4	0.18	111.0	8.2	164.7	62.2	1029	821
8RF5-25	670	1206	0.56	0.0470	9.0	0.1147	9.2	0.0177	1.4	0.16	113.2	1.6	110.2	9.6	47	215
8-RF-11, Coyote Creek pluton, IGSN: P4700000N																
8RF11-1	3679	34951	0.11	0.0516	10.6	0.1146	11.6	0.0161	4.8	0.40	102.9	4.8	110.1	12.2	270	244
8RF11-3	1347	9025	0.15	0.0497	9.0	0.1081	11.2	0.0158	6.8	0.60	100.8	6.8	104.2	11.2	183	209
8RF11-4	3762	9781	0.38	0.0603	24.2	0.1318	25.8	0.0159	8.6	0.33	101.4	8.6	125.7	30.4	613	526
8RF11-7	3621	9053	0.40	0.0652	15.0	0.1389	15.8	0.0155	4.8	0.31	98.9	4.8	132.1	19.4	781	314
8RF11-8	2058	5351	0.38	0.0643	12.4	0.1263	13.8	0.0142	6.2	0.45	91.2	5.6	120.8	15.6	752	260
8RF11-10	3238	12952	0.25	0.0560	10.8	0.1266	11.6	0.0164	4.6	0.39	104.8	4.8	121.1	13.4	453	239
8RF11-11	3062	9186	0.33	0.0571	6.0	0.1330	8.2	0.0169	5.6	0.68	108.0	6.0	126.8	9.8	496	132
8RF11-12	3930	29082	0.14	0.0507	6.2	0.1105	8.4	0.0158	5.6	0.67	101.2	5.6	106.4	8.4	226	144
8RF11-13	2755	5510	0.50	0.0552	9.4	0.1494	9.6	0.0196	2.6	0.26	125.4	3.2	141.4	12.8	419	209
8RF11-14	2052	5746	0.36	0.0547	10.0	0.1316	11.6	0.0174	6.0	0.51	111.5	6.6	125.5	13.8	400	225
8RF11-15	3249	9097	0.36	0.0613	11.4	0.1326	11.4	0.0157	1.0	0.09	100.4	1.0	126.4	13.6	650	246
8RF11-18	2808	6458	0.43	0.0629	20.4	0.1291	22.4	0.0149	9.2	0.41	95.2	8.8	123.3	26.0	706	436
8RF11-19	4878	23902	0.20	0.0524	15.6	0.1150	17.6	0.0159	8.0	0.45	101.9	8.0	110.5	18.4	301	358
8RF11-20	3424	8218	0.42	0.0633	30.4	0.1611	30.6	0.0185	2.2	0.07	117.9	2.6	151.7	43.0	720	649
8RF11-21	4748	10446	0.45	0.0598	17.2	0.1226	17.6	0.0149	4.0	0.22	95.1	3.6	117.4	19.4	597	371
8RF11-22	4209	29884	0.14	0.0485	3.4	0.1166	6.8	0.0174	6.0	0.88	111.3	6.6	112.0	7.2	125	78
8RF11-23	3581	8953	0.40	0.0565	15.2	0.1228	17.6	0.0158	9.0	0.50	100.9	9.0	117.6	19.6	471	338
8RF11-24	2368	5446	0.43	0.0599	5.0	0.1184	6.2	0.0143	3.8	0.60	91.8	3.4	113.6	6.8	599	109
8RF11-25	3503	22770	0.15	0.0543	3.6	0.1201	7.4	0.0160	6.4	0.86	102.6	6.4	115.1	8.0	382	83
8-RF-12, Shorthair Creek pluton, IGSN: P4700000O																
8RF12-1	237	474	0.50	0.0496	26.4	0.1072	26.6	0.0157	1.2	0.04	100.2	1.2	103.4	26.0	178	620
8RF12-2	246	541	0.45	0.0489	35.4	0.1044	35.8	0.0155	5.6	0.16	99.1	5.6	100.8	34.2	142	834
8RF12-3	320	704	0.45	0.0501	17.2	0.1069	18.2	0.0155	5.8	0.32	99.0	5.6	103.1	17.8	200	401
8RF12-4	643	900	0.71	0.0489	10.4	0.1026	12.6	0.0152	7.0	0.55	97.3	6.8	99.2	11.8	145	246

8RF12-5	215	538	0.40	0.0450	45.0	0.0933	45.6	0.0150	7.2	0.16	96.1	7.0	90.5	39.4	-55	1107
8RF12-6	332	730	0.45	0.0437	18.2	0.0873	19.4	0.0145	6.6	0.34	92.7	6.0	85.0	15.8	-128	451
8RF12-7	659	857	0.77	0.0462	11.6	0.0946	12.6	0.0148	5.0	0.40	95.0	4.8	91.8	11.2	10	280
8RF12-8	293	557	0.53	0.0440	35.8	0.0905	37.0	0.0149	9.4	0.25	95.6	9.0	88.0	31.2	-113	889
8RF12-9	571	742	0.77	0.0487	8.6	0.1111	11.4	0.0165	7.6	0.66	105.7	7.8	107.0	11.6	135	201
8RF12-10	273	683	0.40	0.0462	16.8	0.0928	21.8	0.0146	14.0	0.64	93.2	13.0	90.1	18.8	10	404
8RF12-11	490	735	0.67	0.0484	13.2	0.1033	14.2	0.0155	5.2	0.36	99.0	5.0	99.8	13.6	121	313
8RF12-12	432	648	0.67	0.0486	12.0	0.0999	13.4	0.0149	5.8	0.44	95.5	5.6	96.7	12.2	127	282
8RF12-13	249	598	0.42	0.0459	29.2	0.0924	30.4	0.0146	8.4	0.28	93.4	7.8	89.8	26.0	-6	706
8RF12-14	283	594	0.48	0.0448	23.8	0.0934	24.2	0.0151	4.2	0.18	96.7	4.0	90.7	21.0	-65	583
8RF12-15	349	628	0.56	0.0449	14.8	0.0924	15.6	0.0149	4.6	0.29	95.5	4.4	89.8	13.4	-61	362
8RF12-16	616	1602	0.38	0.0491	11.2	0.1052	12.2	0.0156	4.6	0.37	99.5	4.6	101.6	11.8	151	265
8RF12-17	209	481	0.43	0.0433	37.8	0.0962	37.8	0.0161	1.4	0.04	103.1	1.4	93.3	33.6	-152	943
8RF12-18	562	731	0.77	0.0477	8.8	0.0989	9.0	0.0151	1.8	0.20	96.3	1.8	95.8	8.2	82	210
8RF12-19	355	533	0.67	0.0461	11.6	0.0971	12.4	0.0153	4.4	0.35	97.7	4.2	94.1	11.2	4	280
8RF12-20	580	754	0.77	0.0484	10.2	0.1018	11.0	0.0153	3.8	0.35	97.7	3.6	98.4	10.2	117	241
8RF12-21	374	860	0.43	0.0478	16.4	0.0970	16.6	0.0147	3.0	0.18	94.2	2.8	94.0	15.0	88	389
8RF12-22	657	920	0.71	0.0478	7.0	0.1026	8.4	0.0156	4.6	0.56	99.6	4.6	99.2	7.8	89	164
8RF12-23	299	1346	0.22	0.0510	21.6	0.1071	21.6	0.0152	1.2	0.06	97.4	1.2	103.3	21.2	241	500
8RF12-24	832	998	0.83	0.0466	6.2	0.0962	7.6	0.0150	4.2	0.55	95.7	4.0	93.3	6.8	31	150
8RF12-25	535	749	0.71	0.0478	13.0	0.0960	13.2	0.0146	2.4	0.18	93.2	2.2	93.0	11.8	89	309
8RF12-26	285	570	0.50	0.0470	24.8	0.0949	25.4	0.0146	6.2	0.24	93.7	5.8	92.1	22.4	50	592
8RF12-27	298	596	0.50	0.0466	20.2	0.1077	20.4	0.0168	3.2	0.16	107.3	3.4	103.9	20.2	26	484
8RF12-28	204	490	0.42	0.0469	32.0	0.0961	32.6	0.0149	5.8	0.18	95.1	5.4	93.1	29.0	44	771
8RF12-29	366	805	0.45	0.0473	17.8	0.1013	18.6	0.0155	5.6	0.30	99.4	5.4	98.0	17.4	64	424
8-RF-14, lower Bear Creek pluton, IGSN: P4700000P																
8RF14-1	1524	4420	0.34	0.0478	2.0	0.1070	3.8	0.0162	3.4	0.86	103.8	3.4	103.2	3.8	91	46
8RF14-2	1990	5771	0.34	0.0490	2.4	0.1106	3.4	0.0164	2.6	0.74	104.7	2.6	106.6	3.6	147	54
8RF14-3	1722	5510	0.31	0.0480	3.4	0.1085	4.2	0.0164	2.6	0.60	104.8	2.6	104.6	4.2	99	79
8RF14-4	518	1606	0.32	0.0493	7.2	0.1089	7.6	0.0160	2.0	0.27	102.4	2.0	105.0	7.6	163	170
8RF14-5	791	4825	0.16	0.0480	5.4	0.1066	8.2	0.0161	6.2	0.75	103.0	6.2	102.8	8.0	99	128
8RF14-6	2309	5542	0.42	0.0479	2.4	0.1061	8.6	0.0161	8.2	0.96	102.7	8.4	102.3	8.4	94	59
8RF14-7	456	1642	0.28	0.0474	14.8	0.1034	17.4	0.0158	9.4	0.53	101.2	9.4	99.9	16.6	70	352
8RF14-8	372	595	0.63	0.0633	17.4	0.1413	17.6	0.0162	3.6	0.20	103.6	3.6	134.2	22.2	717	368
8RF14-9	955	2006	0.48	0.0478	4.6	0.1014	5.6	0.0154	3.0	0.53	98.5	2.8	98.1	5.2	89	111
8RF14-10	885	3275	0.27	0.0482	5.6	0.1005	5.8	0.0151	1.4	0.26	96.9	1.4	97.3	5.4	107	132
8RF14-11	130	377	0.34	0.0416	28.0	0.0875	29.0	0.0152	7.2	0.25	97.6	7.0	85.2	23.6	-250	712
8RF14-12	293	733	0.40	0.0463	11.0	0.0996	11.0	0.0156	1.2	0.11	99.7	1.2	96.4	10.2	15	265
8RF14-13	1166	4547	0.26	0.0488	4.8	0.1073	5.8	0.0160	3.4	0.57	102.1	3.4	103.5	5.8	136	113
8RF14-14	668	1470	0.45	0.0737	66.0	0.1618	68.4	0.0159	18.0	0.26	101.9	18.2	152.3	96.8	1033	1371
8RF14-15	560	1680	0.33	0.0484	6.6	0.1097	7.2	0.0165	2.8	0.39	105.2	2.8	105.7	7.2	117	156
8RF14-16	1622	5028	0.32	0.0481	2.6	0.1061	3.2	0.0160	2.0	0.62	102.3	2.0	102.4	3.2	106	60
8RF14-17	596	1490	0.40	0.0469	9.4	0.1004	9.6	0.0155	1.8	0.18	99.3	1.6	97.1	8.8	43	226
8RF14-18	826	2065	0.40	0.0508	11.0	0.1041	11.2	0.0149	2.6	0.23	95.0	2.4	100.5	10.8	233	254
8RF14-19	3136	8154	0.38	0.0479	1.8	0.1041	4.0	0.0157	3.4	0.88	100.7	3.4	100.5	3.8	96	45
8RF14-20	2312	8323	0.28	0.0476	3.0	0.1000	4.6	0.0152	3.6	0.76	97.4	3.4	96.8	4.2	80	72
8RF14-21	1918	4795	0.40	0.0481	2.2	0.1058	2.6	0.0160	1.6	0.58	102.1	1.6	102.1	2.6	103	52
8RF14-22	3556	13157	0.27	0.0485	2.8	0.1052	4.6	0.0157	3.6	0.78	100.7	3.6	101.6	4.4	123	68
8RF14-23	2146	7296	0.29	0.0492	5.8	0.1065	8.0	0.0157	5.8	0.70	100.3	5.6	102.8	8.0	159	134
8RF14-24	2182	6546	0.33	0.0482	3.0	0.1037	5.6	0.0156	4.8	0.85	99.8	4.6	100.2	5.4	111	69
8RF14-25	3055	9776	0.31	0.0480	2.6	0.1047	6.0	0.0158	5.4	0.91	101.2	5.4	101.1	5.8	98	59
8-RF-15, Dinkey Dome pluton, IGSN: P4700000Q																
8RF15-1	383	1072	0.36	0.0485	16.8	0.1200	18.6	0.0179	8.0	0.43	114.7	9.0	115.1	20.2	124	394
8RF15-2	695	3267	0.21	0.0470	6.4	0.1188	9.0	0.0183	6.4	0.71	117.1	7.4	114.0	9.8	50	151
8RF15-3	319	798	0.40	0.0491	18.2	0.1257	18.8	0.0186	4.6	0.24	118.5	5.4	120.2	21.4	154	429
8RF15-4	631	883	0.71	0.0483	9.0	0.1283	9.4	0.0193	3.2	0.33	123.0	3.8	122.6	11.0	115	211
8RF15-5	465	977	0.48	0.0465	19.0	0.1227	19.2	0.0191	3.4	0.18	122.1	4.2	117.5	21.4	25	454
8RF15-6	878	3249	0.27	0.0500	39.4	0.1128	39.8	0.0163	5.0	0.13	104.5	5.2	108.5	40.8	196	924
8RF15-7	445	801	0.56	0.0490	11.8	0.1241	12.4	0.0184	3.6	0.29	117.4	4.2	118.8	13.8	147	277
8RF15-8	409	859	0.48	0.0485	9.0	0.1270	11.2	0.0190	6.8	0.61	121.2	8.2	121.4	12.8	126	210
8RF15-9	469	1501	0.31	0.0493	6.8	0.1245	7.6	0.0183	3.4	0.45	117.0	4.0	119.2	8.6	164	160
8RF15-10	496	794	0.63	0.0482	10.6	0.1213	11.6	0.0183	4.4	0.39	116.7	5.2	116.3	12.6	107	250
8RF15-11	409	818	0.50	0.0489	8.8	0.1299	9.4	0.0193	3.4	0.36	123.1	4.0	124.1	11.0	143	206
8RF15-12	342	992	0.34	0.0466	14.2	0.1218	14.4	0.0190	2.0	0.14	121.1	2.4	116.7	15.8	28	340
8RF15-13	272	680	0.40	0.0460	19.8	0.1185	20.6	0.0187	5.6	0.27	119.3	6.6	113.7	22.0	-2	478
8RF15-14	535	1873	0.29	0.0477	11.2	0.1166	11.8	0.0177	3.6	0.31	113.3	4.2	112.0	12.4	84	265
8RF15-15	918	6518	0.14	0.0492	9.8	0.1104	10.4	0.0163	4.0	0.38	104.0	4.0	106.4	10.6	159	228
8RF15-16	380	798	0.48	0.0472	13.0	0.1202	14.6	0.0185	6.6	0.45	118.1	7.6	115.3	15.8	58	310
8RF15-17	637	956	0.67	0.0495	7.8	0.1245	8.6	0.0182	3.6	0.41	116.6	4.2	119.1	9.8	171	183
8RF15-18	393	904	0.43	0.0468	14.4	0.1157	17.0	0.0179	9.0	0.53	114.5	10.2	111.2	17.8	40	343
8RF15-19	433	866	0.50	0.0488	9.8	0.1237	10.2	0.0184	3.4	0.33	117.4	4.0	118.4	11.4	138	228

8RF15-20	288	893	0.32	0.0456	16.2	0.1164	16.4	0.0185	3.0	0.18	118.3	3.6	111.8	17.4	-24	392
8RF15-21	478	1673	0.29	0.0505	12.2	0.1339	13.0	0.0192	4.2	0.33	122.8	5.2	127.6	15.6	218	283
8RF15-22	568	2442	0.23	0.0488	10.0	0.1167	11.4	0.0173	5.2	0.46	110.8	5.6	112.1	12.0	140	236
8RF15-23	433	779	0.56	0.0493	17.6	0.1277	17.6	0.0188	1.4	0.08	120.1	1.6	122.0	20.4	161	413
8RF15-24	258	490	0.53	0.0503	10.0	0.1299	11.2	0.0187	5.2	0.46	119.6	6.2	124.0	13.2	211	232
8RF15-25	527	1054	0.50	0.0498	16.4	0.1245	17.0	0.0181	4.2	0.25	115.9	4.8	119.1	19.2	184	385
8-RF-17, Rainbow Mine pluton, IGSN: P4700000S																
8RF17-1	137	192	0.71	0.0441	48.8	0.0921	49.4	0.0151	7.6	0.15	96.9	7.2	89.4	42.2	-104	1214
8RF17-2	156	203	0.77	0.0515	35.2	0.1105	35.6	0.0156	4.0	0.11	99.5	4.0	106.4	35.8	264	815
8RF17-3	137	206	0.67	0.0417	67.0	0.0916	67.0	0.0159	2.0	0.03	102.0	2.0	89.0	57.0	-247	1734
8RF17-4	130	221	0.59	0.0492	76.6	0.1072	76.8	0.0158	4.8	0.06	101.0	4.8	103.4	75.4	157	1854
8RF17-5	569	797	0.71	0.0473	8.8	0.1048	9.8	0.0161	4.0	0.41	102.8	4.0	101.2	9.4	63	211
8RF17-6	351	527	0.67	0.0495	25.4	0.1110	25.6	0.0163	2.6	0.10	104.1	2.8	106.9	26.0	171	597
8RF17-7	166	232	0.71	0.0563	31.4	0.1187	32.0	0.0153	6.2	0.19	97.9	6.0	113.9	34.4	463	699
8RF17-8	423	465	0.91	0.0492	16.2	0.1095	16.6	0.0162	3.8	0.23	103.3	4.0	105.5	16.6	155	379
8RF17-9	109	207	0.53	0.0417	54.2	0.0920	55.0	0.0160	9.6	0.17	102.5	9.6	89.4	47.0	-247	1390
8RF17-10	178	214	0.83	0.0460	26.0	0.1005	26.4	0.0159	5.0	0.19	101.5	5.0	97.3	24.4	-5	628
8RF17-11	173	294	0.59	0.0399	46.8	0.0889	46.8	0.0162	3.2	0.07	103.5	3.4	86.5	38.8	-360	1224
8RF17-12	266	505	0.53	0.0489	14.2	0.1081	16.8	0.0160	9.0	0.53	102.6	9.0	104.2	16.6	141	336
8RF17-13	286	458	0.63	0.0490	18.4	0.1074	20.8	0.0159	9.8	0.47	101.6	9.8	103.6	20.6	149	431
8RF17-14	215	387	0.56	0.0472	50.0	0.1040	50.4	0.0160	7.0	0.14	102.3	7.0	100.5	48.2	57	1207
8RF17-15	159	334	0.48	0.0528	42.6	0.1151	42.6	0.0158	2.2	0.05	101.2	2.2	110.7	44.6	319	976
8RF17-16	208	291	0.71	0.0509	43.6	0.1057	44.0	0.0151	6.2	0.14	96.5	5.8	102.0	42.8	234	1018
8RF17-17	289	318	0.91	0.0429	24.6	0.0963	24.6	0.0163	2.4	0.10	104.2	2.4	93.4	22.0	-176	613
8RF17-18	527	580	0.91	0.0481	7.4	0.1067	8.0	0.0161	3.0	0.37	102.9	3.0	102.9	7.8	103	175
8RF17-19	290	377	0.77	0.0468	21.0	0.1049	21.6	0.0163	5.2	0.24	103.9	5.2	101.3	21.0	41	506
8RF17-20	406	406	1.00	0.0462	10.4	0.1035	11.0	0.0162	3.2	0.29	103.9	3.2	100.0	10.4	8	252
8RF17-21	346	761	0.45	0.0465	16.0	0.1049	16.4	0.0164	3.4	0.20	104.6	3.4	101.3	15.8	25	385
8RF17-22	170	221	0.77	0.0520	68.0	0.1004	71.0	0.0140	20.0	0.28	89.7	17.8	97.2	65.8	284	1598
8RF17-23	117	281	0.42	0.0621	38.6	0.1378	40.4	0.0161	12.0	0.30	102.9	12.2	131.1	49.6	678	831
8RF17-24	373	410	0.91	0.0460	11.8	0.1028	12.6	0.0162	4.4	0.36	103.8	4.6	99.4	12.0	-5	284
8RF17-25	929	1115	0.83	0.0474	8.8	0.1040	12.0	0.0159	8.2	0.68	101.7	8.2	100.4	11.4	69	210
8RF17-26	328	361	0.91	0.0496	16.8	0.1129	18.6	0.0165	8.0	0.43	105.5	8.2	108.6	19.2	177	394
8RF17-27	464	696	0.67	0.0492	9.2	0.1045	10.6	0.0154	5.4	0.51	98.4	5.4	100.9	10.2	159	214
8RF17-28	170	255	0.67	0.0511	24.0	0.1105	24.4	0.0157	4.8	0.20	100.4	4.8	106.4	24.8	245	554
8RF17-29	561	673	0.83	0.0515	9.8	0.1137	10.4	0.0160	3.4	0.32	102.3	3.4	109.4	10.8	265	226
8RF17-30	385	462	0.83	0.0495	29.4	0.1058	29.6	0.0155	3.0	0.10	99.2	2.8	102.1	28.8	172	690
8-RF-19, Dinkey Lakes pluton, IGSN: P4700000U																
8RF19-1	955	4011	0.24	0.0516	12.2	0.1134	13.4	0.0159	5.4	0.41	101.9	5.6	109.1	13.8	269	281
8RF19-2	1324	3442	0.38	0.0486	7.8	0.1085	10.2	0.0162	6.6	0.65	103.5	6.8	104.6	10.2	131	183
8RF19-3	2335	11675	0.20	0.0489	4.2	0.1003	5.0	0.0149	2.8	0.56	95.2	2.6	97.1	4.6	143	97
8RF19-4	1108	2105	0.53	0.0479	5.0	0.1030	11.6	0.0156	10.6	0.91	99.9	10.4	99.6	11.0	93	117
8RF19-5	859	2749	0.31	0.0471	9.6	0.0990	9.8	0.0152	2.2	0.23	97.5	2.2	95.9	9.0	56	227
8RF19-6	2591	2850	0.91	0.0847	67.6	0.1972	67.8	0.0169	6.2	0.09	108.0	6.6	182.7	113.6	1308	1351
8RF19-7	869	1130	0.77	0.0475	5.4	0.1014	7.0	0.0155	4.4	0.63	99.1	4.4	98.1	6.6	73	130
8RF19-8	535	963	0.56	0.0575	39.6	0.1256	40.0	0.0158	4.6	0.11	101.3	4.6	120.2	45.2	512	879
8RF19-9	997	4586	0.22	0.0506	6.8	0.1118	9.4	0.0160	6.6	0.70	102.5	6.6	107.6	9.6	221	157
8RF19-10	125	463	0.27	0.0446	40.0	0.0918	40.8	0.0149	8.0	0.19	95.4	7.6	89.1	34.8	-76	988
8RF19-11	2767	10238	0.27	0.0485	5.2	0.1032	5.8	0.0155	2.6	0.45	98.8	2.4	99.8	5.4	122	120
8RF19-12	1457	3497	0.42	0.0498	44.2	0.1075	44.6	0.0156	5.4	0.12	100.0	5.4	103.6	43.8	188	1040
8RF19-13	1556	7624	0.20	0.0535	4.8	0.1176	5.4	0.0159	2.6	0.47	101.9	2.6	112.9	5.8	351	109
8RF19-14	1674	5357	0.31	0.0476	5.6	0.0902	8.6	0.0137	6.6	0.77	87.9	5.8	87.7	7.2	82	131
8RF19-15	649	1947	0.33	0.0467	8.0	0.0973	16.8	0.0151	14.8	0.88	96.8	14.2	94.3	15.2	31	190
8RF19-16	867	2774	0.31	0.0467	11.6	0.0996	13.8	0.0155	7.4	0.54	98.9	7.4	96.4	12.6	35	278
8RF19-17	1572	12419	0.13	0.0497	4.8	0.1099	5.8	0.0160	3.4	0.56	102.6	3.4	105.8	6.0	179	113
8RF19-18	524	734	0.71	0.0517	15.2	0.1100	18.0	0.0154	9.6	0.54	98.7	9.4	105.9	18.2	273	349
8RF19-19	1890	9450	0.20	0.0466	6.4	0.1069	6.6	0.0166	2.2	0.31	106.3	2.2	103.2	6.6	31	152
8RF19-20	1669	6008	0.28	0.0481	5.8	0.1077	6.0	0.0162	2.0	0.33	103.8	2.0	103.9	6.0	106	135
8RF19-21	694	1110	0.63	0.0468	13.0	0.1076	13.0	0.0167	1.6	0.13	106.6	1.8	103.8	12.8	40	310
8RF19-22	411	1069	0.38	0.0497	16.2	0.1076	16.6	0.0157	3.2	0.19	100.5	3.0	103.8	16.4	180	379
8RF19-23	2390	8843	0.27	0.0483	4.8	0.1116	7.2	0.0167	5.6	0.76	107.1	5.8	107.4	7.4	115	112
8RF19-24	701	2454	0.29	0.0550	22.0	0.1224	22.2	0.0161	3.2	0.15	103.2	3.2	117.3	24.6	413	491
8RF19-25	1075	2150	0.50	0.0470	9.4	0.1039	9.6	0.0160	1.4	0.15	102.5	1.4	100.3	9.2	49	227
8RF19-26	1463	4974	0.29	0.0478	4.4	0.1034	7.2	0.0157	5.6	0.78	100.4	5.6	100.0	6.8	89	106
8RF19-27	1798	2697	0.67	0.0489	5.4	0.1090	5.6	0.0162	1.8	0.33	103.3	2.0	105.0	5.6	144	124
8RF19-28	1354	2708	0.50	0.0495	5.6	0.0998	7.6	0.0146	5.2	0.68	93.6	4.8	96.6	7.0	171	131
8RF19-29	595	1785	0.33	0.0492	12.0	0.1129	12.6	0.0166	3.2	0.26	106.4	3.4	108.6	12.8	156	283
8RF19-30	484	823	0.59	0.0482	17.8	0.1004	19.6	0.0151	8.2	0.42	96.6	7.8	97.1	18.2	111	421
1S67, north of Snow Corral Meadow pluton, IGSN: P4700000V																
1S67-1	934	1681	0.56	0.0488	6.4	0.1076	8.2	0.0160	5.2	0.63	102.3	5.2	103.8	8.0	138	150
1S67-2	575	920	0.63	0.0473	4.8	0.1021	6.6	0.0156	4.6	0.69	100.1	4.6	98.7	6.2	65	115

1S67-6	314	2135	0.15	0.0479	15.8	0.1030	17.2	0.0156	6.8	0.40	99.8	6.8	99.5	16.4	94	375
1S67-7	1361	6533	0.21	0.0482	2.6	0.1050	5.4	0.0158	4.6	0.87	101.0	4.6	101.4	5.2	110	63
1S67-8	1861	1675	1.11	0.0479	4.2	0.1061	6.6	0.0161	5.2	0.79	102.8	5.4	102.4	6.6	93	97
1S67-12	1288	4122	0.31	0.0480	3.8	0.1102	5.4	0.0167	4.0	0.72	106.5	4.2	106.2	5.4	99	89
1S67-13	433	2165	0.20	0.0471	6.8	0.1024	7.6	0.0158	3.0	0.40	100.9	3.0	99.0	7.0	54	164
1S67-14	1436	6318	0.23	0.0479	4.6	0.1055	5.8	0.0160	3.8	0.64	102.2	3.8	101.8	5.8	94	107
1S67-17	855	2993	0.29	0.0481	2.0	0.1038	7.0	0.0157	6.8	0.96	100.1	6.6	100.3	6.6	105	48
1S67-18	553	2212	0.25	0.0479	7.6	0.1049	8.2	0.0159	3.0	0.37	101.6	3.0	101.3	7.8	95	180
1S67-19	825	1568	0.53	0.0500	4.2	0.1194	4.6	0.0173	2.2	0.47	110.6	2.4	114.5	5.0	197	96
1S67-20	1072	2251	0.48	0.0497	6.4	0.1093	8.4	0.0159	5.4	0.64	101.9	5.4	105.3	8.4	182	151
1S67-21	1547	6807	0.23	0.0488	2.8	0.1094	5.6	0.0163	4.8	0.86	104.0	5.0	105.4	5.6	138	68
1S67-22	298	1013	0.29	0.0545	16.0	0.1326	16.4	0.0177	3.4	0.20	112.8	3.8	126.4	19.6	390	361
1S67-23	662	1787	0.37	0.0498	5.2	0.1061	10.2	0.0154	8.8	0.86	98.8	8.6	102.4	9.8	186	121
1S67-24	773	2319	0.33	0.0492	3.6	0.1068	4.6	0.0158	2.8	0.60	100.8	2.8	103.1	4.4	155	86
1S67-25	442	1193	0.37	0.0475	7.8	0.1027	9.2	0.0157	5.0	0.53	100.2	4.8	99.2	8.8	76	186
1S81, Dinkey Dome pluton, IGSN: P4700000W																
1S81-1	819	3686	0.22	0.0475	4.2	0.1051	8.4	0.0160	7.4	0.87	102.5	7.6	101.5	8.2	77	98
1S81-2	307	1566	0.20	0.0487	13.2	0.1221	14.4	0.0182	5.8	0.40	116.2	6.6	116.9	15.8	132	310
1S81-3	2262	19227	0.12	0.0475	14.4	0.0595	15.0	0.0091	4.2	0.28	58.3	2.4	58.7	8.6	73	344
1S81-4	916	2107	0.43	0.0478	5.4	0.1244	7.8	0.0189	5.6	0.72	120.6	6.6	119.0	8.6	89	127
1S81-5	1100	7920	0.14	0.0473	4.6	0.1015	6.2	0.0156	4.2	0.68	99.5	4.2	98.2	5.8	66	110
1S81-6	339	1220	0.28	0.0497	9.0	0.1255	10.2	0.0183	4.8	0.47	117.0	5.6	120.0	11.6	180	212
1S81-7	450	765	0.59	0.0469	12.6	0.1063	13.4	0.0164	4.6	0.35	105.0	4.8	102.6	13.2	47	302
1S81-8	277	748	0.37	0.0463	11.8	0.1142	12.4	0.0179	4.0	0.32	114.2	4.6	109.8	13.0	15	283
1S81-9	821	1232	0.67	0.0477	4.4	0.1161	6.6	0.0176	5.0	0.74	112.8	5.6	111.5	7.0	85	105
1S81-10	368	773	0.48	0.1948	3.8	9.6549	4.4	0.3594	2.0	0.46	1979.3	34.0	2402.4	39.8	2784	63
1S81-11	2348	6809	0.34	0.0493	3.6	0.0649	19.2	0.0096	18.8	0.98	61.3	11.4	63.8	11.8	160	82
1S81-12	310	651	0.48	0.0468	13.2	0.1215	13.8	0.0188	3.4	0.25	120.3	4.2	116.5	15.0	39	317
1S81-13	193	579	0.33	0.0498	10.8	0.1310	11.6	0.0191	4.4	0.38	121.8	5.4	125.0	13.6	186	250
1S81-14	770	1771	0.43	0.0475	8.2	0.1442	8.6	0.0220	2.8	0.32	140.4	3.8	136.8	11.0	74	195
1S81-15	1362	2452	0.56	0.0481	4.6	0.1190	5.2	0.0180	2.0	0.39	114.7	2.2	114.2	5.6	102	111
1S81-16	391	1603	0.24	0.0470	10.6	0.1259	12.8	0.0194	6.8	0.54	124.0	8.4	120.4	14.4	49	255
1S81-17	324	518	0.63	0.0467	11.0	0.1181	11.2	0.0183	2.4	0.21	117.2	2.8	113.4	12.0	34	261
1S81-18	768	1229	0.63	0.0484	4.4	0.1255	4.8	0.0188	2.2	0.44	120.1	2.6	120.1	5.6	120	103
1S81-19	385	1579	0.24	0.0461	16.6	0.1217	16.8	0.0192	2.0	0.12	122.4	2.4	116.6	18.4	2	401
1S81-20	939	5352	0.18	0.0483	2.6	0.1233	4.0	0.0185	3.0	0.75	118.2	3.4	118.1	4.4	116	61
1S81-21	250	1150	0.22	0.0473	11.6	0.1196	12.4	0.0183	4.2	0.34	117.1	4.8	114.7	13.4	65	276
1S81-22	148	414	0.36	0.0484	13.4	0.1194	16.0	0.0179	8.8	0.55	114.4	10.0	114.5	17.4	117	318
1S81-23	198	554	0.36	0.0498	9.2	0.1311	9.8	0.0191	3.2	0.32	121.9	3.8	125.1	11.4	186	215
1S81-24	743	13523	0.05	0.0474	5.8	0.1244	6.2	0.0191	2.2	0.35	121.7	2.6	119.1	7.0	68	138
1S81-25	595	1547	0.38	0.0468	8.6	0.1162	9.8	0.0180	4.6	0.48	115.1	5.4	111.7	10.4	39	206
1S81-26	1385	7479	0.19	0.0470	6.0	0.1119	12.6	0.0173	11.2	0.88	110.4	12.2	107.7	13.0	49	143
1S81-27	215	516	0.42	0.0472	14.8	0.1270	15.2	0.0195	3.4	0.23	124.7	4.2	121.4	17.4	58	353
1S81-28	864	2160	0.40	0.0504	9.6	0.1199	17.4	0.0172	14.4	0.83	110.1	15.8	114.9	19.0	216	224
1S81-29	104	260	0.40	0.0500	4.0	0.1287	5.2	0.0187	3.4	0.65	119.2	4.0	122.9	6.0	197	92
1S81-30	361	686	0.53	0.0470	8.0	0.1262	8.2	0.0195	2.0	0.24	124.3	2.4	120.7	9.4	51	190
1S81-31	2722	17965	0.15	0.0475	12.8	0.0611	13.6	0.0093	4.6	0.34	59.8	2.8	60.2	7.8	77	302
1S81-32	704	4224	0.17	0.0717	4.4	0.4024	20.2	0.0407	19.8	0.98	257.0	49.8	343.4	58.8	979	88
1S81-33	2287	15323	0.15	0.0480	8.6	0.0680	10.0	0.0103	4.8	0.49	66.0	3.2	66.8	6.4	98	205
1S81-34	1226	3678	0.33	0.0489	4.8	0.1237	5.6	0.0184	2.8	0.50	117.3	3.2	118.5	6.2	141	115
1S81-36	1054	1686	0.63	0.0482	9.4	0.1134	12.6	0.0171	8.6	0.68	109.1	9.2	109.1	13.2	109	220
1S81-37	1580	17064	0.09	0.0475	5.8	0.1149	6.2	0.0176	2.0	0.32	112.2	2.2	110.4	6.4	74	139
1S81-38	1625	23075	0.07	0.0487	12.2	0.1202	12.8	0.0179	3.8	0.30	114.3	4.4	115.3	14.0	134	287
1S81-39	1308	2224	0.59	0.0468	8.4	0.1225	9.2	0.0190	3.6	0.39	121.3	4.4	117.3	10.2	38	202
1S81-40	583	4256	0.14	0.0470	6.8	0.1194	7.8	0.0184	4.0	0.51	117.6	4.6	114.6	8.4	51	160
1S81-41	225	653	0.34	0.0466	10.0	0.1160	13.8	0.0181	9.6	0.69	115.4	10.8	111.4	14.4	28	238
1S81-42	2449	2204	1.11	0.0484	8.4	0.0658	14.6	0.0098	12.0	0.82	63.2	7.6	64.7	9.2	121	196
1S81-43	1820	2730	0.67	0.0490	7.4	0.1169	7.8	0.0173	2.4	0.31	110.4	2.8	112.2	8.4	150	176
1S81-44	1053	3580	0.29	0.0485	2.8	0.1249	5.2	0.0187	4.4	0.84	119.3	5.2	119.5	5.8	124	66
1S81-45	204	796	0.26	0.0448	17.4	0.1139	17.6	0.0184	2.6	0.14	117.8	3.0	109.5	18.2	-66	425
1S81-46	690	8694	0.08	0.0486	5.6	0.1323	10.4	0.0198	8.8	0.85	126.1	11.0	126.1	12.4	127	131
1S81-47	173	1246	0.14	0.0473	7.0	0.1246	7.4	0.0191	2.2	0.31	122.0	2.8	119.2	8.2	64	167
1S81-48	509	5701	0.09	0.0481	9.6	0.1250	11.2	0.0189	5.8	0.52	120.5	7.0	119.6	12.6	103	226
1S81-49	623	1371	0.45	0.0473	6.8	0.1081	18.0	0.0166	16.6	0.92	106.0	17.4	104.2	17.8	64	163
1S81-50	1545	4944	0.31	0.0474	6.2	0.1174	8.0	0.0179	5.2	0.64	114.7	5.8	112.7	8.6	71	146
3S48, Mud Lakes pluton, IGSN: P4700000X																
3S48-1	108	173	0.63	0.0442	35.0	0.0911	35.4	0.0150	5.8	0.16	95.7	5.4	88.5	30.0	-100	866
3S48-2	81	130	0.63	0.0368	67.0	0.0766	67.2	0.0151	5.4	0.08	96.5	5.2	75.0	48.6	-569	1852
3S48-3	90	108	0.83	0.0591	43.4	0.1288	44.4	0.0158	9.0	0.20	101.2	9.0	123.0	51.4	569	955
3S48-4	106	170	0.63	0.0409	36.6	0.0876	37.4	0.0156	7.6	0.20	99.5	7.4	85.3	30.6	-297	940
3S48-5	165	182	0.91	0.0447	20.8	0.0940	21.6	0.0153	5.6	0.26	97.6	5.4	91.2	18.8	-72	511

3S48-6	505	657	0.77	0.0484	6.8	0.1029	7.8	0.0154	3.8	0.48	98.6	3.6	99.4	7.4	118	163
3S48-7	127	216	0.59	0.0487	16.8	0.1078	17.2	0.0161	3.8	0.22	102.7	3.8	104.0	17.0	133	395
3S48-8	231	185	1.25	0.0459	13.0	0.0981	13.6	0.0155	3.8	0.28	99.2	3.8	95.0	12.4	-8	315
3S48-9	124	186	0.67	0.0446	41.8	0.0957	42.2	0.0156	6.2	0.15	99.6	6.0	92.8	37.4	-77	1030
3S48-10	206	185	1.11	0.0441	20.8	0.0950	21.0	0.0156	3.4	0.16	100.0	3.4	92.2	18.4	-105	510
3S48-11	78	101	0.77	0.0477	18.0	0.1006	18.6	0.0153	4.8	0.26	97.9	4.6	97.3	17.4	82	429
3S48-12	156	187	0.83	0.0416	29.0	0.0907	29.2	0.0158	3.2	0.11	101.2	3.2	88.1	24.6	-253	736
3S48-13	161	177	0.91	0.0440	20.6	0.0935	20.8	0.0154	2.8	0.13	98.7	2.8	90.8	18.0	-112	508
3S48-14	105	126	0.83	0.0444	35.8	0.0921	36.0	0.0150	3.6	0.10	96.2	3.6	89.4	30.8	-88	881
3S48-15	84	101	0.83	0.0416	30.8	0.0868	31.4	0.0151	6.8	0.21	96.8	6.4	84.5	25.6	-249	782
3S48-16	106	170	0.63	0.0415	31.0	0.0896	32.8	0.0157	10.8	0.33	100.2	10.8	87.1	27.4	-258	789
3S48-17	104	156	0.67	0.0492	28.6	0.1023	28.8	0.0151	4.0	0.14	96.4	3.8	98.9	27.2	160	670
3S48-18	339	237	1.43	0.0470	9.4	0.1017	10.4	0.0157	4.4	0.42	100.3	4.4	98.3	9.8	50	226
3S48-19	81	113	0.71	0.0484	51.4	0.1019	52.6	0.0153	11.4	0.21	97.7	11.0	98.5	49.4	118	1229
3S48-20	101	141	0.71	0.0462	38.6	0.0949	41.6	0.0149	15.2	0.37	95.4	14.4	92.1	36.6	8	938
3S48-21	160	208	0.77	0.0441	21.4	0.0960	21.4	0.0158	2.4	0.11	100.9	2.4	93.1	19.0	-104	525
3S48-22	106	117	0.91	0.0389	41.8	0.0860	42.0	0.0161	3.0	0.07	102.7	3.0	83.8	33.8	-426	1108
3S48-23	189	246	0.77	0.0444	16.2	0.0968	16.8	0.0158	3.8	0.22	101.2	3.8	93.8	15.0	-90	400
3S48-24	234	164	1.43	0.0459	12.4	0.0970	13.0	0.0153	3.8	0.29	97.9	3.8	94.0	11.6	-6	300
3S48-25	186	205	0.91	0.0446	16.4	0.0996	17.4	0.0162	6.0	0.35	103.7	6.2	96.4	16.0	-79	400
3S48-26	240	216	1.11	0.0468	13.2	0.1026	13.8	0.0159	3.6	0.26	101.6	3.6	99.2	13.0	41	317
3S48-27	83	108	0.77	0.0470	22.4	0.1014	23.0	0.0156	5.4	0.23	100.0	5.4	98.0	21.6	51	537
3S48-28	81	81	1.00	0.0400	36.6	0.0877	36.8	0.0159	5.0	0.13	101.8	5.0	85.4	30.2	-354	950
3S48-29	118	118	1.00	0.0454	34.8	0.0976	35.4	0.0156	6.8	0.19	99.8	6.8	94.6	32.0	-36	849
3S48-30	114	148	0.77	0.0430	23.2	0.0909	23.6	0.0153	4.0	0.17	98.1	3.8	88.3	20.0	-170	581
3S51, Dinkey Lakes pluton, IGSN: P4700000Y																
3S51-1	191	287	0.67	0.0462	22.8	0.1058	23.2	0.0166	4.0	0.18	106.2	4.2	102.1	22.4	8	549
3S51-2	126	353	0.36	0.0421	27.8	0.1000	28.0	0.0172	4.8	0.17	110.2	5.2	96.8	26.0	-221	700
3S51-3	314	722	0.43	0.0726	97.8	0.1525	98.4	0.0152	10.6	0.11	97.4	10.4	144.1	132.4	1003	2116
3S51-4	590	1652	0.36	0.0475	5.4	0.1053	8.0	0.0161	5.8	0.72	102.9	6.0	101.7	7.8	73	131
3S51-5	508	1321	0.38	0.0460	11.8	0.1033	12.0	0.0163	2.6	0.22	104.2	2.8	99.9	11.4	-2	284
3S51-6	391	860	0.45	0.0460	13.6	0.1033	15.8	0.0163	8.0	0.51	104.1	8.2	99.8	15.0	-3	328
3S51-7	317	761	0.42	0.0456	12.4	0.1074	14.8	0.0171	8.0	0.54	109.3	8.6	103.6	14.6	-24	302
3S51-8	294	500	0.59	0.0455	12.6	0.1085	12.8	0.0173	1.4	0.12	110.5	1.6	104.6	12.6	-26	306
3S51-9	337	573	0.59	0.0462	10.8	0.1003	12.6	0.0157	6.6	0.52	100.7	6.6	97.0	11.6	8	259
3S51-10	218	850	0.26	0.0510	16.6	0.1144	17.2	0.0163	4.6	0.26	103.9	4.6	110.0	18.0	242	384
3S51-11	588	1352	0.43	0.0504	20.6	0.1110	20.8	0.0160	3.2	0.16	102.1	3.4	106.8	21.0	214	476
3S51-12	342	1094	0.31	0.0487	51.0	0.1041	51.4	0.0155	5.8	0.11	99.2	5.6	100.6	49.2	132	1216
3S51-13	358	895	0.40	0.0504	10.8	0.1059	11.4	0.0152	3.4	0.30	97.5	3.4	102.2	11.2	214	252
3S51-14	318	859	0.37	0.0487	6.8	0.1102	7.8	0.0164	3.8	0.49	105.0	4.0	106.2	7.8	131	158
3S51-15	454	1317	0.34	0.0497	12.4	0.1071	12.8	0.0156	3.8	0.29	99.9	3.8	103.3	12.6	181	287
3S51-16	544	1360	0.40	0.0482	8.8	0.1052	9.6	0.0158	3.8	0.39	101.1	3.8	101.5	9.2	111	209
3S51-17	260	546	0.48	0.0457	12.6	0.0960	13.2	0.0153	4.2	0.31	97.6	4.0	93.1	11.8	-20	304
3S51-18	545	1254	0.43	0.0468	10.4	0.1016	10.8	0.0158	3.2	0.29	100.8	3.2	98.3	10.2	38	248
3S51-19	379	758	0.50	0.0529	27.2	0.1159	27.8	0.0159	5.4	0.19	101.7	5.4	111.3	29.4	323	623
3S51-20	391	978	0.40	0.0463	9.2	0.1071	9.4	0.0168	1.6	0.17	107.3	1.8	103.3	9.2	13	221
3S51-21	218	567	0.38	0.0488	20.2	0.1113	20.4	0.0165	1.4	0.07	105.8	1.4	107.2	20.6	138	477
3S51-22	562	1236	0.45	0.0480	9.8	0.1050	10.2	0.0159	3.0	0.30	101.5	3.0	101.4	9.8	99	231
3S51-23	463	1065	0.43	0.0472	8.4	0.1019	9.2	0.0157	3.6	0.39	100.3	3.6	98.6	8.6	57	201
3S51-24	476	1333	0.36	0.0482	16.0	0.1017	16.4	0.0153	3.6	0.22	98.0	3.4	98.4	15.4	107	378
3S51-25	609	1462	0.42	0.0471	9.6	0.1029	9.6	0.0159	1.8	0.19	101.4	1.8	99.5	9.2	53	227
95-16, Dinkey Creek Granodiorite, IGSN: P4700000Z																
95-16-1	851	1617	0.53	0.0476	6.2	0.1008	7.0	0.0154	3.2	0.47	98.4	3.2	97.5	6.4	78	146
95-16-2	430	731	0.59	0.0463	13.8	0.0936	14.4	0.0147	4.6	0.32	93.8	4.2	90.9	12.6	15	330
95-16-3	362	1086	0.33	0.0466	19.2	0.1009	19.6	0.0157	4.2	0.21	100.5	4.0	97.6	18.4	28	462
95-16-4	575	1610	0.36	0.0478	13.0	0.1025	13.4	0.0156	3.6	0.27	99.5	3.6	99.1	12.8	89	308
95-16-5	338	946	0.36	0.0474	10.8	0.1041	11.2	0.0159	3.2	0.29	101.9	3.4	100.5	10.8	69	255
95-16-6	255	740	0.34	0.0433	36.8	0.0955	37.4	0.0160	6.4	0.17	102.3	6.4	92.6	33.0	-152	919
95-16-7	477	1717	0.28	0.0471	8.8	0.1015	9.6	0.0156	4.0	0.42	100.1	4.0	98.2	9.0	52	209
95-16-8	1098	2306	0.48	0.0472	4.0	0.1070	6.4	0.0165	5.0	0.79	105.2	5.2	103.2	6.4	58	94
95-16-9	577	2135	0.27	0.0471	15.2	0.1067	15.2	0.0164	1.6	0.11	105.1	1.6	102.9	14.8	52	362
95-16-10	487	1851	0.26	0.0456	11.8	0.1033	12.6	0.0164	4.6	0.36	105.0	4.6	99.9	12.0	-22	284
95-16-11	687	1511	0.45	0.0462	8.6	0.0977	8.8	0.0153	2.6	0.29	98.1	2.4	94.6	8.0	7	205
95-16-12	461	1429	0.32	0.0463	6.6	0.1018	7.2	0.0159	3.0	0.42	101.9	3.0	98.5	6.8	16	158
95-16-13	650	1625	0.40	0.0464	8.8	0.1025	9.4	0.0160	3.4	0.37	102.4	3.4	99.1	9.0	19	211
95-16-14	518	1295	0.40	0.0475	11.0	0.1062	11.2	0.0162	2.2	0.19	103.6	2.2	102.5	11.0	77	264
95-16-15	424	1399	0.30	0.0465	17.6	0.1016	18.0	0.0158	3.2	0.18	101.2	3.4	98.2	16.8	26	424
96-16-16	513	1180	0.43	0.0470	14.0	0.1039	14.6	0.0160	4.0	0.28	102.6	4.0	100.4	13.8	49	333
96-16-17	300	810	0.37	0.0453	17.0	0.1008	17.2	0.0161	3.4	0.20	103.1	3.4	97.5	16.0	-37	412
96-16-18	585	1287	0.45	0.0475	6.2	0.1051	6.8	0.0160	3.0	0.45	102.6	3.2	101.5	6.6	76	146
96-16-19	672	1546	0.43	0.0459	8.0	0.1006	9.4	0.0159	4.8	0.52	101.7	5.0	97.3	8.8	-7	196

96-16-20	774	1316	0.59	0.0467	6.2	0.1000	7.2	0.0155	3.8	0.51	99.3	3.6	96.8	6.8	36	150
95-16-21	451	1443	0.31	0.0501	15.6	0.1126	16.2	0.0163	4.8	0.29	104.2	5.0	108.4	16.8	201	362
95-16-22	846	1946	0.43	0.0474	5.2	0.1005	5.8	0.0154	2.4	0.43	98.4	2.4	97.2	5.4	68	123
95-16-23	485	1504	0.32	0.0439	11.6	0.0954	11.8	0.0158	2.8	0.24	100.8	2.8	92.5	10.4	-115	284
95-16-24	552	1877	0.29	0.0478	13.4	0.1015	13.8	0.0154	3.4	0.24	98.5	3.2	98.1	13.0	88	318
95-16-25	810	2268	0.36	0.0489	10.8	0.1069	12.2	0.0159	5.6	0.46	101.4	5.6	103.1	12.0	142	253
95-17, Dinkey Creek Granodiorite, IGSN: P47000010																
95-17-1	279	753	0.37	0.0493	31.8	0.0984	33.2	0.0145	9.2	0.28	92.6	8.6	95.3	30.2	163	748
95-17-2	652	913	0.71	0.0466	13.6	0.0947	14.0	0.0147	3.4	0.24	94.4	3.2	91.9	12.2	28	325
95-17-3	490	1274	0.38	0.0484	11.4	0.1107	11.6	0.0166	1.8	0.15	106.0	1.8	106.6	11.8	120	270
95-17-4	607	1578	0.38	0.0477	13.2	0.1024	13.6	0.0156	3.2	0.23	99.7	3.0	99.0	12.8	83	314
95-17-6	670	1474	0.45	0.0471	7.0	0.1020	7.2	0.0157	1.8	0.25	100.6	1.8	98.6	6.8	52	165
95-17-7	902	2075	0.43	0.0483	6.8	0.1122	7.6	0.0168	3.4	0.44	107.7	3.6	108.0	7.6	114	159
95-17-8	565	1921	0.29	0.0472	8.0	0.0946	8.8	0.0145	3.4	0.38	93.1	3.2	91.8	7.6	58	193
95-17-9	612	1346	0.45	0.0497	24.8	0.1027	25.2	0.0150	4.2	0.17	95.8	4.0	99.3	23.8	183	579
95-17-10	675	1823	0.37	0.0474	9.6	0.1001	10.6	0.0153	4.4	0.41	98.0	4.2	96.8	9.8	69	229
95-17-11	552	1546	0.36	0.0495	5.2	0.1134	6.4	0.0166	3.6	0.58	106.3	3.8	109.0	6.6	170	121
95-17-12	694	1180	0.59	0.0476	17.8	0.1078	19.0	0.0164	7.0	0.37	105.0	7.2	104.0	18.8	79	421
95-17-13	591	1773	0.33	0.0463	5.2	0.1007	6.0	0.0158	3.2	0.52	100.9	3.2	97.4	5.6	15	125
95-17-14	928	2320	0.40	0.0465	7.4	0.0969	8.8	0.0151	4.8	0.54	96.7	4.6	93.9	8.0	22	179
95-17-16	664	1594	0.42	0.0471	7.4	0.1027	7.6	0.0158	2.2	0.29	101.2	2.2	99.3	7.2	53	176
95-17-17	822	1644	0.50	0.0486	9.6	0.1073	10.2	0.0160	3.8	0.37	102.5	3.8	103.5	10.0	127	224
95-17-18	640	1152	0.56	0.0487	8.0	0.1036	8.8	0.0154	3.6	0.40	98.7	3.4	100.1	8.4	134	188
95-17-19	485	922	0.53	0.0488	19.0	0.1045	19.4	0.0155	3.6	0.18	99.4	3.4	100.9	18.6	138	448
95-17-20	722	1516	0.48	0.0477	6.0	0.1007	7.0	0.0153	3.6	0.52	97.9	3.6	97.4	6.6	85	143
95-17-21	445	1513	0.29	0.0462	20.0	0.1028	20.2	0.0162	3.0	0.15	103.3	3.2	99.4	19.2	6	481
95-17-22	884	2122	0.42	0.0475	4.6	0.1064	6.0	0.0163	3.6	0.62	104.0	3.8	102.7	5.8	73	110
95-17-22	542	1192	0.45	0.0474	9.4	0.1002	11.0	0.0153	5.8	0.52	98.1	5.6	97.0	10.2	69	225
95-17-24	439	702	0.63	0.0469	11.2	0.1054	11.4	0.0163	2.4	0.22	104.2	2.6	101.8	11.0	45	265
95-17-25	398	1313	0.30	0.0469	10.0	0.1033	10.4	0.0160	2.6	0.25	102.2	2.6	99.8	9.8	45	240
95-17-26	858	1888	0.45	0.0471	5.4	0.1015	6.0	0.0156	2.6	0.43	99.9	2.6	98.2	5.6	56	129
96-7, Dinkey Creek Granodiorite, IGSN: P47000011																
96-7-1	648	1944	0.33	0.0474	7.4	0.1027	7.6	0.0157	1.4	0.18	100.4	1.4	99.3	7.0	71	176
96-7-2	730	2117	0.34	0.0476	7.6	0.1007	8.4	0.0154	3.2	0.39	98.3	3.2	97.5	7.8	78	183
96-7-3	616	2033	0.30	0.0490	10.4	0.1094	11.0	0.0162	3.4	0.31	103.5	3.4	105.4	11.0	148	245
96-7-4	596	1907	0.31	0.0487	7.2	0.1051	8.0	0.0157	3.4	0.43	100.2	3.4	101.4	7.8	132	170
96-7-5	579	1737	0.33	0.0488	7.8	0.1050	8.0	0.0156	2.2	0.27	99.8	2.2	101.4	7.8	140	182
96-7-6	435	1349	0.32	0.0493	13.4	0.1063	14.2	0.0157	4.4	0.31	100.1	4.2	102.6	13.8	161	315
96-7-7	463	1528	0.30	0.0471	10.2	0.1026	11.0	0.0158	4.0	0.36	101.0	4.0	99.1	10.4	55	244
96-7-8	383	804	0.48	0.0478	14.8	0.0993	15.0	0.0151	2.8	0.19	96.3	2.8	96.1	13.8	91	350
96-7-9	717	1864	0.38	0.0528	27.6	0.1149	27.6	0.0158	2.4	0.08	100.8	2.4	110.4	28.8	322	628
96-7-10	560	1960	0.29	0.0476	11.2	0.1006	11.8	0.0153	4.0	0.33	98.0	3.8	97.3	11.0	80	264
96-7-11	705	1974	0.36	0.0474	6.6	0.0975	6.8	0.0149	2.0	0.30	95.6	2.0	94.5	6.2	68	156
96-7-12	741	2001	0.37	0.0505	17.6	0.1070	18.4	0.0154	5.6	0.31	98.3	5.6	103.2	18.2	218	407
96-7-13	462	1709	0.27	0.0470	13.4	0.1018	14.0	0.0157	4.2	0.30	100.4	4.2	98.4	13.2	51	320
96-7-14	638	1595	0.40	0.0496	17.2	0.1102	17.6	0.0161	3.6	0.21	103.0	3.8	106.2	17.6	177	401
96-7-15	378	1285	0.29	0.0448	20.2	0.0999	20.6	0.0162	4.2	0.20	103.4	4.4	96.7	19.0	-67	493
96-7-16	408	1550	0.26	0.0468	13.4	0.1097	14.2	0.0170	4.4	0.31	108.8	4.6	105.7	14.2	37	322
96-7-17	482	1205	0.40	0.0495	11.8	0.1078	12.6	0.0158	4.0	0.32	101.0	4.0	103.9	12.4	171	277
96-7-18	912	2462	0.37	0.0492	4.6	0.1183	7.2	0.0175	5.4	0.77	111.5	6.0	113.6	7.6	157	106
96-7-19	396	1030	0.38	0.0634	50.6	0.1433	51.2	0.0164	7.8	0.15	104.8	8.0	136.0	65.2	722	1091
96-7-20	903	4334	0.21	0.0477	4.4	0.1011	6.6	0.0154	5.0	0.76	98.3	5.0	97.8	6.2	86	104
96-7-22	379	1137	0.33	0.0479	20.2	0.1031	20.6	0.0156	4.4	0.22	99.8	4.4	99.6	19.6	95	477
96-7-23	449	1527	0.29	0.0468	11.4	0.1039	11.4	0.0161	1.0	0.09	103.0	1.0	100.4	10.8	40	272
96-7-24	632	1959	0.32	0.0476	8.6	0.1037	9.0	0.0158	2.6	0.29	101.1	2.6	100.2	8.6	79	205
96-7-25	593	1542	0.38	0.0468	12.4	0.1033	12.6	0.0160	2.2	0.18	102.4	2.4	99.8	12.0	38	297
13JLE-4b, Big Meadows Orb Core (Big Meadows pluton), IGSN: P47000013																
4-1	536	219	0.41	0.0488	2.7	0.0998	2.0	0.0148	1.3	0.36	94.7	1.2	96.6	1.9	139	41
4-2	712	294	0.41	0.0483	2.5	0.0994	2.1	0.0149	1.3	0.59	95.0	1.2	96.2	2.0	115	34
4-3	904	347	0.38	0.0488	2.4	0.1008	1.8	0.0150	1.3	0.69	95.7	1.2	97.5	1.6	130	30
4-4	730	358	0.49	0.0476	2.5	0.0976	2.2	0.0149	1.1	0.73	95.5	1.1	94.6	1.9	83	33
4-5	898	420	0.47	0.0492	2.5	0.1022	1.7	0.0151	1.3	0.56	96.6	1.2	98.8	1.6	151	34
4-6	1008	489	0.49	0.0486	2.4	0.0999	1.8	0.0150	1.5	0.73	95.8	1.5	96.7	1.6	122	29
4-7*	324	158	0.49	0.0494	2.8	0.1048	2.6	0.0155	1.1	0.49	99.0	1.1	101.1	2.5	165	46
4-8	339	184	0.54	0.0502	2.8	0.1051	2.4	0.0152	1.3	0.57	96.9	1.3	101.5	2.3	198	43
4-9*	396	229	0.58	0.0492	3.0	0.1055	2.3	0.0156	1.5	0.51	99.9	1.4	101.8	2.2	153	50
4-10	548	354	0.65	0.0486	2.6	0.1004	2.1	0.0150	1.3	0.69	95.8	1.2	97.1	2.0	130	36
4-11	313	119	0.38	0.0506	3.3	0.1046	2.8	0.0149	1.3	0.37	95.5	1.2	101.0	2.6	214	58
4-12	388	179	0.46	0.0494	2.5	0.1015	1.8	0.0150	1.4	0.49	95.8	1.3	98.1	1.7	165	36
4-13	536	211	0.39	0.0493	2.6	0.1034	2.0	0.0152	1.4	0.68	97.2	1.4	99.9	2.0	159	36
4-14	361	229	0.64	0.0492	3.0	0.0993	3.1	0.0147	1.5	0.62	93.8	1.4	96.1	2.8	172	54

4-15	172	68	0.39	0.0527	3.6	0.1090	3.4	0.0152	1.7	0.35	97.0	1.7	105.0	3.4	302	66
4-16	414	180	0.43	0.0498	2.8	0.1023	2.1	0.0148	1.4	0.51	94.5	1.4	98.9	2.0	174	44
4-17*	715	526	0.74	0.0494	2.3	0.0964	1.8	0.0142	1.6	0.77	90.6	1.4	93.5	1.6	165	26
4-18	381	147	0.39	0.0493	2.7	0.1012	2.5	0.0150	1.7	0.64	95.7	1.7	97.9	2.3	158	40
4-19	1453	733	0.50	0.0485	2.2	0.0982	1.6	0.0148	1.4	0.87	94.4	1.3	95.1	1.5	121	21
4-20	711	340	0.48	0.0483	2.6	0.0967	2.5	0.0147	1.7	0.76	93.7	1.6	94.0	2.2	111	35
4-21	1116	558	0.50	0.0479	2.4	0.0967	1.9	0.0147	1.4	0.65	94.3	1.3	94.0	1.6	96	30
4-22	550	346	0.63	0.0478	2.6	0.0986	2.5	0.0149	1.6	0.74	95.3	1.5	95.4	2.3	85	37
4-23	265	139	0.53	0.0487	3.5	0.1015	3.2	0.0150	1.5	0.47	96.1	1.5	98.1	2.9	134	60
4-24	895	465	0.52	0.0489	2.5	0.1012	2.5	0.0149	1.7	0.75	95.4	1.6	97.8	2.3	142	34
13JLE-16, Deer Creek Gabbro Orb Core (in Dinkey Creek Granodiorite), IGSN: P47000015																
16-1	310	119	0.38	0.0502	3.0	0.1058	2.6	0.0156	1.6	0.52	99.5	1.6	102.1	2.5	191	48
16-2	659	244	0.37	0.0498	2.3	0.1056	1.8	0.0156	1.5	0.64	100.0	1.5	101.9	1.7	183	28
16-3	640	254	0.40	0.0540	2.5	0.1177	2.0	0.0157	1.4	0.65	100.3	1.4	113.0	2.1	368	34
16-4	475	166	0.35	0.0489	2.6	0.1062	2.2	0.0156	1.7	0.63	99.8	1.7	102.4	2.1	141	36
16-5	129	47	0.36	0.0519	3.7	0.1139	3.7	0.0156	2.1	0.48	99.8	2.1	109.4	3.8	282	72
16-6	286	102	0.36	0.0490	3.5	0.1092	3.4	0.0160	1.7	0.54	102.5	1.8	105.2	3.4	158	61
16-7	618	258	0.42	0.0494	2.7	0.1054	2.0	0.0155	1.4	0.51	98.8	1.4	102.0	2.0	168	40
16-8	273	111	0.41	0.0496	3.1	0.1073	2.6	0.0157	1.5	0.40	100.4	1.4	103.4	2.5	183	54
16-9	489	177	0.36	0.0500	2.8	0.1066	2.6	0.0156	1.3	0.56	100.0	1.3	102.8	2.6	197	45
16-10	273	226	0.83	0.0493	3.0	0.1045	3.1	0.0153	1.6	0.47	98.0	1.5	100.8	3.0	160	50
16-11	1613	1214	0.75	0.0485	2.2	0.1052	1.8	0.0157	1.5	0.89	100.5	1.5	101.5	1.7	118	19
16-12	256	115	0.45	0.0500	3.0	0.1092	2.3	0.0157	1.4	0.34	100.4	1.4	105.6	2.4	190	49
16-13*	147	47	0.32	0.0508	4.1	0.1140	4.6	0.0164	1.9	0.53	105.1	2.0	109.5	4.8	222	78
16-14	1321	600	0.45	0.0481	2.2	0.1037	1.6	0.0156	1.3	0.80	99.5	1.3	100.2	1.6	101	22
16-15	377	129	0.34	0.0497	2.8	0.1050	2.5	0.0154	1.6	0.61	98.5	1.5	101.4	2.4	178	43
16-16	204	127	0.62	0.0506	3.0	0.1099	2.4	0.0156	1.4	0.32	100.1	1.4	105.8	2.4	218	50
16-17*	390	229	0.59	0.0487	2.9	0.1148	2.9	0.0170	1.6	0.68	108.7	1.8	110.3	3.0	130	47
16-18	265	123	0.46	0.0503	3.3	0.1072	3.1	0.0157	1.4	0.42	100.1	1.4	103.3	3.1	203	59
16-19	810	286	0.35	0.0489	2.5	0.1057	2.1	0.0157	1.5	0.67	100.3	1.5	102.0	2.0	140	36
16-20	699	595	0.85	0.0486	2.5	0.1062	2.0	0.0157	1.7	0.72	100.4	1.7	102.5	1.9	126	35
16-21	946	583	0.62	0.0484	2.3	0.1069	2.1	0.0161	1.4	0.76	102.7	1.5	103.1	2.0	116	27
16-22	595	256	0.43	0.0491	2.5	0.1067	1.8	0.0158	1.6	0.59	101.3	1.6	102.9	1.7	143	37
16-23	703	292	0.41	0.0488	2.4	0.1068	1.7	0.0158	1.5	0.68	100.8	1.5	103.0	1.6	137	30
16-24	719	278	0.39	0.0485	2.6	0.1033	2.1	0.0155	1.5	0.66	99.4	1.4	99.8	2.0	124	36
13JLE-17, Dinkey Creek Granodiorite (Deer Creek orb host), IGSN: P47000016																
17-1	242	78	0.32	0.0495	3.5	0.1093	3.2	0.0160	1.8	0.53	102.0	1.8	105.3	3.2	169	60
17-2	446	175	0.39	0.0484	2.8	0.1032	2.9	0.0156	1.7	0.66	99.9	1.7	99.7	2.8	111	44
17-3	231	94	0.41	0.0495	3.3	0.1052	3.3	0.0155	1.7	0.65	99.1	1.7	101.9	3.2	169	56
17-4	681	403	0.59	0.0486	2.6	0.1018	2.4	0.0153	1.7	0.71	98.0	1.6	98.4	2.2	121	38
17-5	183	84	0.46	0.0496	4.0	0.1045	3.0	0.0154	1.8	0.15	98.7	1.8	100.9	2.8	170	73
17-6	165	63	0.38	0.0515	4.2	0.1113	4.0	0.0158	1.8	0.35	101.1	1.8	107.0	4.0	249	79
17-7	180	83	0.46	0.0530	3.2	0.1113	3.1	0.0154	1.6	0.58	98.6	1.6	107.1	3.2	328	56
17-8	227	91	0.40	0.0505	3.9	0.1101	3.5	0.0159	1.6	0.34	101.7	1.7	105.9	3.5	218	73
17-9	289	111	0.38	0.0491	2.9	0.1031	2.6	0.0154	1.6	0.60	98.7	1.6	99.6	2.5	151	45
17-10	214	91	0.43	0.0508	3.2	0.1071	3.1	0.0153	1.4	0.60	98.1	1.4	103.3	3.0	226	58
17-11	190	73	0.38	0.0493	4.2	0.1072	3.7	0.0157	1.7	0.32	100.1	1.6	103.3	3.7	156	78
17-12	177	83	0.47	0.0512	3.9	0.1083	4.0	0.0154	1.6	0.50	98.2	1.6	104.9	3.8	241	71
17-13	160	65	0.40	0.0517	4.2	0.1089	2.9	0.0155	1.6	0.20	98.9	1.6	104.9	3.0	260	78
17-14	228	69	0.30	0.0488	3.3	0.1040	2.9	0.0155	1.7	0.44	99.3	1.6	100.4	2.8	135	58
17-15	202	93	0.46	0.0515	3.4	0.1096	3.1	0.0154	1.4	0.45	98.3	1.4	105.6	3.1	253	62
17-16	137	57	0.41	0.0510	3.7	0.1086	3.8	0.0154	1.9	0.58	98.3	1.8	104.6	3.7	233	68
17-17	142	55	0.39	0.0504	4.4	0.1081	4.0	0.0155	1.8	0.27	99.0	1.8	104.1	3.9	214	87
17-18	151	60	0.39	0.0513	3.7	0.1086	3.7	0.0155	1.7	0.30	99.4	1.7	104.6	3.6	244	69
17-19	193	84	0.43	0.0495	3.3	0.1078	3.3	0.0157	1.9	0.52	100.4	1.9	103.8	3.3	171	59
17-20	190	77	0.41	0.0502	3.6	0.1088	2.6	0.0155	1.7	0.27	99.0	1.7	104.8	2.6	198	65
17-21	155	59	0.38	0.0506	3.4	0.1105	3.6	0.0155	2.0	0.60	99.1	2.0	106.3	3.7	216	62
17-22	133	58	0.43	0.0522	4.0	0.1127	4.0	0.0155	1.7	0.46	99.0	1.7	108.3	4.1	278	75
17-23	218	98	0.45	0.0498	3.1	0.1078	3.0	0.0157	1.9	0.60	100.4	1.9	103.9	2.9	181	52
17-24	129	59	0.46	0.0518	4.2	0.1101	4.0	0.0155	1.6	0.26	98.9	1.6	106.0	4.0	260	80
13JLE-18, Deer Creek Gabbro Orb Core (in Dinkey Creek Granodiorite), IGSN: P47000017																
18-1	87	42	0.48	0.0494	3.0	0.1061	2.0	0.0154	1.4	0.30	98.7	1.4	102.4	1.9	163	48
18-2	110	64	0.58	0.0493	2.8	0.1058	2.5	0.0155	1.4	0.53	98.8	1.4	102.0	2.4	157	47
18-3	308	184	0.60	0.0478	2.3	0.1026	1.3	0.0156	1.0	0.52	99.8	0.9	99.2	1.2	85	25
18-4	192	85	0.44	0.0514	5.6	0.1116	5.9	0.0157	1.3	0.73	100.1	1.3	107.1	5.8	153	35
18-5	192	76	0.40	0.0522	7.2	0.1130	8.8	0.0155	1.4	0.94	99.2	1.3	108.2	8.5	173	62
18-6*	110	72	0.65	0.0506	3.1	0.1638	2.8	0.0235	1.2	0.85	149.5	1.8	153.9	4.0	210	50
18-7*	308	143	0.46	0.0489	2.4	0.1076	1.6	0.0160	1.0	0.56	102.1	1.0	103.8	1.6	138	30
18-8	173	81	0.47	0.0505	2.4	0.1076	2.0	0.0155	1.3	0.60	99.3	1.3	103.7	2.0	209	33
18-9	167	58	0.35	0.0491	2.8	0.1074	2.6	0.0158	1.3	0.48	101.2	1.4	103.5	2.6	148	41
18-10	216	84	0.39	0.0486	3.2	0.1052	3.0	0.0157	1.3	0.84	100.2	1.3	101.5	2.8	105	32

18-11*	136	56	0.41	0.0486	2.6	0.1131	8.1	0.0162	1.3	0.92	103.6	1.4	108.2	7.4	126	38
18-12	663	551	0.83	0.0480	2.1	0.1057	4.2	0.0156	1.3	0.71	100.0	1.3	101.8	3.8	99	16
18-13	197	111	0.57	0.0489	2.5	0.1052	1.7	0.0156	1.1	0.28	99.5	1.0	101.5	1.6	141	33
18-14	254	94	0.37	0.0482	2.4	0.1030	1.7	0.0157	1.3	0.67	100.3	1.3	99.6	1.7	108	31
18-15	91	29	0.32	0.0493	3.0	0.1071	2.6	0.0158	1.3	0.46	100.9	1.3	103.3	2.5	158	49
18-16	188	114	0.61	0.0482	2.4	0.1030	1.9	0.0154	1.2	0.69	98.7	1.1	99.5	1.8	106	29
18-17	406	125	0.31	0.0486	2.2	0.1037	1.4	0.0156	1.3	0.69	99.6	1.3	100.1	1.3	123	19
18-18	158	84	0.53	0.0488	2.5	0.1048	2.0	0.0156	1.5	0.71	99.5	1.5	101.2	2.0	129	34
18-19	393	297	0.76	0.0487	2.1	0.1041	1.2	0.0155	1.2	0.74	98.9	1.1	100.5	1.2	136	19
18-20	104	39	0.38	0.0496	2.6	0.1081	2.2	0.0157	1.4	0.62	100.1	1.4	104.2	2.2	172	38
18-21	136	47	0.34	0.0493	2.7	0.1074	2.0	0.0158	1.1	0.58	101.0	1.1	103.5	2.0	160	38
18-22	182	78	0.43	0.0489	2.5	0.1040	1.8	0.0154	1.2	0.57	98.7	1.1	100.4	1.8	142	35
18-23	627	276	0.44	0.0481	2.2	0.1028	1.4	0.0156	1.0	0.74	99.5	1.0	99.4	1.3	103	20

APPENDIX 2: ID-TIMS ZIRCON U-PB DATA FOR THE SHAVER INTRUSIVE SUITE

	Composition				Isotopic Ratios							Ages (Ma)						
Fraction	U (ppm)	Pb (pg)[a]	Th/U[b]	Total common Pb (pg)[c]	$^{206}Pb/^{204}Pb$[d]	$^{206}Pb/^{238}U$[e]	Error (2σ%)	$^{207}Pb/^{235}U$[e]	Error (2σ%)	$^{207}Pb/^{206}Pb$[e]	Error (2σ%)	$^{206}Pb/^{238}U$[fg]	Error (2σ abs.)	$^{207}Pb/^{235}U$[g]	Error (2σ abs.)	$^{207}Pb/^{206}Pb$[g]	Error (2σ abs.)	Correlation coefficient
DC12-02, Dinkey Creek Granodiorite, IGSN: P4700000D																		
F-1	934	102	0.39	6.7	976	0.0157572	0.14	0.103670	1.18	0.047717	1.10	100.88	0.14	100.16	1.12	85.3	26.1	0.574
F-7	1270	48	0.41	1.2	2588	0.0157948	0.10	0.103284	0.49	0.047426	0.45	101.12	0.10	99.80	0.47	70.7	10.6	0.554
F-8	1450	68	0.39	2.5	1714	0.0158352	0.29	0.099666	2.07	0.045648	1.66	101.38	0.29	96.47	1.90	-20.9	40.3	1.306
F-9	155	12	0.42	0.8	921	0.0157376	0.12	0.104017	1.26	0.047958	1.19	100.76	0.12	100.48	1.21	96.1	28.1	0.628
F-10	420	25	0.42	1.6	974	0.0158754	0.18	0.106039	1.48	0.048465	1.38	101.63	0.18	102.34	1.44	121.0	32.5	0.594
F-11	1300	103	0.41	3.0	2176	0.0158494	0.11	0.104361	0.53	0.047777	0.48	101.47	0.11	100.79	0.51	87.2	11.5	0.497
F-12	601	66	0.43	2.8	1493	0.0158322	0.14	0.105184	0.82	0.048206	0.76	101.36	0.14	101.55	0.79	108.3	17.9	0.503
F-14	1160	107	0.42	5.0	1356	0.0158128	0.12	0.103762	0.91	0.047613	0.84	101.23	0.12	100.24	0.87	79.0	20.0	0.598
MG12-03, Mount Givens Granodiorite, IGSN: P4700000E																		
F-1	477	92	0.56	2.3	2395	0.0142404	0.13	0.093833	0.65	0.047790	0.60	91.23	0.12	91.07	0.57	88.9	14.2	0.490
F-2	301	42	0.47	1.7	1558	0.0142628	0.12	0.093665	0.83	0.047629	0.75	91.37	0.11	90.91	0.72	80.9	17.7	0.728
F-3	642	114	0.52	1.4	4978	0.0142711	0.17	0.093787	0.55	0.047663	0.45	91.42	0.15	91.03	0.48	82.6	10.8	0.691
F-5	499	29	0.55	2.7	669	0.0142638	0.14	0.094558	1.71	0.048101	1.62	91.38	0.13	91.74	1.50	103.2	38.3	0.696
DC12-04, Dinkey Creek Granodiorite, IGSN: P4700000F																		
F-1	1010	54	0.41	4.6	756	0.0158257	0.12	0.105108	1.47	0.048169	1.40	101.31	0.12	101.48	1.42	107.6	33.0	0.603
F-2	1660	24	0.44	1.3	1200	0.0158455	0.10	0.103999	0.95	0.047602	0.90	101.44	0.11	100.46	0.91	79.5	21.3	0.587
F-5	448	31	0.34	0.8	2440	0.0158473	0.32	0.105780	1.91	0.048411	1.61	101.45	0.32	102.10	1.85	119.4	37.9	0.957
F-6	914	33	0.35	1.3	1628	0.0157714	0.11	0.104497	0.75	0.048054	0.69	100.97	0.11	100.92	0.72	101.9	16.3	0.566
F-7	197	7	0.40	0.8	579	0.0158801	0.14	0.104530	2.09	0.047740	2.02	101.66	0.14	100.95	2.01	86.4	48.0	0.533
DC12-05, Dinkey Creek Granodiorite, IGSN: P4700000G																		
F-1	771	58	0.39	1.4	2557	0.0158218	0.11	0.104538	0.56	0.047941	0.49	101.29	0.11	100.96	0.54	95.3	11.6	0.701
F-3	768	66	0.39	1.8	2385	0.0158371	0.12	0.105183	0.53	0.048190	0.47	101.39	0.12	101.55	0.51	107.6	11.1	0.556
F-4	990	36	0.40	3.3	709	0.0158316	0.19	0.104193	1.66	0.047754	1.59	101.35	0.19	100.64	1.59	86.0	37.6	0.429
F-5	633	58	0.40	1.6	2287	0.0158266	0.09	0.104866	0.52	0.048056	0.48	101.32	0.09	101.26	0.50	102.0	11.4	0.509
F-6	776	45	0.40	1.6	1801	0.0158659	0.12	0.104640	0.80	0.047833	0.73	101.57	0.12	101.05	0.77	91.0	17.3	0.596
F-7	625	38	0.40	1.9	1318	0.0158543	0.13	0.103623	1.10	0.047403	1.01	101.50	0.14	100.11	1.05	69.6	24.0	0.719

[a]Total mass of radiogenic Pb.

[b]Th contents calculated from radiogenic ^{208}Pb and ^{230}Th-corrected $^{206}Pb/^{238}U$ date of the sample, assuming concordance between U-Pb and Th-Pb systems.

[c]Total mass of common Pb.

[d]Measured ratio corrected for fractionation and spike contribution only.

[e]Measured ratios corrected for fractionation, tracer and blank. Pb blank ratios: $^{206}Pb/^{204}Pb = 18.687 \pm 0.25$; $^{207}Pb/^{204}Pb = 15.658 \pm 0.25$; and $^{208}Pb/^{204}Pb = 38.258 \pm 0.5$ (1σ abs.)

[f]Corrected for initial Th/U disequilibrium using radiogenic ^{208}Pb and $Th/U_{[magma]}$, which is assumed to be approximated by the measured whole rock Th/U ratio. Th/U ratios used: 3.60 (DC12-02), 1.79 (MG12-03), 2.86 (DC12-04), 4.13 (DC12-05).

[g]Isotopic dates calculated using $\lambda_{238} = 1.55125E^{-10}$ (Jaffey et al. 1971) and $\lambda_{235} = 9.8485E^{-10}$ (Jaffey et al. 1971).

REFERENCES

Ague, J.J., and Brimhall, G.H., 1987, Granites of the batholiths of California: products of local assimilation and regional-scale crustal contamination (USA): Geology, v. 15, p. 63–66, doi: 10.1130/0091-7613(1987)15<63:GOTBOC>2.0.CO;2.

Ague, J.J., and Brimhall, G.H., 1988a, Regional variations in bulk chemistry, mineralogy, and the compositions of mafic and accessory minerals in the batholiths of California: Geological Society of America Bulletin, v. 100, p. 891–911, doi: 10.1130/0016-7606(1988)100<0891:RVIBCM>2.3.CO;2.

Ague, J.J., and Brimhall, G.H., 1988b, Magmatic arc asymmetry and distribution of anomalous plutonic belts in the batholiths of California: Effects of assimilation, crustal thickness, and depth of crystallization: Geological Society of America Bulletin, v. 100, p. 912–927, doi: 10.1130/0016-7606(1988)100<0912:MAAADO>2.3.CO;2.

Aleinikoff, J.N., Reed, J.C., and Wooden, J.L., 1993, Lead isotopic evidence for the origin of Paleo- and Mesoproterozoic rocks of the Colorado Province, U.S.A.: Precambrian Research, v. 63, p. 97–122.

Ali, G.A.H., Reiners, P.W., and Ducea, M.N., 2009, Unroofing history of Alabama and Poverty Hills basement blocks, Owens Valley, California, from apatite (U–Th)/He thermochronology: International Geology Review, v. 51, p. 1034–1050, doi: 10.1080/00206810902965270.

Annen, C., 2009, From plutons to magma chambers: Thermal constraints on the accumulation of eruptible silicic magma in the upper crust: Earth and Planetary Science Letters, v. 284, p. 409–416, doi: 10.1016/j.epsl.2009.05.006.

Annen, C., and Sparks, R.S.J., 2002, Effects of repetitive emplacement of basaltic intrusions on thermal evolution and melt generation in the crust: Earth and Planetary Science Letters, v. 203, p. 937–955, http://www.sciencedirect.com/science/article/pii/S0012821X02009299 (accessed October 2012).

Bachmann, O., and Bergantz, G.W., 2004, On the Origin of Crystal-poor Rhyolites: Extracted from Batholithic Crystal Mushes: Journal of Petrology, v. 45, p. 1565–1582, doi: 10.1093/petrology/egh019.

Bachmann, O., and Bergantz, G.W., 2008, Rhyolites and their Source Mushes across Tectonic Settings: Journal of Petrology, v. 49, p. 2277–2285, doi: 10.1093/petrology/egn068.

Bachmann, O., Dungan, M.A., and Lipman, P.W., 2002, The Fish Canyon Magma Body, San Juan Volcanic Field, Colorado: Rejuvenation and Eruption of an Upper-Crustal Batholith: Journal of Petrology, v. 43, p. 1469–1503, doi: 10.1093/petrology/43.8.1469.

Bachmann, O., Miller, C.F., and de Silva, S.L., 2007, The volcanic–plutonic connection as a stage for understanding crustal magmatism: Journal of Volcanology and Geothermal Research, v. 167, p. 1–23, doi: 10.1016/j.jvolgeores.2007.08.002.

Bacon, C.R., Bruggman, P.E., Christiansen, R.L., Clynne, M.A., Donnelly-Nolan, J.M., and Hildreth, W., 1997, Primitive Magmas At Five Cascade Volcanic Fields: Melts From Hot, Heterogeneous Sub-Arc Mantle: The Canadian Mineralogist, v. 35, p. 397–423.

Bailley, T., 2010, A reevaluation of the origin of Late Cretaceous and younger magmatism in the southern Rocky Mountain region using space-time-composition patterns in volcanic rocks and geochemical studies of xenoliths [Ph.D. thesis]: Boulder, University of Colorado, 153 p.

Baird, A.K., Baird, K.W., and Welday, E.E., 1979, Batholithic rocks of the northern Peninsular and Transverse Ranges, southern California: Chemical composition and variation: *in* Abbott, P.L., and Todd, V.R., eds., Mesozoic crystalline rocks: Peninsular Ranges batholith and pegmatites, Point Sal ophiolite: San Diego, California, Department of Geological Sciences, San Diego State University, Geological Society of America Annual Meeting Guidebook, p. 111-132.

Baker, E.H., and Jones, J.V., 2008, Age and deformational characteristics of the Paleoproterozoic Denny Creek Granodiorite, Collegiate Peaks Wilderness Area, Colorado: Geological Society of America Abstracts with Programs, v. 40, no. 1, p. 69.

Barbarin, B., Dodge, F.C.W., Kistler, R.W., and Bateman, P.C., 1989, Mafic inclusions, aggregates and dikes in granitoid rocks, central Sierra Nevada batholith, California--Analytic data: U.S. Geological Survey Professional Paper 1899, 28 p.

Barboni, M., and Schoene, B., 2014, Short eruption window revealed by absolute crystal growth rates in a granitic magma: Nature Geoscience, v. 7, p. 524–528, doi: 10.1038/ngeo2185.

Barker, F., and Stein, H.J., 1990, Origin of Laramide magmas of the Colorado Mineral Belt over a leaky transform in the flatly subducted Farallon plate: Geological Society of America Abstracts with Programs, v. 22, no. 3, p. 5.

Bartley, J.M., Glazner, A.F., Coleman, D.S., Kylander-Clark, A., Mapes, R., and Friedrich, A.M., 2007, Large Laramide dextral offset across Owens Valley, California, and its possible relation to tectonic unroofing of the southern Sierra Nevada, *in* Till, A.B., Roeske, S.M., Sample, J.C., and Foster, D.A. eds., Exhumation Associated with Continental Strike-Slip Fault Systems: Geological Society of America Special Paper 434, p. 129–148, doi: 10.1130/2007.2434(07).

Bartley, J.M., Coleman, D.S., and Glazner, A.F., 2008, Incremental pluton emplacement by magmatic crack-seal: Transactions of the Royal Society of Edinburgh: Earth Sciences, v. 97, p. 383–396, doi: 10.1017/S0263593300001528.

Bartley, J.M., Glazner, A.F., and Mahan, K.H., 2012, Formation of pluton roofs, floors, and walls by crack opening at Split mountain, Sierra Nevada, California: Geosphere, v. 8, p. 1086–1103, doi: 10.1130/GES00722.1.

Bateman, P.C., 1965, Geologic map of the Blackcap Mountain quadrangle, Fresno County, California: U.S. Geological Survey Map GQ-428, scale 1:62,500.

Bateman, P.C., 1992, Plutonism in the Central Part of the Sierra Nevada Batholith, California: U.S. Geological Survey Professional Paper 1483, 194 p.

Bateman, P.C., and Wones, D.R., 1972a, Geologic Map of the Huntington Lake Quadrangle, Central Sierra Nevada, California: U.S. Geological Survey Map GQ-987, scale 1:62,500.

Bateman, P.C., and Wones, D.R., 1972b, Huntington Lake Quadrangle, Central Sierra Nevada, California-Analytic Data: U.S. Geological Survey Professional Paper 724-A, 22 p.

Bateman, P.C., Clark, L.D., Huber, N.K., Moore, J.G., and Rirehart, C.D., 1963, The Sierra Nevada batholith-A synthesis of recent work across the central part: U.S. Geological Survey Professional Paper 414-D, p. 1–46.

Bateman, P.C., Lockwood, J.P., and Lydon, P.A., 1971, Geologic map of the Kaiser Peak quadrangle, central Sierra Nevada, California: U.S. Geological Survey Map GQ-894, scale 1:62,500.

Beanland, S., and Clark, M.M., 1994, The Owens Valley Fault Zone, Eastern California, and Surface Faulting Associated with the 1872 Earthquake: U.S. Geological Survey Bulletin 1982, p. 38.

Beck, C.L., 2013, New insights into migration of the Cretaceous Sierran arc using high-precision U-Pb geochronology [M.S. thesis]: Chapel Hill, University of North Carolina at Chapel Hill, 56 p.

Bickford, M.E., and Boardman, S.J., 1984, A Proterozoic Volcano-Plutonic Terrane, Gunnison and Salida Areas, Colorado: The Journal of Geology, v. 92, p. 657–666, doi: 10.1086/628904.

Bickford, M.E., and Hill, B.M., 2007, Does the arc accretion model adequately explain the Paleoproterozoic evolution of southern Laurentia?: An expanded interpretation: Geology, v. 35, p. 167–170, doi: 10.1130/G23174A.1.

Bickford, M.E., Mueller, P.A., Kamenov, G.D., and Hill, B.M., 2008, Crustal evolution of southern Laurentia during the Paleoproterozoic: Insights from zircon Hf isotopic studies of ca. 1.75 Ga rocks in central Colorado: Geology, v. 36, p. 555–558, doi: 10.1130/G24700A.1.

Bierman, P.R., Gillespie, A.R., and Caffee, M.W., 1995a, Cosmogenic Ages for Earthquake Recurrence Intervals and Debris Flow Fan Deposition, Owens Valley, California: Science, v. 270, p. 447–450, doi: 10.2307/2889058.

Bierman, P., Gillespie, A., Caffee, M., and Elmore, D., 1995b, Estimating erosion rates and exposure ages with 36Cl produced by neutron activation: Geochimica et Cosmochimica Acta, v. 59, p. 3779–3798, doi: 10.1016/0016-7037(95)00267-4.

Bindeman, I.N., and Simakin, A.G., 2014, Rhyolites-Hard to produce, but easy to recycle and sequester: Integrating microgeochemical observations and numerical models: Geosphere, v. 10, p. 930–957, doi: 10.1130/GES00969.1.

Boehnke, P., Watson, E.B., Trail, D., Harrison, T.M., and Schmitt, A.K., 2013, Zircon saturation re-revisited: Chemical Geology, v. 351, p. 324–334, doi: 10.1016/j.chemgeo.2013.05.028.

Bookstrom, A.A., Carten, R.B., Shannon, J.R., and Smith, R.P., 1988, Origin of bimodal leucogranite-lamprophyre suites, Climax and Red Mountain porphyry molybdenum systems, Colorado, *in* Drexler, J.W., and Larson, E.E., eds., Cenozoic volcanism in the southern Rocky Mountains revisited: A tribute to Rudy C. Epis—Part 3: Colorado School of Mines Quarterly, v. 83, no. 2, p. 1–24.

Bowring, J.F., McLean, N.M., and Bowring, S.A., 2011, Engineering cyber infrastructure for U-Pb geochronology: Tripoli and U-Pb_Redux: Geochemistry Geophysics Geosystems, v. 12, doi: 10.1029/2010GC003479.

Bradford, K.J., 1995, Petrology of a mafic intrusive suite in the central Sierra Nevada batholith, California [M.S. thesis]: Chapel Hill, University of North Carolina, 63 p.

Calkins, F. C., 1930, The granitic rocks of the Yosemite region, *in* Matthes, F. E., ed., Geologic history of the Yosemite Valley: U.S. Geological Survey Professional Paper 160, p. 120-129.

Campbell, S.K., 1994, A geochemical and strontium isotopic investigation of Laramide and younger igneous rocks in central Colorado, with emphasis on the petrogrensis of the Thirtynine Mile volcanic field (Volumes I and II): University of Florida, 652 p.

Candela, P.A., and Holland, H.D., 1986, A mass transfer model for copper and molybdenum in magmatic hydrothermal systems: the origin of porphyry-type ore deposits.: Economic Geology, v. 81, p. 1–19, doi: 10.2113/gsecongeo.81.1.1.

Carl, B.S., Glazner, A.F., Bartley, J.M., Dinter, D.A., and Coleman, D.S., 1998, Independence dikes and mafic rocks of the eastern Sierra, *in* Behl, R. J., ed., Guidebook to Field Trip #4, Geological Society of America Cordilleran Section Meeting Field Trip Guidebook: California State University Long Beach Department of Geological Sciences, 26 p.

Cecil, M.R., Rotberg, G., and Ducea, M.N., 2012, Magmatic growth and batholithic root development in the northern Sierra Nevada, California: Geosphere, v. 8, p. 1–15, doi: 10.1130/GES00729.1.

Challener, S.C., and Glazner, A.F., 2017, Igneous or metamorphic? Hornblende phenocrysts as greenschist facies reaction cells in the Half Dome Granodiorite, California: American Mineralogist, v. 102, p. 436–444, doi: 10.2138/am-2017-5864.

Chapman, A.D., Ernst, W.G., Gottlieb, E., Powerman, V., and Metzger, E.P., 2015, Detrital zircon geochronology of Neoproterozoic-Lower Cambrian passive-margin strata of the White-Inyo Range, east-central California: Implications for the Mojave-Snow Lake fault hypothesis: Bulletin of the Geological Society of America, v. 127, p. 926–944, doi: 10.1130/B31142.1.

Chaulk, D., 2016, Geometry of Owens Valley in vicinity of Lone Pine and Independence, California based on gravity analysis [B.S. thesis]: Fullerton, California State University, Fullerton, 48 p.

Chen, J.H., and Moore, J.G., 1979, Late Jurassic Independence dike swarm in eastern California: Geology, v. 7, p. 129–133, doi: 10.1130/0091-7613(1979)7<129:LJIDSI>2.0.CO;2.

Chen, J.H., and Moore, J.G., 1982, Uranium-lead isotopic ages from the Sierra Nevada batholith, California: Journal of Geophysical Research: Solid Earth, v. 87, p. 4761–4784.

Chernicoff, C.J., Richards, J.P., and Zappettini, E.O., 2002, Crustal lineament control on magmatism and mineralization in northwestern Argentina: Geological, geophysical, and remote sensing evidence: Ore Geology Reviews, v. 21, p. 127–155, doi: 10.1016/S0169-1368(02)00087-2.

Chin, E.J., Lee, C.T.A., Tollstrup, D.L., Xie, L., Wimpenny, J.B., and Yin, Q.Z., 2013, On the origin of hot metasedimentary quartzites in the lower crust of continental arcs: Earth and Planetary Science Letters, v. 361, p. 120–133, doi: 10.1016/j.epsl.2012.11.031.

Chin, E.J., Lee, C.T.A., and Barnes, J.D., 2014, Thickening, refertilization, and the deep lithosphere filter in continental arcs: Constraints from major and trace elements and oxygen isotopes: Earth and Planetary Science Letters, v. 397, p. 184–200, doi: 10.1016/j.epsl.2014.04.022.

Chapin, C.E., 2012, Origin of the Colorado Mineral Belt: Geosphere, v. 8, p. 28–43, doi: 10.1130/GES00694.1.

Chapin, C.E., and Cather, S.M., 1994, Tectonic setting of the axial basins of the northern and central Rio Grande rift, *in* Keller, G.R. and Cather, S.M. eds., Basins of the Rio Grande Rift: Structure, Stratigraphy, and Tectonic Setting, Geological Society of America Special Papers 291, p. 5–26, doi: 10.1130/SPE291-p5.

Clemens, J.D., and Stevens, G., 2016, Melt segregation and magma interactions during crustal melting: Breaking out of the matrix: Earth-Science Reviews, v. 160, p. 333–349, doi: 10.1016/j.earscirev.2016.07.012.

Clemens, J.D., Helps, P.A., and Stevens, G., 2010, Chemical structure in granitic magmas: A signal from the source? Earth and Environmental Science Transactions of the Royal Society of Edinburgh, v. 100, p. 159–172, doi: Doi 10.1017/S1755691009016053.

Clemens, J.D., Stevens, G., and Farina, F., 2011, The enigmatic sources of I-type granites: The peritectic connexion: Lithos, v. 126, p. 174–181, doi: 10.1016/j.lithos.2011.07.004.

Clemens-Knott, D., 1992, Geologic and isotopic investigations of the Early Cretaceous Sierra Nevada batholith, Tulare, Co., CA, and the Ivrea Zone, NW Italian Alps: Examples of in- teraction between mantle-derived magma and continental crust [Ph.D. dissertation]: Pasadena, California Institute of Technology, 349 p.

Clemens-Knott, D., and Saleeby, J.B., 1999, Impinging ring dike complexes in the Sierra Nevada batholith, California: Roots of the Early Cretaceous volcanic arc: Bulletin of the Geological Society of America, v. 111, p. 484–496, doi: 10.1130/0016-7606(1999)111<0484:IRDCIT>2.3.CO;2.

Coleman, D.S., and Glazner, A.F., 1997, The Sierra Crest Magmatic Event: Rapid Formation of Juvenile Crust during the Late Cretaceous in California: International Geology Review, v. 39, p. 768–787, doi: 10.1080/00206819709465302.

Coleman, D.S., Glazner, A.F., and Frost, T.P., 1992, Evidence from the Lamarck granodiorite for rapid late Cretaceous crust formation in California: Science, v. 258, p. 1924–1926, doi: 10.1126/science.258.5090.1924.

Coleman, D.S., Carl, B.S., Glazner, A.F., and Bartley, J.M., 2000, Cretaceous dikes within the Jurassic Independence dike swarm in eastern California: Geological Society of America Bulletin, v. 112, p. 504–511, doi: 10.1130/0016-7606(2000)112<504:CDWTJI>2.0.CO;2.

Coleman, D.S., Gray, W., and Glazner, A.F., 2004, Rethinking the emplacement and evolution of zoned plutons: Geochronologic evidence for incremental assembly of the Tuolumne Intrusive Suite, California: Geology, v. 32, p. 433, doi: 10.1130/G20220.1.

Coleman, D.S., Glazner, A.F., and Bartley, J.M., 2011, Geochemical trends define three distinct processes operating at different scales during batholith formation: AGU Fall Meeting Abstracts, no. V33F-07.

Coleman, D.S., Bartley, J.M., Glazner, A.F., and Pardue, M.J., 2012, Is chemical zonation in plutonic rocks driven by changes in source magma composition or shallow-crustal differentiation? Geosphere, v. 8, p. 1568–1587, doi: 10.1130/GES00798.1.

Colombini, L.L., Miller, C.F., Gualda, G.A.R., Wooden, J.L., and Miller, J.S., 2011, Sphene and zircon in the Highland Range volcanic sequence (Miocene, southern Nevada, USA): Elemental partitioning, phase relations, and influence on evolution of silicic magma: Mineralogy and Petrology, v. 102, p. 29–50, doi: 10.1007/s00710-011-0177-3.

Condon, D.J., Schoene, B., McLean, N.M., Bowring, S.A., and Parrish, R.R., 2015, Metrology and traceability of U-Pb isotope dilution geochronology (EARTHTIME Tracer Calibration Part I): Geochimica et Cosmochimica Acta, v. 164, p. 464–480, doi: 10.1016/j.gca.2015.05.026.

Coney, P.J., and Reynolds, S.J., 1977, Cordilleran Benioff Zones: Nature, v. 270, p. 403–406, doi: 10.1038/275464a0.

Corfu, F., Hanchar, J.M., Hoskin, P.W.O., and Kinny, P., 2003, Atlas of Zircon Textures: Reviews in Mineralogy and Geochemistry, v. 53, p. 469–500, doi: 10.2113/0530469.

Cosca, M.A., Thompson, R.A., Lee, J.P., Turner, K.J., Neymark, L.A., and Premo, W.R., 2014, $^{40}Ar/^{39}Ar$ geochronology, isotope geochemistry (Sr, Nd, Pb), and petrology of alkaline lavas near Yampa, Colorado: Migration of alkaline volcanism and evolution of the northern Rio Grande rift: Geosphere, v. 10, p. 374–400, doi: 10.1130/GES00921.1.

Costa, F., 2008, Residence Times of Silicic Magmas Associated with Calderas, *in* Gottsmann, J. and Martí, J. eds., Developments in Volcanology, v. 10, p. 1–55, doi: 10.1016/S1871-644X(07)00001-0.

Cruden, A.R., Tobisch, O.T., and Launeau, P., 1999, Magnetic fabric evidence for conduit-fed emplacement of a tabular intrusion: Dinkey Creek Pluton, central Sierra Nevada batholith, California: Journal of Geophysical Research, v. 104, p. 10511, doi: 10.1029/1998JB900093.

Daly, R.A., 1933, Igenous Rocks and the Depths of the Earth: New York, McGraw-Hill, 598 p.

Davies, G.R., and Tommasini, S., 2000, Isotopic disequilibrium during rapid crustal anatexis: Implications for petrogenetic studies of magmatic processes: Chemical Geology, v. 162, p. 169–191, doi: 10.1016/S0009-2541(99)00123-0.

Davis, J.W., 2010, Thermochronology and cooling histories of plutons: implications for incremental pluton assembly [Ph.D. thesis]: Chapel Hill, University of North Carolina at Chapel Hill, 119 p.

Davis, J.W., Coleman, D.S., Gracely, J.T., Gaschnig, R., and Stearns, M., 2012, Magma accumulation rates and thermal histories of plutons of the Sierra Nevada batholith, CA: Contributions to Mineralogy and Petrology, v. 163, p. 449–465, doi: 10.1007/s00410-011-0683-7.

Depaolo, D.J., 1981, A neodymium and strontium isotopic study of the Mesozoic calc-alkaline granitic batholiths of the Sierra Nevada and Peninsular Ranges, California: Journal of Geophysical Research, v. 86, p. 10470–10488, doi: 10.1029/JB086iB11p10470.

Dodge, F.C.W., and Kistler, R.W., 1990, Some additional observations on inclusions in the granitic rocks of the Sierra Nevada: Journal of Geophysical Research, v. 95, p. 848, 17817-17841, doi: 10.1029/JB095iB11p17841.

Dodge, F.C.W., Calk, L.C., and Kistler, R.W., 1986, Lower crustal xenoliths, Chinese peak lava flow, central sierra nevada: Journal of Petrology, v. 27, p. 1277–1304, doi: 10.1093/petrology/27.6.1277.

Dodge, F.C.W., Lockwood, J.P., and Calk, L.C., 1988, Fragments of the mantle and crust from beneath the Sierra Nevada batholith: Xenoliths in a volcanic pipe near Big Creek, California: Bulletin of the Geological Society of America, v. 100, p. 938–947, doi: 10.1130/0016-7606(1988)100<0938:FOTMAC>2.3.CO;2.

Domenick, M.A., Kistler, R.W., Dodge, F.C.W., and Tatsumoto, M., 1983, Nd and Sr isotopic study of crustal and mantle inclusions from the Sierra Nevada and implications for batholith petrogenesis: Geological Society of America Bulletin, v. 94, p. 713–719, doi: 10.1130/0016-7606(1983)94<713:NASISO>2.0.CO;2.

Dorais, M.J., Whitney, J.A., and Roden, M.F., 1990, Origin of mafic enclaves in the Dinkey Creek Pluton, Central Sierra Nevada batholith, California: Journal of Petrology, v. 31, p. 853–881.

Ducea, M.N., 2001, The California Arc: Thick Granitic Batholiths, Eclogitic Residues, Lithospheric-Scale Thrusting, and Magmatic Flare-Ups: GSA Today, v. 11, p. 4–10.

Ducea, M.N., 2002, Constraints on the bulk composition and root foundering rates of continental arcs: A California arc perspective: Journal of Geophysical Research, v. 107, p. 1–13, doi: 10.1029/2001JB000643.

Ducea, M.N., and Saleeby, J.B., 1998, The age and origin of a thick mafic-ultramafic keel from beneath the Sierra Nevada batholith: Contributions to Mineralogy and Petrology, v. 133, p. 169–185, doi: 10.1007/s004100050445.

Dunne, G.C., and Walker, J.D., 1993, Age of Jurassic volcanism and tectonism, southern Owens Valley region, east-central California: Geological Society of America Bulletin, v. 105, p. 1223–1230, doi: 10.1130/0016-7606(1993)105<1223:AOJVAT>2.3.CO;2.

Dunne, G.C., Garvey, T.P., Oborne, M., Schneidereit, D., Fritsche, A.E., and Walker, J.D., 1998, Geology of the Inyo Mountains Volcanic Complex: Implications for Jurassic paleogeography of the Sierran magmatic arc in eastern California: Geological Society of America Bulletin, v. 110, p. 1376–1397, doi: 10.1130/0016-7606(1998)110<1376:GOTIMV>2.3.CO;2.

Economos, R.C., Memeti, V., Paterson, S.R., Miller, J.S., Erdmann, S., and Žák, J., 2009, Causes of compositional diversity in a lobe of the Half Dome granodiorite, Tuolumne Batholith, Central Sierra Nevada, California: Earth and Environmental Science Transactions of the Royal Society of Edinburgh, v. 100, p. 173–183, doi: 10.1017/S1755691009016065.

Eichelberger, J.C., 1975, Origin of andesite and dacite: Evidence of mixing at Glass Mountain in California and at other circum-Pacific volcanoes: Bulletin of the Geological Society of America, v. 86, p. 1381–1391, doi: 10.1130/0016-7606(1975)86<1381:OOAADE>2.0.CO;2.

Eichelberger, J.C., Izbekov, P.E., and Browne, B.L., 2006, Bulk chemical trends at arc volcanoes are not liquid lines of descent: Lithos, v. 87, p. 135–154, doi: 10.1016/j.lithos.2005.05.006.

Eisenberg, J.L., 2014, Structure, Composition, and Emplacement History of Orbicular Granites and Comb Layering, Sierra and Sequoia National Forests, CA [B.A. thesis]: Claremont, Pomona College, 61 p.

Elderfield, H., and Greaves, M.J., 1982, The rare earth elements in seawater: Nature, v. 296, p. 214–219, doi: 10.1038/296214a0.

Engebretson, D.C., Cox, A., and Gordon, R.G., 1985, Relative Motions Between Oceanic and Continental Plates in the Pacific Basin: Geological Society of America Special Paper 206, 66 p., doi: 10.1130/SPE206-p1.

Farmer, G.L., and Depaolo, D.J., 1984, Origin of Mesozoic and Tertiary granite in the western United States and implications for Pre-Mesozoic crustal structure: 2. Nd and Sr isotopic studies of unmineralized and Cu- and Mo-mineralized granite in the Precambrian Craton: Journal of Geophysical Research: Solid Earth, v. 89, p. 10141–10160, doi: 10.1029/JB089iB12p10141.

Feldman, J.D., 2010, The Emplacement and Exhumation History of the Twin Lakes Batholith and Implications for the Laramide Orogeny and Flat Slab Subduction [M.S. thesis]: Soccoro, New Mexico Institute of Mining and Technology, 185 p.

Feldman, J., Heizler, M.T., Karlstrom, K.E., and Kelley, S.A., 2012, Magmatic constraints on the enigmatic Colorado Mineral Belt: Geological Society of America Abstracts with Programs, v. 44, no. 6, p. 30.

Fiske, R.S., and Tobisch, O.T., 1994, Middle Cretaceous ash-flow tuff and caldera-collapse deposit in the Minarets Caldera, east-central Sierra Nevada, California: Geological Society of America Bulletin, v. 106, p. 582, doi: 10.1130/0016-7606(1994)106<0582:MCAFTA>2.3.CO;2.

Frazer, R.E., Coleman, D.S., and Mills, R.D., 2014, Zircon U-Pb geochronology of the Mount Givens Granodiorite: Implications for the genesis of large volumes of eruptible magma: Journal of Geophysical Research: Solid Earth, v. 119, p. 2907–2924, doi: 10.1002/2013JB010716.

Fridrich, C.J., 1987, The Grizzly Peak cauldron, Colorado: structure and petrology of a deeply dissected resurgent ash-flow caldera [Ph.D. dissertation]: Palo Alto, Stanford University, 240 p.

Fridrich, C.J., and Mahood, G.A., 1984, Reverse zoning in the resurgent intrusions of the Grizzly Peak cauldron, Sawatch Range, Colorado.: Geological Society of America Bulletin, v. 95, p. 779–787, doi: 10.1130/0016-7606(1984)95<779:RZITRI>2.0.CO;2.

Fridrich, C.J., and Mahood, G.A., 1987, Compositional layers in the zoned magma chamber of the Grizzly Peak Tuff.: Geology, v. 15, p. 299–303, doi: 10.1130/0091-7613(1987)15<299:CLITZM>2.0.CO.

Fridrich, C.J., Smith, R.P., DeWitt, E., and McKee, E.H., 1991, Structural, eruptive, and intrusive evolution of the Grizzly Peak caldera, Sawatch Range, Colorado: Geological Society of America Bulletin, v. 103, p. 1160–1177, doi: 10.1130/0016-7606(1991)103<1160:SEAIEO>2.3.CO;2.

Fridrich, C.J., Bryant, B., Richard, S., and Smith, R.P., 1998, Geologic map of the Collegiate Peaks Wilderness Area and the Grizzly Peak caldera, Sawatch Range, central Colorado: U.S. Geological Survey Miscellaneous Investigations Series Map I-2565, scale 1:50,000.

Frost, C.D., Frost, B.R., Chamberlain, K.R., and Hulsebosch, T.P., 1998, The Late Archean history of the Wyoming province as recorded by granitic magmatism in the Wind River Range, Wyoming: Precambrian Research, v. 89, p. 145–173, doi: 10.1016/S0301-9268(97)00082-X.

Gaynor, S.P., and Glazner, A.F., 2016, Did the Johnson Granite Porphyry Erupt?: Geological Society of America Abstracts with Programs, v. 48, no. 4.

Gaynor, S., Coleman, D.S., and Rosera, J.M., 2015, Determining the Magma Genesis of Mo Porphyry Deposits: American Geophysical Union, Fall Meeting 2015, abstract #V53C-3139

Gehrels, G.E., Valencia, V.A., and Ruiz, J., 2008, Enhanced precision, accuracy, efficiency, and spatial resolution of U-Pb ages by laser ablation-multicollector-inductively coupled plasma-mass spectrometry: Geochemistry, Geophysics, Geosystems, v. 9, p. 1–13, doi: 10.1029/2007GC001805.

Gilbert, G.K., 1884, A theory of the earthquakes of the Great Basin, with a practical application: American Journal of Science, v. s3-27, p. 49–53, doi: 10.2475/ajs.s3-27.157.49.

Gioncada, A., Vezzoli, L., Mazzuoli, R., Omarini, R., Nonnotte, P., and Guillou, H., 2010, Pliocene intraplate-type volcanism in the Andean foreland at 26 10'S, 64 40'W (NW Argentina): Implications for magmatic and structural evolution of the Central Andes: Lithosphere, v. 2, p. 153–171, doi: 10.1130/L81.1.

Glazner, A.F., 1991, Plutonism, oblique subduction, and continental growth: An example from the Mesozoic of California: Geology, v. 19, p. 784–786.

Glazner, A.F., 2007, Thermal limitations on incorporation of wall rock into magma: Geology, v. 35, p. 319, doi: 10.1130/G23134A.1.

Glazner, A.F., 2014, Magmatic life at low Reynolds number: Geology, v. 42, p. 935–938, doi: 10.1130/G36078.1.

Glazner, A.F., and Sadler, P.M., 2016, Estimating the duration of geologic intervals from a small number of age determinations: A challenge common to petrology and paleobiology: Geochemistry, Geophysics, Geosystems, v. 17, p. 4892–4898, doi: 10.1002/2016GC006542.

Glazner, A.F., Bartley, J.M., Coleman, D.S., Gray, W., and Taylor, R.Z., 2004, Are plutons assembled over millions of years by amalgamation from small magma chambers? GSA Today, v. 14, p. 4–11, doi: 10.1130/1052-5173(2004)014<0004.

Glazner, A.F., Carl, B.S., Coleman, D.S., Miller, J.S., and Bartley, J.M., 2008a, Chemical variability and the composite nature of dikes from the Jurassic Independence dike swarm, eastern California, *in* Wright, J.E. and Shervais, J.W. eds., Ophiolites, Arcs, and Batholiths: A Tribute to Cliff Hopson: Geological Society of America Special Paper 438, p. 455–480, doi: 10.1130/2008.2438(16).

Glazner, A.F., Coleman, D.S., and Bartley, J.M., 2008b, The tenuous connection between high-silica rhyolites and granodiorite plutons: Geology, v. 36, p. 183, doi: 10.1130/G24496A.1.

Glazner, A.F., Coleman, D.S., and Mills, R.D., 2015, The Volcanic-Plutonic Connection, *in* Advances in Volcanology, p. 1–14, doi: 10.1007/11157_2015_11.

Gonzales, D.A., Turner, B.E., Burgess, R.T., Holnback, C.C., and Critchley, M.R., 2010, New insight into the timing and history of diatreme-dike complexes of the northeastern Navajo volcanic field, southwestern Colorado, in Four Corners country: New Mexico Geological Society 61st Field Conference Guidebook, p. 163–172.

Grasse, S.W., Gehrels, G.E., Lahren, M.M., Schweickert, R.A., and Barth, A.P., 2001, U-Pb geochronology of detrital zircons from the Snow Lake pendant , central Sierra Nevada — Implications for Late Jurassic – Early Cretaceous dextral strike-slip faulting:, doi: 10.1130/0091-7613(2001)029<0307.

Gray, W., Glazner, A.F., Coleman, D.S., and Bartley, J.M., 2008, Long-term geochemical variability of the Late Cretaceous Tuolumne Intrusive Suite, central Sierra Nevada, California: Geological Society, London, Special Publications, v. 304, p. 183–201, doi: 10.1144/SP304.10.

Gualda, G.A.R., and Ghiorso, M.S., 2013, Low-Pressure Origin of High-Silica Rhyolites and Granites: The Journal of Geology, v. 121, p. 537–545, doi: 10.1086/671395.

Guy, R.E., 1980, The Dinkey Creek intrusive series, Huntington Lake quadrangle, Fresno County, California [M.S. thesis]: Blacksburg, Virginia Polytechnic Institute, 192 p.

Hahm, W.J., Riebe, C.S., Lukens, C.E., and Araki, S., 2014, Bedrock composition regulates mountain ecosystems and landscape evolution.: Proceedings of the National Academy of Sciences of the United States of America, v. 111, p. 3338–43, doi: 10.1073/pnas.1315667111.

Hamilton, W.B., 1956, Variations in plutons of granitic rocks of the Huntington lake area of the Sierra Nevada, California: Bulletin of the Geological Society of America, v. 67, p. 1585–1598, doi: 10.1130/0016-7606(1956)67[1585:VIPOGR]2.0.CO;2.

Harrison, T.M., Watson, E.B., and Aikman, A.B., 2007, Temperature spectra of zircon crystallization in plutonic rocks: Geology, v. 35, p. 635, doi: 10.1130/G23505A.1.

Harvey, J., and Baxter, E.F., 2009, An improved method for TIMS high precision neodymium isotope analysis of very small aliquots (1-10 ng): Chemical Geology, v. 258, p. 251–257, doi: 10.1016/j.chemgeo.2008.10.024.

Heumann, A., and Davies, G.R., 2002, U–Th Disequilibrium and Rb–Sr Age Constraints on the Magmatic Evolution of Peralkaline Rhyolites from Kenya: Journal of Petrology, v. 43, p. 557–577, doi: 10.1093/petrology/43.3.557.

Hildebrand, R.S., 2009, Did Westward Subduction Cause Cretaceous–Tertiary Orogeny in the North American Cordillera?: Geological Society of America Special Papers 457, 71 p., doi: 10.1130/2009.2457.

Hildebrand, R.S., 2013, Mesozoic Assembly of the North American Cordillera: Geological Society of America Special Paper 495, p. 169.

Hildreth, W., 1981, Gradients in silicic magma chambers: Implications for lithospheric magmatism: Journal of Geophysical Research: Solid Earth, v. 86, p. 10153–10192, doi: 10.1029/JB086iB11p10153.

Hildreth, W., 2004, Volcanological perspectives on Long Valley, Mammoth Mountain, and Mono Craters: several contiguous but discrete systems: Journal of Volcanology and Geothermal Research, v. 136, p. 169–198, doi: 10.1016/j.jvolgeores.2004.05.019.

Hill, B.M., and Bickford, M.E., 2001, Paleoproterozoic rocks of central Colorado: Accreted arcs or extended older crust? Geology, v. 29, p. 1015–1018, doi: 10.1130/0091-7613(2001)029<1015:PROCCA>2.0.CO;2.

Hill, M., Neil, J.R.O., Noyes, H., Frey, F.A., and Wones, D.R., 1988, Sr, Nd, and O isotope variations in compositionally zoned and unzoned plutons in the central Sierra Nevada batholith: American Journal of Science, v. 288–A, p. 213–241.

Hinke, H.J., 2002, Oxygen isotope evolution of the garnet-bearing Dinkey Dome pluton, Sierra Nevada, California [B.S. thesis]:Madison, University of Wisconsin, 48 p.

Hirt, W.H., 2007, Petrology of the Mount Whitney Intrusive Suite, eastern Sierra Nevada, California: Implications for the emplacement and differentiation of composite felsic intrusions: Geological Society of America Bulletin, v. 119, p. 1185–1200, doi: 10.1130/B26054.1.

Hirt, W.H., and Glazner, A.F., 1995, Sr and Nd isotopic co positions of granitoids from the Mount Whitney Intrusive Suite, southern Sierra Nevada, California: Eos (Transactions, American Geophysical Union), v. 76, no. 46, p. F657

Hobbs, W.H., 1910, The earthquake of 1872 in the Owens Valley, California: Beiträge zur Geophysik, v. 10, p. 352–385.

Hole, M.J., Saunders, A.D., Marriner, G.F., and Tarney, J., 1984, Subduction of pelagic sediments: implications for the origin of Ce-anomalous basalts from the Mariana Islands: Journal of the Geological Society, v. 141, p. 453–472, doi: 10.1144/gsjgs.141.3.0453.

Holland, J.E., Surpless, B., Smith, D.R., Loewy, S.L., and Lackey, J.S., 2013, Intrusive history and petrogenesis of the Ash Mountain Complex, Sierra Nevada batholith, California (USA): Geosphere, v. 9, p. 691–717, doi: 10.1130/GES00890.1.

Hough, S.E., and Hutton, K., 2008, Revisiting the 1872 Owens Valley, California, Earthquake: Bulletin of the Seismological Society of America, v. 98, p. 931–949, doi: 10.1785/0120070186.

Huber, N.K., 1968, Geologic map of the Shuteye Peak quadrangle, Sierra Nevada, California: U.S. Geological Survey Map GQ-728, scale 1:62,500.

Huber, N.K., 1983, Preliminary geologic map of the Pinecrest quadrangle, central Sierra Nevada, California: U.S. Geological Survey Miscellaneous Field Studies Map MF-1437, scale 1:62,500.

Jacob, K.H., Farmer, G.L., Buchwaldt, R., and Bowring, S.A., 2015, Deep crustal anatexis, magma mixing, and the generation of epizonal plutons in the Southern Rocky Mountains, Colorado: Contributions to Mineralogy and Petrology, v. 169, doi: 10.1007/s00410-014-1094-3.

Johnson, C.M., 1991, Large-scale crust formation and lithosphere modification beneath Middle to Late Cenozoic calderas and volcanic fields, western North America: Journal of Geophysical Research: Solid Earth, v. 96, p. 13485–13507, doi: 10.1029/91JB00304.

Johnson, C.M., and Fridrich, C.J., 1990, Non-monotonic chemical and O, Sr, Nd, and Pb isotope zonations and heterogeneity in the mafic- to silicic-composition magma chamber of the Grizzly Peak Tuff, Colorado: Contributions to Mineralogy and Petrology, v. 105, p. 677–690, doi: 10.1007/BF00306533.

Johnson, C.M., and Thompson, R.A., 1991, Isotopic Composition of Oligocene Mafic Volcanic-Rocks in the Northern Rio-Grande Rift - Evidence for Contributions of Ancient Intraplate and Subduction Magmatism To Evolution of the Lithosphere: Journal of Geophysical Research: Solid Earth and Planets, v. 96, p. 13593–13608.

Johnson, C.M., Czamanske, G.K., and Lipman, P.W., 1989, Geochemistry of intrusive rocks associated with the Latir volcanic field, New Mexico, and contrasts between evolution of plutonic and volcanic rocks: Contributions to Mineralogy and Petrology, v. 103, p. 90–109, doi: 10.1007/BF00371367.

Johnson, C.M., Lipman, P.W., and Czamanske, G.K., 1990, H, O, Sr, Nd, and Pb isotope geochemistry of the Latir volcanic field and cogenetic intrusions, New Mexico, and relations between evolution of a continental magmatic center and modifications of the lithosphere: Contributions to Mineralogy and Petrology, v. 104, p. 99–124, doi: 10.1007/BF00310649.

Jones, J.V., and Thrane, K., 2012, Correlating Proterozoic synorogenic metasedimentary successions in southwestern Laurentia: New insights from detrital zircon U-Pb geochronology of Paleoproterozoic quartzite and metaconglomerate in central and northern Colorado, U.S.A.: Rocky Mountain Geology, v. 47, p. 1–35, doi: 10.2113/gsrocky.47.1.1.

Kane, M.F., and Pakiser, L.C., 1961, Geophysical study of subsurface structure in southern Owens Valley, California: Geophysics, v. 26, p. 12–26, doi: 10.1190/1.1438835.

Karlstrom, K.E., and Humphreys, E.D., 1998, Persistent influence of Proterozoic accretionary boundaries in the tectonic evolution of southwestern North America: Interaction of cratonic grain and mantle modification events: Rocky Mountain Geology, v. 33, p. 161–179, doi: 10.2113/33.2.161.

Keller, C.B., Schoene, B., Barboni, M., Samperton, K.M., and Husson, J.M., 2015, Volcanic-plutonic parity and the differentiation of the continental crust: Nature, v. 523, p. 301–307, doi: 10.1038/nature14584.

Kessel, R., Schmidt, M.W., Ulmer, P., and Pettke, T., 2005, Trace element signature of subduction-zone fluids, melts and supercritical liquids at 120–180 km depth: Nature, v. 437, p. 724–727, doi: 10.1038/nature03971.

Kerrick, D.M., and Connolly, J.A.D., 2001, Metamorphic devolatilization of subducted oceanic metabasalts: Implications for seismicity, arc magmatism and volatile recycling: Earth and Planetary Science Letters, v. 189, p. 19–29, doi: 10.1016/S0012-821X(01)00347-8.

Kistler, R.W., 1990, Two different lithosphere types in the Sierra Nevada, California, *in* Anderson, J.L. ed., The nature and origin of Cordilleran magmatism: Boulder, Colorado, Geological Society of America Memoir 174, p. 271–281.

Kistler, R.W., 1993, Mesazoic intrabatholithic faulting, Sierra Nevada, California, *in* Dunn, G. and McDougall, K. eds., Mesozoic Paleogeography of the Western United States-II: Pacific Section, Society of Sedimentary Geology (SEPM), Book 71, p. 247–262.

Kistler, R.W., and Bateman, P.C., 1966, Stratigraphy and Structure of the Dinkey Creek Roof Pendant in the Central Sierra Nevada, California: U.S. Geological Survey Professional Paper 524-B, 20 p.

Kistler, R.W., and Peterman, Z.E., 1973, Variations in Sr, Rb, K, Na, and Initial Sr^{87}/Sr^{86} in Mesozoic Granitic Rocks and Intruded wall Rocks in Central California: Geological Society of America Bulletin, v. 84, p. 3489–3512, doi: 10.1130/0016-7606(1973)84<3489:VISRKN>2.0.CO;2.

Kistler, R.W., and Fleck, R.J., 1994, Field guide for a transect of the central Sierra Nevada, California; geochronology and isotope geology: U.S. Geological Survey Open-File Report 94-267, 50 p.

Kistler, R.W., Chappell, B.W., Peck, D.L., and Bateman, P.C., 1986, Isotopic variation in the Tuolumne Intrusive Suite, central Sierra Nevada, California: Contributions to Mineralogy and Petrology, v. 94, p. 205–220, doi: 10.1007/BF00592937.

Klemetti, E.W., Lackey, J.S., and Starnes, J., 2014, Magmatic lulls in the Sierra Nevada captured in zircon from rhyolite of the mineral king pendant, California: Geosphere, v. 10, p. 66–79, doi: 10.1130/GES00920.1.

Knopf, A., 1918, A geologic reconnaissance of the Inyo Range and the eastern slope of the southern Sierra Nevada, California, with a section on the stratigraphy of the Inyo Range: U.S. Geological Survey Professional Paper 110, p. 151, https://pubs.er.usgs.gov/publication/pp110.

Krogh, T.E., 1973, A low-contamination method for hydrothermal decomposition of zircon and extraction of U and Pb for isotopic age determinations: Geochimica et Cosmochimica Acta, v. 37, p. 485–494, doi: 10.1016/0016-7037(73)90213-5.

Krogh, T.E., 1982, Improved accuracy of U-Pb zircon ages by the creation of more concordant systems using an air abrasion technique: Geochimica et Cosmochimica Acta, v. 46, p. 637–649, doi: 10.1016/0016-7037(82)90165-X.

Kylander-Clark, A.R.C., Coleman, D.S., Glazner, A.F., and Bartley, J.M., 2005, Evidence for 65 km of dextral slip across Owens Valley, California, since 83 Ma: Geological Society of America Bulletin, v. 117, p. 962, doi: 10.1130/B25624.1.

Lackey, J.S., Valley, J.W., and Hinke, H.J., 2006, Deciphering the source and contamination history of peraluminous magmas using δ18O of accessory minerals: Examples from garnet-bearing plutons of the Sierra Nevada batholith: Contributions to Mineralogy and Petrology, v. 151, p. 20–44, doi: 10.1007/s00410-005-0043-6.

Lackey, J.S., Valley, J.W., Chen, J.H., and Stockli, D.F., 2008, Dynamic Magma Systems, Crustal Recycling, and Alteration in the Central Sierra Nevada Batholith: the Oxygen Isotope Record: Journal of Petrology, v. 49, p. 1397–1426, doi: 10.1093/petrology/egn030.

Lackey, J.S., Cecil, M.R., Windham, C.J., Frazer, R.E., Bindeman, I.N., and Gehrels, G.E., 2012, The Fine Gold Intrusive Suite: The roles of basement terranes and magma source development in the Early Cretaceous Sierra Nevada batholith: Geosphere, v. 8, p. 292–313, doi: 10.1130/GES00745.1.

Lahren, M.M., and Schweickert, R.A., 1989, Proterozoic and Lower Cambrian miogeoclinal rocks of Snow Lake pendant, Yosemite-Emigrant Wilderness, Sierra Nevada, California: evidence for major Early Cretaceous dextral translation: Geology, v. 17, p. 156–160, doi: 10.1130/0091-7613(1989)017<0156:PALCMR>2.3.CO;2.

Lake, E.T., and Farmer, G.L., 2015, Oligo-Miocene mafic intrusions of the San Juan Volcanic Field, southwestern Colorado, and their relationship to voluminous, caldera-forming magmas: Geochimica et Cosmochimica Acta, v. 157, p. 86–108, doi: 10.1016/j.gca.2015.02.020.

Le, K., Lee, J., Owen, L.A., and Finkel, R., 2007, Late Quaternary slip rates along the Sierra Nevada frontal fault zone, California: Slip partitioning across the western margin of the Eastern California Shear Zone-Basin and Range province: Bulletin of the Geological Society of America, v. 119, p. 240–256, doi: 10.1130/B25960.1.

Lee, C.T.A., and Bachmann, O., 2014, How important is the role of crystal fractionation in making intermediate magmas? Insights from Zr and P systematics: Earth and Planetary Science Letters, v. 393, p. 266–274, doi: 10.1016/j.epsl.2014.02.044.

Lee, C.T.A., and Morton, D.M., 2015, High silica granites: Terminal porosity and crystal settling in shallow magma chambers: Earth and Planetary Science Letters, v. 409, p. 23–31, doi: 10.1016/j.epsl.2014.10.040.

Lee, C.T.A., Morton, D.M., Kistler, R.W., and Baird, A.K., 2007, Petrology and tectonics of Phanerozoic continent formation: From island arcs to accretion and continental arc magmatism: Earth and Planetary Science Letters, v. 263, p. 370–387, doi: 10.1016/j.epsl.2007.09.025.

Lee, J., Spencer, J., and Owen, L., 2001, Holocene slip rates along the Owens Valley fault, California: Implications for the recent evolution of the Eastern California Shear Zone: Geology, v. 29, p. 819–822, doi: 10.1130/0091-7613(2001)029<0819:HSRATO>2.0.CO;2.

Lee, S.G., Asahara, Y., Tanaka, T., Lee, S.R., and Lee, T., 2013, Geochemical significance of the Rb-Sr, La-Ce and Sm-Nd isotope systems in A-type rocks with REE tetrad patterns and negative Eu and Ce anomalies: The Cretaceous Muamsa and Weolaksan granites, South Korea: Chemie der Erde - Geochemistry, v. 73, p. 75–88, doi: 10.1016/j.chemer.2012.11.008.

Lee, W.T., 1906, Geology and Water Resources of Owens Valley, California: U.S. Geological Survey Water-Supply and Irrigation Paper No. 181, 28 p.

Lewis, J.G., and Girty, G.H., 2001, Tectonic implications of a petrographic and geochemical characterization of the Lower to Middle Jurassic Sailor Canyon Formation , northern Sierra Nevada , California: Sierra, p. 627–630, doi: 10.1130/0091-7613(2001)029<0627:TIOAPA>2.0.CO;2.

Lipman, P.W., 2007, Incremental assembly and prolonged consolidation of Cordilleran magma chambers: Evidence from the Southern Rocky Mountain volcanic field: Geosphere, v. 3, p. 42–70, doi: 10.1130/GES00061.1.

Lipman, P.W., and Bachmann, O., 2015, Ignimbrites to batholiths: Integrating perspectives from geological, geophysical, and geochronological data: Geosphere, v. 11, p. 705–743, doi: 10.1130/GES01091.1.

Lipman, P.W., 2000, Central San Juan caldera cluster: regional volcanic framework, *in* Bethke, P.M. and Hay, R.L. eds., Ancient Lake Creede: its volcano-tectonic setting, history of sedimentation, and relation to mineralization in the Creede mining district: Geological Society of America Special Papers 346, p. 9–69, doi: 10.1130/0-8137-2346-9.9.

Lockwood, J.P., and Bateman, P.C., 1976, Geologic map of the Shaver Lake quadrangle, central Sierra Nevada, California: U.S. Geological Survey Map GQ-1271, scale 1:62,500.

Lubetkin, L.K.C., and Clark, M.M., 1988, Geological Society of America Bulletin Late Quaternary activity along the Lone Pine fault , eastern California Late Quaternary activity along the Lone Pine fault , eastern California: , p. 755–766, doi: 10.1130/0016-7606(1988)100<0755.

Ludington, S., and Plumlee, G.S., 2009, Climax-type porphyry molybdenum deposits: U.S. Geological Survey Open-File Report 2009-1215, 16 p.

Ludwig, K.R., 2003, Isoplot 3.00: A Geochronological Tool-Kit for Excel: Berkeley Geochronology Center Special Publication 4, 67 p.

Lundblad, S.P., 1994, Evolution of small carbonate platforms in the Umbria-Marche Apennines, Italy [Ph.D. dissertation]: Chapel Hill, University of North Carolina at Chapel Hill, 145 p.

Lundstrom, C.C., and Glazner, A.F., 2016, Silicic magmatism and the volcanic-plutonic connection: Elements, v. 12, p. 91–96, doi: 10.2113/gselements.12.2.91.

Lyell, C., 1838, Elements of Geology: London, John Murray, 571 p.

Mahan, K.H., Bartley, J.M., Coleman, D.S., Glazner, A.F., and Carl, B.S., 2003, Sheeted intrusion of the synkinematic McDoogle pluton, Sierra Nevada, California: Geological Society of America Bulletin, v. 115, p. 1570, doi: 10.1130/B22083.1.

Masi, U., O'Neil, J.R., and Kistler, R.W., 1981, Stable isotope systematics in mesozoic granites of Central and Northern California and Southwestern Oregon: Contributions to Mineralogy and Petrology, v. 76, p. 116–126, doi: 10.1007/BF00373691.

Matthews, K.J., Seton, M., and Müller, R.D., 2012, A global-scale plate reorganization event at 105-100 Ma: Earth and Planetary Science Letters, v. 355–356, p. 283–298, doi: 10.1016/j.epsl.2012.08.023.

Mattinson, J.M., 1973, Anomalous isotopic composition of lead in young zircons: Carnegie Institution of Washington Yearbook, v. 72, p. 613–616.

Mattinson, J.M., 2005, Zircon U–Pb chemical abrasion ("CA-TIMS") method: Combined annealing and multi-step partial dissolution analysis for improved precision and accuracy of zircon ages: Chemical Geology, v. 220, p. 47–66, doi: 10.1016/j.chemgeo.2005.03.011.

Mattinson, J.M., Graubard, C.M., Parkinson, D.L., and McClelland, W.C., 1996, U-Pb Reverse Discordance in Zircons: The Role of Fine-Scale Oscillatory Zoning and Sub-Micron Transport of Pb: Earth Processes: Reading the Isotopic Code, p. 355–370, doi: 10.1029/GM095p0355.

McDonough, W.F., and Sun, S.-s., 1995, the Composition of the Earth: Chemical Geology, v. 120, p. 223–253, doi: 10.1016/0009-2541(94)00140-4.

McIntosh, W.C., and Chapin, C.E., 2004, Geochronology of the central Colorado volcanic field: New Mexico Bureau of Geology & Mineral Resources Bulletin, v. 160, p. 205–237.

McLean, N.M., Bowring, J.F., and Bowring, S.A., 2011, An algorithm for U-Pb isotope dilution data reduction and uncertainty propagation: Geochemistry Geophysics Geosystems, v. 12, doi: 10.1029/2010GC003478.

McLennan, S.M., Hemming, S.R., Taylor, S.R., and Eriksson, K.A., 1995, Early Proterozoic crustal evolution: Geochemical and NdPb isotopic evidence from metasedimentary rocks, southwestern North America: Geochimica et Cosmochimica Acta, v. 59, p. 1153–1177, doi: 10.1016/0016-7037(95)00032-U.

Meen, J.K., 1990, Negative Ce anomalies in Archean amphibolites and Laramide granitoids, southwestern Montana, U.S.A.: Chemical Geology, v. 81, p. 191–207, doi: 10.1016/0009-2541(90)90115-N.

Memeti, V., Gehrels, G.E., Paterson, S.R., Thompson, J.M., Mueller, R.M., and Pignotta, G.S., 2010a, Evaluating the Mojave-Snow Lake fault hypothesis and origins of central Sierran metasedimentary pendant strata using detrital zircon provenance analyses: Lithosphere, v. 2, p. 341–360, doi: 10.1130/L58.1.

Memeti, V., Paterson, S., Matzel, J., Mundil, R., and Okaya, D., 2010b, Magmatic lobes as "snapshots" of magma chamber growth and evolution in large, composite batholiths: An example from the Tuolumne intrusion, Sierra Nevada, California: Geological Society of America Bulletin, v. 122, p. 1912–1931, doi: 10.1130/B30004.1.

Miller, C.F., 1985, Are Strongly Peraluminous Magmas Derived from Pelitic Sedimentary Sources? The Journal of Geology, v. 93, p. 673–689.

Miller, C.F., McDowell, S.M., and Mapes, R.W., 2003, Hot and cold granites? Implications of zircon saturation temperatures and preservation of inheritance: Geology, v. 31, p. 529, doi: 10.1130/0091-7613(2003)031<0529:HACGIO>2.0.CO;2.

Miller, J.S., Matzel, J.E.P., Miller, C.F., Burgess, S.D., and Miller, R.B., 2007, Zircon growth and recycling during the assembly of large, composite arc plutons: Journal of Volcanology and Geothermal Research, v. 167, p. 282–299, doi: 10.1016/j.jvolgeores.2007.04.019.

Mills, R.D., 2012, Re-evaluatig pluton/volcano connections and igneous textures in light of incremental magma emplacement [Ph.D. dissertation]: Chapel Hill, University of North Carolina at Chapel Hill, 111 p.

Mills, R.D., and Coleman, D.S., 2013, Temporal and chemical connections between plutons and ignimbrites from the Mount Princeton magmatic center: Contributions to Mineralogy and Petrology, v. 165, p. 961–980, doi: 10.1007/s00410-012-0843-4.

Mills, R.D., Glazner, A.F., and Coleman, D.S., 2009, Scale of pluton/wall rock interaction near May Lake, Yosemite National Park, CA, USA: Contributions to Mineralogy and Petrology, v. 158, p. 263–281, doi: 10.1007/s00410-009-0381-x.

Mills, R.D., Simon, J.I., DePaolo, D.J., and Bachmann, O., 2013, Radiogenic ingrowth of ^{40}Ca from decay of ^{40}K provides a powerful tracer for understanding the origins of felsic magmas: Geological Society of America Abstracts with Programs, v. 45, no. 7, p. 84.

Moore, J.G., 1963, Geologic map and sections of the Mount Pinchot quadrangle, California: U.S. Geological Survey Bulletin 1130, scale 1:62,500.

Moore, J.G., 1978, Geologic map of the Marion Peak quadrangle, Fresno County, California: U.S. Geological Survey Geologic Quadrangle Map GQ-1399, scale 1:62,500.

Moore, J.G., 1981, Geologic map of the Mount Whitney quadrangle, Inyo and Tulare Counties, California: U.S. Geological Survey Geologic Quadrangle Map GQ-1545, scale 1:62,500.

Moore, J.G., and Hopson, C.A., 1961, The Independence dike swarm in eastern California: American Journal of Science, v. 259, p. 241–259, doi: 10.2475/ajs.259.4.241.

Moore, J.G., and Lockwood, J.P., 1973, Origin of comb layering and orbicular structure, Sierra Nevada Batholith, California: Bulletin of the Geological Society of America, v. 84, p. 1–20, doi: 10.1130/0016-7606(1973)84<1:OOCLAO>2.0.CO;2.

Moore, J.G., and Sisson, T.W., 1987, Geologic map of the Triple Divide Peak quadrangle, Fresno County, California: U.S. Geological Survey Geologic Quadrangle Map GQ-1636, scale 1:62,500.

Moore, J.G., and Nokleberg, W.J., 1992, Geologic map of the Tehipite Dome quadrangle, Tulare County, California: U.S. Geological Survey Geologic Quadrangle Map GQ-1676, scale 1:62,500.

Mueller, P.A., and Frost, C.D., 2006, The Wyoming Province: a distinctive Archean craton in Laurentian North America: Canadian Journal of Earth Sciences, v. 43, p. 1391–1397, doi: 10.1139/e06-075.

Mueller, P.A., Wooden, J.L., Mogk, D.W., Henry, D.J., and Bowes, D.R., 2010, Rapid growth of an Archean continent by arc magmatism: Precambrian Research, v. 183, p. 70–88, doi: 10.1016/j.precamres.2010.07.013.

Mukhopadhyay, B., and Manton, W.I., 1994, Upper-mantle fragments from beneath the Sierra Nevada Batholith: Partial fusion, fractional crystallization, and metasomatism in a subduction related ancient lithosphere: Journal of Petrology, v. 35, p. 1417–1450, doi: 10.1093/petrology/35.5.1417.

Mundil, R., Ludwig, K.R., Metcalfe, I., and Renne, P.R., 2004, Age and Timing of the Permian Mass Extinctions: U/Pb Dating of Closed-System Zircons: Science, v. 305, p. 1760–1763, doi: 10.1126/science.1101012.

Murray, R.W., Buchholtz ten Brink, M.R., Jones, D.L., Gerlach, D.C., and Russ, G.P., 1990, Rare earth elements as indicators of different marine depositional environments in chert and shale: Geology, v. 18, p. 268–271, doi: 10.1130/0091-7613(1990)018<0268:REEAIO>2.3.CO;2.

Mutschler, F.E., Larson, E.E., and Bruce, R.M., 1987, Laramide and younger magmatism in Colorado—New petrologic and tectonic variations on old themes, *in* Drexler, J.W., and Larson, E.E., eds., Cenozoic volcanism in the southern Rocky Mountains updated: A tribute to Rudy C. Epis—Part I: Colorado School of Mines Quarterly, v. 82, no. 4, p. 1–47.

Nadin, E.S., and Saleeby, J.B., 2008, Disruption of regional primary structure of the Sierra Nevada batholith by the Kern Canyon fault system, California: Geological Society of America Special Paper, v. 438, p. 438–15, doi: 10.1130/2008.2438(15).

Nadin, E.S., Saleeby, J., and Wong, M., 2016, Thermal evolution of the Sierra Nevada batholith, California, and implications for strain localization: Geosphere, v. 12, p. 377–399, doi: 10.1130/GES01224.1.

Nelson, W.R., Dorais, M.J., Christiansen, E.H., and Hart, G.L., 2013, Petrogenesis of Sierra Nevada plutons inferred from the Sr, Nd, and O isotopic signatures of mafic igneous complexes in Yosemite Valley, California: Contributions to Mineralogy and Petrology, v. 165, p. 397–417, doi: 10.1007/s00410-012-0814-9.

Nichols, K.K., Bierman, P.R., Foniri, W.R., Gillespie, A.R., Caffee, M., and Finkel, R., 2006, Dates and rates of arid region geomorphic processes: GSA Today, v. 16, p. 4–11, doi: 10.1130/GSAT01608.1.

Nyman, M.W., Karlstrom, K.E., Kirby, E., and Graubard, C.M., 1994, Mesoproterozoic contractional orogeny in western North America: Evidence from ca. 1.4 Ga plutons: Geology, v. 22, p. 901, doi: 10.1130/0091-7613(1994)022<0901:MCOIWN>2.3.CO;2.

Pakiser, L.C., Kane, M.F., and Jackson, W.H., 1964, Structural Geology and Volcanism of Owens Valley Region, California-A Geophysical Study: U.S. Geological Survey Professional Paper 438, p. 73.

Papanastassiou, D. a., and Wasserburg, G.J., 1969, Initial strontium isotopic abundances and the resolution of small time differences in the formation of planetary objects.: Earth and Planetary Science Letters, v. 5, p. 361–376, doi: 10.1016/S0012-821X(68)80066-4.

Plank, T., and Langmuir, C.H., 1998, The chemical composition of subducting sediment and its consequences for the crust and mantle: Chemical Geology, v. 145, p. 325–394, doi: 10.1016/S0009-2541(97)00150-2.

Parat, F., Dungan, M.A., and Lipman, P.W., 2005, Contemporaneous trachyandesitic and calc-alkaline volcanism of the Huerto Andesite, San Juan Volcanic Field, Colorado, USA: Journal of Petrology, v. 46, p. 859–891, doi: 10.1093/petrology/egi003.

Parker, D.F., Ghosh, A., Price, C.W., Rinard, B.D., Cullers, R.L., and Ren, M., 2005, Origin of rhyolite by crustal melting and the nature of parental magmas in the Oligocene Conejos Formation, San Juan Mountains, Colorado, USA: Journal of Volcanology and Geothermal Research, v. 139, p. 185–210, doi: 10.1016/j.jvolgeores.2004.08.015.

Parrish, R.R., 1987, An improved micro-capsule for zircon dissolution in U-Pb geochronology: Chemical Geology: Isotope Geoscience section, v. 66, p. 99–102, doi: 10.1016/0168-9622(87)90032-7.

Parrish, R.R., and Krogh, T.E., 1987, Synthesis and purification of ^{205}Pb for U-Pb geochronology: Chemical Geology: Isotope Geoscience section, v. 66, p. 103–110, doi: 10.1016/0168-9622(87)90033-9.

Pearson, R.C., Hedge, C.E., Thomeas, H.H., and Stern, T.W., 1966, Geochronology of the St. Kevin Granite and Neighboring Precambrian Rocks, Northern Sawatch Range, Colorado: Geological Society of America Bulletin, v. 77, p. 1109, doi: 10.1130/0016-7606(1966)77[1109:GOTSKG]2.0.CO;2.

Pettke, T., Oberli, F., and Heinrich, C.A., 2010, The magma and metal source of giant porphyry-type ore deposits, based on lead isotope microanalysis of individual fluid inclusions: Earth and Planetary Science Letters, v. 296, p. 267–277, doi: 10.1016/j.epsl.2010.05.007.

Putnam, R., Glazner, A.F., Coleman, D.S., Kylander-Clark, A.R.C., Pavelsky, T., and Abbot, M.I., 2015, Plutonism in three dimensions: Field and geochemical relations on the southeast face of El Capitan, Yosemite National Park, California: Geosphere, v. 11, p. 1133–1157, doi: 10.1130/GES01133.1.

Ranta, D.E., 1974, Geology, alteration, and mineralization of the Winfield (La Plata) district, Chaffee County, Colorado [Ph.D. dissertation]: Golden, Colorado School of Mines, 276 p.

Rapp, R.P., and Watson, E.B., 1995, Dehydration Melting of Metabasalt at 8-32 kbar: Implications for Continental Growth and Crust-Mantle Recycling: Journal of Petrology, v. 36, p. 891–931, doi: 10.1093/petrology/36.4.891.

Ratajeski, K., Glazner, A.F., and Miller, B. V, 2001, Geology and geochemistry of mafic to felsic plutonic rocks in the Cretaceous intrusive suite of Yosemite Valley, California: Geological Society of America Bulletin, v. 113, p. 1486–1502, doi: 10.1130/0016-7606(2002)114<0921.

Renne, P.R., Tobisch, O.T., and Saleeby, J.B., 1993, Thermochronologic record of pluton emplacement, deformation, and exhumation at Courtright shear zone, central Sierra Nevada, California: Geology, v. 21, p. 331–334, doi: 10.1130/0091-7613(1993)021<0331:TROPED>2.3.CO;2.

Renne, P.R., Balco, G., Ludwig, K.R., Mundil, R., and Min, K., 2011, Response to the comment by W.H. Schwarz et al. on "Joint determination of ^{40}K decay constants and ^{40}Ar*/^{40}K for the Fish Canyon sanidine standard, and improved accuracy for ^{40}Ar/^{39}Ar geochronology" by P.R. Renne et al. (2010): Geochimica et Cosmochimica Acta, v. 75, p. 5097–5100, doi: 10.1016/j.gca.2011.06.021.

Richards, J.P., 2009, Postsubduction porphyry Cu-Au and epithermal Au deposits: Products of remelting of subduction-modified lithosphere: Geology, v. 37, p. 247–250, doi: 10.1130/G25451A.1.

Richards, J.P., 2011, High Sr/Y arc magmas and porphyry Cu ?? Mo ?? Au deposits: Just add water: Economic Geology, v. 106, p. 1075–1081, doi: 10.2113/econgeo.106.7.1075.

Richardson, L.K., 1975, Geology of the Alabama Hills, California [M.S. thesis]: Reno, University of Nevada Reno, 159 p.

Riciputi, L.R., Johnson, C.M., Sawyer, D.A., and Lipman, P.W., 1995, Crustal and magmatic evolution in a large multicyclic caldera complex: isotopic evidence from the central San Juan volcanic field: Journal of Volcanology and Geothermal Research, v. 67, p. 1–28, doi: 10.1016/0377-0273(94)00097-Z.

Ricketts, J.W., Kelley, S.A., Karlstrom, K.E., Schmandt, B., Donahue, M.S., and van Wijk, J., 2016, Synchronous opening of the Rio Grande rift along its entire length at 25-10 Ma supported by apatite (U-Th)/He and fission-track thermochronology, and evaluation of possible driving mechanisms: Bulletin of the Geological Society of America, v. 128, p. 397–424, doi: 10.1130/B31223.1.

Riller, U., Petrinovic, I., Ramelow, J., Strecker, M., and Oncken, O., 2001, Late cenozoic tectonism, collapse caldera and plateau formation in the Central Andes: Earth and Planetary Science Letters, v. 188, p. 299–311, doi: 10.1016/S0012-821X(01)00333-8.

Roden, M.F., Smith, D., and Murthy, V.R., 1990, Chemical constraints on lithosphere composition and evolution beneath the Colorado Plateau: Journal of Geophysical Research, v. 95, p. 2811, doi: 10.1029/JB095iB03p02811.

Rooney, T.O., Sinha, A.K., Deering, C., and Briggs, C., 2010, A model for the origin of rhyolites from South Mountain, Pennsylvania: Implications for rhyolites associated with large igneous provinces: Lithosphere, v. 2, p. 211–220, doi: 10.1130/L89.1.

Rosera, J.M., Coleman, D.S., and Stein, H.J., 2013, Re-evaluating genetic models for porphyry Mo mineralization at Questa, New Mexico: Implications for ore deposition following silicic ignimbrite eruption: Geochemistry, Geophysics, Geosystems, v. 14, p. 787–805, doi: 10.1002/ggge.20048.

Rudnick, R.L., and Gao, S., 2003, 3.01 - Composition of the Continental Crust: Treatise on Geochemistry, v. 1, p. 1–64, doi: http://dx.doi.org/10.1016/B0-08-043751-6/03016-4.

Rüpke, L.H., Morgan, J.P., Hort, M., and Connolly, J.A.D., 2004, Serpentine and the subduction zone water cycle: Earth and Planetary Science Letters, v. 223, p. 17–34, doi: 10.1016/j.epsl.2004.04.018.

Saleeby, J.B., and Busby, C., 1993, Paleogeographic and tectonic setting of axial and western metamorphic framework rocks of the southern Sierra Nevada, California, *in* Mesozoic Paleogeography of the Western United States-II: Pacific Section, Society of Sedimentary Geology (SEPM), Book 71, p. 197–226.

Saleeby, J.B., Ducea, M.N., Busby, C.J., Nadin, E.S., and Wetmore, P.H., 2008, Chronology of pluton emplacement and regional deformation in the southern Sierra Nevada batholith, California, in Wright, J.E., and Shervais, J.W., eds., Ophiolites, arcs and batholiths: A tribute to Cliff Hopson: Geological Society of America Special Paper 438, p. 397–427, doi: 10.1130/2008 .2438(14).

Samperton, K.M., Schoene, B., Cottle, J.M., Keller, C.B., Crowley, J.L., and Schmitz, M.D., 2015, Magma emplacement, differentiation and cooling in the middle crust: Integrated zircon geochronological-geochemical constraints from the Bergell Intrusion, Central Alps: Chemical Geology, v. 417, p. 322–340, doi: 10.1016/j.chemgeo.2015.10.024.

Sawka, W.N., Banfield, J.F., and Chappell, B.W., 1986, A weathering-related origin of widespread monazite in S-type granites: Geochimica et Cosmochimica Acta, v. 50, p. 171–175, doi: 10.1016/0016-7037(86)90062-1.

Schaltegger, U., Schmitt, A.K., and Horstwood, M.S.A., 2015, U–Th–Pb zircon geochronology by ID-TIMS, SIMS, and laser ablation ICP-MS: Recipes, interpretations, and opportunities: Chemical Geology, v. 402, p. 89–110, doi: 10.1016/j.chemgeo.2015.02.028.

Schermer, E.R., and Busby, C., 1994, Jurassic magmatism in the central Mojave Desert: Implications for arc paleogeography and preservation of continental volcanic sequences: Geological Society of America Bulletin, v. 106, p. 767–790, doi: 10.1130/0016-7606(1994)106<0767:JMITCM>2.3.CO;2.

Schmitz, M.D., and Bowring, S.A., 2001, U-Pb zircon and titanite systematics of the Fish Canyon Tuff: An assessment of high-precision U-Pb geochronology and its application to young volcanic rocks: Geochimica et Cosmochimica Acta, v. 65, p. 2571–2587, doi: 10.1016/S0016-7037(01)00616-0.

Shannon, J.R., 1988, Geology of the Mount Aetna cauldron complex, Sawatch Range, Colorado [Ph.D. dissertation]: Golden, Colorado School of Mines, 456 p.

Shannon, J.R., Nelson, E.P., and Golden, R.J., Jr., 2004, Surface and underground geology of the world-class Henderson molybdenum porphyry mine, Colorado, *in* Nelson, E.P., and Erslev, E.A., eds., Field trips in the southern Rocky Mountains, USA: Geological Society of America Field Guide 5, p. 207–218, doi: 10.1130 /0-8137-0005-1.207.

Simmons, E.C., and Hedge, C.E., 1978, Minor-element and Sr-isotope geochemistry of tertiary stocks, Colorado mineral belt: Contributions to Mineralogy and Petrology, v. 67, p. 379–396, doi: 10.1007/BF00383298.

Sisson, T.W., and Moore, J.G., 1994, Geologic map of the Giant Forest quadrangle, Tulare County, California: U.S. Geological Survey Geologic Quadrangle Map GQ-1751, scale 1:62,500.

Sisson, T.W., Grove, T.L., and Coleman, D.S., 1996, Hornblende gabbro sill complex at Onion Valley, California, and a mixing origin for the Sierra Nevada batholith: Contributions to Mineralogy and Petrology, v. 126, p. 81–108, doi: 10.1007/s004100050237.

Sisson, T.W., Ratajeski, K., Hankins, W.B., and Glazner, A.F., 2005, Voluminous granitic magmas from common basaltic sources: Contributions to Mineralogy and Petrology, v. 148, p. 635–661, doi: 10.1007/s00410-004-0632-9.

Sliwinski, J.T., Bachmann, O., Dungan, M.A., Huber, C., Deering, C.D., Lipman, P.W., Martin, L.H.J., and Liebske, C., 2017, Rapid pre-eruptive thermal rejuvenation in a large silicic magma body: the case of the Masonic Park Tuff, Southern Rocky Mountain volcanic field, CO, USA: Contributions to Mineralogy and Petrology, v. 172, p. 30, doi: 10.1007/s00410-017-1351-3.

Stacey, J.S., and Kramers, J.D., 1975, Approximation of terrestrial lead isotope evolution by a two-stage model: Earth and Planetary Science Letters, v. 26, p. 207–221, doi: 10.1016/0012-821X(75)90088-6.

Stein, H.J., 1985, A lead, strontium, and sulfur isotope study of Laramide-Tertiary intrusions and mineralization in the Colorado Mineral Belt with emphasis on Climax-type porphyry molybdenum systems plus a summary of other newly acquired isotopic and rare earth element data [Ph.D. dissertation]: Chapel Hill, University of North Carolina at Chapel Hill, 506 p.

Stein, H.J., and Hannah, J., 1985, Movement and origin of ore fluids in Climax-type systems: Geology, v. 13, p. 469–474, doi: 10.1130/0091-7613(1985)13<469:MAOOOF>2.0.CO;2.

Stein, H.J., and Crock, J.G., 1990, Late Cretaceous-Tertiary magmatism in the Colorado Mineral Belt; Rare earth element and samarium-neodymium isotopic studies, *in* Anderson, J.L. ed., The nature and origin of Cordilleran magmatism, Geological Society of America Memoir 174, p. 195–223, doi: 10.1130/MEM174-p195.

Sorensen, S.S., Dunne, G.C., Hanson, R.B., Barton, M.D., Becker, J., Tobisch, O.T., and Fiske, R.S., 1998, From Jurassic shores to Cretaceous plutons: Geochemical evidence for paleoalteration environments of metavolcanic rocks, eastern California: Bulletin of the Geological Society of America, v. 110, p. 326–343, doi: 10.1130/0016-7606(1998)110<0326:FJSTCP>2.3.CO;2.

Staudigel, H., Davies, G.R., Hart, S.R., Marchant, K.M., and Smith, B.M., 1995, Large scale isotopic Sr, Nd and O isotopic anatomy of altered oceanic crust: DSDP/ ODP sites417/418: Earth and Planetary Science Letters, v. 130, p. 169–185, doi: 10.1016/0012-821X(94)00263-X.

Stearns, M.A., and Bartley, J.M., 2014, Multistage emplacement of the McDoogle pluton, an early phase of the John Muir intrusive suite, Sierra Nevada, California, by magmatic crack-seal growth: Bulletin of the Geological Society of America, v. 126, p. 1569–1579, doi: 10.1130/B31062.1.

Stern, T.W., Bateman, P.C., Morgan, B.A., Newell, M.F., and Peck, D.L., 1981, Isotopic U-Pb Ages of Zircon from the Granitoids of the Central Sierra Nevada , California: Geological Survey Professional Paper, v. 1185, p. 17.

Stevens, C., Stone, P., and Blakely, R., 2013, Structural Evolution of the East Sierra Valley System (Owens Valley and Vicinity), California: A Geologic and Geophysical Synthesis: Geosciences, v. 3, p. 176–215, doi: 10.3390/geosciences3020176.

Stevens, G., Villaros, A., and Moyen, J.F., 2007, Selective peritectic garnet entertainment as the origin of geochemical diversity in S-type granites: Geology, v. 35, p. 9–12, doi: 10.1130/ G22959A.1.

Stone, P., Dunne, G.C., Moore, J.G., and Smith, G.I., 2000, Geologic Map of the Lone Pine 15’ Quadrangle, Inyo County, California: U.S. Geological Survey Geologic Investigations Series Map I-2617, scale 1:62,500.

Tanaka, T., Togashi, S., Kamioka, H., Amakawa, H., Kagami, H., Hamamoto, T., Yuhara, M., Orihashi, Y., Yoneda, S., Shimizu, H., Kunimaru, T., Takahashi, K., Yanagi, T., Nakano, T., et al., 2000, JNdi-1: A neodymium isotopic reference in consistency with LaJolla neodymium: Chemical Geology, v. 168, p. 279–281, doi: 10.1016/S0009-2541(00)00198-4.

Tappa, M.J., Coleman, D.S., Mills, R.D., and Samperton, K.M., 2011, The plutonic record of a silicic ignimbrite from the Latir volcanic field, New Mexico: Geochemistry, Geophysics, Geosystems, v. 12, doi: 10.1029/2011GC003700.

Thompson, R.A., Johnson, C.M., and Mehnert, H.H., 1991, Oligocene basaltic volcanism of the Northern Rio Grande Rift: San Luis Hills, Colorado: Journal of Geophysical Research: Solid Earth, v. 96, p. 13577–13592, doi: 10.1029/91JB00068.

Tikoff, B., and Teyssier, C., 1992, Crustal-scale, en echelon "P-shear" tensional bridges: A possible solution to the batholithic room problem: Geology, v. 20, p. 927–930, doi: 10.1130/0091-7613(1992)020<0927.

Tikoff, B., and de Saint Blanquat, M., 1997, Transpressional shearing and strike-slip partitioning in the Late Cretaceous Sierra Nevada magmatic arc, California: Tectonics, v. 16, p. 442, doi: 10.1029/97TC00720.

Tobisch, O.T., Saleeby, J.B., and Fiske, R.S., 1986, Structural history of continental volcanic arc rocks, eastern Sierra Nevada, California: A case for extensional tectonics: Tectonics, v. 5, p. 65–94, doi: 10.1029/TC005i001p00065.

Tobisch, O.T., Renne, P.R., and Saleeby, J.B., 1993, Deformation resulting from regional extension during pluton ascent and emplacement, central Sierra Nevada, California: Journal of Structural Geology, v. 15, p. 609–628, doi: 10.1016/0191-8141(93)90151-Y.

Tobisch, O.T., Saleeby, J.B., Renne, P.R., McNulty, B., and Tong, W., 1995, Variations in deformation fields during development of a large-volume magmatic arc, central Sierra Nevada, California: Geological Society of America Bulletin, v. 107, p. 148–166, doi: 10.1130/0016-7606(1995)107<0148.

Truschel, J.P., 1996, Petrogenesis of the Fine Gold intru- sive suite, Sierra Nevada Batholith, California [M.S. thesis]: Northridge, California State University, 137 p.

Tweto, O., and Sims, P.K., 1963, Precambrian Ancestry of the Colorado Mineral Belt: Geological Society of America Bulletin, v. 74, p. 991, doi: 10.1130/0016-7606(1963)74[991:PAOTCM]2.0.CO;2.

Unruh, J., Humphrey, J., and Barron, A., 2003, Transtensional model for the Sierra Nevada frontal fault system, eastern California: Geology, v. 31, p. 327–330, doi: 10.1130/0091-7613(2003)031<0327:TMFTSN>2.0.CO;2.

Valley, J.W., 2003, Oxygen isotopes in zircon: Reviews in mineralogy and geochemistry, v. 53, p. 343–385.

Valley, J.W., Kitchen, N., Kohn, M.J., Niendorf, C.R., and Spicuzza, M.J., 1995, UWG-2, a garnet standard for oxygen isotope ratios: Strategies for high precision and accuracy with laser heating: Geochimica et Cosmochimica Acta, v. 59, p. 5223–5231, doi: 10.1016/0016-7037(95)00386-X.

Valley, J.W., Kinny, P.D., Schulze, D.J., and Spicuzza, M.J., 1998, Zircon megacrysts from kimberlite: oxygen isotope variability among mantle melts: Contributions to Mineralogy and Petrology, v. 133, p. 1–11, doi: 10.1007/s004100050432.

Villaros, A., Stevens, G., Moyen, J.-F., and Buick, I.S., 2009, The trace element compositions of S-type granites: evidence for disequilibrium melting and accessory phase entrainment in the source: Contributions to Mineralogy and Petrology, v. 158, p. 543–561, doi: 10.1007/s00410-009-0396-3.

Villaros, A., Buick, I.S., and Stevens, G., 2012, Isotopic variations in S-type granites: An inheritance from a heterogeneous source? Contributions to Mineralogy and Petrology, v. 163, p. 243–257, doi: 10.1007/s00410-011-0673-9.

Vogt, P.R., 1974, Volcano spacing, fractures, and thickness of the lithosphere: Earth and Planetary Science Letters, v. 21, p. 235–252, doi: 10.1016/0012-821X(74)90159-9.

von Huene, R., and Scholl, D.W., 1991, Observations at convergent margins concerning sediment subduction, subduction erosion, and the growth of continental crust: Reviews of Geophysics, v. 29, p. 279–316, doi: 10.1029/91RG00969.

von Quadt, A., Erni, M., Martinek, K., Moll, M., Peytcheva, I., and Heinrich, C.A., 2011, Zircon crystallization and the lifetimes of ore-forming magmatic-hydrothermal systems: Geology, v. 39, p. 731–734, doi: 10.1130/G31966.1.

Wahrhaftig, C., 2000, Geologic map of the Tower Peak quadrangle, central Sierra Nevada, California: U.S. Geological Survey Investigations Series I-2697, scale 1:62,500.

Watson, E.B., and Harrison, T.M., 1983, Zircon saturation revisited: temperature and composition effects in a variety of crustal magma types: Earth and Planetary Science Letters, v. 64, p. 295–304, doi: 10.1016/0012-821X(83)90211-X.

Weis, D., Kieffer, B., Maerschalk, C., Barling, J., De Jong, J., Williams, G.A., Hanano, D., Pretorius, W., Mattielli, N., Scoates, J.S., Goolaerts, A., Friedman, R.M., and Mahoney, J.B., 2006, High-precision isotopic characterization of USGS reference materials by TIMS and MC-ICP-MS: Geochemistry, Geophysics, Geosystems, v. 7, doi: 10.1029/2006GC001283.

Wenner, J.M., and Coleman, D.S., 2003, U-Pb zircon ages for high-silica granites in the central Sierra Nevada batholith: implications for crustal generation in continental arcs: Geological Society of America Abstracts with Programs, v. 35, no. 6, p. 326.

Wenner, J.M., and Coleman, D.S., 2004, Magma Mixing and Cretaceous Crustal Growth: Geology and Geochemistry of Granites in the Central Sierra Nevada Batholith, California: International Geology Review, v. 46, p. 880–903, doi: 10.2747/0020-6814.46.10.880.

Wesnousky, S.G., and Jones, C.H., 1994, Oblique slip, slip partitioning, spatial and temporal changes in the regional stress field, and the relative strengths of active faults in the Basin and Range, western United States: Geology, v. 22, p. 1031–1034.

Whitney, J.D., 1872, The Owens Valley Earthquake, Part I: Overland Monthly, v. 9, no. 2, p. 130-140.

Wilshire, H.G., 1969, Mineral Layering in the Twin Lakes Granodiorite, Colorado, *in* Larsen, L.H., Prinz, M., and Manson, V. eds., Igneous and Metamorphic Geology: Geological Society of America Memoirs 115, p. 235–262, doi: 10.1130/MEM115-p235.

Wilson, A.B., and Sims, P.K., 2003, Colorado Mineral Belt revisited - An analysis of new data: U.S. Geological Survey Open-File Report 2003–46, 7 p.

Wooden, J.L., and Mueller, P.A., 1988, Pb, Sr, and Nd isotopic compositions of a suite of Late Archean, igneous rocks, eastern Beartooth Mountains: implications for crust-mantle evolution: Earth and Planetary Science Letters, v. 87, p. 59–72, doi: 10.1016/0012-821X(88)90064-7.

Wotzlaw, J.F., Schaltegger, U., Frick, D.A., Dungan, M.A., Gerdes, A.G., and Günther, D., 2013, Tracking the evolution of large-volume silicic magma reservoirs from assembly to supereruption: Geology, v. 41, p. 867–870, doi: 10.1130/G34366.1.

Zeng, L., Saleeby, J.B., and Ducea, M., 2005, Geochemical characteristics of crustal anatexis during the formation of migmatite at the Southern Sierra Nevada, California: Contributions to Mineralogy and Petrology, v. 150, p. 386–402, doi: 10.1007/s00410-005-0010-2.

Zimmerer, M.J., and McIntosh, W.C., 2012, An investigation of caldera-forming magma chambers using the timing of ignimbrite eruptions and pluton emplacement at the Mt. Aetna caldera complex: Journal of Volcanology and Geothermal Research, v. 245–246, p. 128–148, doi: 10.1016/j.jvolgeores.2012.08.007.